HEINRICH HEINE
UNIVERSITÄT DÜSSELDORF

Dynamically asymmetric colloids under external constraints

Inaugural-Dissertation

zur Erlangung des Doktorgrades
der Mathematisch-Naturwissenschaftlichen Fakultät
der Heinrich-Heine-Universität Düsseldorf

vorgelegt von

Tatjana Sentjabrskaja

aus **Soligorsk, Weißrussland**

Düsseldorf, September 2015

aus dem Institut für experimentelle Physik der kondensierten Materie
der Heinrich-Heine-Universität Düsseldorf,
betreut durch Dr. Marco Laurati und Prof. Dr. Stefan U. Egelhaaf

Gedruckt mit Genehmigung
der Mathematisch-Naturwissenschaftlichen Fakultät der
Heinrich-Heine-Universität Düsseldorf

Referent: Prof. Dr. Stefan U. Egelhaaf
Koreferent: Prof. Dr. Jürgen Horbach
Tag der mündlichen Prüfung: 02.11.2015

Summary

Colloids are particles in a solvent which, due to their size in the nano- to micrometer range, undergo Brownian motion and are very susceptible to external forces. Their size is comparable to the wavelength of light, which allows us to follow individual particle under the optical microscope. Because they behave like large atoms, colloidal dispersions have evolved into fascinating model systems to study fundamental physical problems. Furthermore, they are found in many industrial and natural products giving them a vast industrial and technological importance.

At very high packing fractions, colloidal hard spheres enter a non-equilibrium glass state, which is characterized by arrested dynamics. Despite the simplicity of this system, many facets of the nature of the glass transition have eluded a satisfactory explanation so far. In particular, a detailed microscopic picture of the arrest mechanism, which is expected to be governed by „caging“ through neighboring particles, and how these cages can be broken and ergodicity restored still has to be explored.

Here we follow two strategies to investigate glassy dynamics. We use binary hard-sphere mixtures with large dynamical asymmetry, which allow us to experimentally explore and contrast different caging mechanisms: for example, the large particles can be caged by large or small particles. Furthermore, we expose these mixtures to strong external constraints, namely shear, to push the systems far from their quiescent state and observe the shear-induced enhancement of the dynamics. The recently developed rheoscopy enables us to follow the particles in situ by confocal microscopy while they are exposed to external shear. We find that different caging mechanisms can lead to different glass states that have very distinct properties, like structure, dynamics or viscoelastic moduli. These caging mechanisms, together with the short- and long-time single particle dynamics as well as dynamical heterogeneities, are also responsible for the different yielding behaviors, i.e. transitions to flow.

Finally, we have investigated the dynamics of dilute small particles confined by dense large spheres. Very small tracer particles can pass through the narrow channels between large spheres, whereas larger tracers become increasingly localized. Due to the motion of the large particles, however, localization is never perfect and results in slow anomalous dynamics of the tracers. The competition between localization and diffusion has been found to result in a logarithmic decay of the intermediate scattering function of the tracer particles. The dynamics of the tracer particles could only be determined thanks to a novel combination of fluorescent labeling methods, confocal microscopy and differential dynamic microscopy, which was combined during this PhD.

Contents

1. Introduction

1.1. What is soft matter?

Tooth paste, mud, plastic bags, DNA and soap have a lot in common: they constitute examples of Soft Matter systems. Characteristic of such systems is that the size of their building blocks or of their structures are mesoscopic: smaller than a grain of sand and much larger than a simple molecule, hence their size is in the range of a few nanometers to a few microns. With the exception of systems like polymer melts, the entities are typically embedded in a solvent, for example water. Compared to atomic systems, soft matter assemblies consist of large building blocks, resulting in a small energy density and a small elastic modulus. Consequently soft matter systems can be easily deformed, while exhibiting a strong response to small external forces [1].

Soft matter systems also include complex fluids such as solutions of amphiphilic molecules, polymers and colloids, – numerous examples can be found in nature and technology. Soft matter also constitutes the very basis for any biological system, since a living cell is a well-orchestrated system composed of a plethora of soft matter subsystems. For instance, the cell membrane consists of a bilayer of surfactant molecules decorated by various membrane proteins, whereas the cell cortex is in the first place a dense polymeric network. The cell inside, i.e. the cytoplasm, can be viewed as a dense colloidal suspension, dispersed in a matrix of actin filaments and microtubules, resembling a concentrated polymer solution.

1.2. Colloids

Colloids are particles ranging in size from 1 nm to 10 µm and are small enough to display significant thermal agitation, i.e. Brownian motion, and on the other hand are much bigger than the molecules of the dispersion medium, which can thus be viewed as a continuum. Although the fluid surrounding the colloids appears as a structureless continuum, it drives the motion of the colloids. Brownian motion performed by particles is the random motion and originates from collisions of the solvent molecules with the

particles. For very dilute solution of particles, the probability that the particle moves a distance $\Delta\vec{r}$ in a lag time t is Gaussian distributed. In the general case the probability distribution of displacements, also referred to as van Hove (self-correlation) function, is defined via

$$p(\Delta\vec{r},t) := \langle \frac{1}{N}\sum_{i=1}^{N} \delta(\Delta\vec{r} - (\vec{r}_i(t+t_0) - \vec{r}_i(t_0))\rangle. \tag{1.1}$$

Here $\langle ... \rangle$ indicates a temporal average over different initial times t_0, $\vec{r}_i(t)$ denotes the position of particle i at time t, and N is the total number of colloidal particles in the suspension. In particular, all moments of the time-dependent random displacement $\Delta\vec{r}(t)$ are encoded in the van Hove function $p(\Delta\vec{r},t)$. If the particle motion is isotropic, the probability for a displacement in each direction is equal, in particular, the average displacement $\langle\Delta\vec{r}(t)\rangle$ vanishes identically. Hence, the simplest non-trivial characterization of the particle dynamics is the mean-squared displacement (MSD)

$$\langle\Delta\vec{r}(t)^2\rangle = \langle \frac{1}{N}\sum_{i=0}^{N} (\vec{r}_i(t+t_0) - \vec{r}_i(t_0))^2\rangle. \tag{1.2}$$

Einstein showed in his seminal work on the molecular kinetic interpretation of Brownian motion that for diffusive dynamics the mean-squared displacement is proportional to time, $\langle\Delta\vec{r}(t)^2\rangle = 2dDt$, where d is the dimension of the embedding space. The transport coefficient characterizing the increase of the MSD is referred to as diffusion coefficient D.

Colloidal dispersions exhibit many phenomena known also from molecular systems, such as a gas-liquid phase transition, crystallization, and vitrification. Therefore colloids are used as a model system to study physical phenomena of atomic materials. Due to their huge size in comparison to atoms and the induced slow dynamics of colloids, they can be studied by small-scale lab techniques such as light scattering or optical microscopy, whereas for atomic systems the use of large-scale techniques, e.g. X-rays or neutron scattering becomes unavoidable. Moreover, the slow dynamics of colloids offers the opportunity to monitor directly the trajectories of single particles. Yet, the interest in colloidal systems is not limited to the use as model systems for atomic systems. In contrast to atoms, where the interaction potential is determined by the electronic structure, the interactions between colloidal particles can be of various origins and can be manipulated and controlled by smart surface chemistry and a clever choice of the solvent.

1.3. Colloidal hard spheres

The simplest interaction between spherical particles is provided by the hard-sphere potential: the interaction potential becomes infinite when the distance between particles is smaller than the particle size, i.e. they cannot overlap, and is zero otherwise [2–4]. Thus they behave as an assembly of billiard balls, yet their macroscopic behavior is dominated by thermal fluctuations rather than gravity. The hard-sphere repulsion constitutes an idealization of the interparticle interaction focusing on the mutual exclusion, while ignoring the attractive part of the potential at intermediate length scales. Surprisingly, hard spheres still contain virtually all the relevant physics and therefore are an ideal playground for theoretical models, computer simulations, and experiments [5,6].

Experimentally, the hard-sphere interaction potential is realized to a good approximation in a system of sterically stabilized polymethylmethacrylate (PMMA) particles. Without any stabilization, PMMA particles tend to aggregate due to the attraction caused by van-der-Waals forces [7,8]. One possibility to achieve stabilization is by coating the colloids with a thin layer of polymer chains [9]. The polymer chains are chemically attached to the surface and build a brush around the colloid core. If two particles are getting close to each other, the polymer brushes start to interdigitate. This leads to a reduction of the configurational entropy of the chains and, as a result, to an effective repulsion between the chains. Consequently, the van-der-Waals attraction becomes balanced by a short-range repulsion caused by the polymer brush. In this work, the sterically stabilized PMMA particles are dispersed in a mixture of bromocycloheptane (CHB) and cis-Decahydronaphthalene (cis-decalin). Mixing of the two solvents, one (cis-decalin) with a density below the particle density and the second one (CHB) above, allows matching the density of the particles to the density of the surrounding solution, thereby suppressing the effects of gravity. Moreover, the refractive index of the solvent mixture matches the refractive index of the particles, resulting in a reduction of the van-der-Waals forces and virtually eliminating multiple scattering (the dispersion becomes almost transparent). In CHB the PMMA particles become slightly charged, with the consequence of an additional long-range repulsion between them, yet this can be circumvented by adding a small amount of salt, in our case tetrabutylammoniumchloride [10], to screen the residual charges.

1.4. Colloidal glass

Since in hard-sphere systems all accessible configurations have the same potential energy, temperature sets merely the time scale in dynamical processes while being irrelevant for the thermodynamic and structural behavior. Hence, the particle density $n = N/V$ is the single control parameter determining the phase behavior of a colloidal hard-sphere dispersion, a convenient dimensionless measure is the packing fraction

$$\phi = \frac{V_{\text{particles}}}{V} = \frac{\pi}{6} n\sigma^3, \tag{1.3}$$

with $V_{\text{particles}} = N\pi\sigma^3/6$ the volume occupied by N spheres of exclusion diameter σ and V the total sample volume. The most compact way to arrange spheres in a disordered structure is the random close packing which results in a volume fraction $\phi_{\text{RCP}} \approx 0.64$ for monodisperse spheres [11–13]. Depending on ϕ, monodisperse hard spheres assemble in different equilibrium phases or non-equilibrium states [5]. A fluid phase with amorphous structure and diffusive dynamics of particles is found for $\phi < 0.49$, while increasing concentration, $0.49 < \phi < 0.54$, leads to fluid-crystal coexistence, followed by full crystallization for $\phi > 0.54$. In the liquid-crystal phase transition the structure of the system changes from the amorphous structure of the liquid to the ordered structure of the crystal.

A rapid increase of particle concentration from the fluid to the region where the crystal is the thermodynamic equilibrium state, leads to the formation of an additional, non-equilibrium state, a colloidal glass. The free volume accessible for rearrangement in a liquid becomes smaller by increasing ϕ. At a critical volume fraction $\phi \approx 0.58$ the free volume becomes too small and the rearrangement becomes postponed to longer and longer times — the hallmark of a glass. The same phenomenon occurs in molecular liquids by a rapid quench to low temperatures. Unlike the crystalline phase, a colloidal glass is characterized by an amorphous liquid-like structure, where each particle is surrounded by a shell of neighbors, inhibiting large excursions of the particle. Hence particles are transiently caged by their neighbors, which in turn are trapped by their respective neighbors [14–16]. Due to the dramatical reduction of free volume, the particles perform essentially only movements within their cage and may escape from it only after some much longer time. A further increase in concentration reduces the probability of escaping from the cage, the particles stay in their cages for an increasingly longer time, and no long-range motion is observed on experimental time scales. The transition from a liquid to a glass state is recognized as a dynamical arrest transition without any qualitative change in the structure, at least at the level of the pair distribution

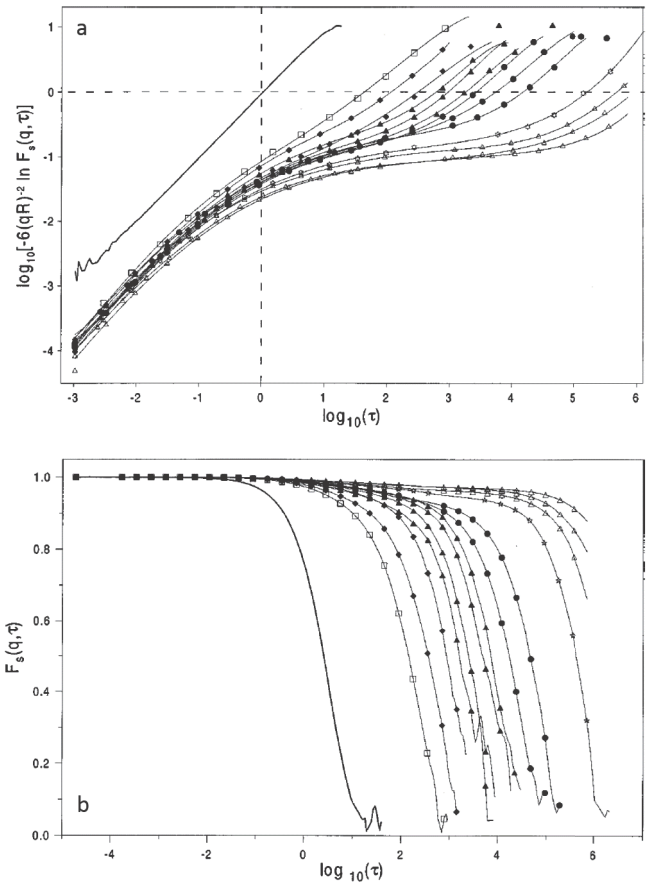

Figure 1.1.: a) Logarithm of particle mean-squared displacement and b) intermediate scattering function $F_s(q,\tau)$ versus logarithm of time τ for latex/silica spheres in suspensions. Each line corresponds to a different volume fraction, increasing from left to right. The solid line without symbols corresponds to a dilute solution where particles freely diffuse. Taken from Ref.[19]

function[5,17,18].

The qualitative changes in the dynamics of the particles have been thoroughly studied. Amongst others, it was shown in light scattering experiments[17] and molecular dynamics simulations[20] that the approach to the glass transition is associated with an increase of the structural relaxation time of the system by many orders of magnitude[21]. This is also reflected in the evolution of the mean-squared displacement[19] (see Figure 1.1 a). In a dilute solution of colloidal particles, free diffusion is characterized by a linear increase of the MSD with time. For larger concentrations, where particles are temporary caged, a linear increase of the MSD can be observed as well, but only at short times, corresponding to in-cage Brownian motion. At later times, where the average displacement reaches

the size of the cage, the free motion becomes hindered by the collisions with neighboring particles and only motion within the cage is possible. The caging effect leads to a sub-linear increase or a plateau, indicating particle localization. The time window over which this plateau is observed becomes longer with increasing concentration in hard-sphere colloidal systems, or decreasing temperature in other kinds of glassy materials. For larger times, where particles are eventually able to escape the cage, a second linear regime corresponding to diffusion out of the cage is observed. The process associated with the breaking of the cage is referred to as α- or structural relaxation. Increasing the concentration makes the escape from the cages very difficult or even impossible, so that the plateau extends to very long times.

The cage effect can be inferred from the intermediate scattering function (ISF) which is given by

$$f(q,t) = \langle \exp(i\vec{q} \cdot \Delta\vec{r}(t) \rangle, \tag{1.4}$$

where $\langle ... \rangle$ indicates ensemble averages and $\Delta\vec{r}(t)$ is the displacement of a particle in time t. It initially decays for short times (β-relaxation due to the short-time in-cage Brownian motion), but then shows a plateau, indicating localization of the dynamics [17,20] (see Figure 1.1 b). At low concentrations from time to time an opening of the cage, due to the movement of the particles building the cage, may occur. This allows particles to escape from the cage after some time and leads to a second decay of the ISF, the α relaxation. This shifts to longer times when approaching the glass transition, eventually exceeding the experimental time scales.

Besides the effect of dynamical arrest, which has been observed in several studies, further phenomena are associated with the glass transition [22]. One of them is dynamical heterogeneity, studied by computer simulations, theory and experiments [23–25]. It was shown that the individual dynamics of each particle may be different (spatial and transient) from the other particles. This indicates that the average structural relaxation of the system is related to a broad distribution of local relaxation events. The distribution of particle displacements, quantified by the van Hove function, shows a deviation from the Gaussian behavior which would be expected for isotropic diffusion [18,23,26] (see Figure 1.2). These findings indicate the existence of particle populations with mobility higher than average. The rather exponential instead of Gaussian shape of the tails of the van Hove functions measured in glasses implies a qualitative deviation of the relaxation mechanism in glassy systems from the diffusion-driven mechanism of normal liquids.

Colloidal glasses are an example of glassy materials. The most famous and best-known example of a glassy material is silicate glass, which is used for windows. Different from a colloidal glass, the temperature, instead of particle concentration, is the natural con-

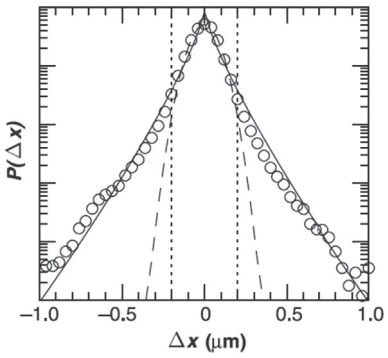

Figure 1.2.: Van Hove function $P(\Delta x)$ for a suspension of hard spheres at volume fraction $\phi = 0.56$. The best fit Gaussian is represented by the dashed line. The solid line corresponds to a fit of a stretched exponential. From Ref.[18]

trol parameter for the slowing down of the dynamics, which, in addition, is Newtonian instead of Brownian. Further examples for glassy materials are polymers, for instance polycarbonates which are used as a substrate for compact discs, plexiglass and styrofoam. Also metallic glasses have been investigated extensively, primarily because their mechanical and magnetic properties are used in electronics, aeronautics and medicine. In all cases, the glassy systems are characterized by the presence of long lived non-equilibrium metastable states.

1.5. Flow behavior of colloidal glasses

Beyond the quiescent properties of glasses, their behavior under application of a mechanical deformation, for example shear, is of great interest. Indeed, in many applications glass-forming systems need to flow to be able to process them. The application of shear to a dense suspension of colloids leads to a competition between the internal slow relaxation process and the time scale imposed by the external driving. One consequence of this competition is that the strongly sheared systems relax faster than those which are only weakly or not sheared. Consequently, the viscosity η of the fluidized material depends on the shear rate $\dot{\gamma}$. Simultaneously the structural relaxation time of a sheared dispersion is decreased. In a glass the acceleration of the dynamics leads to fluidization. In the flowing steady state the glass loses the memory about its prior structural configuration[27] (but not completely). In a glass at low shear rates the stress becomes independent of $\dot{\gamma}$, indicating the divergence of the viscosity and the presence of a finite yield stress $\sigma_y(\dot{\gamma} \to 0)$[28] (see Figure 1.3 a).

From rest to steady shear flow, transient phenomena are observed. After applying

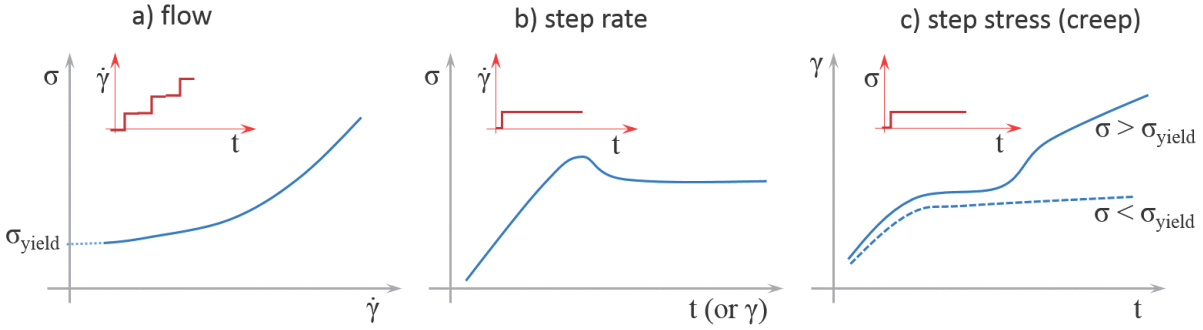

Figure 1.3.: Schematical representation of typically measured signal for colloidal glasses using different shear protocols.

a shear with a constant rate of deformation, a stress overshoot is observed in stress-strain curves for intermediate times [29–31] (see Figure 1.3 b). The magnitude of the stress overshoot shows a dependence on the imposed shear rate, age of the system and the distance to the glass transition. Moreover, the study of the microscopic structure show the build-up of structural anisotropy indicating shear-induced cage deformation [29]. The cages become elongated and the maximum cage deformation coincides with the occurrence of the stress overshoot. Super-diffusive dynamics sets in when the particles can leave the cages due to the breakdown following cage deformation.

Instead of a constant shear rate, a constant stress can be applied to a glass (see Figure 1.3 c). The response of the glasses to the applied stress can be divided into different regimes. The appearance of the regimes depends on the magnitude of the applied stress, time and the age of the system. It was shown that a fluidization of the glass, indicated by a linear increase of the strain over time, can only be achieved by a stress larger than the yield stress of the system [32]. Before the steady state of flow is reached, a transient super-linear increase of $\gamma(t)$ can be observed. In contrast to that, for stresses below the yield stress, no flow behavior can be found. Instead, the creep regime with a very slow, sub-linear increase of $\gamma(t)$ is observed. The creep behavior can also be found in other systems, soft-matter as well as hard-matter systems [8,33,34]. The microscopic picture related to the absence of flow and the creep response is still incomplete.

1.6. Model system

In this study two component dispersions called binary mixtures are used as a model system. Different kinds of glasses, like attractive and repulsive glasses, and dense fluids can be obtained and systematically studied in the framework of a single model system.

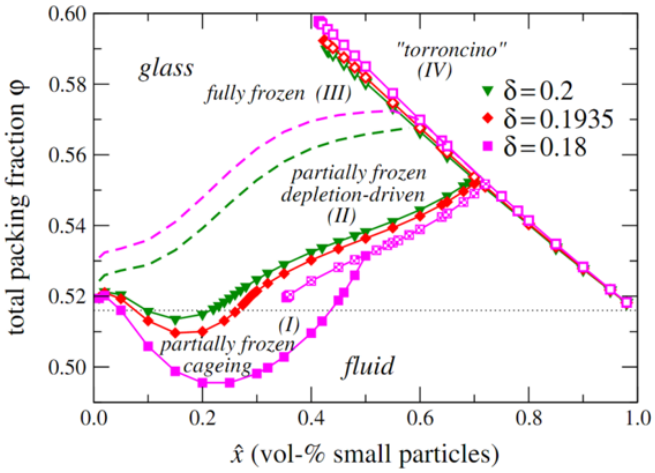

Figure 1.4.: State diagram of binary hard-sphere mixtures obtained from mode-coupling theory for different size ratios δ, as indicated. From Ref.[35]

Binary mixtures with their three-dimensional non-equilibrium state diagram offer a wide research field for the study of flow behavior of dense fluids and glasses.

The phase behavior of binary mixtures is determined by three control parameters. These are the size ratio

$$\delta = \frac{R_{Small}}{R_{Large}}, \tag{1.5}$$

with R_{Small} and R_{Large} the radius of small and large particles, respectively, the composition of mixture

$$x_s = \frac{V_{Small}}{V_{Particles}}, \tag{1.6}$$

with V_{Small} the volume of small particles, and the total volume fraction ϕ given by Eq. (1.3).

Binary mixtures at different size ratios and volume fractions were studied previously. It was found that in binary mixtures the volume fraction ϕ_{RCP}, at which random closed packing is occurring, shifts to larger values demonstrating a more efficient packing ability of mixtures compared to one-component systems[41]. Keeping the total volume fraction constant, the more efficient packing ability at intermediate mixing compositions leads to plasticization: the glass transition for mixtures occurring at larger total volume fractions[42,43].

For size disparity $\delta \lesssim 0.2$, beside the plasticization, the phase behavior is characterized by formation of additional kinds of glasses. The Mode-Coupling theory predicts four different glasses (see Figure 1.4): fully frozen or double glass (both species are frozen); partially frozen depletion-driven or attractive glass (large particles are bonded due to the

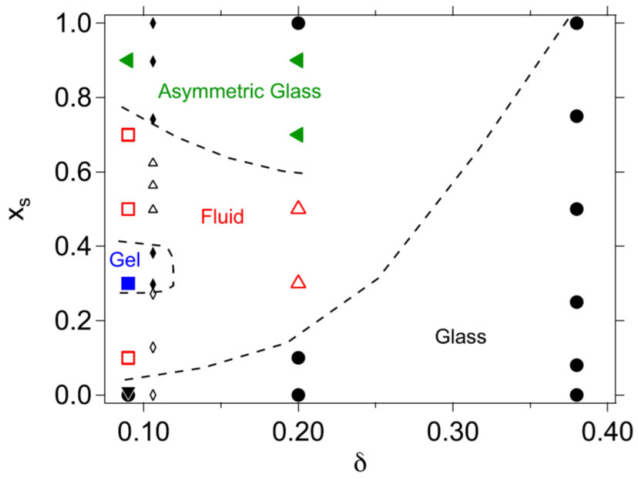

Figure 1.5.: State diagram of binary hard-sphere systems for samples with different compositions x_s and size ratios δ based on experimental data from Ref.[36–40]. Different states can be distinguished: repulsive glass (•), asymmetric glass (◀), attractive glass (▼), gel (■), fluids (△,□), fluid-crystal coexistence (◊) and amorphous solids (⧫). From Ref.[36]

depletion interaction induced by small spheres, small spheres stay mobile); asymmetric or 'torroncino glass' (large particles are diluted in the repulsive glass of small spheres). Up to $\delta = 0.18$ partially frozen caging-driven or single glass (repulsive glass of large particles driven by big-particle caging, small spheres remain mobile) may occur[35]. In experiments on colloidal suspensions[37,44] and in simulations of soft spheres[45,46] with large size disparity, the existence of a single glass, where only small spheres remain mobile, and of a double glass have been demonstrated. Besides single and double glasses, an asymmetric glassy state was found in star polymers mixtures[47,48]. Recent experiments on colloidal binary mixtures with $\delta = 0.09$ (see Figure 1.5) indicate different arrested states of large particles caused by bonding, namely an attractive glass and even a gel[36].

Bibliography

[1] M. Doi, *Soft Matter Physics*, Oxford University Press, 2013.

[2] L. V. Woodcock, *Ann. NY Acad. Sci.*, 1981, **371**, 274–298.

[3] R. J. Speedy, *Mol. Phys.*, 1998, **95**, 169–78.

[4] B. J. Alder, D. M. Gass and T. E. Wainwright, *J. Chem. Phys.*, 1970, **53**, 3813–3826.

[5] P. N. Pusey and W. van Megen, *Nature*, 1986, **320**, 340 – 342.

[6] P. N. Pusey and W. van Megen, *Phys. Rev. Lett.*, 1987, **59**, 2083–2086.

[7] W. B. Russel, D. A. Saville and W. R. Schowalter, *Colloidal Dispersions*, Cambridge, 1989.

[8] R. G. Larson, *The Structure and Rheology of Complex Fluids*, Oxford University Press, Oxford, England, 1998.

[9] L. Antl, J. Goodwin, R. Hill, R. Ottewill, S. Owens, S. Papworth and J. Waters, *Colloids Surf.*, 1986, **17**, 67 – 78.

[10] A. Yethiraj and A. van Blaaderen, *Nature*, 2003, **421**, 513–517.

[11] J. D. Bernal and J. Mason, *Nature*, 1960, **188**, 910 – 911.

[12] J. D. Berryman, *Phys. Rev. A*, 1983, **27**, 1053–1061.

[13] C. Song, P. Wang and H. Makse, *Nature*, 2008, **453**, 629–632.

[14] E. R. Weeks and D. A. Weitz, *Phys. Rev. Lett.*, 2002, **89**, 095704.

[15] E. R. Weeks and D. Weitz, *Chem. Phys.*, 2002, **284**, 361 – 367.

[16] A. H. Marcus, J. Schofield and S. A. Rice, *Phys. Rev. E*, 1999, **60**, 5725–5736.

[17] W. van Megen and S. M. Underwood, *Phys. Rev. E*, 1994, **49**, 4206–4220.

[18] E. R. Weeks, J. C. Crocker, A. C. Levitt, A. Schofield and D. A. Weitz, *Science*, 2000, **287**, 627–631.

[19] W. van Megen, T. C. Mortensen, S. R. Williams and J. Müller, *Phys. Rev. E*, 1998, **58**, 6073–6085.

[20] A. Malins, J. Eggers, C. P. Royall, S. R. Williams and H. Tanaka, *J. Chem. Phys.*, 2013, **138**, 12A535.

[21] C. A. Angell, *Science*, 1995, **267**, 1924–1935.

[22] L. Berthier and G. Biroli, *Rev. Mod. Phys.*, 2011, **83**, 587–645.

[23] W. Kob, C. Donati, S. J. Plimpton, P. H. Poole and S. C. Glotzer, *Phys. Rev. Lett.*, 1997, **79**, 2827–2830.

[24] D. N. Perera and P. Harrowell, *Phys. Rev. E*, 1996, **54**, 1652–1662.

[25] M. D. Ediger, *Annu. Rev. Phys. Chem.*, 2000, **51**, 99–128.

[26] P. Chaudhuri, L. Berthier and W. Kob, *Phys. Rev. Lett.*, 2007, **99**, 060604.

[27] A. J. Liu and S. R. Nagel, *Jamming and Rheology: Constrained Dynamics on Microscopic and Macroscopic Scales*, Taylor and Francis, New York, 2001.

[28] M. Fuchs and M. Ballauff, *J. Chem. Phys.*, 2005, **122**, 094707.

[29] N. Koumakis, M. Laurati, S. U. Egelhaaf, J. F. Brady, and G. Petekidis, *Phys. Rev. Lett.*, 2012, **108**, 098303.

[30] C. P. Amann, M. Siebenbürger, M. Kräger, F. Weysser, M. Ballauff and M. Fuchs, *J. Rheol.*, 2013, **57**, 149–175.

[31] F. Varnik, L. Bocquet and J.-L. Barrat, *J. Chem. Phys.*, 2004, **120**, 2788–2801.

[32] M. Siebenbürger, M. Ballauff and T. Voigtmann, *Phys. Rev. Lett.*, 2012, **108**, 255701.

[33] P. Oswald, *Rheophysics*, Cambridge University Press, Cambridge, England, 2009.

[34] J. Rosti, J. Koivisto, L. Laurson and M. J. Alava, *Phys. Rev. Lett.*, 2010, **105**, 100601.

[35] T. Voigtmann, *Europhys. Lett.*, 2011, **96**, 36006.

[36] J. Hendricks, R. Capellmann, A. B. Schofield, S. U. Egelhaaf and M. Laurati, *Phys. Rev. E*, 2015, **91**, 032308.

[37] A. Imhof and J. K. G. Dhont, *Phys. Rev. Lett.*, 1995, **75**, 1662–1665.

[38] T. Sentjabrskaja, E. Babaliari, J. Hendricks, M. Laurati, G. Petekidis and S. U. Egelhaaf, *Soft Matter*, 2013, **9**, 4524–4533.

[39] T. Sentjabrskaja, D. Guu, M. P. Lettinga, S. U. Egelhaaf and M. Laurati, *AIP Conf. Proc.*, 2013, **1518**, 206.

[40] T. Sentjabrskaja, M. Hermes, W. C. K. Poon, C. D. Estrada, R. Castañeda-Priego, S. U. Egelhaaf and M. Laurati, *Soft Matter*, 2014, **10**, 6546–6555.

[41] I. Biazzo, F. Caltagirone, G. Parisi and F. Zamponi, *Phys. Rev. Lett.*, 2009, **102**, 195701.

[42] W. Götze and T. Voigtmann, *Phys. Rev. E*, 2003, **67**, 021502.

[43] S. R. Williams and W. van Megen, *Phys. Rev. E*, 2001, **64**, 041502.

[44] A. Imhof and J. K. G. Dhont, *Phys. Rev. E*, 1995, **52**, 6344–6357.

[45] A. J. Moreno and J. Colmenero, *J. Chem. Phys.*, 2006, **125**, 164507.

[46] A. J. Moreno and J. Colmenero, *Phys. Rev. E*, 2006, **74**, 021409.

[47] C. Mayer, E. Zaccarelli, E. Stiakakis, C. N. Likos, F. Sciortino, A. Munam, M. Gauthier, N. Hadjichristidis, H. Iatrou, P. Tartaglia, H. Löwen and D. Vlassopoulos, *Nat. Mat.*, 2008, **7**, 780.

[48] C. Mayer, F. Sciortino, C. N. Likos, P. Tartaglia, H. Löwen and E. Zaccarelli, *Macromol.*, 2009, **42 (1)**, 423 – 434.

2. Overview

This chapter summarizes the main results of this work and is divided into two parts. The first part addresses observations of binary mixtures at rest. The focus here will be on the structure and the particle dynamics. First, will discuss the properties of the large-particle matrix and its dynamics. Afterwards the characteristics of the small-particle dynamics under the geometrical constrictions due to the larger species is presented.

In the second part binary mixtures are studied under the influence of shear. A broad range of rheological properties of the mixtures are discussed. In particular the identification of the link between local microscopic behavior and results from rheology is a main achievement of our studies.

2.1. Quiescent binary mixtures

The study of binary mixtures with large size disparity of the constituents requires to overcome several limitations of otherwise common experimental techniques. Let us illustrate some limitations by considering an example system. We assume a binary mixture of size ration 1:5 in which the large particles have a diameter of 2 µm, resulting in a small-sphere diameter of 0.4 µm. Both, structure and dynamics of the large particles, can be inferred from single-particle tracking using confocal microscopy which is a powerful tool for the study of highly concentrated colloidal systems. In particular the possibility of fluorescent marking of only a selected population of particles (for example, only large spheres) opens up many experimental possibilities. Confocal (point-by-point) illumination and a pinhole in the conjugate focal plane reduce the out-of-focus light [1,2]. This allows studying very dense systems and makes the technique irreplaceable. On the downside, point-by-point illumination and scanning implies a limitation of the acquisition speed (here: 30 frames per second). Hence, even if the size of the small particles is above the resolution limit (around 200 nm) the motion of the particles is too fast to be followed by tracking. Therefore, single-particle tracking cannot be used to determine the dynamical properties of the small particles. Instead, the small spheres are studied by Differential Dynamic Microscopy (DDM), which was adapted for multi-component

systems at large concentrations. DDM is based on the time-correlation analysis of the fluctuations of the fluorescence intensity. An introduction and details to the experimental techniques used for this research can be found in appendix A.4.

2.1.1. Large particle configuration and dynamic

The admixture of a second component with a different size into the system leads to the distortion of the primary structure. The focus of this section lies on the structural and dynamical changes observed in the system of large particles when a second component, smaller particles, is added to the system. The structural and dynamical changes are studied using confocal microscopy for different compositions x_s, keeping the total volume fraction ϕ and the size ratio δ constant (here $\delta \approx 0.2$, $\phi \approx 0.61$ and 0.58).

Figure 2.1 shows the reconstruction of large particle positions in binary mixtures for different compositions x_s from 0 to 0.9 at a fixed volume fraction $\phi \approx 0.61$. For clarity only particles within a thin slice of the volume are shown. With increasing fraction of small spheres, the large particles become effectively more diluted. The amorphous nature of the structure is maintained. No evidence for phase separation predicted in Ref.[3,4] was found. This is quantified by the radial distribution functions $g(r)$ for different compositions x_s, see Figure 2.2. As expected, for a one-component glass, $x_s = 0$, the position of the first maximum corresponds to the diameter d_L of large spheres, i.e. the first-neighbor shell or cage. At large distances r, further peaks are recognizable, but they become less and less pronounced with increasing r. This general behavior indicates a decay of the layering beyond the third-neighbor shell.

Adding small particles changes the structure of the larger species. The small particles perturb the cages formed by the large ones, resulting in a deformation of the cages formed by the large particles. When the amount of small spheres reaches a critical number, each large particle is almost completely surrounded by a layer of small particles. At this point the large-particle cage is loosened. The layer of small particles can be identified in $g(r)$, where for $x_s = 0.5$ an additional maximum at $r = d_L + d_S$ appears and eventually becomes even larger than the first one at $r = d_L$. The caging by small or large particles plays a central role, since it determines the dynamics of large spheres and the rheology of binary mixtures, as will be discussed below.

Other experiments on binary mixtures show that the cage-transition effect appears only for a small range of the size ratios. In systems with a larger size ratio of $\delta \approx 0.3$ for example no transition in the caging mechanism takes place[5–7]. Here only the state of repulsive glass is observed. Decreasing the size ratio to 0.09 on the other hand leads to the formation of additional phases[8]. Different arrested states, like attractive glass or

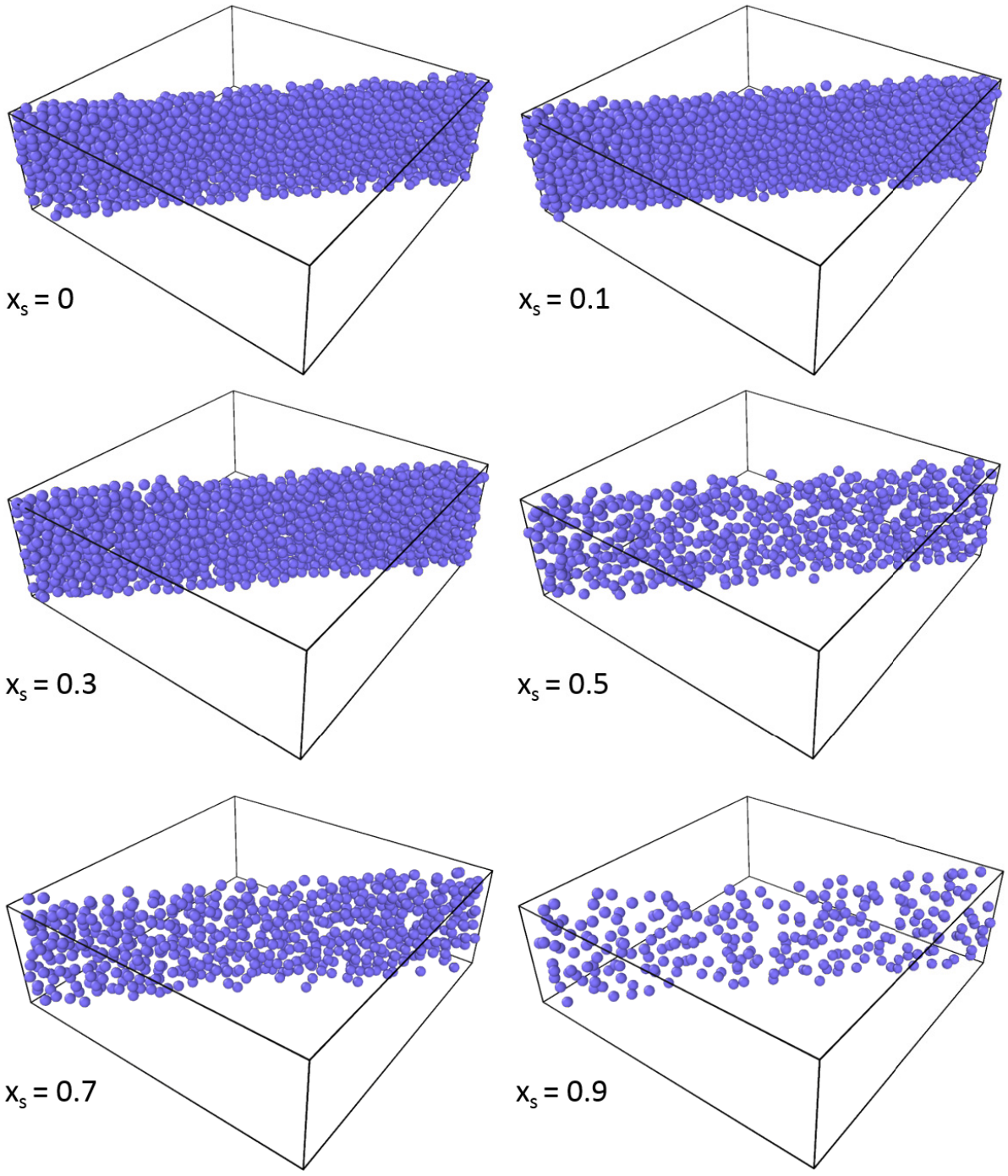

Figure 2.1.: Reconstruction of the large particle positions within a thin slice of thickness $3d_L$ in mixtures with volume fraction $\phi \approx 0.61$, size ratio $\delta \approx 0.2$ and different amount of small spheres (which are not shown) as obtained from confocal microscopy measurements.

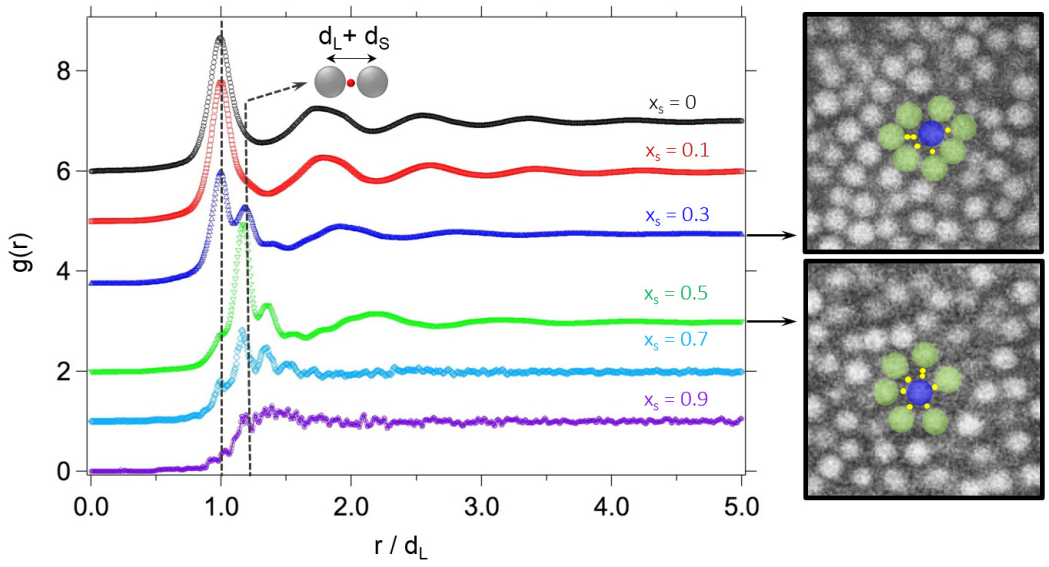

Figure 2.2.: Left: Radial distribution function $g(r)$ of the large spheres for different compositions x_s as a function of normalized radius r/d_L. The lines are shifted along the vertical axis for clarity. The total volume fraction of the samples is $\phi \approx 0.61$ and the size ratio of the mixtures is $\delta \approx 0.2$. The additional maximum at the distance $d_L + d_S$ corresponds to the structure, where one small particle lies in between two large spheres, as shown in the sketch. Right: Confocal microscopy frames for $x_s = 0.3$ (top) and 0.5 (bottom). Only large particles are visible. The large particles (green) surrounding one randomly chosen particle (blue) are indicated. The yellow points represent possible positions of small particles, resulting in the first and second additional peaks of $g(r)$ at $d_L + d_S$ and $d_L + 2d_S$, respectively.

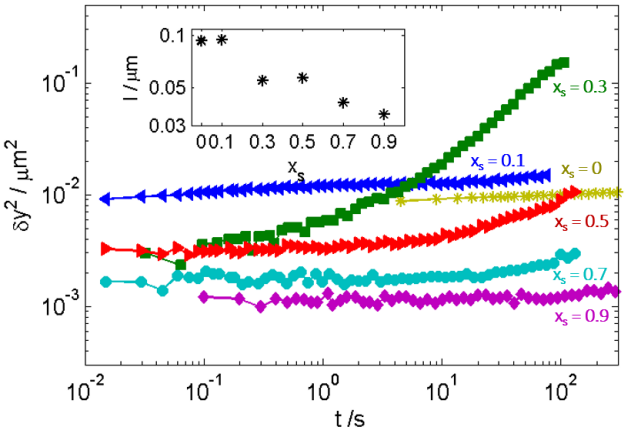

Figure 2.3.: Mean-squared displacement δy^2 as a function of time t for mixtures with total volume fraction $\phi \approx 0.61$ and size ratio $\delta \approx 0.2$ for different compositions x_s as indicated. Inset: The localization length l defined as $l = \sqrt{\delta y^2(t \to 0)}$ for different x_s.

even gel, are found. The bonding of the large spheres caused by depletion determines the dynamics of large particles in such systems.

Figure 2.3 shows mean-squared displacements δy^2 of the large particles as a function of time for mixtures of different compositions. Obviously, the type of large particle dynamics, and not only their structure, depends on the composition. For a large particle only system, i.e. $x_s = 0$, the glassy dynamics, characterized by a long-time localization of particles in the cages is found. Adding a small amount of small spheres to the glass, $x_s = 0.1$, does not alter the appearance of slow in-cage dynamics of the large spheres. Yet, the presence of small spheres induces a small increase of the localization length l, reflecting the widening of the cage[9] (see Figure 2.3 inset). For $0.3 \leq x_s \leq 0.7$, an acceleration of the dynamics of the large particles is observed. This can be attributed to an increase of the free space due to the more efficient packing ability of binary mixtures reflected in the random close packing[10]. The change of the packing ability leads to a shift in the glass transition for binary mixtures, which now takes place at larger total volume fractions. Keeping the total volume fraction constant, we obtain soft glasses with $0.3 \leq x_s \leq 0.7$ which are closer, compared to the one-component system, to the glass transition. Further increase of x_s up to 0.9 leads again to the formation of the localization plateau observed in the MSD. Hence, the particles become localized very tightly. The amount of small spheres is now so high, that the large particles are dilute in a sea of small particles, which surround the large spheres and build a very tight cage. The localization length of large particles l decreases for $0.1 \leq x_s \leq 0.9$ continuously, indicating a competition between softening and the transition in caging mechanism.

Let us sum up the situation at a fixed total volume fraction. An increase of x_s

in binary mixtures is followed by: (i) an acceleration of large-particles dynamics for $0.3 \leq x_s \leq 0.7$, (ii) a transition in the caging of large spheres from large-particle cages for $0 \leq x_s \leq 0.3$ to small-particle cages for $0.5 \leq x_s \leq 1$, (iii) a tighter localization of large spheres.

2.1.2. Small particles

In this section we will discuss the dynamics of the small component in a binary mixture. Here, mixtures with varying total volume fractions ϕ and size ratios δ are studied. The amount of small spheres is kept constant at the small value $x_s \approx 0.01$. At large volume fractions the large particles form a matrix with an amorphous structure and slow glassy dynamics. The holes formed in-between the large spheres may be connected with each other by channels. The combination of holes and channels forms a porous medium which is explored by the small spheres. At high concentrations of large particles, the channels become narrower or some of them even close, forming finite pockets, where the small particles become localized.

The motion of tracer particles in porous media is a currently very active research field. Examples for systems of interest are binary mixtures of starpolymers [11], proteins in a crowded cell [12–14], binary mixtures of soft spheres [15,16] and fluids confined in porous matrices [17]. Theoretical studies, based on the Lorenz model, where point-like particles move through the channels of a matrix of randomly overlapping fixed obstacles, predict anomalous diffusion of the small component [18–21]. Molecular dynamics simulations of a colloidal fluid in a matrix of frozen particles show two distinct arrest scenarios, namely the trapping in disconnected voids and a caging mechanism [22]. These and further model systems [23–25] are based on the assumption that the matrix is completely frozen.

In our experiments we face a more complicated situation compared to the studies mentioned above. The void size, position in space, and the presence of void connections are additionally time dependent due to the slow, glass-like dynamic of the large particles. The slow dynamics of the large component are typical for crowded biological systems like cells, where the macromolecules exhibit slow, glass-like dynamics [12,13]. Thus, the binary mixture represents a step forward towards a more realistic model system that mimics anomalous transport of proteins within the crowded environments in cells.

Changes in the voids of the matrix as a function of time are indirectly visualised in Figure 2.4, which shows the measured positions (the intensity peaks) of small particles in a 2D plane of the size 100×100 Pixel for two size ratios $\delta \approx 0.18$ and 0.28, respectively. The positions of the small particles are shown for different time-intervals. We find that some of the voids are accessible for only one time interval (single colored speckles),

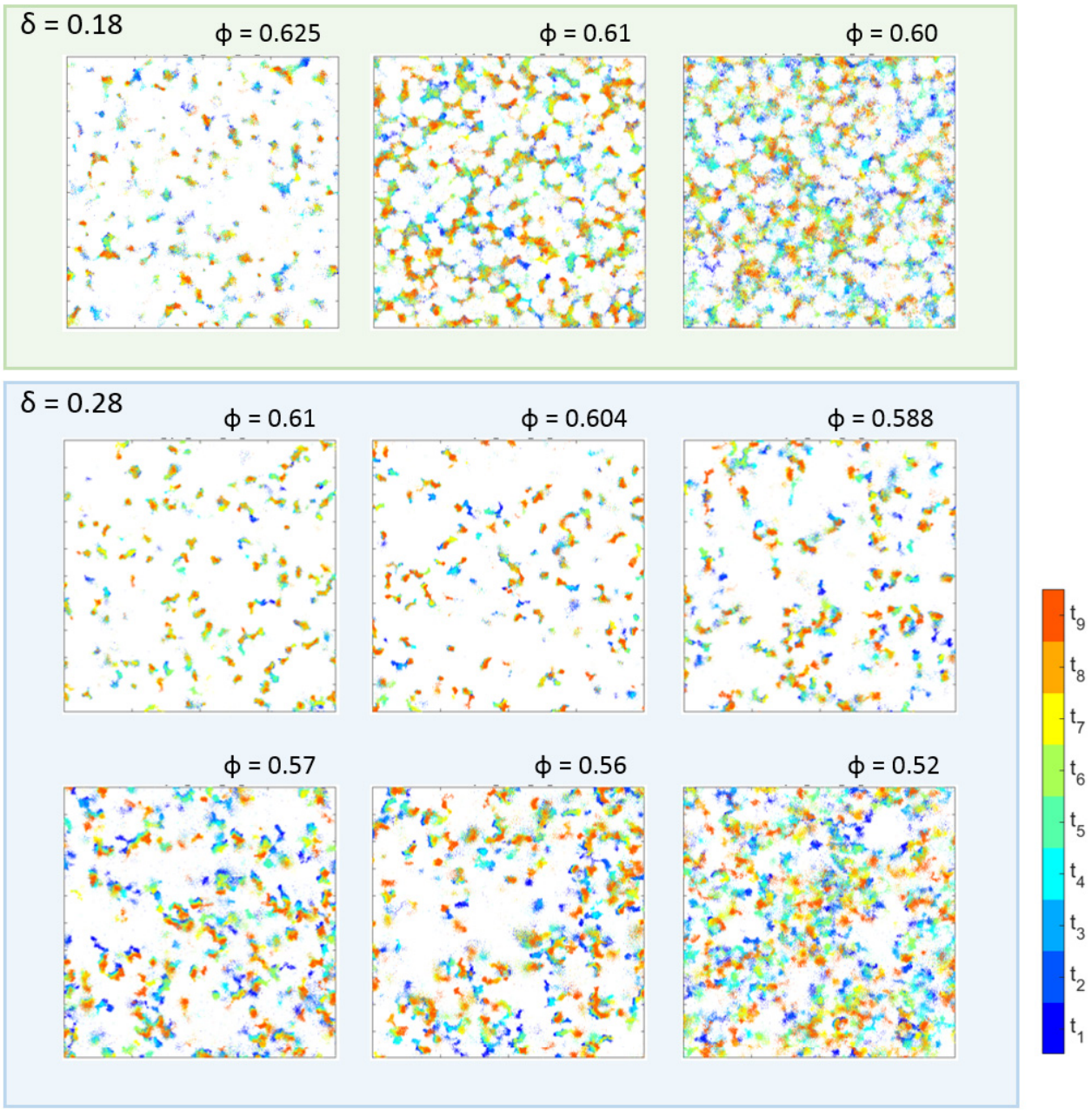

Figure 2.4.: Positions of small particles in mixtures with size ratio $\delta \approx 0.18$ and 0.28 for different total volume fractions as indicated. The colors indicate the positions of particles for different time intervals, each with the length $\frac{1000\,\text{frames}}{30\,\text{fps}} \approx 33\,\text{s}$. 100x100 pixel

whereas other ones are accessible for longer times (multicolored speckles). Dilution of the system leads to an increase of the average hole size, some of the channels expand and the time-dependent changes of the voids become faster due to the fluidization of the matrix.

Whether a tracer particle can pass through a channel or not depends on the size of the particle relative to the channel width. At low size ratio $\delta \approx 0.18$ and high volume fraction $\phi \approx 0.625$ the tracers are usually localized in the voids for long times. A small decrease of the volume fraction to $\phi \approx 0.61$ leads to the formation of channels which are wide enough to let the particles pass through. Now the particles may move between the voids. In contrast to that, if the size of the tracers is large ($\delta \approx 0.28$) at the volume fraction $\phi \approx 0.61$, the channels are not big enough to let the tracers pass. Further dilution of the system would be necessary to delocalize the tracers.

The dynamics of the small particles is described by the intermediate scattering function $f(q, \delta t)$ which can be measured by confocal Differential Dynamic Microscopy. At $\delta \approx 0.18$ and at fixed wave-number q, the intermediate scattering function can be divided into three temporal intervals: the initial decay at short time, the plateau at intermediate times and the second decay to 0 at late times, see Figure 2.5. The initial decay is caused by in-void Brownian dynamics of the small spheres. In a dense matrix, i.e. at large ϕ, the dynamics of the small particles slows down and the decay takes longer. The existence of the plateau in $f(q, \delta t)$ indicates that a fraction of the small particles stays localized for long time without the possibility to diffuse. The plateau height indicates how large the fraction of the localized particles is and corresponds to the non-ergodicity parameter[11,15,16]. At later times diffusion takes place again and $f(q, \delta t)$ decays to 0.

Besides the dependence on ϕ, the intermediate scattering function depends additionally on the considered length scale determined by q^{-1}. Increasing q leads to a faster initial decrease of $f(q, \delta t)$. The plateau height decreases exponentially with increasing q (not shown here). This indicates a localization of the particles at length scales between $2d_S$ for $\phi \approx 0.625$ and $6d_S$ for $\phi \approx 0.60$, where d_S the diameter of the small particles[26].

At $\delta \approx 0.28$ we find anomalous dynamics at high volume fractions ϕ. The intermediate scattering function now shows an extended logarithmic decay for a series of q. This behavior of $f(q, \delta t)$ is the result of the dynamical heterogeneities caused by the influence of two processes. On the one hand, the dense host of large spheres causes a geometrical constriction to the motion of the small particles. And on the other hand, the matrix of the large particles is slowly evolving, which leads to the transient opening or closing of the channels connecting the voids. The transient opening of the channels allows the small particles, which otherwise only explore their local environments, to diffuse out of the

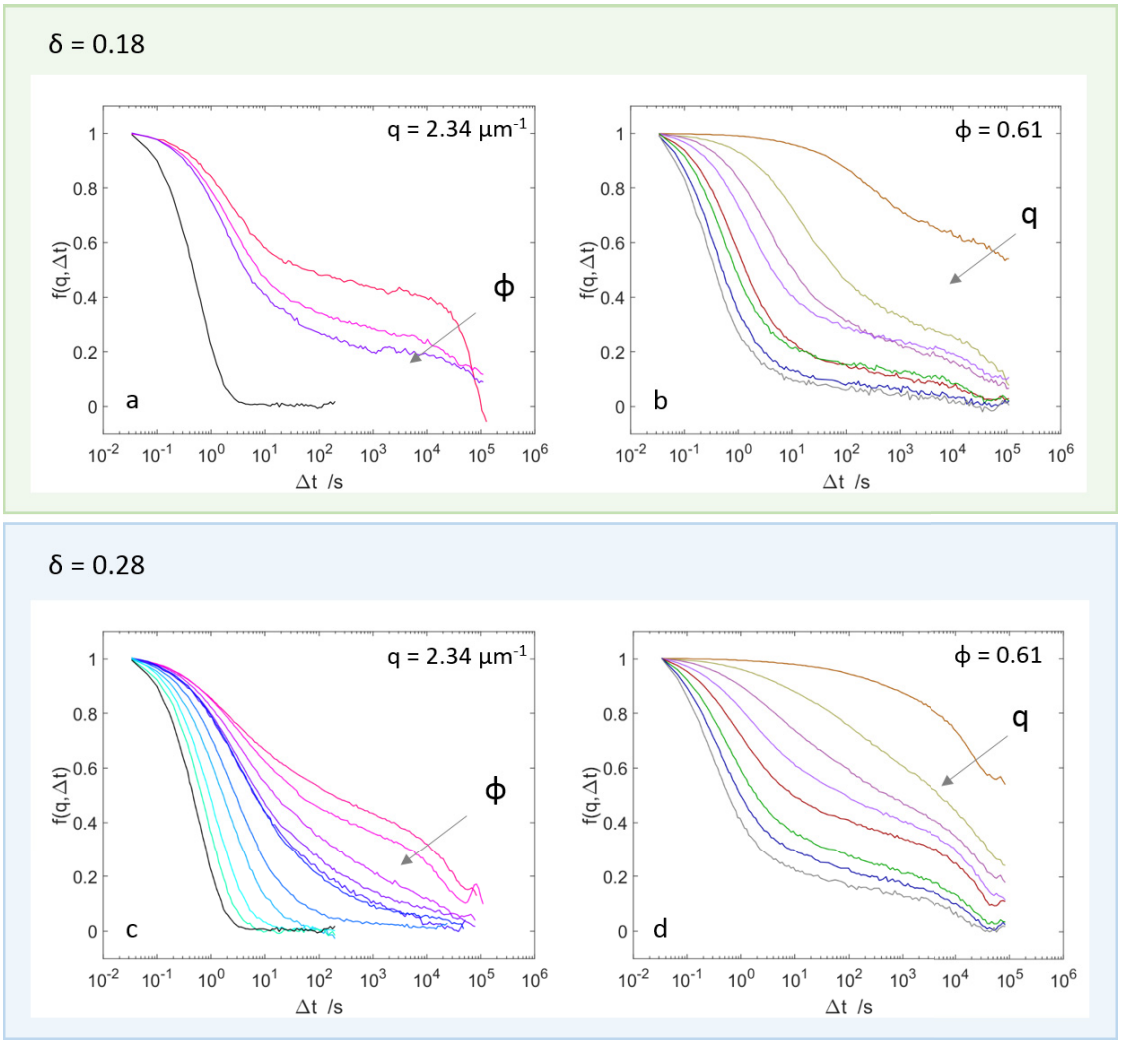

Figure 2.5.: Intermediate scattering function $f(q, \delta t)$ for small particles in binary mixtures with $x_s = 0.01$ and (a) $\delta \approx 0.18$, $\phi \approx 0.625, 0.61$ and 0.60 from top to bottom at $q = 2.34\,\mu m^{-1}$; (c) $\delta \approx 0.28$, $\phi \approx 0.61, 0.604, 0.588, 0.58, 0.57, 0.56, 0.52, 0.5, 0.4$ and 0.3 from top to bottom at $q = 2.34\,\mu m^{-1}$; (b,d) $\phi \approx 0.61$, $q = 0.23, 1.05, 1.87, 2.69, 3.51, 4.32, 5.14, 5.96\,\mu m^{-1}$, $\delta \approx 0.18$ (b) and $\delta \approx 0.28$ (d). The black line in (a,c) corresponds to the $f(q, \delta t)$ for dilute solution of small particles without matrix.

local cages. Three different situations, depending on the size ratio, can now be observed. At a small size ratio of $\delta \approx 0.18$, the small particles are so small that they can easily pass through the channels. In this case, the voids percolate even at high concentrations of the obstacles. Simulation results show that instead in the opposite limit of large $\delta = 0.5$, the small spheres explore only the local voids where they are trapped [26]. For the intermediate size ratio $\delta \approx 0.28$ (experiment) and $\delta = 0.35$ (simulations) an intermediate situation is observed. The small particles move most of the time in the local environment, but sometimes migrate through the channels into the next void. Only a small fraction of the particles diffuses through the tight channels connecting the voids. This leads to a large distribution of residence times and, as a consequence, to anomalous diffusion. Interestingly not only the channels, but also the spatial position and the size of the voids are transient on the time scale of the large-spheres in-cage dynamics.

2.2. Binary mixtures under shear

In this section we will present results obtained from rheological and simultaneous microscopy measurements of binary mixtures. By combining microscopy and rheology, single-particle dynamics can be linked to the macroscopic response of the system for different types of shear. To this end, we studied binary mixtures with $\delta \approx 0.2$, volume fraction $\phi \approx 0.58$ and 0.61 and different composition x_s under shear.

Shearing at very low strain γ, i.e. in the linear visco-elastic regime, causes deformations which weakly perturb the quiescent structure [27]. The glass retains its structure and behaves like a solid. For such almost unperturbed samples the rheological measurements can be directly compared to the microscopic observations of the sample at rest.

Applying a larger shear leads to the fluidization of the binary glass, similar to recent results on one-component glasses [28,29]. The transition from solid- to fluid-like shear response differs depending on the nature of the applied shear signal and on the internal structure of the sample. In this regime we can no longer compare the rheological response of mixtures to the microscopic dynamics at rest. Thus, a confocal measurement of the single particle dynamics is required while the system is sheared.

The short following overview summarizes the main results.

2.2.1. Oscillatory shear

For the experiments with oscillatory shear the shear signal has a constant frequency ω, while the amplitude increases (Dynamical Strain Sweep or DSS). The frequency ω is

adjusted for each sample such that the Peclet number $Pe_\omega = \omega\langle\tau_0^{short}\rangle$ is the same for all mixtures (which differ in x_s). Peclet number quantifies the ratio between the timescale of brownian motion and the timescale imposed by shear. Here, $\langle\tau_0^{short}\rangle = 6\pi\eta\langle R^3\rangle/k_BT$ is the composition-averaged short-time Brownian time in the dilute limit and $\langle R^3\rangle = R^3_{Large}[x_s(\frac{1}{\delta^3} - 1) + 1]$.

As long as only a small deformation is applied to the sample, the linear visco-elastic regime, characterized by strain-independent shear moduli G' and G'', is observed. The storage modulus G' for a fixed $Pe_\omega \approx 0.55$, extracted at $\gamma \approx 0.2\,\%$, is shown in Figure 2.6 a) for different mixtures in units of the energy density ρk_BT. Presenting the results in these units removes the trivial dependence of the rheological signal on the particle size. In this representation one-component systems consisting of only small or large particles show comparable linear rheological responses to oscillatory shear, i.e. both systems have similar values of $G'(\omega)/\rho k_BT$. For binary mixtures we observe a reduction of the shear modulus, corresponding to a weaker elastic response of the mixtures. For $\delta \approx 0.2$ and $x_s = 0.3$, the value of $G'/\rho k_BT$ is up to two orders of magnitude smaller compared to the one-component systems. The weaker elastic response of mixtures is consistent with the acceleration of large-particle dynamics in mixtures, discussed in section 2.1.1, and indicates a softening effect of binary glasses. An increase of the size ratio to $\delta \approx 0.38$ results in less pronounced softening.

The solid-like behavior of a sample in the linear visco-elastic regime is indicated by $G' > G''$. Increasing the shear amplitude leads to irreversible rearrangements of the particles, cage breaking and fluidization of the glass with $G' < G''$. The transition from solid to fluid occurs at a critical value of deformation γ_y, the yield strain of the system, extracted at the crossing point of G' and G''[9,30,31]. Similar to the evolution of the elastic modulus, a pronounced reduction of the yield strain was found. The minimal value of γ_y is observed at $x_s = 0.3$. The reduction of γ_y for binary mixtures supports the idea of a glass softening effect. The decrease of total volume fraction to $\phi \approx 0.58$ leads to the melting of the glass, indicated by the absence of γ_y for $x_s = 0.3$ and 0.5. These two mixtures show a fluid-like response with $G' < G''$ even at very small deformations. At large size ratio $\delta \approx 0.38$, the yield strain remains almost constant, consistent with the weak softening effect described earlier.

One can guess that the glass softening effect is only a result of more efficient packing ability of the binary mixtures. The yielding behavior of one-component glasses and binary glasses was compared as a function of the free volume $\phi_{free} = \phi_{RCP} - \phi$, taking into account the variation of ϕ_{RCP} in the mixtures[10]. At free volumes, where the one-component system melts, we found binary mixtures in a weak but still solid-like state,

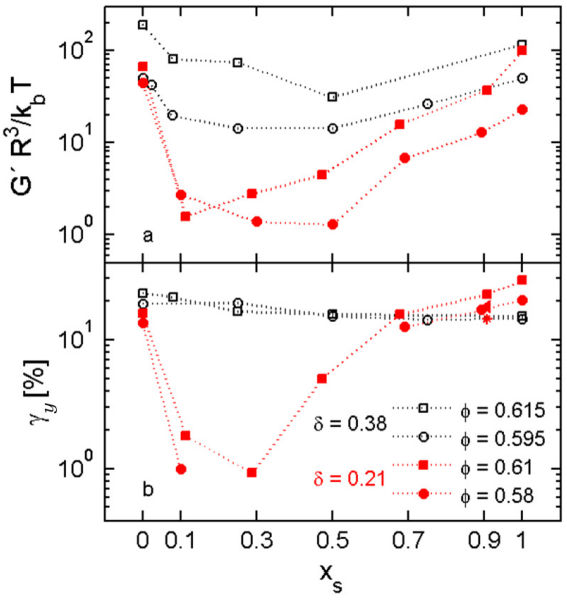

Figure 2.6.: a) Storage modulus G' measured at small amplitude ($\gamma \approx 0.2\,\%$) and b) yield strain γ_y estimated from the crossing point of G' and G'' as a function of relative volume fraction of small spheres x_s for samples with size ratio $\delta \approx 0.21$ and total volume fraction $\phi \approx 0.61$ and $\phi \approx 0.58$ and $Pe_\omega = 0.55$, and $\delta \approx 0.38$, $\phi \approx 0.615$ and 0.595 and $\omega = 1\,\mathrm{rad\,s^{-1}}$. The data for $\delta = 0.38$ were obtained by the Group of G. Petekidis.

indicated by a small finite yield strain [6]. Rheological properties of binary mixtures thus not only depend only on the total volume fraction, like it is the case for one-component glasses, but also on the role which each population plays in the microscopic structure and dynamics.

2.2.2. Constant shear rate

In step-rate experiments a constant shear rate $\dot{\gamma}$ is applied and the stress σ is measured as a function of time t or strain $\gamma = \dot{\gamma}t$. Applying a constant shear rate to a colloidal glass leads to an initial almost linear increase of stress σ with strain γ, followed by a non-linear increase until the stress reaches a maximum, see Figure 2.7 for an example. Eventually, the stress decays to a constant steady-state value σ_{steady} when the system flows [32]. For one-component systems, it was shown that the stress overshoot is associated to the storage of the stress during elastic cage deformation, which is maximal at the overshoot [28,33] and decreases when the cage is broken and the system flows. Around cage-breaking super-diffusive particle motion is observed in experiments, simulations, and predicted by mode coupling theory [28,29,33,34].

From the stress-strain curves two quantities are extracted, the strain at the overshoot

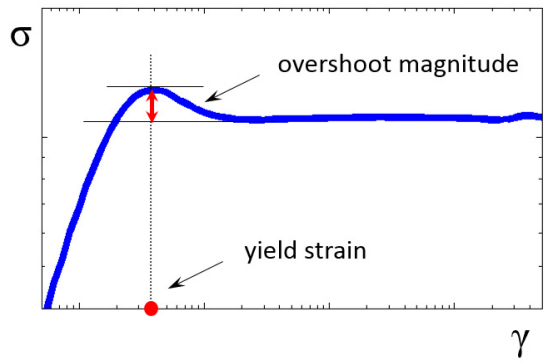

Figure 2.7.: Stress σ measured in step rate experiment by applying of the constant shear rate plotted as a function of strain γ. The yield strain γ_{peak} and the magnitude of the overshoot $\sigma_{peak}/\sigma_{steady} - 1$ are labeled.

γ_{peak}, associated to the yield strain, and the magnitude of the overshoot $\sigma_{peak}/\sigma_{steady} - 1$. The results are shown in Figure 2.8 (a,b) as functions of x_s and (c,d) Peclet number $Pe_{\dot{\gamma}} = \dot{\gamma}\langle\tau^{short}\rangle$, with $\langle\tau^{short}\rangle = \langle\tau_0^{short}\rangle/f$. The ϕ-dependent factor f is estimated to be $f \approx 1/32$ for the studied volume fraction $\phi \approx 0.61$ (extrapolate the data in Figure 8 of Ref.[35]).

Two different regimes are observed for γ_{peak} as a function of $Pe_{\dot{\gamma}}$. In the first regime, for small Peclet numbers $Pe_{\dot{\gamma}} \leq 1$, the yield strain remains almost constant at a value of about 10 %, similar to MCT (mode coupling theory) predictions for one-component glasses[36]. In this regime the deformation induced by shear is slow compared to the Brownian dynamics. The second regime, $Pe_{\dot{\gamma}} > 1$, is characterized by an increase of the yield strain with increasing $Pe_{\dot{\gamma}}$, in agreement with experimental results obtained for one-component colloidal glasses[28,29]. In this regime, the shear is fast compared to the Brownian dynamics and the affine motion becomes dominating. Collisions and cage escape due to the Brownian motion become less probable and, and therefore the cage can deform more before it breaks.

The two regimes can also be identified in the $Pe_{\dot{\gamma}}$ dependence of the magnitude of the stored stress, see Figure 2.8 d). The first regime is characterized by the increase of the magnitude of the overshoot, which is followed by the second regime where $\sigma_{peak}/\sigma_{steady}-1$ decreases. For one-component glasses, similar regimes are observed[28]. The study of binary mixtures with different compositions demonstrates that, different from the yield strain, the transition between these two regimes appears at different $Pe_{\dot{\gamma}}$, depending on x_s. It is particularly noticeable that for the mixture with $x_s = 0.5$ the transition occurs at considerably larger $Pe_{\dot{\gamma}}$ compared to other mixtures. This implies that the process of stress storage does not scale with the Peclet number, i.e. the composition-averaged

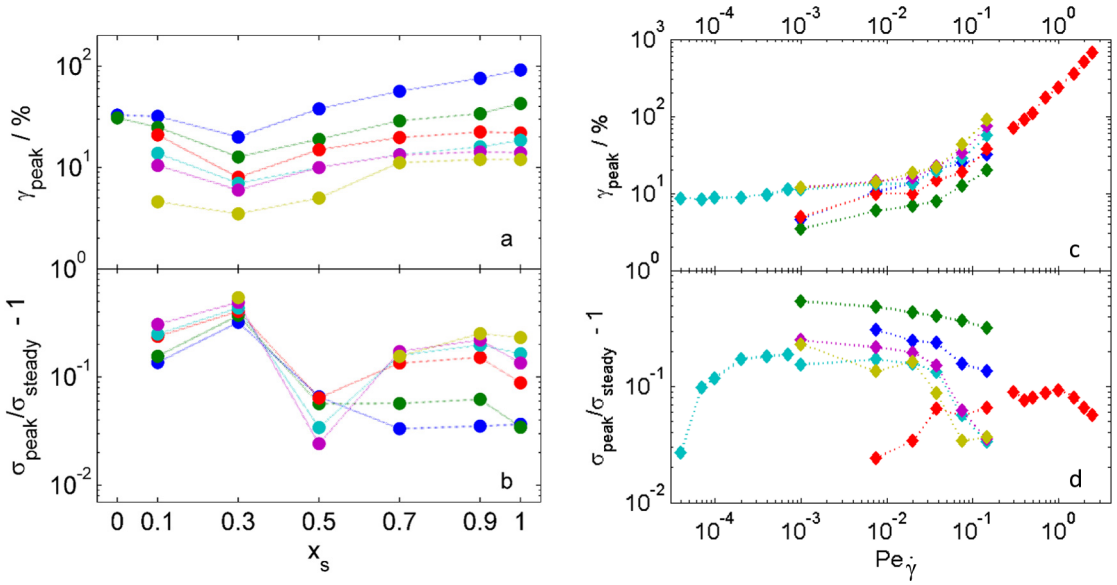

Figure 2.8.: a)Yield strain, γ_{peak}, and d) the magnitude of the stress overshoot, $\sigma_{peak}/\sigma_{steady} - 1$, as a function of composition x_s for Peclet numbers $Pe_{\dot\gamma} = 0.03$ (yellow), 0.24 (purple), 0.64 (turquoise), 1.20 (red), 2.40 (green) and 4.70 (blue). c) γ_{peak} and d) $\sigma_{peak}/\sigma_{steady} - 1$ as a function of Peclet number $Pe_{\dot\gamma}$ for different compositions x_s: 0.1 (blue), 0.3 (green), 0.5 (red), 0.7 (turquoise), 0.9 (purple), 1.0 (yellow). Binary mixtures with $\delta \approx 0.2$ and $\phi \approx 0.61$ are studied.

short-time Brownian time. The correct time-scale was found by considering the long-time structural relaxation time. The long-time structural relaxation time was estimated for large and small particles in binary mixtures from MD simulations by C.D. Estrada and R. Castañeda-Priego (not shown here, see Ref. [5]). For mixtures with $x_s < 0.5$, the amount of the stored stress is related to the long-time structural relaxation time of the large particles and for $x_s \geq 0.5$ of the small ones, respectively. This observation leads to the conclusion that the amount of the stored stress is affected by the caging mechanism and is determined by the long-time structural relaxation time of the caging species.

Similar to the yield strain measured by oscillatory shear, the dependence of γ_{peak} on x_s shows a softening effect, which is most pronounced for the mixture with $x_s = 0.3$. In contrast to that, a complicated behavior was found for the magnitude of the stress overshoot as a function of x_s, see Figure 2.8 b). The largest stress overshoot is found for values of $x_s \leq 0.3$, independent of the Peclet number $Pe_{\dot\gamma}$. At $x_s = 0.5$ the stress overshoot is about an order of magnitude smaller than at $x_s = 0.3$. For large $Pe_{\dot\gamma}$ the overshoot is almost constant for $x_s \geq 0.5$, whereas for small values of $Pe_{\dot\gamma}$ it increases again to almost the same level as for $x_s = 0.1$.

In order to understand the microscopic origin of the macroscopic rheological response,

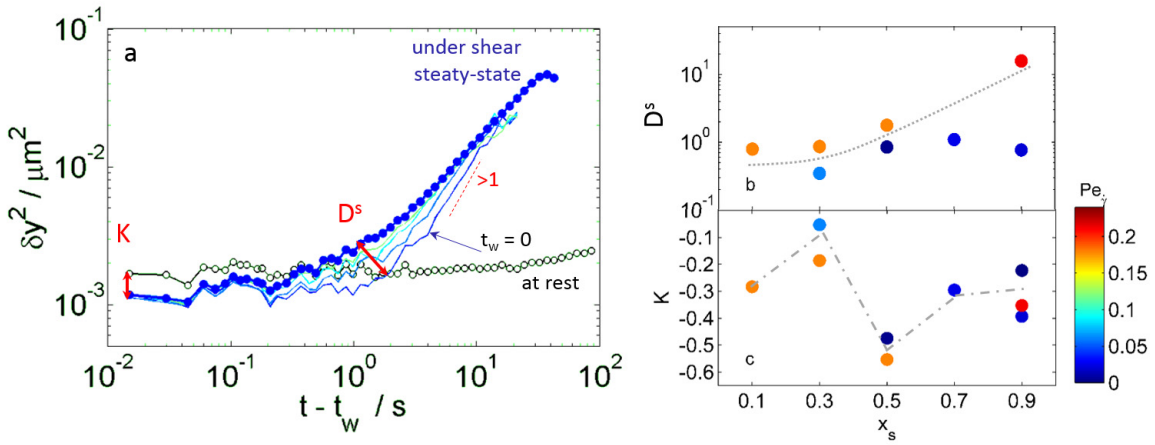

Figure 2.9.: a) Mean squared displacement in the vorticity direction δy^2 for mixture with $x_s = 0.7$ at $Pe_{\dot{\gamma}} = 0.0035$. The black circles correspond to the MSD at rest, the blue circles to the MSD under shear in the steady state and the thin lines to the transient MSD for different waiting times t_w. The values K, the shear induced cage compression (eq. 2.1), and D^s, the amount of super diffusion (eq. 2.2), are indicated schematically. b) D^s and c) K as functions of x_s for different $Pe_{\dot{\gamma}}$ as it is shown in the color code. Dashed lines are drawn for clarity.

we study the individual particle dynamics during shear. The particle trajectories during shear are obtained via a rheoscope. From these particle trajectories we calculate the MSD during steady-state shear and the transient MSD obtained after a waiting time t_w after applying the shear. Figure 2.9 a) shows typical results for the MSD during shear (blue circles) and t_w after shearing (thin color lines). Note, that the contributions of affine motions are absent. The dynamics under shear are compared to the MSD in the quiescent state (black circles).

For long times the MSD in the regime of steady flow increases proportional to $\delta y^2 \sim t^n$ with $n \approx 1$, showing diffusive dynamics of large particles. The shear-induced acceleration of the dynamics is associated with shear thinning. This result is in agreement with previous studies for one-component glasses [28,29,32,32,34,37].

At short times, the dynamics are determined by the in-cage motion. The plateau of δy^2 for $t \to 0$ corresponds to the localization length of particles in their cages. The localization length at rest l was discussed in section 2.1.1, were a decrease of l with increasing x_s was found. The MSD under shear at short times indicates a tighter localization of particles. To characterize the shear-induced cage compression we introduce the factor K, calculated as

$$K = \delta y^2_{shear} / \delta y^2_{rest} - 1\,, \tag{2.1}$$

where δy^2_{shear} is the MSD under shear and δy^2_{rest} the MSD at rest, both taken at short

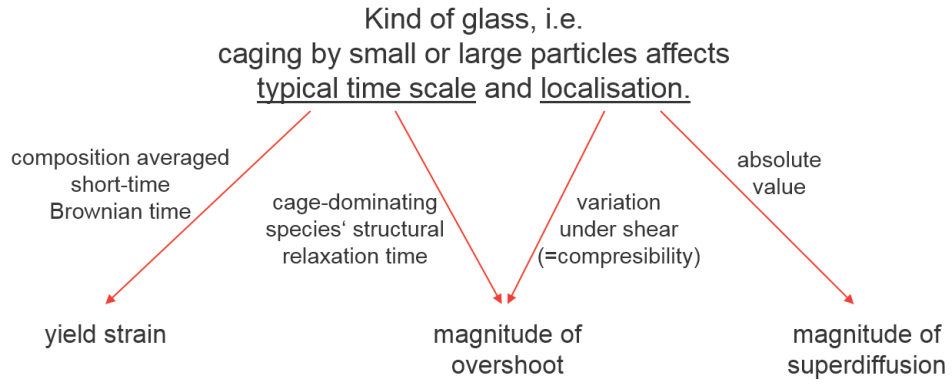

Figure 2.10.: Schematic summary of the results obtained by comparing the rheological data to the microscopical observations during the step rate experiments.

times. The variation of K for different compositions x_s and Peclet numbers $Pe_{\dot{\gamma}}$ is shown in Figure 2.9 c). Interestingly, the cage compression follows the variations of stored stress amount measured in rheology. The large cage compressibility corresponds to a small stored stress and vice versa. This suggests that a part of the stress is released through the compression of the cage.

The qualitative change in caging mechanism, from large to small particle caging, is reflected in the cage compression and in the amount of the stored stress as well. At rest, the large particles in mixtures with $x_s = 0.3$ and 0.5 are localised on similar lengths. For $x_s = 0.3$ the shear-induced cage compression is very poor, whereas at $x_s = 0.5$ we observe the highest cage compression. Under shear the small spheres, caging the large particles, can be rearranged easier due to the higher mobility, allowing further compression.

From Figure 2.9 a) we can see that the transient MSD for $t_w = 0$ shows an extended localization plateau. After starting to shear, the particles stay for some time tightly localised, demonstrating a resistance to shear up to the point where the system yields. The structure of the system breaks, the particles can now escape from the cages. This process is related to super-diffusive dynamics of particles. The amount of super-diffusion is given by

$$D^s = D^{steady}/D^{sdiff} - 1, \tag{2.2}$$

where D^{steady} corresponds to the steady-state and D^{sdiff} to the transient diffusion coefficient of the large particles. The variation of D^s as a function of x_s leads to the conclusion that a tighter localization at rest results in more pronounced transient super-diffusion under shear, see Figure 2.9 b).

Figure 2.10 schematically summarizes the findings and shows the link between macro-

scopic rheological response of binary mixtures and the microscopic single-particle dynamics. The kind of glass, i.e. the caging by small or large particles, sets the typical time scale and the localization length. The typical time scale for the yield strain is the composition averaged short-time Brownian time. In contrast to that, the amount of the stored stress is sensitive to the structural relaxation time of the cage-dominating species. Through cage compression a part of the stress is released. The absolute value of the localization length is connected to the magnitude of super diffusion. A tighter localization at rest leads to a more pronounced super-diffusion and an abrupt transition to flow.

2.2.3. Constant shear stress

In the previous section and in Ref.[9,28–33,38–40] it was shown that the application of an arbitrary constant shear rate leads to the fluidization of the glass. In contrast to that, the shear at constant shear stress may show different scenarios. In a step-stress or creep experiment a constant shear stress σ is applied on an initially quiescent system. The evolution of the deformation γ is now measured as a function of time t. Figure 2.11 a) shows a typical response of a glassy system in a creep experiment. Only the application of a stress above the yield stress σ_y results in a flow response. The flow response is characterized by a linear increase of strain with time, i.e. $\dot{\gamma}$ is constant. For stresses $\sigma < \sigma_y$, a sub-linear increase of $\gamma(t)$ is observed[41–43]. This indicates a solid-like response associated to the creep of the system. An intermediate response is found for $\sigma \gtrsim \sigma_y$. For short times the system shows a creep-like response, but at longer times the system starts to show fluid-like behavior. The transition from one regime to the other takes place during a finite time interval, during which a super-linear increase of $\gamma(t)$ is observed. Note that the oscillations of γ at small times for small stresses are due to instrument inertia[44,45] and will not be discussed here.

To distinguish the regimes of creep and flow, the logarithmic time derivative of the strain $\lambda_{creep}(\gamma) = \mathrm{d}log(\gamma)/\mathrm{d}log(t)$ is calculated. The derivative λ_{creep} corresponds to the exponent of the time dependence of $\gamma(t)$ and is shown in Figure 2.11 b). The value $\lambda_{creep} = 1$ corresponds to flow and $\lambda_{creep} < 1$ to creep response, respectively. The transition from creep response to super-linear increase, characterized by $\lambda_{creep} > 1$, is marked by the strain value γ_1. The value γ_{max} represents the strain with the steepest increase in $\gamma(t)$, i.e. a maximum in λ_{creep}.

The values of γ_{max} and γ_1 are shown in Figure 2.12 as functions of applied stress. The strain γ_{max} increases continuously with applied stress. Moreover, the universal scaling $\gamma_{max} \sim \sigma^{0.3}$, independent of composition or size ratio, is found. The strain γ_1 shows a

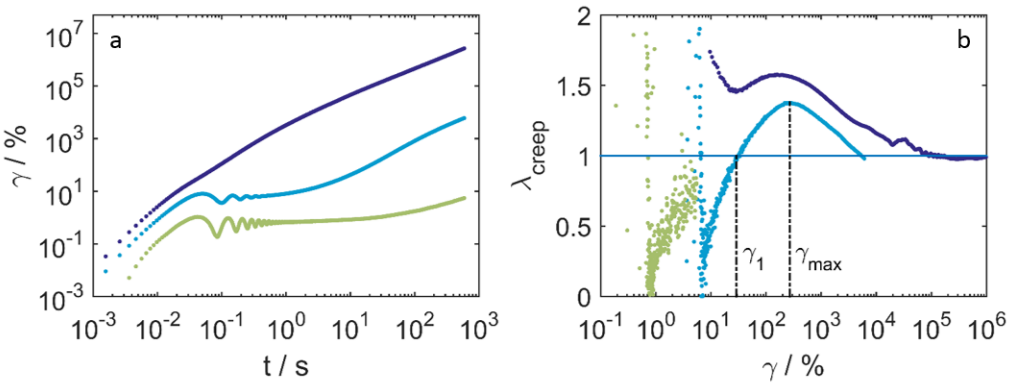

Figure 2.11.: a) Strain γ as a function of time t measured in a creep test for applied stress $\sigma > \sigma_y$, $\sigma \approx \sigma_y$, $\sigma < \sigma_y$ (from top to bottom). b) Logarithmic time derivative of the strain $\lambda_{creep}(t) = \mathrm{d}log(\gamma)/\mathrm{d}log(t)$ as a function of strain γ. γ_1 is the value of strain where $\lambda_{creep} = 1$, γ_{max} indicates the maximum of λ_{creep}.

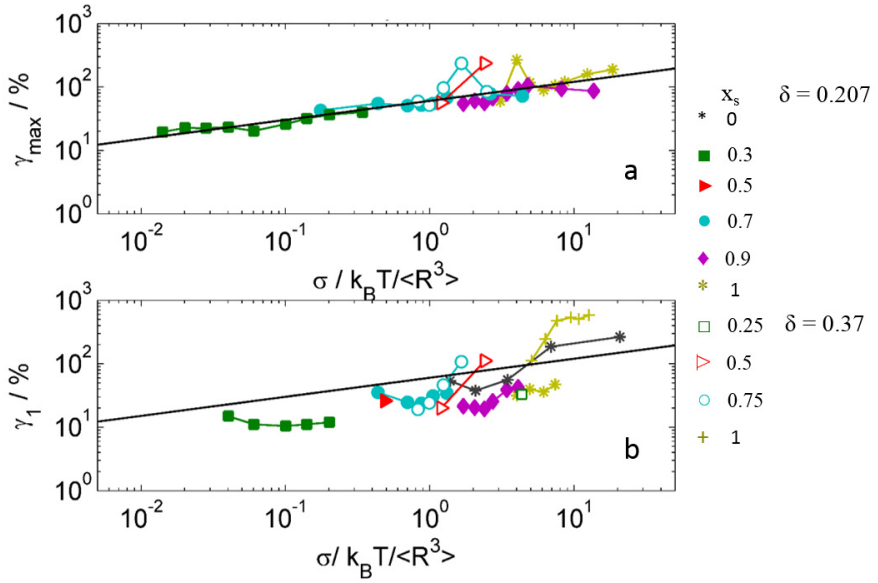

Figure 2.12.: a) Strain γ_{max} and b) γ_1 as a function of applied stress σ in units of energy density for different mixtures with the volume fraction $\phi = 0.61$ and fit $\gamma_{max} \sim \sigma^{\alpha}$ with $\alpha = 0.3$ (black line).

similar behavior. This result is comparable to the evolution of γ_{peak} as a function of $\dot{\gamma}$ as obtained from step-rate experiments (see Figure 2.8 c)). Two regimes in the dependence $\gamma_{peak}(\dot{\gamma})$ are observed. At small shear rates Brownian motion determines the dynamics. For large $\dot{\gamma}$ the particle motion becomes increasingly affected by affine motion. The creep experiments show that the application of large stresses lead to an increase of the strain where the transition to flow happens. That implies that the cage can be deformed more at large stresses before it eventually breaks. This observation may correspond to the second regime of $\gamma_{peak}(\dot{\gamma})$ from step rate experiments.

From what has been discussed in this and the previous section, we see that there are two ways to achieve a fluidization of the glass. Either we apply a constant shear rate or a shear stress $\sigma > \sigma_y$. A priori it is not clear that in both cases the steady flow states are similar. To investigate this, we compare two quantities. The first one is the $\dot{\gamma}(\sigma)$ obtained in creep measurement in the steady flow regime, where the deformation increases linearly with time. The second quantities, $\sigma(\dot{\gamma})$, is extracted from step rate measurement, where the stress decays to his steady state value if the system flows. In this way, each flow state can be characterized by two parameters, σ and $\dot{\gamma}$. When we apply a shear and fix one of these parameters we can measure the second. If the pair (σ, $\dot{\gamma}$) is independent of the choice which parameter is fixed and which is measured, then the flow states are equivalent.

With the help of Figure 2.13 we can perform such an analysis. It shows two creep and two step-rate measurements for one sample. In the creep experiment, the steady flow is characterized by a linear increase of the strain with time, i.e. a constant shear rate which is estimated to be $\dot{\gamma}(\sigma = 20\,\mathrm{Pa}) \approx 1.9\,\mathrm{s}^{-1}$. Now, in the step-rate experiments a similar shear rate, $\dot{\gamma} = 2.034\,\mathrm{s}^{-1}$, is applied. After the stress overshoot the system flows and the stress decays to its steady-state value, $\sigma \approx 18.5\,\mathrm{Pa}$. Obviously both ways to shear the system (by a stress or strain controlled shear) lead to the fluidization of the glass and result in the same steady flow state.

Plotting the product $\sigma\dot{\gamma}$ (see Figure 2.13 c) reveals a second interesting point, associated to the question whether the dynamics by which the final steady-state flow is achieved depends on the way shear is applied. When we compare the results from strain-controlled and creep experiments it is clearly visible that steady flow is achieved earlier in time in the strain-controlled experiment. This is particularly well visible for the parameter $\sigma = 30\,\mathrm{Pa}$ and $\dot{\gamma} = 10.17\,\mathrm{s}^{-1}$. The transient regime prior to the onset of steady flow seems to be very different for step-rate and creep experiments. The evolution of $\sigma\dot{\gamma}$ obtained from the creep experiment (yellow line in Figure 2.13 c)) resembles the stress overshoot measured in the step-rate experiment at $\dot{\gamma} = 2.034\,\mathrm{s}^{-1}$. However, this feature

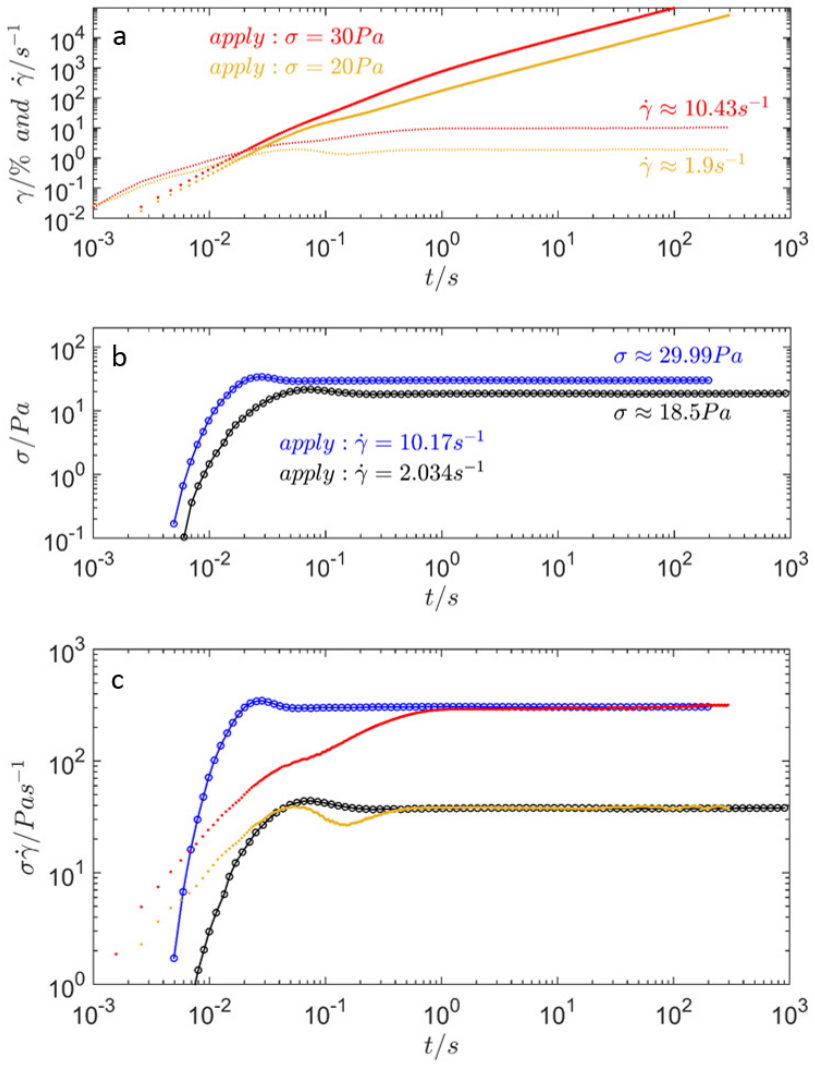

Figure 2.13.: a) The evolution of the strain $\gamma(t)$ (solid line) and the corresponding shear rate $\dot{\gamma}(t)$ (dotted line) measured in creep experiments for applied stress $\sigma = 20\,\text{Pa}$ and $30\,\text{Pa}$ and b) the evolution of the stress $\sigma(t)$ obtained by applying the shear with shear rate $\dot{\gamma} = 2.034\,\text{s}^{-1}$ and $10.17\,\text{s}^{-1}$ on a binary mixture with $\delta \approx 0.2$, $\phi \approx 0.61$ and $x_s = 0.7$. c) The curves from a) and b) plotted as $\sigma\dot{\gamma}(t)$.

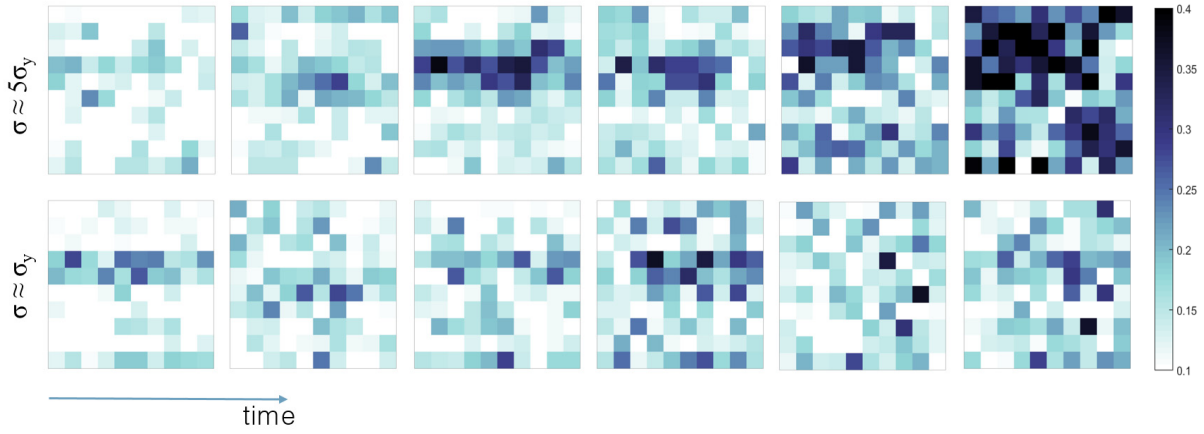

Figure 2.14.: Maps of particle mobilities for applied stress $\sigma \approx 5\sigma_y$ (top) and $\sigma \approx \sigma_y$ (bottom) and times $t = 7, 54, 67, 107, 134$ and $201\,\mathrm{s}$.

does not appear in the measurement for $\sigma = 30\,\mathrm{Pa}$ and $\dot{\gamma} = 10.17\,\mathrm{s}^{-1}$. These findings indicate that eventually the same flow state is reached in both cases, but via different transient dynamics.

The difference between these two kinds of rheological experiments, strain-controlled and creep, becomes even more clear when one observes the microscopic dynamics of particles during shear. In the previous chapter we discussed the dynamics of large particles under strain-controlled shear for a wide range of mixing compositions. For all glassy systems we found that the transition to flow is accompanied by super-diffusive dynamics of particles.

The microscopic single-particle dynamics of large particles during the application of stress-controlled shear was studied for a mixture with $\delta \approx 0.2$, $\phi \approx 0.61$ and $x_s = 0.1$[46]. Similar to the step-rate experiments, at short waiting times super-diffusive dynamics was observed in the regime for $\sigma > \sigma_y$, where the fluidization of the glass takes place. For small applied stresses, i.e. in the creep regime with $\sigma \lesssim \sigma_y$, the MSD increases sub-linearly with time without any waiting-time dependence.

How do the microscopic dynamics relate to the macroscopic rheology? For stress-controlled shear a linear relation between the macroscopic strain $\gamma(t)$ and the mean squared displacement $\delta y^2(t)$ was found. The relation $\delta y^2(t) \sim \gamma(t)$ holds in the steady-flow regime as well as in creep ($\sigma \lesssim \sigma_y$) and the transient regime before flow ($\sigma > \sigma_y$). We attribute this finding to the fact that the time evolution of the fraction of more mobile particles determines the changes in time of both the microscopic dynamics and the macroscopic strain. In contrast to that, the linear relation between mean squared displacement δy^2 and the macroscopic strain γ cannot hold when a constant shear rate

is applied. On the one hand, the constant $\dot{\gamma}$ implies a linear increase of $\gamma(t)$ with time, and, on the other hand, a super-linear increase of $\delta y^2(t)$ with t was found [5,29,34].

To get more insight into the dynamical activities of the particles the field of view of the microscope is divided into 10 $\times$ 10 boxes. The size of each box is $(2.8d_L)^2$. The mobility μ_{lm} of the particles in the box with index lm $(l, m = 1...10)$, is given by

$$\mu_{lm}(t) = \langle \Delta y_i(t) \rangle_{lm}, \tag{2.3}$$

where $\Delta y_i(t) = y_i(t) - y_i(t_0)$ is the displacement of particle i in the vorticity direction and $\langle ... \rangle_{lm}$ the average over all particles in box lm which are within the box at $t = t_0$. The map of the mobility for large applied stress $\sigma > \sigma_y$ and low stress $\sigma \approx \sigma_y$ is visualized in Figure 2.14 for different times. It can be seen that for $\sigma > \sigma_y$ the amount of boxes with high mobility (dark colored) increases with time. Moreover, a linear proportionality between the amount of high-mobility boxes and macroscopic strain was found. Interestingly, this proportionality holds also for small applied stresses, i.e. $\sigma \approx \sigma_y$.

A difference between two regimes, i.e. large and small applied stresses, was found in the spatial distribution of the particle mobility. For $\sigma \approx \sigma_y$ randomly distributed boxes with high and low mobility are found at any time. In contrast to that, for $\sigma > \sigma_y$, the randomly distributed regions of higher mobility observed at short times merge into a large region which subsequently spans the whole system. The appearance of the extended region of large mobility occurs for times where the onset of super-diffusion in the MSDs is observed.

To conclude, in contrast to the strain-controlled shear, the stress-controlled shear leads not necessarily to the flow of the glassy system. Two regimes for stress-controlled shear are observed: for $\sigma \lesssim \sigma_y$ the creep regime with sub-linear increase of $\gamma(t)$ and the flow regime for $\sigma > \sigma_y$. It was found, that the resulting steady-flow state may be compared to the one observed in the strain-controlled shear. Albeit both kinds of shear lead eventually to the same flow, the microscopic dynamics during the onset of flow is found to be different. For constant stress in both stress regimes, $\sigma > \sigma_y$ and $\sigma \lesssim \sigma_y$, a linear increase of the mean squared displacement with time was found. This and the heterogeneous distribution of the high-mobility regions found in the creep experiments do not have an analogy in the strain-controlled case.

Bibliography

[1] T. Wilson, *Confocal Microscopy*, Academic Press, London, 1990.

[2] M. Minsky, *Scanning*, 1988, **10**, 128–138.

[3] M. Dijkstra, D. Frenkel and J. P. Hansen, *J. Chem. Phys.*, 1994, **101**, year.

[4] P. D. Kaplan, J. L. Rouke, A. G. Yodh and D. J. Pine, *Phys. Rev. Lett.*, 1994, **72**, 582–585.

[5] T. Sentjabrskaja, M. Hermes, W. C. K. Poon, C. D. Estrada, R. Castañeda-Priego, S. U. Egelhaaf and M. Laurati, *Soft Matter*, 2014, **10**, 6546–6555.

[6] T. Sentjabrskaja, E. Babaliari, J. Hendricks, M. Laurati, G. Petekidis and S. U. Egelhaaf, *Soft Matter*, 2013, **9**, 4524–4533.

[7] T. Sentjabrskaja, D. Guu, M. P. Lettinga, S. U. Egelhaaf and M. Laurati, *AIP Conf. Proc.*, 2013, **1518**, 206.

[8] J. Hendricks, R. Capellmann, A. B. Schofield, S. U. Egelhaaf and M. Laurati, *Phys. Rev. E*, 2015, **91**, 032308.

[9] K. N. Pham, G. Petekidis, D. Vlassopoulos, S. U. Egelhaaf, P. N. Pusey and W. C. K. Poon, *Europhys. Lett*, 2006, **75**, 624.

[10] I. Biazzo, F. Caltagirone, G. Parisi and F. Zamponi, *Phys. Rev. Lett.*, 2009, **102**, 195701.

[11] C. Mayer, F. Sciortino, C. N. Likos, P. Tartaglia, H. Löwen and E. Zaccarelli, *Macromol.*, 2009, **42 (1)**, 423 – 434.

[12] F. Höfling and T. Franosch, *Rep. Prog. Phys.*, 2013, **76**, 046602.

[13] R. J. Ellis and A. P. Minton, *Nature*, 2003, **425**, 27–28.

[14] R. Ellis, *Trends Biochem. Sci.*, 2001, **26**, 597 – 604.

[15] A. J. Moreno and J. Colmenero, *Phys. Rev. E*, 2006, **74**, 021409.

[16] A. J. Moreno and J. Colmenero, *J. Chem. Phys.*, 2006, **125**, 164507.

[17] R. Raccis, A. Nikoubashman, M. Retsch, U. Jonas, K. Koynov, H. J. Butt, C. N. Likos and G. Fytas, *ACS Nano*, 2011, **5**, 4607–4616.

[18] H. A. Lorentz, *Proc. Roy. Acad. Amst.*, 1905, **7**, 684.

[19] H. van Beijeren, *Rev. Mod. Phys.*, 1982, **54**, 195–234.

[20] S. Leitmann and T. Franosch, *Phys. Rev. Lett.*, 2013, **111**, 190603.

[21] F. Höfling, T. Franosch and E. Frey, *Phys. Rev. Lett.*, 2006, **96**, 165901.

[22] J. Kurzidim, D. Coslovich and G. Kahl, *Phys. Rev. E*, 2010, **82**, 041505.

[23] J. Kurzidim, D. Coslovich and G. Kahl, *Phys. Rev. Lett.*, 2009, **103**, 138303.

[24] V. Krakoviack, *Phys. Rev. Lett.*, 2005, **94**, 065703.

[25] K. Kim, K. Miyazaki and S. Saito, *Europhys. Lett*, 2009, **88**, year.

[26] T. Sentjabrskaja, E. Zaccarelli, C. D. Michele, F. Sciortino, P. Tartaglia, S. U. Egelhaaf and M. Laurati, in preparation.

[27] T. G. Mason and D. A. Weitz, *Phys. Rev. Lett.*, 1995, **75**, 2770–2773.

[28] N. Koumakis, M. Laurati, S. U. Egelhaaf, J. F. Brady, and G. Petekidis, *Phys. Rev. Lett.*, 2012, **108**, 098303.

[29] M. Laurati, K. J. Mutch, N. Koumakis, J. Zausch, C. P. Amann, A. B. Schofield, G. Petekidis, J. F. Brady, J. Horbach, M. Fuchs and S. U. Egelhaaf, *J. Phys.: Condens. Matter*, 2012, **24**, 431207.

[30] G. Petekidis, A. Moussaid and P. N. Pusey, *Phys. Rev. E*, 2002, **66**, 51402.

[31] K. N. Pham, G. Petekidis, D. Vlassopoulos, S. U. Egelhaaf, W. C. K. Poon and P. N. Pusey, *J. Rheol.*, 2008, **52**, 649.

[32] R. Besseling, E. R. Weeks, A. B. Schofield and W. C. K. Poon, *Phys. Rev. Lett.*, 2007, **99**, 028301.

[33] K. J. Mutch, M. Laurati, C. P. Amann, M. Fuchs and S. U. Egelhaaf, *Eur. Phys. J. Special Topics*, 2013, **222**, 2803.

[34] J. Zausch, J. Horbach, M. Laurati, S. U. Egelhaaf, J. M. Brader, T. Voigtmann and M. Fuchs, *J. Phys.: Condens. Matter*, 2008, **20**, 404210.

[35] W. van Megen, T. C. Mortensen, S. R. Williams and J. Müller, *Phys. Rev. E*, 1998, **58**, 6073–6085.

[36] C. P. Amann, M. Siebenbürger, M. Kräger, F. Weysser, M. Ballauff and M. Fuchs, *J. Rheol.*, 2013, **57**, 149–175.

[37] N. Koumakis, J. F. Brady and G. Petekidis, *Phys. Rev. Lett.*, 2013, **110**, 178301.

[38] C. Christopoulou, G. Petekidis, B. Erwin, M. Cloitre and D. Vlassopoulos, *Philosophical Transactions of the Royal Society of London A: Mathematical, Physical and Engineering Sciences*, 2009, **367**, 5051–5071.

[39] M. Siebenbürger, M. Fuchs and M. Ballauff, *Soft Matter*, 2012, **8**, 4014–4024.

[40] C. Eisenmann, C. Kim, J. Mattsson and D. A. Weitz, *Phys. Rev. Lett.*, 2010, **104**, 035502.

[41] M. Siebenbürger, M. Ballauff and T. Voigtmann, *Phys. Rev. Lett.*, 2012, **108**, 255701.

[42] P. Chaudhuri and J. Horbach, *Phys. Rev. E*, 2013, **88**, 040301.

[43] J. Rosti, J. Koivisto, L. Laurson and M. J. Alava, *Phys. Rev. Lett.*, 2010, **105**, 100601.

[44] P. Coussot, H. Tabuteau, X. Chateau, L. Tocquer and G. Ovarlez, *J. Rheol.*, 2006, **50**, 975.

[45] R. H. Ewoldt and G. H. McKinley, *Rheol. Bull.*, 2007, **76**, 4.

[46] T. Sentjabrskaja, P. Chaudhuri, M. Hermes, W. K. Poon, J. Horbach, S. Egelhaaf and M. Laurati, *Sci. Rep.*, 2015, **5**, 11884.

3. Publications in refereed journals

3.1. Publication 1: Glasses of dynamically asymmetric binary colloidal mixtures: Quiescent properties and dynamics under shear

Journal: AIP Conference Proceedings
Reference: *AIP Conf. Proc.*, 2013, **1518**, 206
Authors: **T. Sentjabrskaja**, D. Guu, M. P. Lettinga, S. U. Egelhaaf and M. Laurati
1st author
TS prepared all materials, performed the experiments and analyzed the data. The confocal measurements under shear were performed on the setup developed by DG and MPL. TS, ML and SUE conceived and discussed the project and ML and SUE supervised the project. All authors contributed to the writing of the manuscript.
70 % contribution of TS

This page has been left intentionally blank.

Glasses of dynamically asymmetric binary colloidal mixtures: Quiescent properties and dynamics under shear

Tatjana Sentjabrskaja*, Donald Guu†, M Paul Lettinga†, Stefan U Egelhaaf* and Marco Laurati*

*Condensed Matter Physics Laboratory, Heinrich Heine University Düsseldorf, 40225 Germany
†ICS-3, Institut Weiche Materie, Forschungszentrum Jülich, 52425 Jülich, Germany.

Abstract. We investigate mixing effects on the glass state of binary colloidal hard-sphere-like mixtures with large size asymmetry, at a constant volume fraction $\phi = 0.61$. The structure, dynamics and viscoelastic response as a function of mixing ratio reflect a transition between caging by one or the other component. The strongest effect of mixing is observed in systems dominated by caging of the large component. The possibility to pack a large number of small spheres in the free volume left by the large ones induces a pronounced deformation of the cage of the large spheres, which become increasingly delocalised. This results in faster dynamics and a strong reduction of the elastic modulus. When the relative volume fraction of small spheres exceeds that of large spheres, the small particles start to form their own cages, slowing down the dynamics and increasing the elastic modulus of the system. The large spheres become the minority and act as an impurity in the ordering beyond the first neighbour shell, i.e. the cage, and do not directly affect the particle organisation on the cage level. In such a system, when shear at constant rate is applied, melting of the glass is observed due to facilitated out-of-cage diffusion which is associated with structural anisotropy induced by shear.

Keywords: glass, binary mixtures, viscoelasticity, dynamics, structure
PACS: 61.43.Fs,64.70.pV,81.05.kf,82.70.Dd,83.10.Pp,83.60.Bc,83.80.Hj

INTRODUCTION

Many different systems, among them polymers, metals and colloids, can form thermodynamically equilibrated states, but also non-equilibrium, metastable states, including amorphous solid materials called glasses [1, 2]. The glass transition is generally associated with a dramatic slowing down of the particle dynamics which is driven by changes in thermal energy or crowding.

One of the simplest model systems to study crowding induced glass formation are suspensions of colloidal hard spheres. By increasing the particle volume fraction ϕ formation of a glass state above $\phi = \phi_g$ prevents crystallisation, if the system has a sufficiently broad distribution of sizes. The formation of the glass state is explained in terms of the cage effect: At $\phi > \phi_g$ each particle is trapped in the cage of its neighbours resulting in dynamical arrest, i.e. the absence of long distance diffusion over a large window of times [3, 4]. Dynamical arrest and formation of a solid state above $\phi \geq \phi_g$ are also manifested in the viscoelastic properties as a sudden increase of the viscosity [5] and the appearance of a Maxwell plateau modulus in the linear response [6].

The addition of a second component with a significantly different mean size compared to the first component, leads to an even richer scenario. Depending on the total volume fraction of the system and the mixing ratio of the two species, mode coupling theory (MCT) predicts the existence of different glass states [7]. When the size-ratio $\delta = R_s/R_l = d_s/d_l$, where R_s, d_s and R_l, d_l are the radii and diameters of the small and large components respectively, becomes about 0.2 and smaller, four different glass states are expected [7]: In the first state both components are caged; in the second state dynamical arrest of the large component is driven by depletion attraction induced by the small species; in the third state the large component is arrested through caging, while the small component is mobile; finally the small particles can be caged, while the large particles are not caged, but only localised by the surrounding dense matrix of small particles. Despite the rich behaviour predicted by theory, the glass state of colloidal binary mixtures at such large size disparities is hardly studied experimentally [8]. In [8] the formation of a glass despite the mobility of the small component is reported. A similar glass state has also been found in simulations of soft sphere mixtures [9, 10].

In order to extend these studies and to explore the formation of different glasses, we performed experiments to determine the microscopic structure, dynamics and viscoelastic response of colloidal hard-sphere mixtures of large size disparity ($\delta = 0.2$) and constant total volume fraction $\phi \simeq 0.61$. We vary the relative volume fraction of the small component, $x_s = \phi_s/\phi$, to explore the effect of mixing on the glass state. We find that the composition of the mixture strongly affects the dynamics and elastic modulus of the system, in particular in mixtures contain-

ing a smaller volume fraction of small spheres, $x_s < 0.5$. In addition, we compare the dynamics of a sample under shear to its quiescent state, showing that the driving introduced by shear leads to an acceleration of the non-affine particle motions, inducing glass melting. A discussion of the non-linear rheology of these mixtures and comparison to predictions of mode-coupling theory are reported in separate publications [11, 12].

METHODS

Samples

Suspensions of poly-methylmethacrylate (PMMA) particles sterically stabilized with a layer of polyhydroxystearic acid (PHS) were prepared in a solvent mixture of cycloheptyl bromide (CHB) and cis-decalin, closely matching the density and refractive index of the colloids. In the CHB/decalin solvent mixture, the spheres acquire a small charge which is screened by adding 4 mM tetrabutylammoniumchloride [13]. This system shows almost hard-sphere behaviour, with the volume fraction $\phi = (4\pi/3)nR^3$ being the only thermodynamic control parameter, with n the number density of particles and R the sphere radius. Binary colloidal mixtures with $\delta \simeq 0.2$, fixed total volume fraction $\phi \simeq 0.61$ and different mixing ratios were prepared starting from one component stock suspensions. The stock suspensions were obtained by diluting a sediment of large particles of mean size $d_l = 1.76 \pm 0.02$ μm (relative polydispersity $\sigma = 0.057$), or small particles of mean size $d_s = 0.350 \pm 0.004$ μm ($\sigma = 0.150$). The large particles were fluorescently labeled with nitrobenzoxadiazole (NBD). For the two one-component colloidal stock suspensions, the values of the radius and polydispersity were determined from the angular dependence of the scattered intensity and diffusion coefficient obtained by means of static and dynamic light scattering, respectively, on a very dilute colloidal suspension ($\phi \simeq 10^{-4}$). The volume fraction of the sediment of large spheres was experimentally determined as follows: A first guess for the volume fraction ϕ_{RCP} of the sediment was obtained using simulation results [14]. The sediment was then diluted to a nominal volume fraction $\phi \simeq 0.4$ and observed using confocal microscopy. The imaged volume was partitioned into Voronöi cells and the mean size of the Voronöi volume per particle calculated. The ratio of the particle volume to the mean Voronöi volume serves as an estimate of the volume fraction of the sample. This was found to be $\phi = 0.43$ which corresponds to $\phi^l_{RCP} = 0.68$. The small spheres were too small to be imaged. Therefore their volume fraction was adjusted to give an equivalent rheological response to the large spheres. For ideal hard spheres, the energy density scales as nk_BT, so that the shear moduli must be equal in these units. The volume fraction of the one-component small particles suspension was adjusted to obtain the same normalised shear moduli as for the one-component large particles. Although their linear viscoelasticities are thus within experimental resolution the same, their volume fractions could be slightly different, since the samples have different polydispersities. Accordingly, for intermediate x_s, shear moduli are reported in reduced units of the energy density.

Confocal microscopy

Quiescent State

Confocal microscopy experiments on quiescent samples were performed using a VT-Eye confocal unit (Visitech International), mounted on a Nikon Ti-U inverted microscope with a 100x Nikon Plan-Apo VC oil-immersion objective, and a laser with $\lambda = 488$ nm. Samples were contained in vials where the bottom was cut and replaced by a coverslip to allow for imaging [15]. Stacks of images of 512×512 pixels, corresponding to an x-y plane size of approx. 50×50 μm^2 were acquired. Each stack was composed of 101 images obtained every 0.2 μm in z-direction, leading to an imaged volume of approximately $50 \times 50 \times 20$ μm^3 per stack. The time needed to acquire one stack was approximately 3.8 s. Stacks were acquired at a depth of approx. 30μm from the coverslip. Typically for each sample 7 different volumes were imaged for 1200s during which 300 stacks were collected for each volume to follow the dynamics of the samples. The stacks were analysed using standard routines [16] to extract particle coordinates and trajectories. Figure 1 shows typical two-dimensional images corresponding to a plane in a stack, acquired for samples with different mixing ratios x_s.

Under Shear

Under shear, samples were imaged using a custom-built rotational shear cell (a modified version of the model described in [17]), mounted on a Zeiss Axiovert M200 microscope with a 63x Zeiss Plan Neo Fluar water-glycerol immersion objective and equipped with a VT-Infinity confocal unit (Visitech International). A glass coverslip serves as bottom plate of the cell to allow for imaging with high numerical aperture objectives. The glass surface was covered with polydisperse colloidal hard spheres with a size comparable to the large spheres to minimise the effects of wall slip [18]. The top

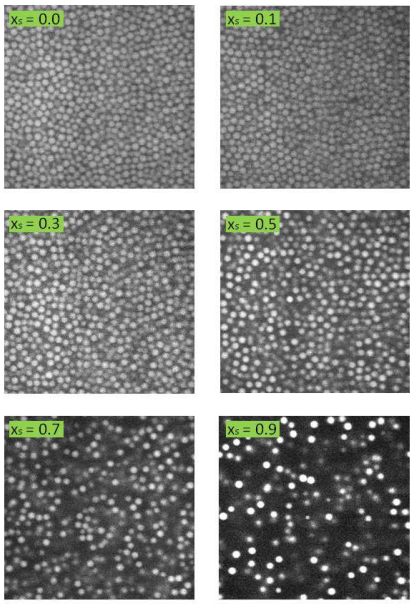

FIGURE 1. Typical confocal microscopy images of quiescent samples showing the large fluorescently-labelled particles only. The total volume fraction of the samples is $\phi = 0.61$ and the relative volume fraction of small particles x_S are as indicated.

of the cell is formed by a metal cone with 14 mm diameter and 2° cone angle. Images are acquired at a radial distance of 7 mm from the center. The plate and cone rotate in opposite directions, giving rise to a zero-velocity plane in the sample, the depth of which can be adjusted through the relative speed of the cone and plate. Images were acquired with an Andor iXon 897 EMCCD camera for 300s, at an average rate of 10 frames per second. Solvent evaporation was minimised using a solvent sealing at the top of the cell.

Rheology

Rheology measurements were performed with a AR2000ex stress-controlled rheometer, using a cone-plate geometry with 20 mm diameter, 2° cone angle and 0.054 mm gap. A solvent trap was used to minimise solvent evaporation during the measurements. The temperature was set to 20 °C and controlled within ±0.1 °C via a standard Peltier plate. The effects of sample loading and aging were minimized by performing a standard rejuvenation procedure before each test: directly after loading, we performed a dynamic strain

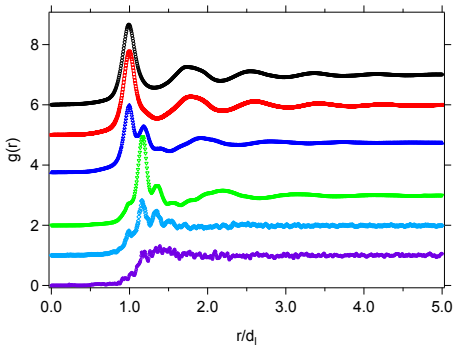

FIGURE 2. Radial distribution function $g(r)$ of the large spheres, determined using confocal microscopy. The total volume fraction of the samples is $\phi = 0.61$ and the relative volume fractions of small particles are $x_S = 0$, 0.1, 0.3, 0.5, 0.7, 0.9 (top to bottom). Data are shifted along the vertical axis for clarity.

sweep, i.e. applied oscillatory shear to the samples with a frequency ω = 1 rad/s and an increasing strain amplitude until the sample was flowing. Before each measurement, flow of the sample was induced applying oscillatory shear at strain γ = 300%. Shear was applied for the time needed to achieve a steady-state response, i.e. the storage modulus G′ and the loss modulus G″ become time-independent, typically 200 s. Successively, the linear viscoelastic moduli were measured at 0.1% $\leq \gamma \leq$ 0.5% (depending on sample) as a function of time to monitor reformation of structure, until the moduli reached a time-independent value, typically after 100 s to 900 s (depending on sample). After this, the experiment was started immediately.

RESULTS AND DISCUSSION

Quiescent Structure

To understand mixing-induced changes on the cage structure of a one-component glass, we used confocal microscopy to determine the radial distribution functions $g(r)$ of large spheres, the only species which is fluorescently labeled and therefore visible (Figs. 1 and 2).

The $g(r)$ for $x_s = 0$ is typical of a glass-forming one-component suspension with size polydispersity. It shows a pronounced correlation peak at $r \approx d_l$, corresponding to the highest probability of finding particles in the first-neighbour shell, and additional peaks at larger r related to particles in the successive neighbour shells. For a small volume fraction of small particles ($x_s = 0.1$, $\phi_l = (1 - x_s)\phi = 0.549$) these features remain, but in addition a small shoulder to the right of the first maximum is observed. This indicates a perturbation of the

cage formed by the large spheres. When increasing x_s to 0.3 ($\phi_l = 0.427$), the height of the first-neighbour peak decreases, which indicates dilution (also evident in Fig. 1), and that some particles formerly constituting the cage are located at larger distances. These particles are found at distances $d_l + d_s$ (where the shoulder was observed at $x_s = 0.1$) and $d_l + 2d_s$, as seen from the corresponding peaks in g(r). This implies that small particles are located in between large particles and hence loosen the cage structure. In line with this observation the layering of large spheres only extends to the third neighbour shell. At $x_s = 0.5$ ($\phi_l = 0.305$) particles are mostly located at distance $d_l + d_s$ and also the probability of finding particles at $d_l + 2d_s$ is increased. Moreover, additional peaks at $d_l + n\,d_s$ are visible. This indicates that at $x_s = 0.5$ a first neighbour shell of large spheres does no longer surround large particles (Fig. 1), and a transition to a cage of small spheres takes place. This is consistent with the following geometrical argument: Each small sphere of radius R_s projects on a sphere of radius $R_l = R_s/\delta$ an angle $\theta = 2\arcsin(1/(1+1/\delta))$. The maximum packing of small spheres having the centers separated by this angular distance, i.e. covering the surface area of a large sphere, can be calculated as $N = 120$ [19]. At $x_s = 0.5$ the number fraction of small particles for each big particle is $\xi_s/\xi_l = x_s/\delta^3(1-x_s) = 125$, i.e. on average each large particle is covered by small particles for $x_s = 0.5$ and hence the first neighbour shell and cage of large particles disappear. At $x_s = 0.7$ ($\phi_l = 0.183$) correlations at distances $d_l + n\,d_s$ dominate and layering beyond the second neighbour shell vanishes due to the pronounced dilution of the large spheres (Fig. 1). Correlations are further reduced at $x_s = 0.9$ ($\phi_l = 0.061$) due to the increased dilution of the large spheres (Fig. 1). From the evolution of the radial distribution function with increasing x_s one can therefore conclude that the small spheres occupy an increasingly larger fraction of the free volume in between the large spheres, inducing a distortion of the cage of large spheres until a transition to a system dominated by the cage of small spheres is observed.

Quiescent Dynamics

To explore the effect of the structural changes discussed in the previous section on the microscopic dynamics, we investigate the mean squared displacements (MSDs) of the large particles, δr_l^2, as a function of x_s (Figure 3). The system of only large spheres ($x_s = 0.0$) presents an MSD which, within the accessible time range, shows no long-time diffusion, i.e. glassy dynamics. Moreover, the plateau of the MSD corresponds to a localisation of the particles on distances of the order $\nu_l(x_S = 0) \approx 0.1 d_l$, which is typical for a cage in a one-

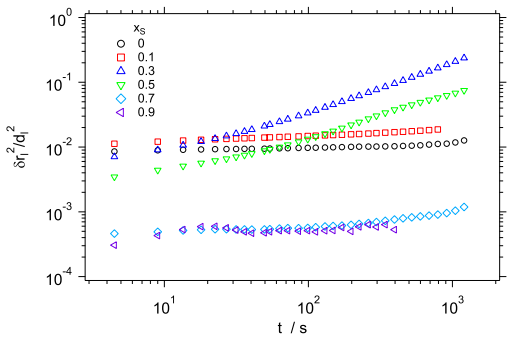

FIGURE 3. Mean squared displacements δr_l^2 of the large spheres, normalised by their diameter squared (d_l^2), determined using confocal microscopy. The total volume fraction of the samples is $\phi = 0.61$ and the relative volume fractions of small particles are $x_S = 0.0$ (○), 0.1 (□), 0.3 (△), 0.5 (▽), 0.7 (◇), 0.9 (◁).

component glass. The time-dependence of the dynamics is similar for $x_s = 0.1$, but the localisation length is slightly larger. This reflects the small perturbation of the cage structure (Figure 2). For $x_s = 0.3$ a significant acceleration of the dynamics is observed, for times $t > 10$ s the particles are no longer localised and the MSD increases sub-linearly with t. It is expected that diffusive dynamics is established beyond the accessible time scale. The acceleration of the dynamics is related to the considerable distortion of the cage of large spheres induced by the presence of the small spheres, which increase the mobility. A comparable time-dependence of the MSD is obtained at $x_s = 0.5$, but the displacements are smaller, indicating a stronger localisation. A stronger localisation can be associated with the transition to the cage structure of small spheres, as also evidenced in the $g(r)$. Note that the caging of the small spheres is apparently incomplete yet, and therefore the large particles are not localised. For the two largest values of x_s the large spheres are localised by a cage of small spheres. Accordingly their MSD again show no diffusion. The localisation length is of the order of $\nu_l(x_s \geq 0.7, 0.9) \approx 0.02 d_l$, i.e. about $\delta\nu_l(x_S = 0)$, which indicates that the particles are indeed localised on the length scale of the cage of small particles. Note that the plateau values of the MSDs of these samples approach the resolution limit of the setup.

Linear Viscoelastic Moduli

In order to establish a link between the microscopic structure and dynamics of the samples and their mechanical response, we measured the frequency dependent linear viscoelastic moduli of the mixtures (Figure 4). The moduli are reported in units of energy density

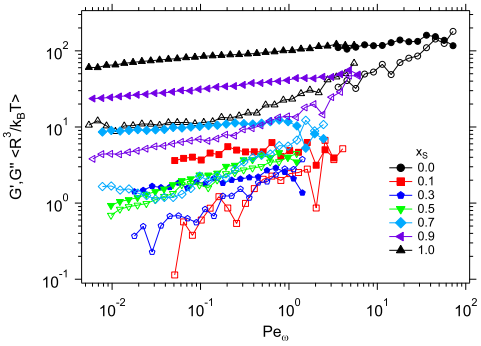

FIGURE 4. Storage modulus G' (full symbols) and loss modulus G'' (open symbols), in units proportional to the energy density ($k_BT/\langle R^3\rangle$), as a function of oscillatory Peclet number Pe_ω, for samples with $\phi = 0.61$ and relative volume fractions of small particles $x_S = 0.0$ (○), 0.1 (□), 0.3 (⬠), 0.5 (▽), 0.7 (◇), 0.9 (◁), 1.0 (△).

$\langle nk_BT\rangle \sim k_BT/\langle R^3\rangle$, with n particle density and:

$$\frac{1}{\langle R^3\rangle} = \frac{1}{R_L^3}\left[x_S\left(\frac{1}{\delta^3}-1\right)+1\right] \qquad (1)$$

This representation removes the trivial effect of different average particle sizes for different values of x_s on the absolute values of the shear moduli. The data are shown as a function of the oscillatory Peclet number $Pe_\omega = \tau_B/\tau_\omega = (6\pi\eta\omega\langle R^3\rangle)/k_BT$ which represents the ratio between the period of oscillation, $\tau_\omega = 1/\omega$, and the Brownian time, $\tau_B = \langle R^2/D_0\rangle$, where D_0 is the free diffusion coefficient.

At large values of Pe_ω, for all samples G'' is larger than G'. This response can be associated to the in-cage dynamics, i.e. the short time diffusion of a particle in its cage. In contrast at smaller frequencies, i.e. longer times, the structural relaxation associated with long-time diffusion allows us to distinguish the response of a glass from that of a fluid.

The one-component systems ($x_s = 0.0, 1.0$) show the response of a glass. The storage modulus G' is larger than the loss modulus G'' and no crossing of the two moduli can be observed at low Pe_ω, indicating that no structural relaxation is observed in the accessible frequency window. At $x_s = 0.1$ the Pe_ω (frequency) dependence of the viscoelastic moduli is similar to that of the one-component systems, i.e. still characteristic of a glass, but the viscoelastic moduli are reduced by more than an order of magnitude, despite the only limited structural deformation of the cage induced by the presence of the small spheres. This is however consistent with the larger localisation length observed in the dynamics, which indicates a looser cage structure. At $x_s = 0.3$ the reduction of the shear moduli is even more pronounced than at $x_s = 0.1$. Moreover G' and G'' become similar, indicating

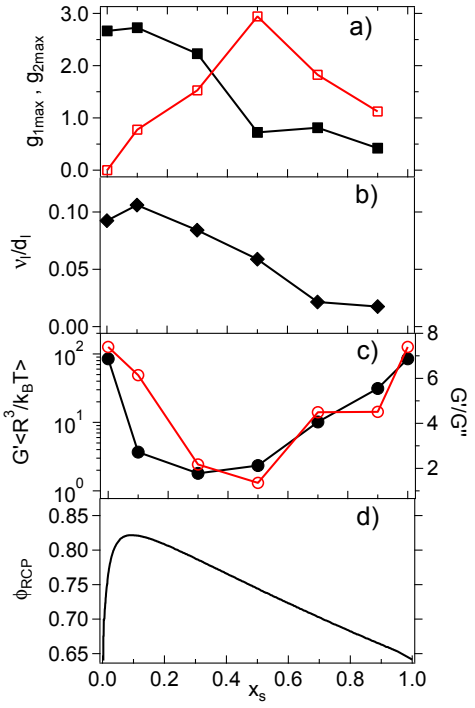

FIGURE 5. (a) Height of the first, $g_{1\max}$ (black, full symbols), and second, $g_{2\max} = g(d_l + d_s)$ (red, open symbols), peaks of $g(r)$ (Figure 2), (b) Localisation length ν_l in units of d_l, estimated from MSDs at $t = 4.5s$ (Figure 3) (c) Storage modulus $G'(Pe_\omega = 0.1)$ (black, full symbols, left axis) and ratio G'/G'' at the same Pe_ω (red, open symbols, right axis), in units of energy density $k_BT/\langle R^3\rangle$) and (d) theoretical prediction [23] for changes in ϕ_{RCP} at $\delta = 0.175$ as a function of x_s.

a weaker solid-like response. This is consistent with the large structural distortion of the cage manifested in the radial distribution function (Figure 2) and with the faster dynamics (Figure 3). Compared to $x_s = 0.3$, at $x_s = 0.5$ the moduli at large Pe_ω are bigger, but smaller at low Pe_ω, which is due to the stronger frequency dependence of the shear moduli. In addition, G' and G'' have almost identical values. Such a response is similar to that observed for depletion driven colloidal gels in the vicinity of the gelation boundary [20, 21, 22]. Further increasing x_s to 0.7 and 0.9, the moduli become larger and for $x_s = 0.9$ approach the values of the one-component systems. This is consistent with a transition to a system dominated by cages formed by the small particles and with structure and dynamics of these samples. Note that the residual distortion induced by the large spheres leads to a reduction of the overall elastic response of these samples.

The trends discussed above are summarized by plotting G' and the ratio G'/G'' as a function of x_s, at a fixed value of $Pe_\omega = 0.1$ (Figure 5c). The ratio G'/G'' attains the

smallest value at $x_s = 0.5$, which could reflect a transition from a system dominated by cages formed by large spheres to a system dominated by cages formed by small spheres. This interpretation is supported by the trends of the heights of the first and second peaks of $g(r)$ (Figure 5a): Between $x_s = 0.3$ and $x_s = 0.5$ the first peak strongly drops and then remains nearly constant for larger x_s, indicating the disappearance of the first neighbor shell of large particles, i.e the large spheres cage. The second peak reaches its maximum at $x_s = 0.5$, corresponding to formation on average of a shell of small particles around each large particle, and then decreases for larger values of x_s, due to the further intercalation of small spheres in between two large spheres, which leads to caging of the small spheres. In contrast, the elasticity of the samples, represented by G', reaches a minimum at $x_s = 0.3$. This could be explained by the larger localisation length of the large spheres at $x_s = 0.3$ (Figure 5b). Furthermore, changes in G' are considerably larger in systems with a larger volume fraction of large spheres. This can be rationalized by considering the effects of the inclusion of the second component on the structure of the system in the two cases: In systems at small x_s, the small spheres can be packed in the free volume in between the large spheres, including the free volume within the cages. This deforms the cage and shifts random close packing (Figure 5d, data for $\delta = 0.175$ taken from [23]). On the other hand, addition of large spheres to a system of small spheres only affects the order beyond the first shell, i.e. beyond the cage, since the large spheres cannot fill the space in between the small spheres. This results in structural heterogeneity rather than cage deformation, and in a small shift of random close packing (Figure 5d, $x_s > 0.5$).

Dynamics under shear

We investigated the effect of shear on the motions of large particles in a sample with a major relative volume fraction of small spheres ($x_s = 0.9$). The mean squared displacements δr_l^2 of large particles were determined in the quiescent and steady state of shear, for two different shear rates $\dot{\gamma}$. For the applied shear rates, the time scale introduced by shear, $1/\dot{\gamma}$, is considerably longer than the Brownian time τ_B associated with the short-time diffusion of both large and small spheres. This is quantified through the Peclet number $Pe_{\dot{\gamma}} = (6\pi\eta\dot{\gamma}\langle R^3\rangle)/k_BT$. Both time scales are smaller than the structural relaxation time of the system, which diverges, although activated processes typically lead to diffusion at long times [24].
The velocity profiles obtained in the steady state of shear are shown in figure 6. They were obtained by determining the velocity of the particles from their trajectories. The zero-velocity plane is located at about 15 μm into

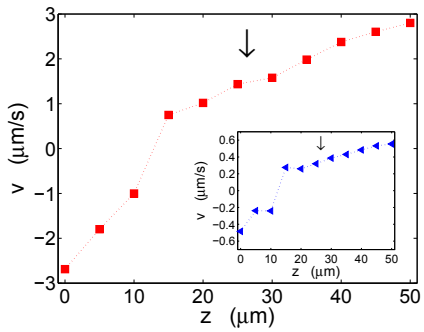

FIGURE 6. Average velocity of the large spheres as a function of position z in the gap, for sample with a relative volume fraction of small spheres $x_s = 0.9$ and $Pe_{\dot{\gamma}}^l = 4.2 \times 10^{-1}$ (main plot) and 6.7×10^{-2} (inset). Arrows indicate the location of the plane where the dynamics were measured.

the sample for both shear rates. The velocity profiles show a larger velocity gradient below the zero-velocity plane than above. Within each band though the velocity profile is linear, indicating laminar flow. For the higher shear rate the slower band corresponds to $\dot{\gamma} \simeq 0.06$ s^{-1}, while the faster band to $\dot{\gamma} \simeq 0.25$ s^{-1}. The weighted average $\dot{\gamma} \simeq 0.117$ s^{-1} agrees within uncertainties with the expected value of $\dot{\gamma} \simeq 0.120$ s^{-1}. Similarly for the slower shear rate the slower band corresponds to $\dot{\gamma} \simeq 0.0095$ s^{-1} and the faster one to $\dot{\gamma} \simeq 0.041$ s^{-1}, with an average of 0.017 s^{-1}. The formation of the two bands might be due to the different roughness of the particles coated surface of the bottom plate and the smooth metallic surface of the cone. The dynamics under shear were determined in a velocity-vorticity plane within the slower bands for both shear rates, corresponding for the large spheres to $Pe_{\dot{\gamma}}^l = 4.2 \times 10^{-1}$ and 6.7×10^{-2}, and at about $z = 27\,\mu$m in the sample (arrows in Figure 6).

The results of measurements with the shear cell setup are reported in Figure 7 as MSDs vs. strain $\gamma = \dot{\gamma}t$. The strain axis for the quiescent MSD was obtained using the faster shear rate $\dot{\gamma} \simeq 0.06$ s^{-1}. The quiescent dynamics show a time dependence similar to that obtained using the other confocal microscope setup (compare figures 7 and 3): particles are localised on the experimentally accessible time window and no long-time diffusion is observed. One can observe though that the localisation length is larger for the measurements with the shear cell setup. This might be attributed to the combination of two factors [25]: the larger noise level of the multi-beam VT-infinity confocal microscope, which arises from the cross-talk of the fluorescence emission from many different particles simultaneously excited; the smaller magnification (63x instead of 100x) and the larger pixel size (0.25 μm compared to 0.115 μm), which increase the uncertainty in the determination of particle coordinates.

Note also that, in order to compare to measurements under shear, the quiescent MSDs are measured in a two-dimensional plane instead of a three dimensional volume as in the other setup. Application of a slow shear rate, corresponding to $Pe^l_{\dot\gamma} = 6.7 \times 10^{-2}$, induces a significant acceleration of the non-affine dynamics of the large particles, as shown in figure 7: The particles are initially localised on the same length scale as in the quiescent state but become delocalised at $\gamma \geq 6$ %, with the MSD increasing first sub-linearly and then linearly with γ over the remaining range of measured times. The final linear increase of $\delta r_l^2 \sin t$ ($\gamma \propto t$) indicates diffusive behavior. At the larger shear rate ($Pe^l_{\dot\gamma} = 4.2 \times 10^{-1}$) the particle dynamics first show localisation on a length scale smaller than in the quiescent state and for $\gamma > 3$ % the MSD increases more than linearly with time t and might at larger γ tend to normal diffusion. For the smaller shear rate, the cage-deformation introduced by shear enables the initially caged particles to diffuse, resulting in the observed acceleration of the average single-particle dynamics and glass melting. The larger shear rate is sufficiently large to possibly induce cage constriction at short times resulting in the lower localisation length of the MSD. Moreover, the observed super-diffusive behavior could result from the transition from highly constrained in-cage motions to out-of cage shear induced diffusive motions. The observed behavior is similar to the one which occurs in one-component colloidal glasses and dense fluids under application of a constant shear rate, as shown in experiments [26, 27, 28, 29, 30], simulations [31, 27, 30] and Mode-Coupling theory [27, 30]. In particular, a link between shear-induced cage break up and acceleration of the dynamics has been found [29]. Upon application of shear, the cage increasingly deforms, until the maximum elastically sustainable deformation is achieved, where a stress overshoot is observed in rheology, and the cage opens, allowing for diffusion in the steady state of shear where residual structural anisotropy is observed. Before steady state is achieved, super-diffusion is observed at the transition from caging to diffusion, corresponding to cage yielding. When the shear rate becomes sufficiently large, cage constriction is continuously induced by shear and a super-diffusive regime is observed in the steady state [29], similar to what is observed in the mixture for the larger shear rate. Note that for $x_s = 0.9$ the cage being deformed is that composed of small spheres. The $Pe^s_{\dot\gamma} = \delta^3 Pe^l_{\dot\gamma}$ values for the small spheres are 5.4×10^{-4} and 3.4×10^{-3} for the slower and faster shear rates respectively. Cage constriction effects are typically observed for $Pe_{\dot\gamma} > 0.1$ in one-component glasses [29].

For glasses composed by only one species of particles the long-time diffusion coefficient D_L in the steady state of shear is dominated by the time scale introduced by the shear rate and scales as $\dot\gamma^{0.8}$ [26, 31]. The scaling clearly does not hold in this case, since the values on the x-axis scale with $\dot\gamma$. The ratio between the D_L values for the two applied shear rates apparently scales with a larger exponent of approximately 1.6, which could be related to the peculiar properties of the mixture.

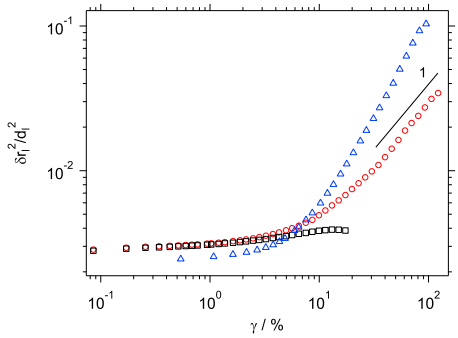

FIGURE 7. Mean squared displacements δr_l^2 of the large spheres as a function of strain $\gamma = \dot\gamma t$, in units of the squared large spheres diameter d_l^2, determined by confocal microscopy for sample with a relative volume fraction of small spheres $x_s = 0.9$, in the quiescent state (□) and in the steady state of shear at $Pe^l_{\dot\gamma} = 6.7 \times 10^{-2}$ (○) and 4.2×10^{-1} (△). The MSDs under shear only contain non-affine particle motions. The strain axis for the quiescent state was calculated using the lower shear rate $\dot\gamma \simeq 0.06$ s^{-1}.

CONCLUSIONS

We presented experimental results on the structure, dynamics and viscoelasticity of glasses formed by binary colloidal mixtures with size ratio $\delta = 0.2$ and different mixing ratios. Changes in the properties of these glasses as a function of mixing ratio can be rationalized in terms of a transition from caging of the large spheres to caging of the small spheres. In comparison to a glass composed of only large spheres, mixing a large fraction of large spheres with a small fraction of small spheres induces pronounced changes in the glass state. The cage of large spheres is deformed due to the inclusion of small spheres in the free volume between the large particles. This loosening of the cage results in increased mobility of the large particles and an acceleration of their dynamics. Correspondingly a strong decrease of the elastic modulus is observed. Further increasing the fraction of small spheres, the cage distortion increases as more and more small particles fill the free volume. This is consistent with random close packing occurring at a larger total volume fraction [23]. It also results in a further speeding up of the dynamics and reduction of the elastic modulus. At $x_s = 0.5$ on average each large sphere can be completely covered by small spheres and leads to a dis-

ruption of the cage structure of the large spheres. Concomitantly the response of the system starts to be dominated by caging of the small spheres. This is seen as a tighter localisation of the large spheres and a modulus which starts to increase again. This trend continues with increasing x_s. In systems dominated by the cage of the small particles, the large spheres reduce the order on the intermediate length scale beyond the first shell, i.e. the cage. If shear is imposed on a mixture where caging by the small component dominates the response, the initially frozen dynamics become diffusive in the experimental time-window at small shear rates, and super-diffusive at larger shear rates. A stronger localisation at short times is also observed at larger shear rates. This indicates that application of shear induces melting of the glass by facilitating out-of-cage diffusion through elongation and deformation of the cage, and cage constriction at large shear rates, similar to recent results on one-component glasses [29, 30].

ACKNOWLEDGMENTS

We acknowledge support from the Deutsche Forschungsgemeinschaft through the FOR1394 Research unit. We also thank G. Petekidis, Th. Voigtmann, K. J. Mutch, P. Chauduri, J. Horbach, M. Fuchs and W. C. K. Poon for stimulating discussions.

REFERENCES

1. E. Dhont, *The Glass Transition: Relaxation Dynamics in Liquids and Disordered Materials*, Springer-Verlag, Berlin, 2001.
2. P. N. Pusey, *Liquids, Freezing and Glass Transition*, North-Holland, Amsterdam, 1991.
3. P. N. Pusey, and W. van Megen, *Phys. Rev. Lett.* **59**, 2083–2086 (1987).
4. W. van Megen, T. C. Mortensen, S. R. Williams, and J. Müller, *Phys. Rev. E* **58**, 6073–6085 (1998).
5. R. G. Larson, *The Structure and Rheology of Complex Fluids*, Oxford University Press, 1999.
6. T. G. Mason, and D. A. Weitz, *Phys. Rev. Lett.* **75**, 2770–2773 (1995).
7. Th. Voigtmann, *Europhys. Lett.* **96**, 36006 (2011).
8. A. Imhof, and J. K. G. Dhont, *Phys. Rev. Lett.* **75**, 1662–1665 (1995).
9. A. J. Moreno, and J. Colmenero, *Phys. Rev. E* **74**, 021409 (2006).
10. A. J. Moreno, and J. Colmenero, *J. Chem. Phys.* **125**, 164507 (2006).
11. T. Sentjabrskaja, J. Hendricks, M. Laurati, and S. U. Egelhaaf, Yielding of binary colloidal glasses (2012), in preparation.
12. T. Sentjabrskaja, M. Laurati, S. U. Egelhaaf, E. Babaliari, G. Petekidis, and Th. Voigtmann (2012), in preparation.
13. A. Yethiraj, and A. Van Blaaderen, *Nature* **421**, 513–517 (2003).
14. W. Schaertl, and H. Silescu, *J. Stat. Phys.* **77**, 1007–1025 (1994).
15. M. C. Jenkins, and S. U. Egelhaaf, *Adv. Coll. Interface Sci.* **136**, 65–92 (2008).
16. J. C. Crocker, and D. G. Grier, *J. Colloid Interface Sci.* **179**, 298 – 310 (1996).
17. D. Derks, H. Wisman, A. van Blaaderen, and A. Imhof, *J. Phys.: Condens. Matter* **16**, S3917–S3927 (2004).
18. P. Ballesta, G. Petekidis, L. Isa, W. C. K. Poon, and R. Besseling, *Journal of Rheology* **56**, 1005–1037 (2012).
19. J. H. Conway, and N. J. A. Sloane, *Sphere packing, lattices and groups*, Spring-Verlag, New York, 1998.
20. F. Chambon, Z. S. Petrovic, W. J. MacKnight, and H. H. Winter, *Macromolecules* **19**, 2146 (1986).
21. H. H. Winter, and F. Chambon, *J. Rheol* **30**, 367 (1986).
22. M.Laurati, G. Petekidis, N. Koumakis, F. Cardinaux, A. B. Schofield, J. M. Brader, M. Fuchs, and S. U. Egelhaaf, *J. Chem. Phys.* **130**, 134907 (2009).
23. I. Biazzo, F. Caltagirone, G. Parisi, and F. Zamponi, *Phys. Rev. Lett.* **102**, 195701 (2009).
24. G. Brambilla, D. E. Masri, M. Pierno, L. Berthier, L. Cipelletti, G. Petekidis, and A. B. Schofield, *Phys. Rev. Lett.* **102**, 085703 (2009).
25. T. Savin, and P. S. Doyle, *Biophys. J.* **88**, 623–638 (2005).
26. R. Besseling, E. R. Weeks, A. B. Schofield, and W. C. K. Poon, *Phys. Rev. Lett.* **99**, 028301 (2007).
27. J. Zausch, J. Horbach, M. Laurati, S. U. Egelhaaf, J. M. Brader, T. Voigtmann, and M. Fuchs, *J. Phys.: Condens. Matter* **20**, 404210 (2008).
28. R. Besseling, L. Isa, E. R. Weeks, and W. C. Poon, *Adv. Coll. Int. Sci.* **146**, 1 – 17 (2009).
29. N. Koumakis, M. Laurati, S. U. Egelhaaf, J. F. Brady, and G. Petekidis, *Phys. Rev. Lett.* **108**, 098303 (2012).
30. M. Laurati, K. J. Mutch, N. Koumakis, J. Zausch, C. P. Amann, A. B. Schofield, G. Petekidis, J. F. Brady, J. Horbach, M. Fuchs, and S. U. Egelhaaf, *J. Phys. Condens. Matter* **24**, 464104 (2012).
31. F. Varnik, *J. Chem. Phys.* **125**, 164514 (2006).

3.2. Publication 2: Yielding of binary colloidal glasses

Journal: Soft Matter
Reference: *Soft Matter*, 2013, **9**, 4524
Impact factor: 4.151
Authors: **T. Sentjabrskaja**, E. Babaliari, J. Hendricks, M. Laurati, G. Petekidis and S. U. Egelhaaf
1st author
The materials are prepered and the experiments are performed by TS ($\delta = 0.20$) and EB, JH ($\delta = 0.38$ and $\delta = 0.19$). TS analyzed all data. TS, ML, GP and SUE conceived and discussed the project. ML and SUE supervised the project. All authors contributed to the writing of the manuscript.
55 % contribution of TS

This page has been left intentionally blank.

Soft Matter

RSC Publishing

PAPER

View Article Online
View Journal | View Issue

Yielding of binary colloidal glasses

Cite this: *Soft Matter*, 2013, **9**, 4524

T. Sentjabrskaja,[a] E. Babaliari,[b] J. Hendricks,[a] M. Laurati,*[a] G. Petekidis[b] and S. U. Egelhaaf[a]

The rheological response, in particular the non-linear response, to oscillatory shear is experimentally investigated in colloidal glasses. The glasses are highly concentrated binary hard-sphere mixtures with relatively large size disparities. For a size ratio of 0.2, a strong reduction of the normalized elastic moduli, the yield strain and stress and, for some samples, even melting of the glass to a fluid is observed upon addition of the second species. This is attributed to the more efficient packing, as indicated by the shift of random close packing to larger total volume fractions. This leads to an increase in free volume which favours cage deformations and hence a loosening of the cage. Cage deformations are also favoured by the structural heterogeneity introduced by the second species. For a limited parameter range, we furthermore found indications of two-step yielding, as has been reported previously for attractive glasses. In samples containing spheres with more comparable sizes, namely a size ratio of 0.38, the cage seems less distorted and structural heterogeneities on larger length scales seem to become important. The limited structural changes are reflected in only a small reduction of the moduli, yield strain and stress.

Received 19th December 2012
Accepted 1st March 2013

DOI: 10.1039/c3sm27903k

www.rsc.org/softmatter

1 Introduction

Many particle dispersions used in applications, for example paint, ink, cement, ceramics or foodstuffs, are characterised by a size distribution of the dispersed phase. Even if a monodisperse system is desirable, it is often difficult to avoid a distribution of particle sizes. Furthermore, through the size distribution, the properties of a dispersion, such as its rheological behaviour, can be tuned, for instance to meet processing or application needs. To investigate the effect of a distribution of sizes, binary mixtures of spherical colloidal particles represent the simplest model system.

The interactions and the phase behaviour of binary colloidal hard-sphere mixtures have been studied by theory[1–5] and simulations.[4–6] In equilibrium, binary colloidal mixtures exhibit a wider fluid–solid coexistence region than one-component systems, which has been thoroughly investigated in experiments.[7–10] Additionally, formation of complex crystalline structures through co-crystallisation of the two species is predicted and observed.[11–14] For size ratios $\delta = R_S/R_L \lesssim 0.2$, where R_S and R_L are the radii of the small and large spheres, respectively, theory expects fluid–fluid and solid–solid coexistences,[4] which are also observed in simulations[15] but not yet in experiments. In addition, non-equilibrium glass states have been predicted theoretically[16–19] and observed experimentally.[9,20] In particular, Mode Coupling Theory (MCT) predicts that, at constant total volume fraction ϕ, a one-component glass is melted upon addition of a sufficient amount of spheres with a different size ($\delta \leq 0.65$).[16,17] This is consistent with the faster structural relaxation experimentally observed in samples with $\delta \approx 0.6$, $\phi \approx 0.58$ and intermediate mixing ratios.[20] This leads to a strong decrease of the viscosity, which has been determined in experiments and simulations for a sufficiently large degree of mixing.[21,22] Recent MCT results[17] furthermore predict that for a large size disparity, $\delta \leq 0.2$, different glass states exist, which are distinguished by caging of one or both species, or by depletion induced bonding of the large spheres. The latter, for which some experimental evidence exists for $\delta \approx 0.1$,[9] is expected to show similarities with attractive glasses as those observed in colloid–polymer mixtures.[23,24]

Similar to the interactions and the phase behavior, also the rheological response of binary mixtures changes upon varying the size and mixing ratios. This has been studied experimentally,[21,25–31] theoretically[32–34] and by simulations.[35–37] In the granular limit, *i.e.* when Brownian motion becomes irrelevant, binary mixtures with a size ratio $\delta = 0.2$ exhibit a minimum of the viscosity at a relative volume fraction of small spheres, $x_S \approx 0.4$,[38] which is known as the *Farris* effect. In contrast, for colloidal mixtures a minimum of the viscosity is only observed at high total volume fractions $\phi \geq 0.4$ and at a mixing ratio which depends on ϕ and δ.[34] With decreasing δ, the minimum occurs at smaller fractions of small spheres, which results from a balance between the more efficient packing, since small spheres can fill the space between large spheres, and the depletion attraction induced between large spheres.[34]

[a]*Condensed Matter Physics Laboratory, Heinrich-Heine University, 40225 Düsseldorf, Germany. E-mail: marco.laurati@uni-duesseldorf.de*

[b]*FORTH/IESL and Department of Materials Science and Technology, University of Crete, 71110, Heraklion, Greece*

Nevertheless, the rheology of concentrated binary colloidal mixtures has hardly been studied,[21,39] especially of spheres with significantly different sizes, *i.e.* small size ratios δ.

Here we investigate the rheology of dispersions containing binary mixtures with small size ratios, $\delta \simeq 0.2$ and 0.38, over a broad range of total volume fractions ϕ and mixing ratios, characterized by the relative volume fraction of small spheres $x_S = \phi_S/\phi$. Their response to oscillatory shear is studied with a particular focus on the non-linear viscoelastic properties, while the linear response, together with the structure and dynamics at rest, will be discussed in detail elsewhere.[40,41] In the present case of spheres with significantly different sizes (*i.e.* small δ), the non-linear response contains contributions related to the different length scales present in the samples. This is similar to colloid–polymer mixtures, where systems with attractive interactions, such as gels or attractive glasses, are characterized by two yielding processes.[42–45] The two yielding processes reflect the breaking of inter-particle 'bonds' and cluster breaking, in the case of gels, or irreversible cage deformation, in the case of attractive glasses.[44,45] The yielding behaviour of attractive systems is hence different from the one of repulsive systems, which typically only show one yielding mechanism related to cage distortion.[42,43,46,47]

2 Materials and methods

2.1 Rheology

Rheological measurements were performed with an AR2000ex stress-controlled rheometer, and ARES G2 and ARES strain-controlled rheometers from TA instruments, using cone and plate geometries of diameter $D = 20$ mm, cone angle $\alpha = 2^\circ$ and gap $d = 0.054$ mm (AR2000ex), $D = 25$ mm, $\alpha = 2^\circ$ and $d = 0.048$ mm (ARES G2) and $D = 25$ mm and 50 mm, $\alpha = 2^\circ$ and $d = 0.048$ mm (ARES). Solvent traps were used in all rheometers to minimize solvent evaporation. The temperature was set to $T = 20$ °C and controlled within ± 0.1 °C *via* a standard Peltier plate (AR2000ex, ARES) or an advanced Peltier system (ARES G2). The effects of sample loading and aging were reduced by performing the following rejuvenation procedure before each test. Directly after loading, a dynamic strain sweep was performed to estimate the strain amplitude γ at which the system starts to flow, *i.e.* oscillatory shear was applied to the samples with frequency $\omega = 1$ rad s^{-1} and increasing γ until the sample showed a liquid-like response. Then, before each measurement, flow of the sample was induced by applying oscillatory shear at a sufficiently large strain. In the case of the size ratio $\delta = 0.20$, $\gamma = 300\%$ was used for all samples. For $\delta = 0.38$ and $\delta = 0.19$, different values $200\% \leq \gamma \leq 1000\%$ were used depending on the volume fraction ϕ and relative volume fraction of small particles x_s. Shear was applied until a steady-state response, *i.e.* a time-independent storage G' and loss modulus G'', was achieved, which typically took about 200 s. Subsequently the samples were sheared at $0.1\% \leq \gamma \leq 1.5\%$ (depending on the sample) until the linear viscoelastic moduli reached a time-independent value, typically after 100 s to 900 s (depending on the sample). This indicated that no further structural changes occurred and hence a reproducible state of the sample was reached and a new measurement could be started. Note that ageing effects might be present at longer waiting times. Measurements with serrated and smooth geometries, respectively, yielded comparable results suggesting the absence of wall slip.

2.2 Samples

Polymethylmethacrylate (PMMA) spheres sterically stabilized with a layer of polyhydroxystearic acid (PHSA) were dispersed in a mixture of cycloheptyl bromide (CHB) and *cis*-decalin that closely matched the density and refractive index of the colloids ($\delta = 0.20$ and 0.19) or in a mixture of octadecene and bromonaphthalene which minimizes solvent evaporation ($\delta = 0.38$). For samples in octadecene–bromonaphthalene, measurements of the time evolution of the linear viscoelastic moduli indicate the absence of significant gravitational effects over times much longer than typical measurement times. In the CHB–decalin mixture, the particles acquire a small charge which was screened by adding 4 mM tetrabutylammoniumchloride.[48] In this case, the colloids behave like hard-spheres in both solvent mixtures. PMMA spheres with different average radii were used; $R_L^F = 880$ nm (polydispersity 0.057) and $R_{S1} = 175$ nm (polydispersity 0.150) to result in $\delta = 0.20$; $R_L^{NF} = 942$ nm (polydispersity 0.06) and the same R_{S1} to result in $\delta = 0.19$; $R_L = 358$ nm (polydispersity 0.140) and $R_{S2} = 137$ nm (polydispersity 0.120) to result in $\delta = 0.38$. The radii and polydispersities were determined from the angular dependencies of the scattered intensity and the diffusion coefficients, obtained using static and dynamic light scattering, respectively, with very dilute colloidal suspensions ($\phi \simeq 10^{-4}$). For the large spheres, a similar radius, $R_L^F = 885$ nm, has been estimated from the position of the first peak of the radial distribution function, which was obtained by confocal microscopy.[49] Confocal microscopy could be performed with these large spheres, because they were fluorescently labelled with nitrobenzoxadiazole (NBD). Confocal microscopy was also used to determine the volume fraction of a dispersion of these spheres as follows. A random close packed sample was obtained by sedimenting a dilute suspension in a centrifuge. The sediment, whose volume fraction was roughly estimated using simulation results,[50] was subsequently diluted to a volume fraction $\phi \simeq 0.4$ and imaged by confocal microscopy. The imaged volume was partitioned into Voronöi cells and their mean volume was determined. The ratio of the particle volume to the mean Voronöi volume provides an estimate of the volume fraction of the sample, $\phi = 0.43$. This allowed us to calculate the volume fraction of the random close packed stock solution $\phi_{RCP}^L = 0.68$. The smaller spheres were too small to be imaged (thus also not fluorescently labelled). The volume fraction of their sediment was estimated taking into account their polydispersity:[50] $\phi_{RCP}^{S1} \simeq 0.68$ for spheres with radius $R_{S1} = 175$ nm and $\phi_{RCP}^{S2} \simeq \phi_{RCP}^L \simeq 0.67$ for spheres with radii $R_{S2} = 137$ nm and $R_L = 358$ nm. The value of the volume fraction is known to suffer from relatively large uncertainties.[51] Thus the value of ϕ obtained for the large spheres was used as a reference value and the volume fraction of the two batches containing the smaller particles was adjusted using rheological measurements as follows. Linear

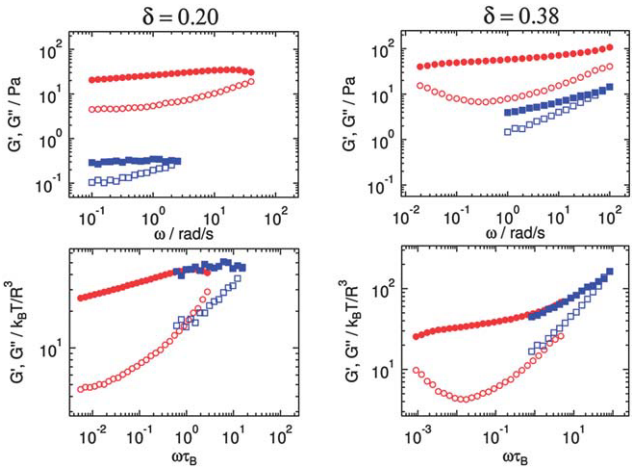

Fig. 1 (top) Storage, G' (full symbols), and loss, G'' (open symbols), moduli of samples containing large (□) and small (○) spheres, respectively, as a function of frequency ω obtained by Dynamic Frequency Sweep measurements for (left) a size ratio $\delta = 0.20$ and total volume fraction $\phi = 0.58$ and (right) $\delta = 0.38$ and $\phi = 0.595$. (bottom) Same data in units proportional to the energy density, *i.e.* k_BT/R^3, and Brownian time $\tau_B = D_0/R^2$. The strain amplitude was $\gamma = 0.5\%$ for $\delta = 0.20$ and $\gamma = 1.5\%$ for $\delta = 0.38$.

viscoelastic moduli for samples at nominally equal volume fraction ($\phi \simeq 0.58$ for $\delta = 0.20$, $\phi \simeq 0.595$ for $\delta = 0.38$, $\phi \simeq 0.61$ for $\delta = 0.19$) were measured in Dynamic Frequency Sweeps (DFS) at a strain amplitude $0.1\% \leq \gamma \leq 1.5\%$ (depending on sample). The obtained storage moduli G' and loss moduli G'' as a function of oscillation frequency ω are expected to agree for spheres of different sizes but with the same volume fraction, if the moduli are rescaled by the energy density $\sim k_BT/R^3$ and the frequency by the Brownian time $\tau_B = R^2/D_0$ with $D_0 = 6\pi\eta R$ the Stokes–Einstein–Sutherland diffusion coefficient in the dilute limit[52] and η the solvent viscosity. The dispersion of small spheres was diluted until its rescaled linear response matched that of the dispersion of large spheres with the desired volume fraction, *i.e.* until an equivalent rheological response in the linear regime was obtained (Fig. 1). Furthermore, it was verified that the normalised elastic modulus G' and its ϕ dependence coincides, for all particles used, with that of a dispersion containing crystallising colloids with a low polydispersity, whose volume fraction was determined in the crystal–fluid coexistence region.[52] When illuminated by laser light, Bragg reflections were not observed, indicating the absence of crystallinity in the one-component dispersions. By mixing appropriate amounts of the one-component dispersions, samples with different total volume fractions ϕ and relative volume fractions of small particles $x_s = \phi_S/(\phi_S + \phi_L)$ were prepared, where ϕ_S and ϕ_L are the volume fractions of small and large particles, respectively. Samples with different x_S and two different values of ϕ (for $\delta = 0.20$ and 0.38) as well as fixed $x_S = 0.65$ and different values of ϕ (for $\delta = 0.19$) were investigated.

3 Results and discussion

In Dynamic Strain Sweep (DSS) experiments, a sinusoidal strain is applied whose frequency ω is constant but whose amplitude γ is increased in steps, starting in the linear viscoelastic regime and progressing into the non-linear regime. The stress response of the system is recorded as a function of strain amplitude γ. Fig. 2 shows the results of DSS measurements for samples with size ratio $\delta = 0.20$, total volume fractions $\phi = 0.61$ and 0.58, and different relative volume fractions of small spheres x_S. Beyond the linear viscoelastic regime the stress response in DSS experiments significantly deviates from a simple sinusoidal form and can be decomposed into higher order (odd) harmonics, as shown before for one-component hard-sphere glasses.[52] However, the G' and G'' values shown in Fig. 2 correspond to the first harmonic contribution of the stress response. To allow for a comparison of the different samples, measurements were not performed at a constant frequency ω, but at a fixed oscillatory Peclet number $\mathrm{Pe}_\omega = \omega\tau_B$. It is the ratio of the Brownian time of the system, $\tau_B = \langle R^2/D_0 \rangle$, and the timescale imposed by shear, *i.e.* the inverse of the frequency, $\tau_\omega = 1/\omega$. Thus, $\mathrm{Pe}_\omega = \langle (6\pi\eta R^3)/(k_BT) \rangle\ \omega$ and

$$\langle R^3 \rangle = {R_L}^3 \left[x_S \left(\frac{1}{\delta^3} - 1 \right) + 1 \right]^{-1}. \quad (1)$$

We applied $\mathrm{Pe}_\omega = 5.55 \times 10^{-1}$ corresponding to 7.6×10^{-2} rad $s^{-1} \leq \omega \leq 9.7$ rad s^{-1}, depending on x_S.

The one component systems ($x_S = 0$ and 1) for both ϕ show the characteristic response of a hard sphere glass (Fig. 2a and b).[42,43,47,52] (Note that due to the much lower energy density of the samples with the large spheres, their response is much weaker and thus more affected by noise.) The storage modulus G' is larger than the loss modulus G'' in the linear viscoelastic regime, with their values comparable to the ones obtained in dynamic frequency sweeps (Fig. 1).[40] The two moduli become equal at a strain amplitude γ_y (highlighted with circles in Fig. 2), which is identified with the yield strain of the glass. At the yield strain γ_y and the corresponding yield stress σ_y, the local environment of a particle is irreversibly rearranged, *i.e.* its cage broken.[42,43,46,47] For $\gamma > \gamma_y$, G'' is larger than G' and the system starts to flow. In this regime, G'' shows a maximum which indicates the largest energy dissipation and has also been previously used to estimate the yield strain associated with irreversible rearrangements of the cage.[43,46] Upon increasing the volume fraction from $\phi = 0.58$ to 0.61, the linear viscoelastic moduli and the yield strain γ_y increase. This is consistent with previous studies,[46,47,52] which found γ_y to increase with volume fraction up to $\phi \approx 0.62$, beyond which it decreases due to the approach toward random close packing.

Keeping the total volume fraction ϕ constant, but changing the composition to $x_S = 0.9$, the storage and loss moduli decrease (Fig. 2). The decrease is not only due to the presence of large particles and hence a lower energy density, but remains even if the moduli are rescaled by the energy density $\langle nk_BT \rangle \sim 1/\langle R^3 \rangle$. This indicates a softening of the glass. A softer response is also reflected in a reduced yield strain γ_y and yield stress σ_y (circles in Fig. 2). A further decrease of the relative volume fraction of small spheres to $x_S = 0.7$ leads to an additional reduction of the storage, G', and loss, G'', modulus, yield strain γ_y and stress σ_y, which indicates that the glass still becomes mechanically

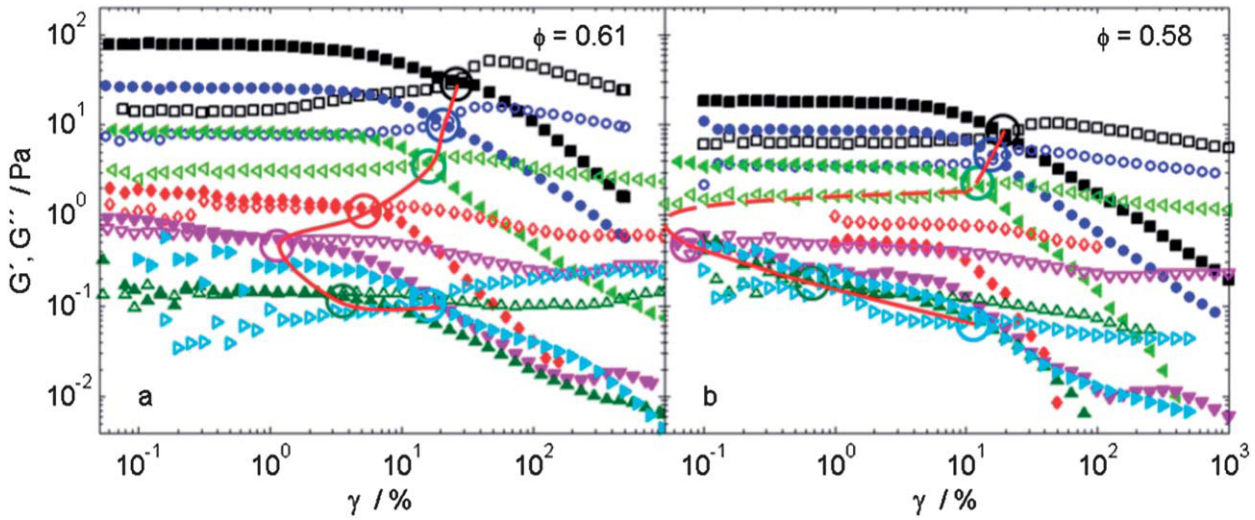

Fig. 2 Storage, G', (full symbols) and loss, G'', (open symbols) moduli as a function of the strain amplitude γ obtained in DSS measurements. The size ratio $\delta = 0.20$, the total volume fraction (a) $\phi = 0.61$ and (b) $\phi = 0.58$, the relative volume fraction of small particles $x_S = 0.0$ (▷), 0.1 (△), 0.3 (▽), 0.5 (◇), 0.7 (◁), 0.9 (○), 1.0 (□) and $Pe_\omega = 5.55 \times 10^{-1}$ (corresponding to 7.6×10^{-2} rad s$^{-1} \leq \omega \leq 9.7$ rad s^{-1}). Circles indicate the yield points and the red solid line indicates their x_S-dependence (the dashed line in (b) is used for fluid samples, which do not present a yield point).

weaker. For $x_S \geq 0.7$, comparable effects are found for $\phi = 0.61$ and 0.58.

This is different for $x_S < 0.7$. For the higher total volume fraction $\phi = 0.61$, the samples with $x_S = 0.5$ and 0.3 have a much smaller G' which, however, is still slightly larger than G'' and the samples hence show a weak solid-like response in the linear viscoelastic regime (Fig. 2a). This is consistent with γ_y and σ_y values which are more than one and almost three orders of magnitude smaller, respectively, than typical values of one-component hard-sphere glasses at the same total volume fraction. Hence the samples become very brittle and may flow plastically at smaller strain amplitudes or stresses. A closer inspection of the response of the sample with $\phi = 0.61$ and $x_S = 0.3$ reveals a particularly interesting strain amplitude dependence of the moduli (Fig. 3). The linear response ends already at $\gamma \approx 0.2\%$ (Fig. 3, arrow on the left), beyond which G' decreases smoothly up to $\gamma \approx 4\%$, where it shows a kink and subsequently decreases with a power-law, while G'' shows a small maximum (Fig. 3, arrow on the right). This response suggests the presence of two length scales, most likely associated with the small and large spheres, which both contribute to the yielding of the system at this x_S. The first yielding at small strains $\gamma \approx 0.2\%$ might correspond to plastic rearrangements of cages formed by small spheres. Cage distortion and yielding might be facilitated by the shear-induced interaction with the large spheres, *i.e.* contact forces between large and small spheres. Once these cages are rearranged, the system is still prevented from flowing by the cages of large spheres which are only slightly deformed. At strains of about 4% the cages of large spheres deform and the system starts to flow. The ratio between the two yield strains, $0.2/4 \simeq 0.04$, corresponds to $\delta/4$ which suggests a non-trivial scaling of the yield strains with the cage size (which would give a factor δ). This finding could also result from the moderate polydispersity of the small spheres, which implies a distribution of the effective size ratio and in particular accelerates the dynamics,[53] and could contribute to reduce the magnitude of the maxima of G'', which are characteristic of the double yielding phenomenon. A two-step yielding behavior has also been observed for attractive glasses and gels.[42–45] Compared to $\phi = 0.61$, at $\phi = 0.58$ decreasing the relative volume fraction of small spheres to $x_S = 0.5$ has an even stronger effect (Fig. 2b). Within the whole examined range of strain amplitudes, $G'' > G'$ which implies fluid-like behavior. Thus, the glass is melted. Fluid-like behavior in the whole range of the measured γ is also observed for $x_S = 0.3$, with the response being similar to that obtained for $\phi = 0.61$, except for the smallest γ (Fig. 3). Samples

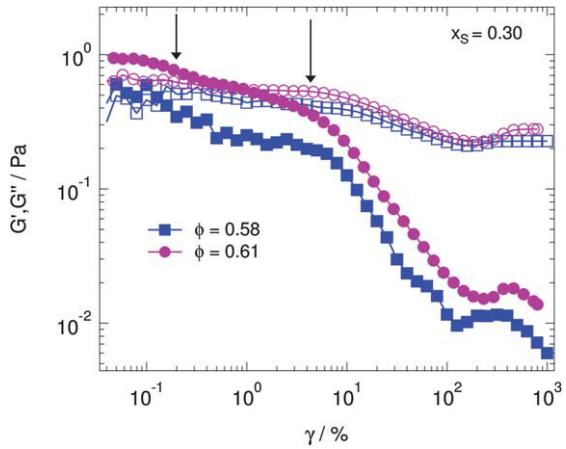

Fig. 3 Storage, G', (full symbols) and loss, G'', (open symbols) moduli as a function of the strain amplitude γ obtained in DSS measurements for size ratio $\delta = 0.20$, a relative volume fraction of small spheres $x_S = 0.3$ and the total volume fraction $\phi = 0.61$ (○) and $\phi = 0.58$ (□). Arrows indicate the two yielding points observed for the sample with $\phi = 0.61$.

showing fluid-like behavior ($x_S = 0.3$ and 0.5) do not present a finite value of yield strain and stress, corresponding to the missing circles in Fig. 2b. The melting of the glass is caused by the larger free volume fraction created by the presence of small spheres, as will be discussed in more detail later. This is similar to the behaviour of one-component systems when ϕ is decreased below the glass transition.

Finally, the samples at both total volume fractions show the response of a weak solid for $x_S = 0.1$. For $\phi = 0.61$ the storage modulus G' is further reduced and becomes similar to G'', indicating the proximity of a transition to the fluid state. On the other hand the yield strain γ_y and stress σ_y are slightly increased (Fig. 2). In contrast, for $\phi = 0.58$ the response again changes qualitatively, which implies a reentrant behavior; the melting and re-formation of a solid glass state as the fraction of small spheres is reduced.

A second size ratio, $\delta = 0.38$, was investigated also at two total volume fractions $\phi = 0.595$ and 0.615 and different relative volume fractions of small particles x_S (Fig. 4). Starting from the one-component systems and increasing the amount of the second component, the storage modulus G' decreases in the linear viscoelastic regime indicating a softening of the glass, similar to the findings with $\delta = 0.20$ (Fig. 2). However, in the case of $\delta = 0.38$, the minimum of G' is located at $x_S \approx 0.5$ for both ϕ. Note that in terms of the relative number of small spheres $\xi_S = n_L/(n_S + n_L) = x_S[\delta^3 + x_S(1 - \delta^3)]^{-1}$, where n_S and n_L are the number densities of small and large spheres, respectively, the minimum of G' is found for both size ratios at values of $\xi_S > 0.85$. Furthermore, the minimum in the x_S-dependence is much weaker for the yield stress σ_y and absent for the yield strain γ_y (Fig. 4). Thus, no melting of the glass is observed for $\delta = 0.38$.

Having studied the rheological response as a function of the relative volume fraction of small spheres x_S, we now turn to the dependence on the total volume fraction ϕ for constant $x_S = 0.65$ ($\delta = 0.19$) and 0.5 ($\delta = 0.38$) (Fig. 5). With decreasing ϕ, the storage modulus G' decreases in the linear regime and approaches the loss modulus G'' (Fig. 5a,b and e). Thus, with decreasing ϕ, the solid-like response becomes weaker. This is particularly pronounced for $\delta = 0.19$, which shows a fluid-like response for $\phi = 0.55$, that is $G'' > G'$ in the linear viscoelastic regime (Fig. 5a and e). The yield point, *i.e.* the yield strain γ_y and stress σ_y, decreases with decreasing ϕ for both values of δ and, for $\delta = 0.19$ it disappears at $\phi = 0.55$, *i.e.* the sample becomes a fluid (Fig. 5c and d). This is consistent with the response of

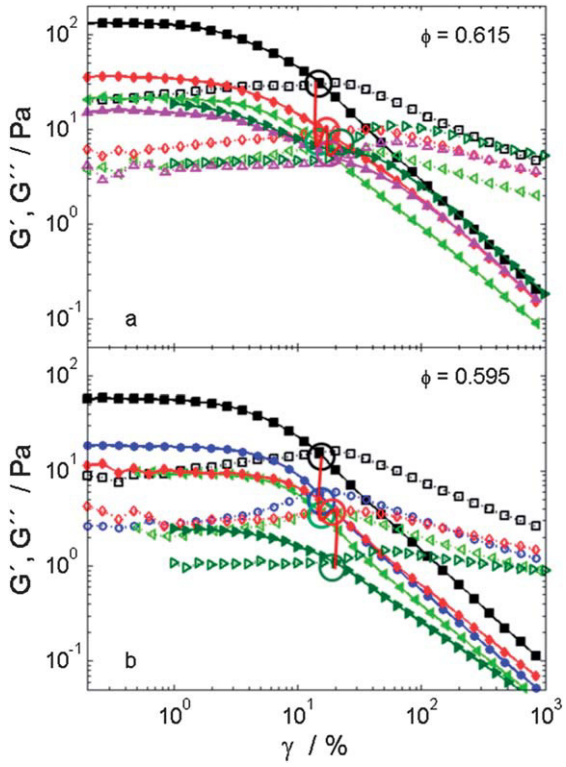

Fig. 4 Storage, G', (full symbols) and loss, G'', (open symbols) moduli as a function of strain amplitude γ obtained in DSS measurements. The size ratio $\delta = 0.38$, (a) the total volume fraction $\phi = 0.615$ and the relative volume fraction of small particles $x_S = 0.0$ (▷), 0.08 (△), 0.25 (◇), 0.5 (◁), 1.0 (□) and (b) $\phi = 0.595$ and $x_S = 0.0$ (▷), 0.25 (◇), 0.5 (◁), 0.75 (○) and 1.0 (□). The frequency $\omega = 1$ rad s^{-1}. Circles indicate the yield points and the red solid line indicates their x_S-dependence.

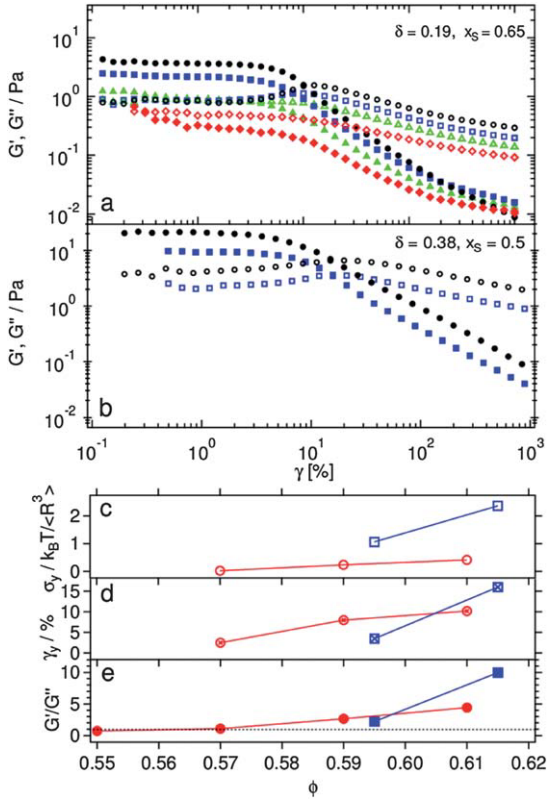

Fig. 5 (a,b) Storage, G', (full symbols) and loss, G'', (open symbols) moduli as a function of strain amplitude γ obtained in DSS measurements for (a) the size ratio $\delta = 0.19$, the relative volume fraction of small particles $x_S = 0.65$, total volume fractions $\phi = 0.61$ (○), 0.59 (□), 0.57 (△) and 0.55 (◇). (b) $\delta = 0.38$, $x_S = 0.5$, $\phi = 0.615$ (○) and 0.595 (□). Frequency $\omega = 1$ rad s^{-1}, corresponding to $Pe_\omega = 8.99 \times 10^{-2}$ for $\delta = 0.19$ and $Pe_\omega = 8.85 \times 10^{-2}$ for $\delta = 0.38$. (c) Yield stress σ_y, (d) yield strain γ_y and (e) ratio G'/G'' in the linear viscoelastic regime ($\gamma = 0.5\%$ and 1% for $\delta = 0.2$ and 0.38, respectively), as a function of total volume fraction ϕ for samples of plots (a) (○) and (b) (□).

one-component systems, whose yield strain γ_y also decreases with decreasing ϕ until a transition to a fluid occurs.[46,47,52]

The decrease in γ_y is attributed to the fact that, upon decreasing ϕ, the cages become larger and looser and thus increasingly smaller distortions of the cages are sufficient to allow the particles to escape through Brownian motion. Finally, in the fluid phase ($\phi = 0.55$), particles can leave the cage even in the absence of shear. The sample with $\delta = 0.19$, $x_S = 0.65$ and $\phi = 0.57$ shows a dependence of G' and G'' on the strain amplitude γ similar to that of the sample with $\delta = 0.20$, $x_S = 0.3$ and $\phi = 0.61$ (Fig. 3), which again suggests the presence of two yielding points. Note that this sample is a dense, slowly relaxing fluid and not a glass, according to the frequency dependence of the linear viscoelastic moduli (data not shown). Nevertheless, the similarity of the response of the two samples suggests that a glass state similar to that of $\delta = 0.20$, $x_S = 0.3$ and $\phi = 0.61$, *i.e.* characterized by a double yielding process and caging on two length scales, might be obtained at ϕ slightly larger than 0.57 for $x_S = 0.65$. This is in agreement with MCT predictions, where a transition from a glass characterized by caging on one length scale (that of the small spheres) at high ϕ, to a glass characterized by caging on two length scales at lower ϕ, and successive melting of this glass with further decreasing ϕ, is expected at comparable, constant x_S.[17,19]

The results of the DSS measurements show a slight dependence on frequency (Fig. 6). In the linear viscoelastic regime, the storage modulus G' increases with increasing frequency ω, in agreement with the results of our Dynamic Frequency Sweep (DFS) measurements (Fig. 1) and as discussed in more detail elsewhere.[40] With increasing frequency ω, the probed times decrease and are progressively shorter than the structural relaxation time. This leads to an increasingly more elastic response. Also the yield strain γ_y and stress σ_y increase with increasing Pe_ω (Fig. 7b and c). This is similar to the behavior of one-component colloidal glasses[42,43,46,47] and can be understood as follows. Shear-induced cage deformation facilitates the escape of particles from their cage through Brownian motion, which results in yielding.[54] In oscillatory shear, the maximum cage deformation is achieved at the largest excursion. In the vicinity of this point a particle is most likely to escape from the cage by Brownian motion. With increasing frequency, the particles spend less time at the maximum (but more frequently) and are therefore less likely to escape because the escape probability depends rather on the balance between the residence time at the maximum and the Brownian time than on the attempt rate.[44,55,56] The reduced escape probability must be compensated by a larger cage deformation. Thus, with increasing frequency ω, a larger strain and stress will be required, and hence stored, before the cage breaks.

Our findings are summarized in Fig. 7. For a given total volume fraction ϕ, adding a second component to the one-component systems results in a weaker elastic response. For $\delta = 0.20$, the glass softens particularly strongly and, if the sample is sufficiently close to the glass transition (here $\phi = 0.58$), even melts and shows a fluid-like response. This reduction in G' is not symmetric with respect to the one-component systems, but

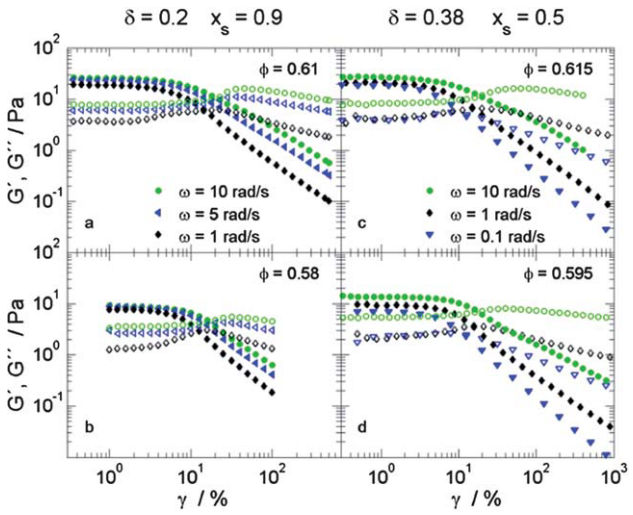

Fig. 6 Storage, G', (full symbols) and loss, G'', (open symbols) moduli as a function of strain amplitude γ obtained in DSS measurements. (left) The size ratio $\delta = 0.20$, total volume fraction (top) $\phi = 0.61$ and (bottom) 0.58, relative volume fraction of small spheres $x_S = 0.9$, and frequencies $\omega = 1$ rad s^{-1} (◇), 5 rad s^{-1} (◁) and 10 rad s^{-1} (○). (right) $\delta = 0.38$, (top) $\phi = 0.615$ and (bottom) 0.595, $x_S = 0.5$, $\omega = 0.1$ rad s^{-1} (▽), 1 rad s^{-1} (◇) and 10 rad s^{-1} (○).

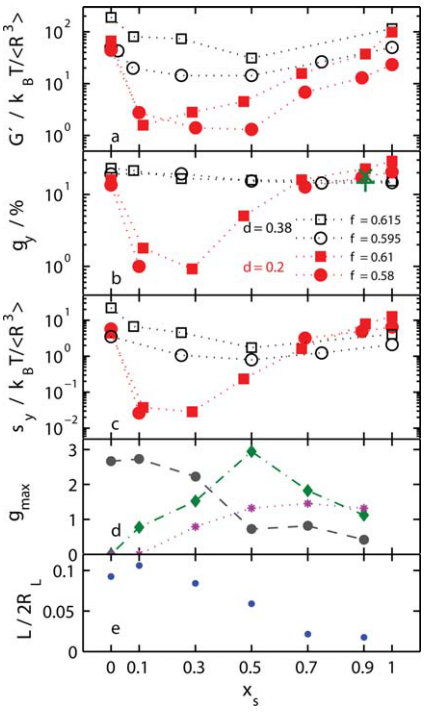

Fig. 7 (a) Storage modulus G' in the linear viscoelastic regime ($\gamma = 0.2\%$), (b) yield strain γ_y estimated from the crossing point of G' and G'' and (c) corresponding yield stress σ_y as a function of the relative volume fraction of small particles x_S for samples with size ratio $\delta = 0.20$ and total volume fraction $\phi = 0.61$ (■) and $\phi = 0.58$ (●) and $Pe_\omega = 5.55\ 10^{-1}$, and $\delta = 0.38$, $\phi = 0.615$ (□) and $\phi = 0.595$ (○) and $\omega = 1$ rad s.$^{-1}$ (b) also contains results for $Pe_\omega = 2.75\ 10^{-1}$ (×) and $Pe_\omega = 5.55\ 10^{-2}$ (+) for the sample with $x_S = 0.9$ and $\phi = 0.61$. (d) Height of the maxima of the pair distribution function $g(r)$, g_{max}, corresponding to $r = 2R_L$ (●), $r = 2(R_L + R_S)$ (◆) and $r = 2(R_L + 2R_S)$ (✳) and (e) localisation length L extracted from the plateaus of mean squared displacements as a function of x_S, for samples with $\delta = 0.2$ and $\phi = 0.61$.[40,41] Error bars are smaller than the symbols in all plots.

is more pronounced for glasses mainly consisting of large spheres to which a small fraction of small spheres has been added. This is evident when comparing, for example, G' for samples with $x_S = 0.1$ and 0.9. This asymmetry might, however, be due to the choice of the control parameter, here the relative volume fraction of small particles x_S. Instead, one could use the relative number of small spheres, ξ_S. Hence $x_S = 0.1$ corresponds to $\xi_S = 0.93$ while $x_S = 0.9$ implies a relative number of large spheres of only $\xi_L = 8.9 \times 10^{-4}$. This might explain why for $x_S = 0.9$ the cage of small spheres is not significantly affected by the small number of large spheres. In contrast, for $x_S = 0.1$ a large number of small spheres has to be accommodated by the large spheres, which is likely to induce a significant cage deformation and to result in a significant softening.

This is supported by confocal microscopy measurements of the structure and dynamics of the large spheres,[40,41] which are summarized in Fig. 7d and e. Already at $x_S = 0.1$, the pair distribution function $g(r)$ does not only show a peak at $r = 2R_L$, but also a shoulder at $r = 2(R_L + R_S)$ indicating that the cage of large spheres is deformed and that a significant fraction of large particles is separated by small particles. This cage deformation leads to a slight increase in the particle localisation length extracted from the plateau of mean-squared displacements, but the dynamics of the system is still arrested.[40,41] The reduced localisation is thought to be responsible for the strong decrease in yield strain. Rearrangement of the cage of large spheres becomes even more pronounced as x_S is increased to 0.3 and 0.5, as demonstrated by the increasingly larger reduction of the peak at $r = 2R_L$ and the corresponding increase at $r = 2(R_L + R_S)$ as well as the appearance of additional peaks at distances $r = 2(R_L + nR_S)$, with n an integer number. For these x_S, the dynamics show diffusion at $\phi = 0.58$ and sub-diffusion at $\phi = 0.61$ with a decreasing localization length suggesting that large particles start to be localized more tightly by small spheres.[40,41] During this process of cage rearrangement, for $\phi = 0.58$ the elasticity decreases and the yield strain γ_y disappears due to the melting of the glass, while at $\phi = 0.61$ both G' and γ_y start to increase again significantly above $x_S = 0.3$ possibly due to the emergent caging and localisation of large spheres by small spheres. For $x_S > 0.5$ the localisation in cages of small spheres, *i.e.* the transition to a different glass state, is accomplished: large particles represent a dilute phase in a dense matrix of small spheres and are localised on distances which are about a factor $\delta = 0.2$ smaller than at $x_S = 0$ and their dynamics are again arrested.[40,41] The tighter localisation and dynamical arrest induce an increased G' and γ_y toward the values of the one-component glass of small spheres. A pronounced effect of size and mixing ratios on the structure and dynamics of the glass was also reported for 2D colloidal glass formers.[57–61] In particular, changes in the relative content of the small component and the size ratio have been reported to have pronounced effects on the dynamics.[58,59]

For $\delta = 0.38$, the softening is less pronounced and no melting is observed. Moreover, the dependence of G' on x_S is more symmetrical with respect to the one-component systems. The smaller effect is attributed to the fact that the small particles have a reduced ability to occupy the interstitial space between the large particles at this size ratio. The critical value δ_c at which the small spheres cannot fill the space in between two large ones in a dense packing of large spheres can be estimated: in a group of 9 spheres arranged as in a body-centred cubic lattice and in contact with each other, the centers of two spheres along a face diagonal are separated by $2\sqrt{2}R_L$ and a small sphere can fill the space left in between the large spheres if $R_S \leq (\sqrt{2} - 1)R_L \approx 0.41R_L$, *i.e.* $\delta \leq \delta_c \approx 0.41$, which is comparable to $\delta = 0.38$. Although in the glass states considered here, ordered configurations are not expected, the size of the void space might be similar. Thus the cage itself, *i.e.* the first neighbour shell, is not expected to be rearranged significantly and the softening hence appears to be caused by the heterogeneity of the cage on an intermediate length scale rather than a more efficient packing. The weaker cage deformation induced by the smaller packing ability at $\delta = 0.38$ can also explain the weaker reduction of the yield strain and stress observed at intermediate mixing ratios for this δ.

Instead of the relative volume, x_S, or number, ξ_S, fraction of small particles, we now consider the distance to the two limiting volume fractions of the glass state, corresponding to the glass transition and random close packing. Mode Coupling Theory (MCT) predicts[17] that in mixtures the glass transition is shifted to higher total volume fractions. For example, for the size ratio $\delta = 0.38$ the maximum volume fraction for the glass transition is expected at $x_S \approx 0.4$, which is consistent with the occurrence of maximum softening in our experiments. The shift of the glass transition could be related to the addition of small particles with their larger mobility. This might favour structural rearrangements of the large spheres through collective motions and lead to a glass with a reduced elasticity, *i.e.* G'. In mixtures, MCT predicts qualitative changes of the relative particle mobilities, associated with different glass states.

In addition, the more efficient packing in mixtures results in an increased total volume fraction at random close packing, ϕ_{RCP}. Theoretical predictions for ϕ_{RCP} are available for binary mixtures of monodisperse hard spheres, with different size ratios δ and mixing ratios, *i.e.* x_S.[62,63] Based on the predictions for ϕ_{RCP}, we calculate the available free volume $\phi_{free} = \phi_{RCP} - \phi$ as a function of x_S and δ. (Predictions for $\delta = 0.17$ and 0.39 are used for the experimental $\delta = 0.20$ and 0.38, respectively.) Note that the predicted values of ϕ_{RCP} were shifted by the difference between the value of ϕ_{RCP} in the monodisperse case ($\phi_{RCP} = 0.64$) and the experimental values of ϕ_{RCP} ($\phi_{RCP} = 0.68$ for $\delta = 0.2$ and $\phi_{RCP} = 0.67$ for $\delta = 0.38$, Section 2.2). With decreasing free volume ϕ_{free}, that is toward random close packing, the storage modulus G' is found to increase (Fig. 8). The dependence of G' on ϕ_{free} indicates a common behavior for all δ and ϕ investigated and can be approximately described by a power-law dependence $G'\langle R^3\rangle/k_BT \sim (\phi_{free})^{-p}$, with $p \approx 3$. A similar power-law dependence is observed for one-component hard-sphere systems up to $\phi_{free} \leq 0.1$ (Fig. 8, dashed line).[46,47,52,64] At larger values of ϕ_{free} the one-component system shows a sharper decay.

We now consider the dependence of the yield point on the free volume ϕ_{free}. The x_S-dependence of the yield strain γ_y and stress σ_y is quite different for the two size ratios (Fig. 7b and c).

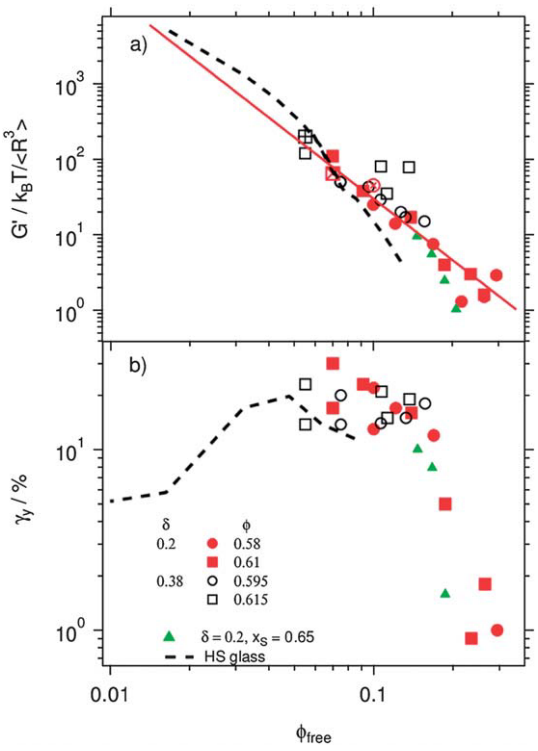

Fig. 8 (a) Storage modulus G' in the linear viscoelastic regime and (b) yield strain γ_y as a function of the free volume ϕ_{free} for the same samples as presented in Fig. 7, and for samples of Fig. 5 (▲). The red line in (a) shows a power-law fit $G'\langle R^3\rangle/k_BT \sim \phi_{free}^{-p}$, with $p = 2.7$. The dashed lines represent data of one-component hard-sphere glasses.[52]

In particular, both, γ_y and σ_y, show a much weaker dependence on x_S for $\delta = 0.38$ than $\delta = 0.2$. This can also be linked to the free volume available for structural rearrangements. The dependence of γ_y on ϕ_{free} (Fig. 8b) indicates that toward small free volumes, the yield strain saturates at an approximately constant value $\gamma_y \approx 20\%$, which agrees with the yield strain observed in one-component glasses.[42,43,52,64] At smaller values of ϕ_{free}, *i.e.* very close to RCP, which are not reached here, in the one-component systems the yield strain decreases (Fig. 8). In contrast, toward large $\phi_{free} > 0.1$ a strong decrease of γ_y is observed (for samples with $\delta = 0.20$ since only they reach large enough ϕ_{free} due to their large ϕ_{RCP}). This decrease indicates that if a sufficiently large free volume, *i.e.* a sufficiently loose packing, is present, significant structural rearrangements can be induced by small strains. The strong decrease of the yield strain is observed for samples in which the small spheres occupy the free space between the large spheres. The intercalation of small spheres in between large spheres possibly induces a strong deformation of the cage. Similar effects have been observed in mixtures of star polymers with significant size disparity.[65] This supports our previous finding that yielding is not only facilitated by the increase of free volume but also by structural heterogeneities leading to cage deformation. Interestingly, the strong decrease in the yield strain γ_y for $\phi_{free} > 0.1$ is not observed in one-component systems,[46,47,52] since in this regime the glass is melted. This is also consistent with G' sharply decreasing for $\phi_{free} \geq 0.1$ for the one-component system (Fig. 8a, dashed line). We speculate that in the glass state $G'\langle R^3\rangle/k_BT \sim (\phi_{free})^{-p}$ with $p \approx 3$ for one and two-component systems. The slight shift between our system (red line) and the previous one-component data (dashed line) might be due to different interactions mediated by different solvents.[51] These findings show that at large values of ϕ_{free}, a glass can still be formed in the mixture (possibly due to attractions) while a dense fluid is observed in one-component systems.

4 Conclusions

The linear and non-linear response to oscillatory shear has been studied in concentrated binary hard-sphere mixtures with large size disparities, $\delta \approx 0.20$ and 0.38. In the linear regime, the response of mixtures is softer than that of the corresponding one-component systems at the same total volume fraction ϕ, as demonstrated by the smaller normalised storage modulus G'. The softening is associated with a shift of random close packing to larger total volume fractions, and thus a larger free volume fraction ϕ_{free}, which results from the more efficient packing in two-component systems.[62] Pronounced softening occurs for the size ratio $\delta = 0.20$ and for samples containing a majority of large spheres ($x_S \lesssim 0.5$). This indicates that softening is not only a result of an increased free volume ϕ_{free} but also of cage distortions due to small particles filling the space between the large spheres. In contrast, in the samples with a smaller size disparity ($\delta = 0.38$) and a majority of small spheres ($x_S \gtrsim 0.5$), we can speculate that on average the cage structure should be poorly affected due to the reduced ability of the small component to fill space in between the large spheres, and heterogeneities are thus only introduced beyond the first neighbour shell, which results in a weaker softening of the glass.

In the non-linear regime, the more efficient packing in the mixtures affects the yielding behaviour. When the free volume ϕ_{free} is only slightly increased, yielding is characterised by a one-step cage break-up, as in one-component systems. With increasing free volume, yielding occurs at smaller deformations. Interestingly, at large values of the free volume, the presence of a small but finite yield strain indicates the persistence of a weak solid-like state in the mixtures, while at comparable free volume a one-component system melts. This occurs in systems where the small spheres can occupy the space in between the large spheres, which suggests that the intercalation of small spheres induces a strong deformation and loosening of the cage structure and thus contributes to the reduction of the yield strain. Moreover, the yielding behaviour could be affected by a possible transition between different glass states, in particular if it is associated with the mobility of the small spheres, which could facilitate yielding through collective motions. In addition to the one-step yielding behaviour, we also found indications of a more complex two-step yielding behavior for a sample with $x_S = 0.3$, $\phi = 0.61$. The two steps could be linked to the two different length scales present in these samples, representing caging of small and large spheres, respectively. While two length scales are present in all mixtures, in most samples one of the two dominates, rendering the second yielding insignificant.

Acknowledgements

We acknowledge support from the Deutsche Forschungsgemeinschaft through the Research unit FOR1394 (Project P2) and EU funding through the FP7-Infrastructures 'ESMI' (CP&CSA-2010-262348). We also thank A. B. Schofield for the synthesis of the PMMA particles and N. Koumakis for his help at the initial stages of experiments at FORTH. We thank in addition Th. Voigtmann, K. J. Mutch, P. Chauduri, J. Horbach, M. Fuchs, R. Castañeda Priego and W. C. K. Poon for stimulating discussions.

References

1 S. Amokrane, A. Ayasdim and J. Malherbe, *J. Chem. Phys.*, 2005, **123**, 174508.
2 R. Roth, R. Evans and S. Dietrich, *Phys. Rev. E: Stat. Phys., Plasmas, Fluids, Relat. Interdiscip. Top.*, 2000, **62**, 5360.
3 D. J. Ashton, N. B. Wilding, R. Roth and R. Evans, *Phys. Rev. E: Stat., Nonlinear, Soft Matter Phys.*, 2011, **84**, 061136.
4 M. Dijkstra, R. van Roij and R. Evans, *Phys. Rev. E: Stat. Phys., Plasmas, Fluids, Relat. Interdiscip. Top.*, 1999, **59**, 5744.
5 B. Götzelmann, R. Roth, S. Dietrich, M. Dijkstra and R. Evans, *Europhys. Lett.*, 1999, **47**, 398.
6 J. G. Malherbe and W. Krauth, *Mol. Phys.*, 2007, **105**, 2393.
7 J. S. van Duijneveldt, A. W. Heinen and H. N. W. Lekkerkerker, *Europhys. Lett.*, 1993, **21**, 369.
8 A. D. Dinsmore, A. G. Yodh and D. J. Pine, *Phys. Rev. E: Stat. Phys., Plasmas, Fluids, Relat. Interdiscip. Top.*, 1995, **52**, 4045.
9 A. Imhof and J. K. G. Dhont, *Phys. Rev. Lett.*, 1995, **75**, 1662.
10 N. Hunt, R. Jardine and P. Bartlett, *Phys. Rev. E: Stat. Phys., Plasmas, Fluids, Relat. Interdiscip. Top.*, 2000, **62**, 900.
11 P. Bartlett, R. H. Ottewill and P. N. Pusey, *Phys. Rev. Lett.*, 1992, **68**, 3801.
12 X. Cottin and P. A. Monson, *J. Chem. Phys.*, 1995, **102**, 3354.
13 A. B. Schofield, *Phys. Rev. E: Stat., Nonlinear, Soft Matter Phys.*, 2001, **64**, 051403.
14 A.-P. Hynninen, L. Filion and M. Dijkstra, *J. Chem. Phys.*, 2009, **131**, 064902.
15 M. Dijkstra, R. van Roij and R. Evans, *Phys. Rev. Lett.*, 1998, **81**, 2268.
16 W. Götze and Th. Voigtmann, *Phys. Rev. E: Stat., Nonlinear, Soft Matter Phys.*, 2003, **67**, 021502.
17 Th. Voigtmann, *Europhys. Lett.*, 2011, **96**, 36006.
18 Ph. Germain and S. Amokrane, *Phys. Rev. Lett.*, 2009, **102**, 058301.
19 F. Tchangnwa Nya, A. Ayadim, Ph. Germain and S. Amokrane, *J. Phys.: Condens. Matter*, 2012, **24**, 325106.
20 S. R. Williams and W. van Megen, *Phys. Rev. E: Stat., Nonlinear, Soft Matter Phys.*, 2001, **64**, 041502.
21 B. E. Rodriguez, E. W. Kaler and M. S. Wolfe, *Langmuir*, 1992, **8**, 2382.
22 G. Foffi, W. Götze, F. Sciortino, P. Tartaglia and Th. Voigtmann, *Phys. Rev. Lett.*, 2003, **91**, 085701.
23 K. N. Pham, A. M. Puertas, J. Bergenholtz, S. U. Egelhaaf, A. Moussaid, P. N. Pusey, A. B. Schofield, M. Cates, M. Fuchs and W. C. K. Poon, *Science*, 2002, **296**, 104–106.
24 K. N. Pham, S. U. Egelhaaf, P. N. Pusey and W. C. K. Poon, *Phys. Rev. E: Stat., Nonlinear, Soft Matter Phys.*, 2004, **69**, 011503.
25 A. T. J. M. Woutersen and C. G. de Kruif, *J. Rheol.*, 1993, **37**, 681.
26 P. D'Haene and J. Mewis, *Rheol. Acta*, 1994, **33**, 165.
27 W. Richtering and H. Müller, *Langmuir*, 1995, **11**, 3699.
28 W. J. Hunt and C. F. Zukoski, *Langmuir*, 1996, **12**, 6257.
29 P. Gondret and L. Petit, *Langmuir*, 1997, **41**, 1261.
30 R. Greenwood, P. F. Luckham and T. Gregory, *J. Colloid Interface Sci.*, 1997, **191**, 11.
31 T. Shikata, H. Niwa and Y. Morishima, *J. Rheol.*, 1998, **42**, 765.
32 T. Ohtsuki, *Physica A*, 1983, **122**, 212.
33 G. Nägele and J. Bergenholtz, *J. Chem. Phys.*, 1998, **108**, 9893.
34 R. A. Lionberger, *Phys. Rev. E: Stat., Nonlinear, Soft Matter Phys.*, 2002, **65**, 061408.
35 C. Y. Chang and R. L. Powell, *J. Fluid Mech.*, 1993, **253**, 1.
36 C. Y. Chang and R. L. Powell, *J. Rheol.*, 1994, **38**, 85.
37 C. Y. Chang and R. L. Powell, *Phys. Fluids*, 1994, **6**, 1628.
38 R. J. Farris, *Trans. Soc. Rheol.*, 1968, **12**, 281.
39 R. Foudazi, I. Masalova and A. Y. Malkin, *J. Rheol.*, 2012, **56**, 1299.
40 T. Sentjabrskaja, M. Laurati, S. U. Egelhaaf and Th. Voigtmann, in preparation.
41 T. Sentjabrskaja, S. U. Egelhaaf and M. Laurati, *AIP Conf. Proc.*, 2013, **1518**, 206–213.
42 K. N. Pham, G. Petekidis, D. Vlassopoulos, S. U. Egelhaaf, P. N. Pusey and W. C. K. Poon, *Europhys. Lett.*, 2006, **75**, 624–630.
43 K. N. Pham, G. Petekidis, D. Vlassopoulos, S. U. Egelhaaf, W. C. K. Poon and P. N. Pusey, *J. Rheol.*, 2008, **52**, 649–676.
44 M. Laurati, S. U. Egelhaaf and G. Petekidis, *J. Rheol.*, 2011, **55**, 673–706.
45 N. Koumakis and G. Petekidis, *Soft Matter*, 2011, **7**, 2456–2470.
46 G. Petekidis, A. Moussaid and P. N. Pusey, *Phys. Rev. E: Stat., Nonlinear, Soft Matter Phys.*, 2002, **66**, 051402.
47 G. Petekidis, D. Vlassopoulos and P. N. Pusey, *Faraday Discuss.*, 2003, **123**, 287.
48 A. Yethiraj and A. van Blaaderen, *Nature*, 2003, **421**, 513–517.
49 M. C. Jenkins and S. U. Egelhaaf, *Adv. Colloid Interface Sci.*, 2008, **136**, 65–92.
50 W. Schaertl and H. Silescu, *J. Stat. Phys.*, 1994, **77**, 1007–1025.
51 W. C. K. Poon, E. R. Weeks and C. P. Royall, *Soft Matter*, 2012, **8**, 21–30.
52 N. Koumakis, A. Pamvouxoglou, A. S. Poulos and G. Petekidis, *Soft Matter*, 2012, **8**, 4271–4284.
53 H. J. Schöpe, G. Bryant and W. van Megen, *J. Chem. Phys.*, 2007, **127**, 084505.
54 N. Koumakis, M. Laurati, S. U. Egelhaaf, J. F. Brady and G. Petekidis, *Phys. Rev. Lett.*, 2012, **108**, 098303.
55 P. A. Smith, G. Petekidis, S. U. Egelhaaf and W. C. K. Poon, *Phys. Rev. E: Stat., Nonlinear, Soft Matter Phys.*, 2007, **76**, 041402.

56 J. C. Conrad, H. M. Wyss, V. Trappe, S. Manley, K. Miyazaki, L. J. Kaufman, A. B. Schofield, D. R. Reichman and D. A. Weitz, *J. Rheol.*, 2010, **54**, 421–438.
57 H. König, R. Hund, K. Zahn and G. Maret, *Eur. Phys. J. E*, 2005, **18**, 287–293.
58 T. Hamanaka and A. Onuki, *Phys. Rev. E: Stat., Nonlinear, Soft Matter Phys.*, 2007, **75**, 041503.
59 P. Yunker, Z. Zhang and A. G. Yodh, *Phys. Rev. Lett.*, 2010, **104**, 015701.
60 F. Ebert, P. Keim and G. Maret, *Eur. Phys. J. E*, 2008, **26**, 161.
61 L. J. Bonales, F. Martinez-Pedrero, M. A. Rubio, R. G. Rubio and F. Ortega, *Langmuir*, 2012, **28**, 16555.
62 I. Biazzo, F. Caltagirone, G. Parisi and F. Zamponi, *Phys. Rev. Lett.*, 2009, **102**, 195701.
63 R. S. Farr and R. D. Groot, *J. Chem. Phys.*, 2009, **131**, 244104.
64 N. Koumakis, A. B. Schofield and G. Petekidis, *Soft Matter*, 2008, **4**, 2008–2018.
65 C. Mayer, E. Zaccarelli, E. Stiakakis, C. N. Likos, F. Sciortino, A. Munam, M. Gauthier, N. Hadjichristidis, H. Iatrou, P. Tartaglia, H. Löwen and D. Vlassopoulos, *Nat. Mater.*, 2008, **7**, 780.

3.3. Publication 3: Transient dynamics during stress overshoots in binary colloidal glasses

Journal: Soft Matter
Reference: *Soft Matter*, 2014, **10**, 6546
Impact factor: 4.151
Authors: **T. Sentjabrskaja**, M. Hermes, W. C. K. Poon, C. D. Estrada, R. Castañeda-Priego, S. U. Egelhaaf and M. Laurati
1st author
TS prepared all materials, performed the experiments and analyzed the data. The confocal measurements under shear were performed on the setup developed by MH and WCKP. CDE and RCP performed the computer simulations. TS, ML and SUE conceived and discussed the project. ML and SUE supervised the project. All authors contributed to the writing of the manuscript.
75 % contribution of TS

This page has been left intentionally blank.

Soft Matter

PAPER

View Article Online
View Journal | View Issue

Cite this: *Soft Matter*, 2014, **10**, 6546

Transient dynamics during stress overshoots in binary colloidal glasses

T. Sentjabrskaja,[a] M. Hermes,[b] W. C. K. Poon,[b] C. D. Estrada,[c] R. Castañeda-Priego,[c] S. U. Egelhaaf[a] and M. Laurati*[a]

Received 15th March 2014
Accepted 17th June 2014

DOI: 10.1039/c4sm00577e

www.rsc.org/softmatter

We investigate, using simultaneous rheology and confocal microscopy, the time-dependent stress response and transient single-particle dynamics following a step change in shear rate in binary colloidal glasses with large dynamical asymmetry and different mixing ratios. The transition from solid-like response to flow is characterised by a stress overshoot, whose magnitude is linked to transient superdiffusive dynamics as well as cage compression effects. These and the yield strain at which the overshoot occurs vary with the mixing ratio, and hence the prevailing caging mechanism. The yielding and stress storage are dominated by dynamics on different time and length scales, the short-time in-cage dynamics and the long-time structural relaxation respectively. These time scales and their relation to the characteristic time associated with the applied shear, namely the inverse shear rate, result in two different and distinct regimes of the shear rate dependencies of the yield strain and the magnitude of the stress overshoot.

1 Introduction

A wide range of technical applications is based on glassy materials, including polymeric,[1] metallic[2] and colloidal systems.[3] One-component dispersions of hard-sphere like colloids have been intensively used as model systems to study the glass transition.[3] In this system, the volume fraction ϕ is the only control parameter. The glass state is driven by crowding: for $\phi > 0.58$ particles are permanently localised in cages formed by their neighbours, which they can only escape through activated processes.[4] Colloidal glasses melt and flow under application of shear.[5–13] Shear-induced melting is associated with an irreversible deformation of the cage[9,13] and the onset of diffusive dynamics.[8] It occurs *via* a transient regime in which the system yields. At yielding a stress overshoot is observed in the rheological response and reflects maximal cage distortion in the structure and a transient super-diffusive regime in the dynamics.[9,13–15]

Many glassy materials used in applications are not one-component systems, but composed of particles with different sizes. This raises the question whether, and if so how, the shear-induced melting process, in particular the transient macroscopic rheology and the microscopic structure and dynamics, is affected by the presence of multiple components. The simplest multi-component model system is a binary mixture of colloidal hard spheres. The phase behavior of binary colloidal hard spheres has been studied in experiments,[16–20] simulations[21–23] and theory.[23–29] It depends on several parameters, namely the total volume fraction, the size ratio and the mixing ratio of the two components. Theory predicts that at small to moderate size disparities the glass transition shifts to larger total volume fractions, similar to the effect of polydispersity.[24,30–32] This implies that for constant total volume fraction, glass melting can be induced by mixing. This is reflected in the acceleration of the dynamics measured by light scattering[16] as well as the strong reduction of the viscosity observed by rheology.[33] At large enough size disparities multiple glass states are expected.[30] They differ by the mechanism driving the arrest of the large spheres, either caging or depletion-induced bonding, and the dynamics of the small spheres, either dynamical arrest or mobility.[25,30] Some of these states have been observed experimentally[17–19] and in molecular dynamics simulations.[21]

The yielding behaviour of binary glasses under oscillatory shear was recently studied for size ratios $\delta = R_s/R_L = 0.38$ and 0.2,[20] with R_s and R_L the radii of the small and large spheres respectively. At constant total volume fraction ϕ, a decrease of the yield strain and stress is observed at intermediate mixing ratios, and is particularly pronounced for the larger size disparity. This effect has been associated with the variation in the free volume due to changes in the volume fraction of random close packing, which also becomes more pronounced at larger size disparities.

Here, we extend this study to explore the response after switch-on of a constant shear rate. In particular the link

[a]*Condensed Matter Physics Laboratory, Heinrich Heine University, Universitätsstraße 1, 40225 Düsseldorf, Germany. E-mail: marco.laurati@uni-duesseldorf.de*

[b]*SUPA, School of Physics & Astronomy, The University of Edinburgh, Mayfield Road, Edinburgh EH9 3JZ, UK*

[c]*Division of Sciences and Enginering, University of Guanajuato, Loma del Bosque 103, 37150 León, Mexico*

between the macroscopic non-linear rheology and the transient single-particle dynamics is investigated using confocal microscopy. A stress overshoot and super-diffusive transient dynamics is found to characterise yielding, similar to the behaviour of one-component systems.[9,13–15] However, in binary mixtures the yield strain and magnitude of the overshoot depend in a complex and different way on the shear rate and show a dependence on the composition of the mixture. The composition determines the caging mechanism, localization length as well as the short and long-time dynamics, including the degree of super-diffusion.

The manuscript is structured as follows. Section 2 describes the experimental systems and methods, namely simultaneous rheology and confocal microscopy, as well as the simulations. In Section 3 we first present the equilibrium structure and dynamics of the large particles in the mixtures and a resume of the linear viscoelastic properties of the binary mixtures. Then we discuss the results of the non-linear rheology and the dynamics under shear before offering some conclusions in Section 4.

2 Methods

2.1 Rheology

Rheological measurements are performed using an ARES G2 strain controlled rheometer (TA instruments) with a cone-plate geometry (diameter 20 mm, cone angle 2°, truncation gap 0.054 mm). A solvent trap minimizes solvent evaporation. Rheological measurements on colloidal glasses can be affected by loading effects, shear history and aging. Therefore, before each test a renjuvenation procedure is performed in order to obtain a reproducible initial state. First, after loading we perform a dynamic strain sweep to estimate the yield strain γ_{yield} of the system. Oscillatory shear at strain amplitude $\gamma = 300\% \gg \gamma_{yield}$ is applied to induce flow and maintained until the viscoelastic storage, G', and loss, G'', moduli reach a stationary state, typically after 200 s. Afterwards, oscillatory shear in the linear viscoelastic regime ($0.05\% < \gamma < 0.1\%$, depending on sample) is applied until G' and G'' become stationary, typically for times 200 s $< t <$ 700 s, depending on the sample. The state characterised by the stationary values of G' and G'' thus represents the initial reproducible state. The absence of wall slip is verified by comparison with measurements obtained with roughened geometries (data not shown).

2.2 Confocal microscopy under shear

Confocal microscopy measurements under shear are performed with a confocal rheoscope, which is a combination of an MCR301 WSP rheometer (Anton Paar) and a fast-scanning VT-Eye confocal scanner (Visitech), mounted on a Nikon Ti-U inverted microscope with a Nikon Plan Apo 60× objective (NA = 1.40). Details of the setup can be found in previous work.[34] We use a cone-plate geometry with diameter 50 mm, cone angle 1° and truncation gap 0.10 mm. To minimise wall-slip the cone is sandblasted, while the bottom plate, consisting of a thin glass plate, is coated with PMMA particles of size 0.885 μm and 0.174 μm.[35] A solvent trap is used to reduce solvent evaporation. Images of the samples (512 × 512 pixels, corresponding to about 48 μm × 48 μm for samples with $0.3 < x_s < 0.9$, 51 μm × 51 μm for $x_s = 0.0$, and 53 μm × 53 μm for $x_s = 0.1$) are acquired at a depth of 30 μm from the bottom plate and at a distance of about 6 mm from the center. Time series of 2D images are taken at a rate of 31 or 67 frames per second, depending on the sample. Particle coordinates and trajectories are extracted from the pictures using previously-explained routines.[36]

2.3 Samples

We use suspensions of polymethylmethacrylate (PMMA) colloids, sterically stabilized with polyhydroxystearic acid (PHS) and dispersed in a solvent mixture of *cis*-decalin and cycloheptyl bromide (CHB). The solvent mixture matches the density and almost the refractive index of the particles. The charge that the particles acquire in the CHB/decalin solvent is screened by adding 4 mM tetrabutylammoniumchloride (TBAC).[37] Under these conditions the interactions in the system are hard-sphere-like.[38] For the most sensitive rheological measurements we use particles with radii $R_L^{rheo} = 0.304$ μm and $R_s^{rheo} = 0.063$ μm, and polydispersities of approximately 10% and 15%, respectively. The size ratio of the mixture is $\delta^{rheo} = 0.207$. The high energy density of these small particles leads to a strong rheological signal. The sample set corresponding to these particles is referred to as RH in the following. For measurements on the confocal rheoscope, a mixture of PMMA particles with radii $R_L^{mic} = 0.885$ μm (6% polydispersity) and $R_s^{mic} = 0.174$ μm (15% polydispersity) is prepared resulting in $\delta^{mic} = 0.197$. The large spheres with radius R_L^{mic} are fluorescently labelled with nitrobenzoxadiazole (NBD) and can be observed with the confocal microscope using a solid state laser with wavelength $\lambda = 488$ nm. This sample set is referred to as CO in the following. The particle radii and polydispersities are determined by static and dynamic light scattering with an uncertainty in the radius of about 2%.

The volume fraction of the sediment of the large spheres is determined by imaging the sample by confocal microscopy and using the Voronoi construction to estimate the mean Voronoi volume per particle. The procedure of determining the volume fraction is described in detail in[20] and leads to the estimate $\phi_L^{RCP} \approx 0.68$. A one-component sample with $\phi = 0.61$ is prepared by diluting the sediment. This sample is used as a reference. The volume fractions of the samples containing the small particles are adjusted in order to obtain comparable linear viscoelastic moduli in units of the energy density $3k_BT/4\pi R^3$, where k_B is the Boltzmann constant, T the temperature and R the particles' radius, while multiplying the frequency by the free-diffusion Brownian time $\tau_0 = 6\pi\eta R^3/k_BT$, where $\eta = 2.2$ mPa s is the solvent viscosity. In this way we obtain samples with comparable dynamics, according to the generalised Stokes–Einstein relation.[39] Samples with constant total volume fraction $\phi = 0.61$ and different compositions, namely fractions of small particles $x_s = \phi_s/\phi$, where ϕ_s is the volume fraction of small particles, are prepared by mixing the stock solutions.

2.4 Simulations

Event-driven molecular dynamics simulations are performed to investigate the dynamics of binary hard spheres with the same size ratio $\delta = 0.2$ as in the experiments. To render simulations with this size disparity feasible, we applied the double-cell scheme,[23] which uses a combination of large cells with a size just above $2R_L$ and small cells with a size just above $2R_s$. This allows us to compute long enough sequences of particle configurations. Due to the nature of the hard-sphere potential, the system is conservative and additionally the temperature is constant. Thus, its evolution can be determined by calculating a sequence of elastic collisions; the particles move in a straight line before any collision. Given the positions, $\vec{r}_i$, and velocities, $\vec{v}_i$, of each pair (i,j) of particles at time t, the collision time Δt is determined by the physical solution (real and positive) of the quadratic equation $\vec{r}_{ij}^{\,2}(t+\Delta t) = [\vec{r}_{ij}(t) + \vec{v}_{ij}(t)\Delta t]^2 = [(2R_i + 2R_j)/2]^2$. The set of collision times of each particle is stored in an ordered list to monitor its trajectory with a nonuniform time step sequence. In each collision, the change in the velocities of the colliding particles is obtained by the energy and momentum conservation laws as $\Delta\vec{v}_i = -2m_j(\vec{v}_{ij}\cdot\vec{r}_{ij})\hat{r}_{ij}/(m_i + m_j)$. Hence, the next collision can be predicted. Thus, the simulations provide particle trajectories, based on which the mean squared displacement can be determined, as well as, *e.g.*, the mean free path l_0 and the mean time between collisions, $\mathscr{T}_s^{\text{short}}$. With increasing volume fraction, $\mathscr{T}_s^{\text{short}}$ approaches zero and thus the rate of collisions quickly grows. With our computing resources we can investigate volume fractions $\phi \leq 0.58$, *i.e.* below the experimental volume fraction. Experiments with $\phi = 0.61$ (Fig. 2) and $\phi = 0.58$ (ref. 40) indicate that the qualitative variations of the dynamics, quantified by the mean squared displacements, as a function of mixing ratio are comparable for the two volume fractions. We thus compare our experimental findings to simulation results for $\phi = 0.58$. The simulations cover $0.1 \leq x_s \leq 0.7$ and the one-component limits $x_s = 0.0$ and 1.0. The numbers of large particles are 125 ($x_s = 0.7$), 250 ($x_s = 0.5$), 500 (other x_s) and according numbers of small particles. The large and small spheres have the same mass density and the two populations are monodisperse. The simulations start with random particle configurations. At least 10 different runs are averaged for each x_s to reduce statistical uncertainties.

3 Results and discussion

3.1 Quiescent structure

Binary mixtures with a size ratio $\delta = 0.2$, a total volume fraction $\phi = 0.61$ and different compositions $0 \leq x_s \leq 1$ are investigated. The pair distribution functions $g(r)$ of the large particles in the quiescent state were determined by confocal microscopy (Fig. 1). They indicate an amorphous structure for all x_s. Similar data were reported and discussed in detail in ref. 19. We thus only recall the main findings. The one-component glass of large spheres shows a fluid-like structure typical of a colloidal glass; a main peak corresponding to the first shell of nearest neighbours at distance $r = 2R_L$ (the caging particles) and additional peaks indicating the successive shells of nearest neighbours.

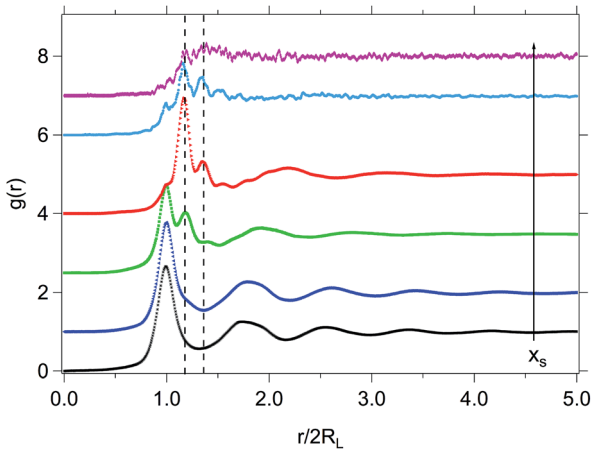

Fig. 1 Pair distribution function $g(r)$ of large particles R_L^{mic} in mixtures with $\phi = 0.61$, $\delta = 0.2$ and different compositions $x_s = 0.0$ (✱), 0.1 (◀), 0.3 (■), 0.5 (▶), 0.7 (●), 0.9 (♦). Data for $x_s > 0$ are shifted vertically. Dashed lines indicate particle–particle distances $r = 2(R_L + R_s)$ and $r = 2(R_L + 2R_s)$, corresponding to configurations in which two large particles are separated by one or two small particles, respectively.

Upon addition of small spheres, additional particle configurations appear due to the intercalation of small spheres between large spheres. While a small shoulder at $r = 2R_L + 2R_s$ is already visible for $x_s = 0.1$, peaks at this distance and also at $r = 2R_L + 4R_s$ are observed for $x_s = 0.3$, which correspond to configurations in which two large particles are separated by one or two small particles, respectively (Fig. 1, dashed lines). This indicates a loosening of the cage of large particles with increasing x_s, which leads to a transition in caging at $x_s = 0.5$, as indicated by the disappearing first peak at $r = 2R_L$ and the pronounced peak at $r = 2R_L + 2R_s$. Hence, at $x_s = 0.5$ the large spheres are prevalently caged by small spheres. Upon further increasing x_s the large particles, still caged by small particles, become increasingly more dilute. Particle configurations in which small particles intercalate between large particles were not observed in mixtures with larger $\delta = 0.67$,[41] in agreement with geometrical arguments[20] predicting a limiting value $\delta \leq 0.41$.

3.2 Quiescent dynamics

The mean squared displacement (MSD) of the large particles in one direction is:

$$\delta y^2(t) = \langle (y_i(t + t_0) - y_i(t_0))^2 \rangle_{i,t_0}, \quad (1)$$

where t is the delay time, t_0 a selected time along the trajectory of particle i and $\langle\ \rangle_{i,t_0}$ indicates the average over all particles i in the field of view and all times t_0. It is determined from time series of 3D stacks in the quiescent state before applying shear (Fig. 2). For $x_s = 0.0$ and 0.1 the MSDs are flat, indicating localisation of particles in cages and absence of long-time diffusion within the measurement window. The localisation length $L = \sqrt{\delta y^2(t_1)}$, with t_1 the shortest delay time measured, corresponds to that expected for a cage of large particles. For $x_s = 0.3$ the large-particle dynamics become diffusive at long times. Similarly, for $x_s = 0.5$ mobility is observed at long times

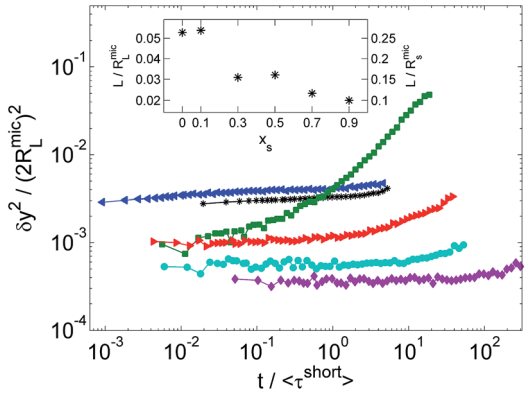

Fig. 2 Quiescent mean squared displacement in one direction δy^2 of large particles R_L^{mic} in mixtures with $\phi = 0.61$, $\delta = 0.2$ and different compositions $x_s = 0.0$ (✳), 0.1 (◀), 0.3 (■), 0.5 (▶), 0.7 (●), 0.9 (♦). The delay time t is normalised by the composition-averaged short-time Brownian time $\langle\tau^{short}\rangle$. (Inset) The x_s-dependence of the localisation length $L = \sqrt{\delta y^2(t_1)}$ in units of R_L^{mic} (left y-axis) and R_s^{mic} (right y-axis), where t_1 is the shortest delay time measured.

even though no diffusive regime is visible within the experimental time window. In addition, the localisation length L is reduced, indicating the presence of small particles around the large particles, hindering their motions. This is consistent with the pair distribution function of the large particles (Fig. 1), which shows an increasingly more pronounced shoulder at a distance corresponding to the sum of a large and small particle.[19,20] For larger fractions of small particles, $x_s > 0.5$, the long-time dynamics again slow down and particles continue to become increasingly localised in the cage of small particles. This transition in caging and the faster dynamics at intermediate compositions have been observed previously for the same δ.[19] However, the acceleration of the dynamics in the present mixtures is much more pronounced than at larger δ.[16,20,31,32,42,43] This could result from the melting of the cage of large spheres, which accompanies the glass–glass transition observed at $x_s = 0.5$ in our system. This appears to affect the particle dynamics more than the smaller cage polydispersity in mixtures of particles with more comparable sizes. Furthermore, the dependence of the MSD on x_s can be related to the available free volume in the mixtures, which can be estimated on the basis of the x_s dependence of the volume fraction of random close packing, ϕ_{RCP}.[19,20]

The intrinsic time scales of the samples can be obtained from the corresponding short- and long-time diffusion coefficients. The short-time Brownian time of the small particles, $\tau_s^{short} = R_s^2/D_s^{short}$ with the short-time diffusion coefficient $D_s^{short} = fD_{0,s}$. It is related to the free (dilute) diffusion coefficient $D_{0,s} = k_BT/6\pi\eta R_s$ by the ϕ-dependent factor f. In a one-component system, f can be estimated by extrapolating the data in Fig. 8 of ref. 44 to $\phi = 0.61$, yielding $f \approx 1/32$. Similarly, the short-time Brownian time of the large particles, $\tau_L^{short} = \tau_s^{short}/\delta^3$, can be determined. For binary mixtures, the composition-averaged short-time Brownian time in the dilute limit is $\langle\tau_0^{short}\rangle = 6\pi\eta\langle R^3\rangle/k_BT$ and at a volume fraction ϕ we obtain $\langle\tau^{short}\rangle = \langle\tau_0^{short}\rangle/f$, where $\langle R^3\rangle = R_L{}^3/[1 - x_s(1 - 1/\delta^3)]$ is the number-averaged cube of the radius.

We studied the long-time dynamics using event-driven molecular dynamics simulations of binary mixtures of hard-spheres[23] with the same size ratio $\delta = 0.2$, but a reduced total volume fraction $\phi = 0.58$ to keep the simulation times reasonable (Section 2.4). Although the simulations do not consider a solvent and thus do not include Brownian motion at short times, an effective short-time diffusion coefficient D_s^0 can be determined; $D_s^0 = l_0{}^2/\mathcal{T}_s^{short}$ with the mean free path l_0 and mean free time $\mathcal{T}_s^{short}$.[45] With this rescaling the ratio D_s^* is equivalent to that obtained in a system with Brownian dynamics; $D_s^* = D_s^{long}/D_s^{short}$, with D_s^{short} the short-time Brownian diffusion coefficient.[45] The same equivalence applies to the ratio of the long time relaxation time $\mathcal{T}_s^{long}$ and the mean free time $\mathcal{T}_s^{short}$. Then D_s^* for the small (and, similarly, the large) spheres can be extracted from the MSDs rescaled by $l_0{}^2$ with times rescaled by $\mathcal{T}_s^{short}$. To simplify the comparison with experiments, in what follows we will indicate the ratio $\mathcal{T}_s^{long}/\mathcal{T}_s^{short}$ using the equivalent ratio of the Brownian relaxation times $\tau_s^{long}/\tau_s^{short}$. From D_s^*, the normalised long-time structural relaxation time of the small spheres, $\tau_s^{long}/\tau_s^{short} = 1/D_s^*$, and, similarly, of the large spheres, $\tau_L^{long}/\tau_s^{short} = 1/(\delta^3 D_L^*)$, can be calculated (Fig. 3).

The structural relaxation time of the small spheres, τ_s^{long}, monotonously increases with x_s indicating the progressive arrest of the small spheres. However, the structural relaxation time of the large spheres, τ_L^{long}, exhibits an intermediate minimum ($x_s = 0.1$) consistent with the melting of the one-component glasses as a second species is added. While the addition of small spheres to the glass of large spheres melts the glass, the addition of large spheres not only melts the glass of small spheres, but also induces obstacles.[46] This leads to the asymmetric dependence of τ_L^{long} on x_s. We expect the minimum to be more pronounced for the higher $\phi = 0.61$ of the experiments, since the large and small spheres are deeper in the glassy state at $x_s < 0.3$ and $x_s \geq 0.7$ than at $\phi = 0.58$. Previous experimental work on binary mixtures with the same size ratio and comparable $x_s = 0.7$ indicates glass states for $\phi > 0.57$ and

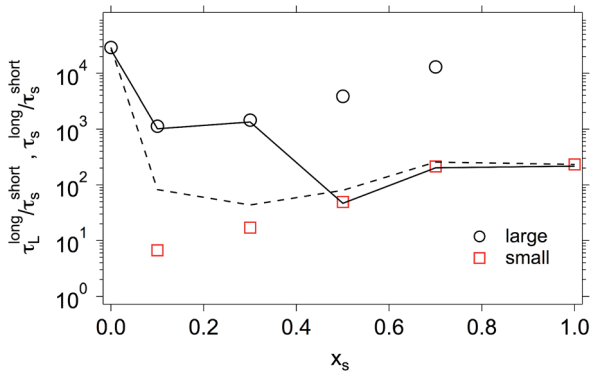

Fig. 3 Long-time structural relaxation times of large, τ_L^{long} (○), and small, τ_s^{long} (□), spheres as a function of composition x_s, obtained from MD simulations of binary hard sphere mixtures with size ratio $\delta = 0.2$ and total volume fraction $\phi = 0.58$. The relaxation times are normalised by the mean free time of the small spheres τ_s^{short}. The dashed and solid lines indicate the number-averaged, $\langle\tau^{long}\rangle$, and dominant, $\tilde{\tau}^{long}$, structural relaxation times, respectively.

fluid states for $\phi \leq 0.57$.[20] In addition, the number-averaged long-time structural relaxation time at a volume fraction $\phi = 0.58$ can be calculated according to $\langle\tau^{\text{long}}\rangle = [(1 - x_s)\delta^3\tau_L^{\text{long}} + x_s\tau_s^{\text{long}}]/[(1 - x_s)\delta^3 + x_s]$ (Fig. 3, dashed line). This exhibits a minimum at $x_s \approx 0.3$. The minimum is shifted with respect to the minimum of τ_L^{long} ($x_s \approx 0.1$) due to the increasing weight of the smaller τ_s^{long}. As mentioned above, a transition in caging is expected at $x_s \approx 0.5$ with caging by large and small spheres at small and large x_s, respectively.[20] Thus, the systems are expected to be dominated by τ_L^{long} and τ_s^{long} for $x_s \lesssim 0.5$ and $x_s \gtrsim 0.5$, respectively, which we denote by $\tilde{\tau}_s^{\text{long}}$ (Fig. 3, solid line).

3.3 Linear viscoelasticity

The storage modulus, G', as a function of composition x_s is extracted from the linear viscoelastic regime of dynamic strain sweeps ($0.5\% < \gamma < 1\%$, depending on sample), Fig. 4. Values of G' are determined for an oscillatory Péclet number $\text{Pe}_\omega = 1.2$ with $\text{Pe}_\omega = \omega\langle\tau^{\text{short}}\rangle$, where ω is the oscillation frequency. They are reported in units of the composition-averaged energy density, $k_BT/\langle R^3\rangle$, to remove the trivial dependence on the particle size. The large values of G' at $x_s = 0.0$ and 1.0 are consistent with their one-component glass states. By adding a second species, G' decreases, indicating glass softening with the results for both sample sets, RH (radii 0.304 μm, 0.063 μm) and CO (radii 0.885 μm, 0.174 μm) being comparable. The glass softening is thought to result from the transition in caging and the faster long-time dynamics at intermediate compositions (Fig. 2).[19] It is particularly pronounced for $0.1 \leq x_s \leq 0.5$, *i.e.* upon adding small particles to large particles. This reflects the asymmetry observed in the dynamics. The dependence of G' on x_s hence appears related to changes in the microscopic dynamics.[19,20]

3.4 Non-linear stress response

In a step rate experiment, a constant shear rate $\dot{\gamma}$ is applied to the initially quiescent sample and the evolution of the stress σ as a function of time t or, equivalently, strain $\gamma = \dot{\gamma}t$ is measured. The dependence of the measured stress on strain is presented in Fig. 5 for binary mixtures with size ratio $\delta = 0.2$, total volume fraction $\phi = 0.61$ and different compositions x_s as

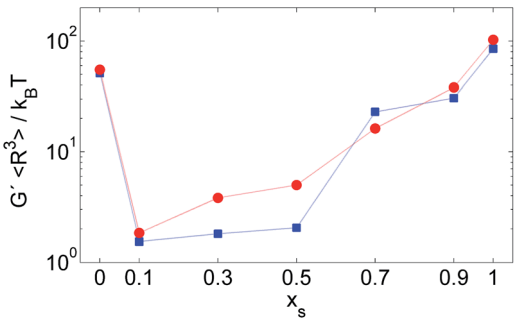

Fig. 4 Storage modulus $G'/(k_BT/\langle R^3\rangle)$ in the linear viscoelastic regime, extracted from dynamic strain sweep measurements at oscillatory Péclet numbers $\text{Pe}_\omega = 1.2$ for two sample sets with $\phi = 0.61$, $\delta = 0.2$: (●) CO (larger spheres, also used for microscopy) and (■) RH (smaller spheres, only used for rheology).

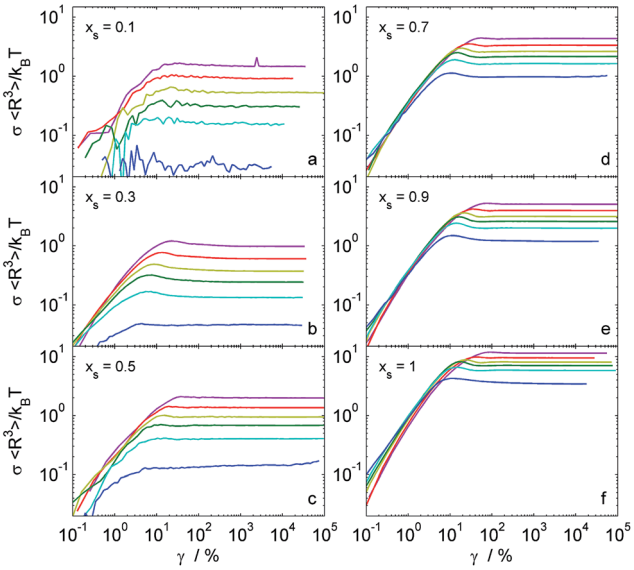

Fig. 5 Stress σ scaled by the average energy density $k_BT/\langle R^3\rangle$ *vs.* strain γ measured in step rate experiments for samples with compositions x_s (as indicated) and Péclet numbers $\text{Pe}_{\dot{\gamma}} = 0.03$, 0.24, 0.64, 1.20, 2.40 and 4.70 (bottom to top).

well as different shear rates $\dot{\gamma}$ or Péclet numbers $\text{Pe}_{\dot{\gamma}} = \dot{\gamma}\langle\tau^{\text{short}}\rangle$. For these values of $\text{Pe}_{\dot{\gamma}}$ and ϕ, homogeneous flow, *i.e.* laminar flow in the absence of shear banding, is expected for one component systems.[35,47] In order to compare different mixing ratios, the stress σ is scaled by the composition-averaged energy density. For all x_s and $\text{Pe}_{\dot{\gamma}}$, at small strains γ the stress increases almost linearly and reaches a maximum or overshoot, σ_{peak}, at a strain γ_{peak}. Subsequently the stress decreases to a constant value, σ_{steady}, which is the steady state value of the stress when the system flows. The noise in the measurements is seen to decrease with increasing x_s as a result of the increasingly larger energy density of the mixtures as the fraction of small spheres increases. From the curves in Fig. 5 we extract the value of the strain at the peak, γ_{peak} and the magnitude of the stress overshoot $\sigma_{\text{peak}}/\sigma_{\text{steady}} - 1$ to quantify the stress overshoot as a function of x_s and $\text{Pe}_{\dot{\gamma}}$. For one-component hard-sphere glasses ($x_s = 0$ and 1) this stress response, in particular the stress overshoot, has previously been observed and studied as a function of $\text{Pe}_{\dot{\gamma}}$.[9,13–15,48] It has been associated with the maximal cage distortion before the cage breaks.[9,13] During cage distortion stress is stored, and is only released when the deformation of the cage is partially relaxed by out-of-cage motion, resulting in the overshoot. Moreover, the overshoot is linked to super-diffusive particle motion observed in experiments and simulations, and predicted by mode coupling theory.[13–15]

The strain at the overshoot, γ_{peak}, is associated with the yield strain. It exhibits a dependence on composition x_s, which is comparable for all $\text{Pe}_{\dot{\gamma}}$ (Fig. 6a). The yield strain γ_{peak} initially decreases until it reaches a minimum at $x_s = 0.3$ and then increases again. This x_s dependence reflects the x_s dependence of the number-averaged long-time structural relaxation time $\langle\tau^{\text{long}}\rangle$ (Fig. 3), which is associated with the distance to the glass transition. This suggests that the yield strain is larger for systems

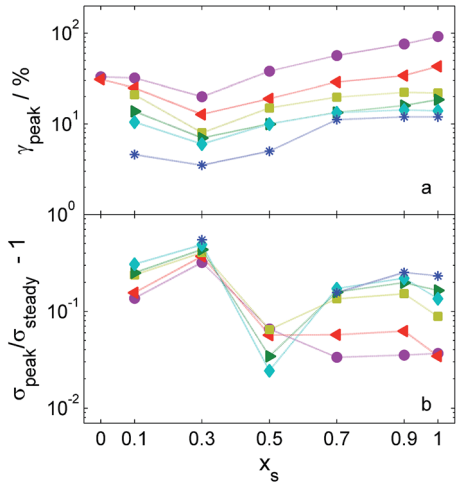

Fig. 6 (a) Strain at the stress overshoot, γ_{peak}, which can be taken as the yield strain, and (b) magnitude of the stress overshoot, $\sigma_{peak}/\sigma_{steady} - 1$, as a function of composition x_s for Péclet numbers $Pe_{\dot\gamma} = 0.03$ (✳), 0.24 (♦), 0.64 (▶), 1.20 (■), 2.40 (◀) and 4.70 (●).

which are deeper in the glass state. It might also be related to variations in the localisation length of the caging species.

In samples for which a broad range of $Pe_{\dot\gamma}$ values is explored, namely $x_s = 0.5$ and 0.7, two regimes in the $Pe_{\dot\gamma}$ dependence of the yield strain γ_{peak} are observed (Fig. 7a). The yield strain γ_{peak} remains approximately constant at $\gamma_{peak} \approx 10\%$ for $Pe_{\dot\gamma} \lesssim 1$, in agreement with MCT predictions for one-component glasses,[48] but increases for larger $Pe_{\dot\gamma}$, similar to experimental results on one-component colloidal glasses of hard-sphere like particles.[9,15] This behaviour becomes clearer by rescaling the yield strain γ_{peak} with a scaling factor $Z'(x_s)$ (Fig. 7, inset), which is the average of the γ_{peak} values obtained for the different Pe values at a given composition x_s (Fig. 6a). As expected, the scaling factor $Z'(x_s)$ (Fig. 8) follows the x_s dependence of γ_{peak} and hence also $\langle\tau^{long}\rangle$, similar to the data in Fig. 6a.

The behaviour in the two regimes can be understood by considering the relevant time scales; the characteristic time scale of shear, $\tau_{shear} = 1/\dot\gamma$, and the inherent time scale of the sample, namely the number-averaged short-time Brownian time $\langle\tau^{short}\rangle$ (defined in Section 3.2). If $\tau_{shear} > \langle\tau^{short}\rangle$, *i.e.* $Pe_{\dot\gamma} < 1$, the shear-induced deformation is slow compared to the Brownian dynamics. Therefore structural rearrangements and yielding can occur once the shear-induced cage deformation is sufficiently large to facilitate escape through Brownian motion. This cage deformation is expected to be similar to the size of the cage in a glass or dense fluid (Fig. 2, inset), consistent with the observed $\gamma_{peak} \approx 10\%$. At larger shear rates $\dot\gamma$, when $\tau_{shear} \lesssim \langle\tau^{short}\rangle$ or equivalently $Pe_{\dot\gamma} \gtrsim 1$, the probability of cage escape due to Brownian motion decreases. With increasing $Pe_{\dot\gamma}$, the particle displacements are increasingly dominated by the affine motion imposed by shear while the contribution by (random) Brownian motion decreases and thus particle collisions become less probable. Therefore, before yielding occurs the cage is deformed more, *i.e.* γ_{peak} increases. The rescaled yield strain γ_{peak}/Z' is found to increase linearly with $Pe_{\dot\gamma}$ for $Pe_{\dot\gamma} \gtrsim 1$ (Fig. 7a, inset). Thus $\gamma_{peak} = \dot\gamma t_{peak} = 0.1 Pe_{\dot\gamma} = 0.1\dot\gamma\langle\tau^{short}\rangle$ and

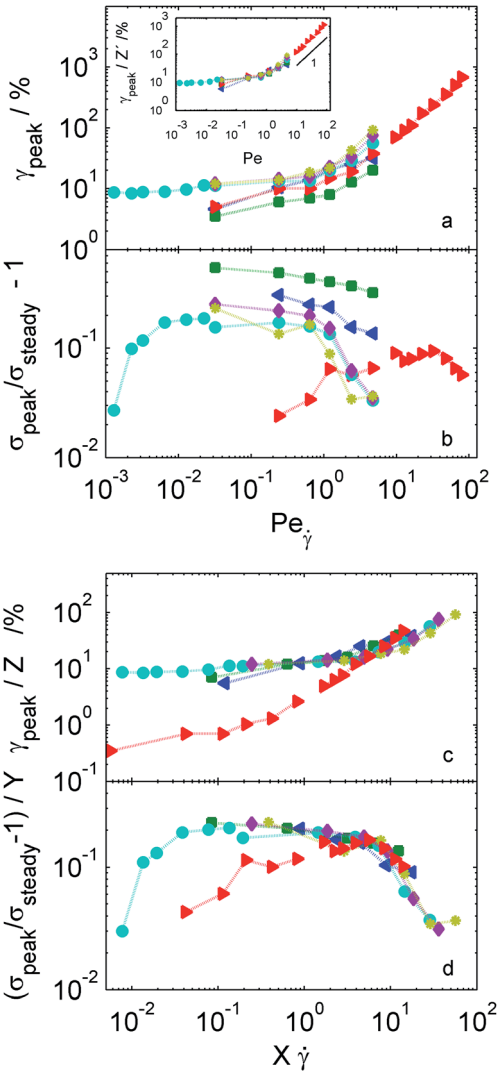

Fig. 7 (a) Strain at the stress overshoot, γ_{peak}, and (b) magnitude of the stress overshoot, $\sigma_{peak}/\sigma_{steady} - 1$, as a function of Péclet number $Pe_{\dot\gamma}$ and (c) rescaled yield strain, $\gamma_{peak}/Z(x_s)$, and (d) rescaled magnitude of the stress overshoot, $(\sigma_{peak}/\sigma_{steady} - 1)/Y(x_s)$, as a function of rescaled shear rate, $X(x_s)\dot\gamma$, for compositions $x_s = 0.1$ (◀), 0.3 (■), 0.5 (▶), 0.7 (●), 0.9 (♦), 1.0 (✳). The data in (c) and (d) are the same as in (a) and (b), respectively. The inset to (a) shows the same data as in the main plot, but superimposed along the ordinate using the scaling factor $Z'(x_s)$. The line indicates a slope of 1. (See text for details on the rescaling.)

hence $t_{peak} = 0.1\langle\tau^{short}\rangle$. Therefore, independent of $\dot\gamma$ or, equivalently, $Pe_{\dot\gamma}$, yielding occurs after the same time, about $0.1\langle\tau^{short}\rangle$. This suggests that for yielding to occur, at least a shear-induced (affine) displacement of about 10% and a minimum Brownian (random) displacement are required. The minimum mean squared displacement $\delta y_{peak}^2 = 2D^{shear}t_{peak} = 2D^{shear}0.1\langle\tau^{short}\rangle \lesssim 0.2\langle R^2\rangle$, where the last relation provides an upper boundary since the diffusion coefficient under shear, D^{shear} (Section 3.5), is smaller than the one in the quiescent state, which is implicitly contained in $\langle\tau^{short}\rangle$. The minimum displacement hence is about the size of the cage. A more quantitative comparison needs to consider the anisotropic structure of the sheared cages.[9,13]

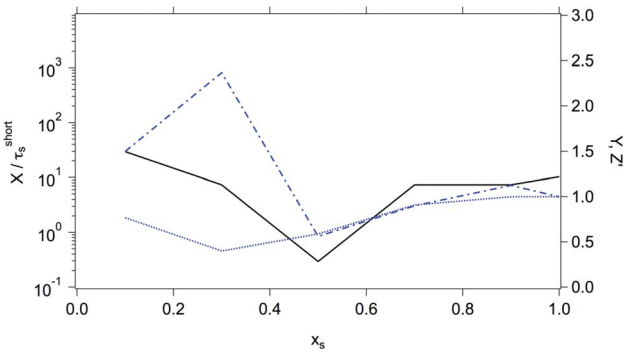

Fig. 8 Composition dependence of the scaling factors of the shear rate, X (solid line), of the strain at the stress overshoot, Y (dashed-dotted line), and of the magnitude of the stress overshoot, Z' (dotted line). The scaling factor X represents a characteristic time and is normalized by the short-time Brownian time of the small spheres τ_s^{short}. (For details on the scaling factors see text.)

Two regimes are also observed for the shear rate dependence of the magnitude of the stress overshoot, quantified by $\sigma_{peak}/\sigma_{steady} - 1$, for $x_s = 0.5$ and 0.7 (Fig. 7b). At small $Pe_{\dot\gamma}$, the magnitude of the stress overshoot increases with increasing $Pe_{\dot\gamma}$, as already observed in experiments on thermosensitive pNIPAM particles and as predicted by MCT for one-component systems.[48] It then reaches a maximum and decreases for large $Pe_{\dot\gamma}$, similar to one-component glasses of hard-sphere like PMMA particles.[9,49] The transition between the two regimes occurs at transitional Péclet numbers which depend on x_s, in contrast to the dependence of γ_{peak} on Pe. In particular, the $\sigma_{peak}/\sigma_{steady} - 1$ dependence for $x_s = 0.5$ (Fig. 7b, ▶) is shifted to considerably larger values of $Pe_{\dot\gamma}$ compared to dependencies observed for other x_s. That the transitional Péclet number depends on x_s implies that the time at which the transition occurs does not scale with the composition-averaged short-time Brownian time $\langle\tau^{short}\rangle$, which determines $Pe_{\dot\gamma}$.

To determine the appropriate characteristic time of the transition in $\sigma_{peak}/\sigma_{steady} - 1$ as a function of x_s, the data in Fig. 7b are rescaled as $(\sigma_{peak}/\sigma_{steady} - 1)/Y(x_s)$ *versus* $X(x_s)\dot\gamma$, where the scaling factors $X(x_s)$ and $Y(x_s)$ are chosen such that the resulting curves superimpose (Fig. 7d), that is the curves are shifted horizontally such that the transition occurs at $X(x_s)\dot\gamma = 1$ and vertically that the curves overlap. The scaling factor $X(x_s)$ hence represents the characteristic time of the transition between the increasing and the decreasing branches of $\sigma_{peak}/\sigma_{steady} - 1$ for the different x_s. It exhibits a pronounced minimum at $x_s = 0.5$ (Fig. 8, solid line). The x_s dependence is thus qualitatively different from the monotonously decreasing $\langle\tau^{short}\rangle$. However, the dependence appears similar to the one of the dominant structural relaxation time in the quiescent state, $\tilde\tau^{long}$ (Fig. 3, solid line), which is the relaxation time of the relevant caging species, *i.e.* the large particles for $x_s \leq 0.3$ and the small particles for $x_s > 0.3$.

Therefore, the transition between the two regimes depends on the balance between τ_{shear} and the dominant structural relaxation time $\tilde\tau^{long}$. This indicates that the processes relevant for stress transmission involve particle movements on length scales of out-of-cage diffusion. This is consistent with the fact that in one-component systems the overshoot has been associated with the yielding of the cage.[9,13] The out-of-cage movements are longer than those required for cage deformation, which determine γ_{peak}, and hence the timescale of out-of-cage diffusion is not relevant for the transition between the two regimes of the Péclet number dependence of γ_{peak}. This is supported by the poor overlap of the γ_{peak} curves if scaled by the same $X(x_s)$ used for scaling the stresses (Fig. 7c). The overlap is not significantly improved by also scaling γ_{peak} by $Z(x_s)$ such that all curves superimpose in the ordinate and on the right branch of the curve with $x_s = 1.0$ in the abscissa (Fig. 7c).

The value of $Y(x_s)$ (Fig. 8) corresponds to the average value of $\sigma_{peak}/\sigma_{steady} - 1$ for a given x_s. The magnitude of the overshoot, $\sigma_{peak}/\sigma_{steady} - 1$ (Fig. 6b) increases from $x_s = 0.1$, attains a maximum at $x_s = 0.3$ and reaches a minimum at $x_s = 0.5$. Subsequently it stays about constant for large $Pe_{\dot\gamma}$ (2.40 to 4.70) or increases to an also approximately constant value for small $Pe_{\dot\gamma}$ (0.03 to 1.20). The difference between small and large $Pe_{\dot\gamma}$ is related to the two regimes of the stress response discussed above (Fig. 7a and b).

3.5 Dynamics under shear

We aim to link the effects observed in the rheological measurements to the individual-particle dynamics under shear determined by confocal microscopy. Confocal microscopy allows us to image colloids during the step rate experiments and hence to follow shear-induced changes in the dynamics of the large particles, which are fluorescently labelled. Based on the particle trajectories in the velocity-vorticity plane, $(x_i(t), y_i(t))$, transient mean squared displacements in the vorticity direction, δy^2, are calculated for different waiting times t_w after application of shear:

$$\delta y^2(t, t_w) = \langle (y_i(t + t_w) - y_i(t_w))^2 \rangle_i, \quad (2)$$

where the average runs over all large particles i in the field of view, but not the waiting time t_w (eqn (1)). In the vorticity (neutral) direction contributions of affine particle motions are absent, and thus do not affect an investigation of the effects of shear on the Brownian motion of the particles. The particle dynamics can only reliably be determined using particle tracking if the particles move less than about a tenth of their radius between two successive frames. This limits the shear rates $\dot\gamma$ or Péclet numbers $Pe_{\dot\gamma}$ to $10^{-2} < Pe_{\dot\gamma} < 1$, which corresponds to the regime where Brownian motion significantly contributes to yielding and stress relaxation (Fig. 7a and b).

After shear is switched on, a steady-state develops. The corresponding MSDs in the steady-state are reported in Fig. 9 (thick color lines), together with the MSDs in the quiescent state (thick black lines). Compared to the quiescent state, the steady-state MSDs exhibit stronger localization at short times, but also faster long-time dynamics, namely a significantly increased long-time diffusion coefficient D_L^{steady}, which increases with increasing $Pe_{\dot\gamma}$ for all compositions x_s (Fig. 10a). The increase in D_L^{steady} corresponds to shear thinning and is in agreement with previous studies on one-component glasses[8,9,14,15,50] and measurements

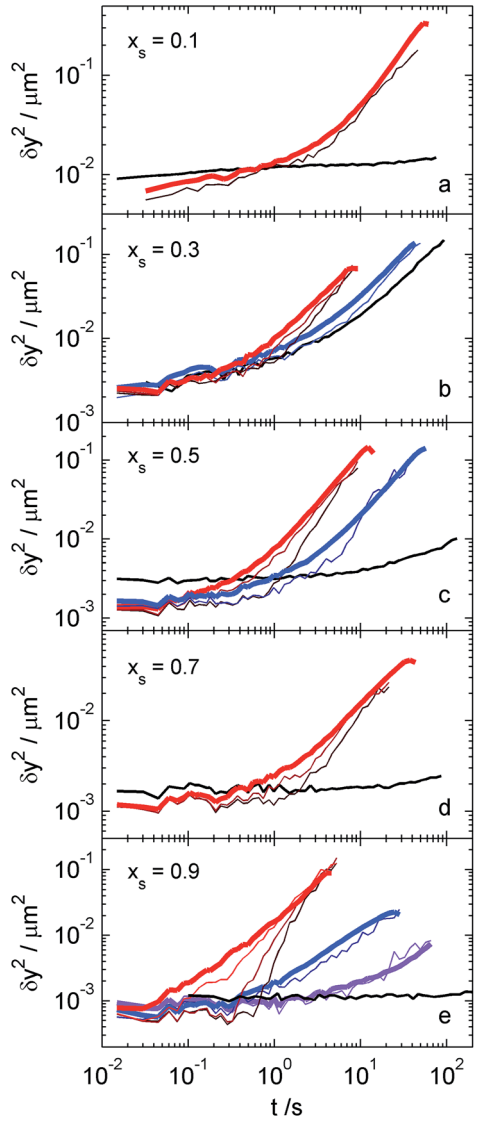

Fig. 9 Mean squared displacement in the vorticity direction δy^2 for different compositions x_s and Péclet numbers. (a) $x_s = 0.1$, $Pe_{\dot\gamma} = 0.24$ (red), (b) $x_s = 0.3$, $Pe_{\dot\gamma} = 0.24$ (red), 0.08 (blue), (c) $x_s = 0.5$, $Pe_{\dot\gamma} = 0.24$ (red), 0.005 (blue), (d) $x_s = 0.7$, $Pe_{\dot\gamma} = 0.035$, and (e) $x_s = 0.9$, $Pe_{\dot\gamma} = 0.28$ (red), 0.028 (blue), 0.003 (violet). The black lines correspond to the MSDs in the quiescent state, thick lines to the MSDs in the steady-state, and thin lines to transient MSDs at waiting time $t_w = 0$ and, where present, at longer t_w, increasing from bottom to top.

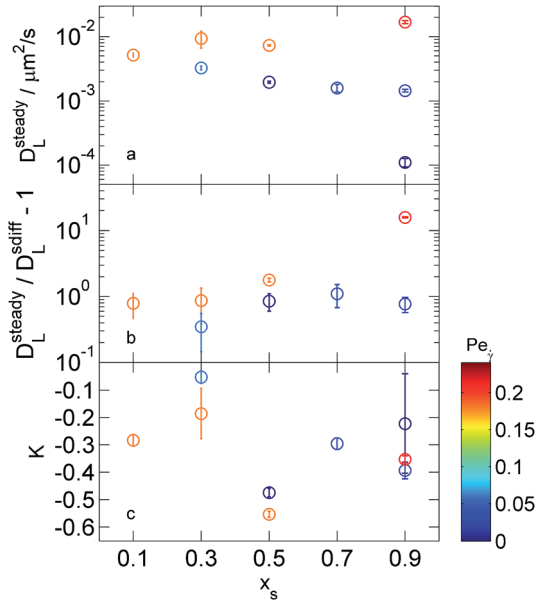

Fig. 10 (a) Steady-state diffusion coefficient D_L^{steady} of the large spheres, (b) amount of superdiffusion $D_L^{steady}/D_L^{sdiff} - 1$ of the large spheres at waiting time $t_w = 0$, and (c) magnitude of the cage compression $K = \delta y_{shear}{}^2/\delta y_{rest}{}^2 - 1$, as a function of x_s. Different $Pe_{\dot\gamma}$ values are indicated according to the color scale. The error bars represent variations between repeated measurements with same x_s and $Pe_{\dot\gamma}$.

of a two-component glass with $\delta = 0.2$ and $x_s = 0.9$.[19] For the largest $Pe_{\dot\gamma}$ values, D_L^{steady} as a function of x_s presents a weak maximum, and hence the fastest shear-induced dynamics, at $x_s = 0.3$ (Fig. 10a). The same composition also exhibits the fastest long-time dynamics of the large particles in the quiescent state (Fig. 2 and 3). In addition, this composition shows the smallest γ_{peak} (Fig. 6a), which indicates a link between facilitated yielding, *i.e.* a smaller yield strain, and fast dynamics in the steady-state, *i.e.* a larger diffusion coefficient. This is consistent with the observation that yielding requires a minimum mean squared displacement, which is reached earlier for faster dynamics. For the group of data at smaller $Pe_{\dot\gamma}$, D_L^{steady} slightly decreases for $x_s \geq 0.3$, *i.e.* the steady-state dynamics slows down with increasing x_s. This seems to be consistent with the slow-down of the dynamics in the quiescent state and corresponds to the increase of γ_{peak} (Fig. 6a), in agreement with the proposed link between yielding and dynamics in the steady-state.

In addition to the steady-state, the transient state following switch-on of shear is investigated (Fig. 9, thin color lines). At short delay times the transient MSDs moderately increase, associated with a slight expansion of the cage, but they remain below the quiescent MSD indicating tighter localization. At long delay times, and for all waiting times, we observe relatively fast diffusion, already with the steady-state diffusion coefficient D_L^{steady}. While D_L^{steady} is reached already at the shortest waiting time t_w, it is reached at a relatively late delay time t, which becomes increasingly shorter as t_w increases. The steady-state MSDs are recovered after a waiting time t_w^* which depends on the mixing ratio x_s, and has apparently no relation with τ_{shear}, different from one-component systems.[13–15]

At intermediate delay times a super-linear increase of the MSDs is observed which indicates superdiffusion. The time range with superdiffusion progressively disappears as t_w increases, but also depends on $Pe_{\dot\gamma}$ and x_s. The amount of superdiffusion is quantified by $D_L^{steady}/D_L^{sdiff} - 1$ with D_L^{sdiff} the apparent diffusion coefficient at maximum superdiffusion, estimated from the minimum of $\delta y^2/t$ *vs.* t (not shown). With increasing x_s, the amount of superdiffusion, $D_L^{steady}/D_L^{sdiff} - 1$ increases for (almost) constant, large $Pe_{\dot\gamma}$ ($Pe_{\dot\gamma} = 0.24$ for $x_s = 0.1$, 0.3, 0.5 and $Pe_{\dot\gamma} = 0.28$ for $x_s = 0.9$, Fig. 10b orange/red

color). As expected, this does not reflect the dependence of the stress overshoot, $\sigma_{peak}/\sigma_{steady} - 1$ (Fig. 6b), since the large particles, whose dynamics is studied here, dominate the rheological response only for $x_s \lesssim 0.5$ (Section 3.4). However, the increase in $D_L^{steady}/D_L^{sdiff} - 1$ with x_s might reflect the decrease of the localisation length at rest (Fig. 2, inset). This suggests that a tighter localisation at rest leads to a more abrupt and pronounced transition to flow once shear sufficiently deforms the cage to allow particles to escape. The increase of the degree of super-diffusion with increasing x_s seems to become more pronounced with increasing $Pe_{\dot\gamma}$ (Fig. 10b). With increasing $Pe_{\dot\gamma}$, $D_L^{steady}/D_L^{sdiff} - 1$ increases for all x_s and $t_w = 0$ s (Fig. 10b, different colors). The Pe dependence is similar to the one of D_L^{steady} and the magnitude of the stress overshoot, $\sigma_{peak}/\sigma_{steady} - 1$ (Fig. 7b). This is consistent with the idea that $\sigma_{peak}/\sigma_{steady} - 1$ is related to the probability of particle collisions, which occur more frequent as the dynamics becomes faster. Furthermore, it suggests that a larger stored stress results in a more pronounced super-diffusive response, in agreement with similar findings for one-component systems.[15]

At short delay times ($t \lesssim 1$ s, range decreasing with increasing t_w), the MSDs are dominated by caging (Fig. 9). At these times, the transient MSDs under shear remain below the quiescent state, although they slightly increase with waiting time t_w toward the steady-state. Thus, shear results in a stronger localisation of the large particles in the vorticity direction. The magnitude of cage compression in the vorticity direction is quantified by $K = \delta y_{shear}^2/\delta y_{rest}^2 - 1$, where δy_{shear}^2 and δy_{rest}^2 are the value of the MSD under shear and at rest, respectively, at the same time 0.015 s $\leq t \leq$ 0.030 s (Fig. 10c). The magnitude of the cage compression, $|K|$ decreases from $x_s = 0.1$ to 0.3 and 0.5 to 0.9. Increasing x_s from 0.1 to 0.3, and from 0.5 to 0.9, the localization length of the large spheres at rest decreases (Fig. 2a, inset). This implies that the cage is tighter and a smaller free volume is available for compressing the cage, accordingly $|K|$ decreases. However, at $x_s = 0.5$, the cage is strongly compressed although the localisation length at $x_s = 0.5$ is comparable to that at $x_s = 0.3$ in the quiescent state (Fig. 2, inset). Nevertheless, for $x_s = 0.5$ the cage is composed of small spheres which might easier rearrange under shear and closely pack around the large spheres than large spheres can. This supports the suggestion that a qualitative change in caging occurs at $x_s \approx 0.5$.

Moreover, K closely resembles the stress overshoot, $\sigma_{peak}/\sigma_{steady} - 1$ (Fig. 6b), with both exhibiting only a limited dependence on $Pe_{\dot\gamma}$ (within the limited range of $Pe_{\dot\gamma}$ investigated by confocal microscopy). In particular, a large $|K|$ corresponds to a small $\sigma_{peak}/\sigma_{steady} - 1$ and *vice versa*. This suggests that stress is partially released through irreversible cage compression, resulting in a smaller stress overshoot. In contrast, if stress can not sufficiently be released through cage compression, it is stored in the system. This storage of stress requires particle movements beyond the cage size and involves several particles. These large movements are related to the long-time diffusion of the cage particles. Hence the relevant timescale is the dominant long-time structural relaxation time $\tilde\tau^{long}$, consistent with the conclusions based on the x_s dependence of $\sigma_{peak}/\sigma_{steady} - 1$ (Section 3.4). This illustrates the importance of caging and the transition in caging. In contrast, yielding requires many particles to move, although each particle might only move on the length scale of the cage. Moreover, the yield strain γ_{peak} is a relative, dimensionless quantity and hence insensitive to whether the cage is formed by large or small spheres.

4 Conclusions

The addition of a second species to a one-component glass results in the loosening of the cage. The transition between caging by small and large particles, respectively, occurs at $x_s \approx 0.5$.[19,20] The degree of arrest is reflected in the dynamics at rest,[19,20] and, as shown here, also under shear. We have shown that under both conditions, at rest and under shear, the mobility is maximum at $x_s \approx 0.3$ (Fig. 2 and 10a).

The change in caging also affects the shear-induced cage compression in vorticity direction, with the strongest compression at $x_s \approx 0.5$ (Fig. 10c). This is attributed to the high mobility of the small particles at $x_s \approx 0.5$ allowing them to realize their higher packing ability in the mixtures. In addition to this particular behaviour, in general the cage compression decreases upon addition of small spheres, which is attributed to an increasingly tighter cage at rest that leaves space for small cage compressions only (Fig. 2, inset). A tight localisation at rest results in an abrupt and pronounced transition to flow once shear-induced cage deformations allow particles to escape. This transition is characterised by transient superdiffusion (Fig. 9 and 10b).

Yielding appears to require Brownian motion beyond a minimum excursion. When this excursion is reached depends on the composition-averaged dynamics of the samples and the shear rate. Slow glassy dynamics thus results in larger yield strains γ_{peak}, which is found to increase linearly with the shear rate as long as $\dot\gamma \langle \tau^{short} \rangle \gtrsim 1$ (Fig. 7a, inset). For the Brownian motion to be effective, an affine shear deformation with $\gamma_{peak} \gtrsim 10\%$ seems necessary, which limits yielding at small shear rates. We therefore suggest that different processes set a lower limit to the yield strain γ_{peak} at small and large shear rates, respectively.

Since stress is released during cage compression, the magnitude of the stress overshoot is inversely related to the degree of compression and the overshoot linked to super-diffusion. Storage of stress requires rearrangements and particle movements which, in contrast to the processes during yielding, extend significantly beyond the cage and thus occur on the structural relaxation time $\tilde\tau^{long}$ of the caging species, that is the large spheres for $x_s \lesssim 0.5$ and the small spheres for $x_s \gtrsim 0.5$.

In future work, the macroscopic rheological behaviour and the microscopic single-particle dynamics need to be related to the evolution of the microscopic structure during the application of shear, similar to the link established in one-component glasses.[9]

Acknowledgements

We thank A. B. Schofield for the colloidal particles, J. Horbach and P. Chaudhuri for stimulating discussions, and K. J. Mutch for help with the analysis of the experimental data. We acknowledge funding by the Deutsche Forschungsgemeinschaft

through the Research unit FOR1394 (Project P2), which also supported the visit of R.C.-P. to Düsseldorf, and EU funding through the FP7-Infrastructures ESMI (CP&CSA-2010-262348). The Edinburgh work was supported by EPSRC grant EP/J007404/1.

References

1 E.-J. Donth, *The Glass Transition: Relaxation Dynamics in Liquids and Disordered Materials*, Springer-Verlag, Berlin Heidelberg, 2001.
2 C. Suryanarayana and A. Inoue, *Bulk Metallic Glasses*, CRC Press, Taylor and Francis Group, 2011.
3 P. N. Pusey and W. van Megen, *Nature*, 1986, **320**, 340–342.
4 G. Brambilla, D. El Masri, M. Pierno, L. Berthier, L. Cipelletti, G. Petekidis and A. B. Schofield, *Phys. Rev. Lett.*, 2009, **102**, 085703.
5 G. Petekidis, A. Moussaid and P. N. Pusey, *Phys. Rev. E: Stat., Nonlinear, Soft Matter Phys.*, 2002, **66**, 051402.
6 K. N. Pham, G. Petekidis, D. Vlassopoulos, S. U. Egelhaaf, P. N. Pusey and W. C. K. Poon, *Europhys. Lett.*, 2006, **75**, 624–630.
7 K. N. Pham, G. Petekidis, D. Vlassopoulos, S. U. Egelhaaf, W. C. K. Poon and P. N. Pusey, *J. Rheol.*, 2008, **52**, 649.
8 R. Besseling, E. R. Weeks, A. B. Schofield and W. C. K. Poon, *Phys. Rev. Lett.*, 2007, **99**, 028301.
9 N. Koumakis, M. Laurati, S. U. Egelhaaf, J. F. Brady and G. Petekidis, *Phys. Rev. Lett.*, 2012, **108**, 098303.
10 C. Eisenmann, C. Kim, J. Mattsson and D. A. Weitz, *Phys. Rev. Lett.*, 2010, **104**, 035502.
11 M. Siebenbürger, M. Fuchs and M. Ballauff, *Soft Matter*, 2012, **8**, 4014–4024.
12 C. Christopoulou, G. Petekidis, B. Erwin, M. Cloitre and D. Vlassopoulos, *Philos. Trans. R. Soc., A*, 2009, **367**, 5051–5071.
13 K. J. Mutch, M. Laurati, C. P. Amann, M. Fuchs and S. U. Egelhaaf, *Eur. Phys. J.: Spec. Top.*, 2013, **222**, 2803.
14 J. Zausch, J. Horbach, M. Laurati, S. U. Egelhaaf, J. M. Brader, T. Voigtmann and M. Fuchs, *J. Phys.: Condens. Matter*, 2008, **20**, 404210.
15 M. Laurati, K. J. Mutch, N. Koumakis, J. Zausch, C. P. Amann, A. B. Schofield, G. Petekidis, J. F. Brady, J. Horbach, M. Fuchs and S. U. Egelhaaf, *J. Phys.: Condens. Matter*, 2012, **24**, 431207.
16 S. Williams and W. van Megen, *Phys. Rev. E: Stat., Nonlinear, Soft Matter Phys.*, 2001, **64**, 041502.
17 A. Imhof and J. K. G. Dhont, *Phys. Rev. E: Stat. Phys., Plasmas, Fluids, Relat. Interdiscip. Top.*, 1995, **52**, 6344–6357.
18 A. Imhof and J. K. G. Dhont, *Phys. Rev. Lett.*, 1995, **75**, 1662–1665.
19 T. Sentjabrskaja, D. Guu, M. P. Lettinga, S. U. Egelhaaf and M. Laurati, *AIP Conf. Proc.*, 2013, **1518**, 206.
20 T. Sentjabrskaja, R. Babaliari, J. Hendricks, M. Laurati, G. Petekidis and S. U. Egelhaaf, *Soft Matter*, 2013, **9**, 4524–4533.
21 A. Moreno and J. Colmenero, *J. Chem. Phys.*, 2006, **125**, 164507.
22 T. Voigtmann and J. Horbach, *Phys. Rev. Lett.*, 2009, **103**, 205901.
23 E. López-Sánchez, C. D. Estrada-Álvarez, G. Pérez-Ángel, J. M. Méndez-Alcaraz, P. González-Mozuelos and R. Castañeda-Priego, *J. Chem. Phys.*, 2013, **139**, 104908.
24 W. Götze and T. Voigtmann, *Phys. Rev. E: Stat., Nonlinear, Soft Matter Phys.*, 2003, **67**, 021502.
25 T. Voigtmann, *Europhys. Lett.*, 2011, **96**, 36006.
26 J. Bosse and J. S. Thakur, *Phys. Rev. Lett.*, 1987, **59**, 998–1001.
27 J. Bosse and Y. Kaneko, *Phys. Rev. Lett.*, 1995, **74**, 4023–4026.
28 L. Sjögren, *Phys. Rev. A*, 1986, **33**, 1254–1260.
29 R. Seyboldt, D. Hajnal, F. Weysser and M. Fuchs, *Soft Matter*, 2012, **8**, 4132–4140.
30 R. Juárez-Maldonado and M. Medina-Noyola, *Phys. Rev. E: Stat., Nonlinear, Soft Matter Phys.*, 2008, **77**, 051503.
31 S. R. Williams, I. K. Snook and W. van Megen, *Phys. Rev. E: Stat., Nonlinear, Soft Matter Phys.*, 2001, **64**, 021506.
32 G. Foffi, W. Götze, F. Sciortino, P. Tartaglia and T. Voigtmann, *Phys. Rev. Lett.*, 2003, **91**, 085701.
33 B. E. Rodriguez, E. W. Kaler and M. S. Wolfe, *Langmuir*, 1992, **8**, 2382.
34 R. Besseling, L. Isa, E. R. Weeks and W. C. K. Poon, *Adv. Colloid Interface Sci.*, 2009, **146**, 1–17.
35 P. Ballesta, G. Petekidis, L. Isa, W. C. K. Poon and R. Besseling, *J. Rheol.*, 2012, **56**, 1005–1037.
36 J. C. Crocker and D. G. Grier, *J. Colloid Interface Sci.*, 1996, **179**, 298–310.
37 A. Yethiraj and A. van Blaaderen, *Nature*, 2003, **421**, 513–517.
38 C. P. Royall, W. C. K. Poon and E. R. Weeks, *Soft Matter*, 2013, **9**, 17–27.
39 T. G. Mason and D. A. Weitz, *Phys. Rev. Lett.*, 1995, **75**, 2770–2773.
40 T. Sentjabrskaja, M. Laurati, S. U. Egelhaaf and Th. Voigtmann, in preparation.
41 R. Higler, J. Appoel and J. Sprakel, *Soft Matter*, 2013, **9**, 5372.
42 T. Hamanaka and A. Onuki, *Phys. Rev. E: Stat., Nonlinear, Soft Matter Phys.*, 2007, **75**, 041503.
43 P. Yunker, Z. Zhang and A. G. Yodh, *Phys. Rev. Lett.*, 2010, **104**, 015701.
44 W. van Megen, T. C. Mortensen, S. R. Williams and J. Müller, *Phys. Rev. E: Stat. Phys., Plasmas, Fluids, Relat. Interdiscip. Top.*, 1998, **58**, 6073–6085.
45 L. López-Flores, P. Mendoza-Méndez, L. E. Sánchez-Díaz, L. L. Yeomans-Reyna, A. Vizcarra-Rendón, G. Pérez-Ángel, M. Chávez-Páez and M. Medina-Noyola, *Europhys. Lett.*, 2012, **99**, 46001.
46 T. O. E. Skinner, S. K. Schnyder, D. G. A. L. Aarts, J. Horbach and R. P. A. Dullens, *Phys. Rev. Lett.*, 2013, **111**, 128301.
47 R. Besseling, L. Isa, P. Ballesta, G. Petekidis, M. E. Cates and W. C. K. Poon, *Phys. Rev. Lett.*, 2010, **105**, 268301.
48 C. P. Amann, M. Siebenbürger, M. Krüger, F. Weysser, M. Ballauff and M. Fuchs, *J. Rheol.*, 2013, **57**, 149–175.
49 N. Koumakis, M. Laurati, K. J. Mutch, J. F. Brady, S. U. Egelhaaf and G. Petekidis, in preparation.
50 N. Koumakis, J. F. Brady and G. Petekidis, *Phys. Rev. Lett.*, 2013, **110**, 178301.

3.4. Publication 4: Yielding and recovery of binary colloidal glasses

in preparation

Authors: **T. Sentjabrskaja**, J. Hendricks, A. R. Jacob, G. Petekidis, S.U. Egelhaaf and M. Laurati

1st author

The materials are prepered and the experiments are performed by TS ($\delta = 0.207$) and JH, ARJ ($\delta = 0.38$). TS analyzed all data. TS, ML, GP and SUE conceived and discussed the project and are contributed to the writing of the manuscript. ML and SUE supervised the project.

60 % contribution of TS

This page has been left intentionally blank.

Yielding and recovery of binary colloidal glasses

Tatjana Sentjabrskaja,[a] Jan Hendricks,[c] Alan R. Jacob,[b] George Petekidis,[b] Stefan U Egelhaaf,[a] Marco Laurati,[a]

Received Xth XXXXXXXXXX 20XX, Accepted Xth XXXXXXXXX 20XX
First published on the web Xth XXXXXXXXXX 20XX
DOI: 10.1039/b000000x

1 Introduction

The behavior of glasses under application of a mechanical deformation, like shear, is of great interest for many applications in which glass-forming systems need to flow, e.g., to be able to process them. One model system to study this behavior is a colloidal suspension in the glass state. Colloidal glasses are characterized by frozen-in dynamics resulting in a very slow internal relaxation. External driving by application of a shear field leads to a competition between slow internal relaxation and the time scale imposed by shear. Therefore, for small deformations, i.e. in the linear viscoelastic regime, the rheological properties of colloidal glasses are dominated by elasticity and the glass behaves like a solid [1–3]. On the other hand, if the deformation becomes larger, for example due to an increase of the deformation amplitude, viscosity starts to dominate and eventually the system flows [3,4].

For continuous shear, an application of a constant strain rate or a constant stress larger than the yield stress leads to a steady flow. The transition from rest to steady flow is characterized by transient phenomena. In particular, after applying a step rate of deformation, an anisotropy of the microscopic structure develops with increasing the time elapsed after application of shear. The cages become elongated and the maximum cage deformation coincides with the occurrence of a stress overshoot in the macroscopic rheology [5–8]. The breakdown of the cage following cage deformation is associated with superdiffusive dynamics [5–8].

The application of a constant stress also leads to the fluidization of the glassy system if the stress is larger than the yield stress of the system [3,9,10]. For stresses below the yield stress, the system does not flow. Instead a creep regime, characterized by a slow, sublinear increase of the deformation as a function of time, is observed. The study of the microscopic single-particle dynamics during the application of a constant stress indicates a linear relation between the macroscopic strain and the mean squared displacement, which has no analogue in the strain-controlled case. This finding can be related to the fact that under stress-control both the dynamics and the strain are dominated by groups of highly mobile particles and their spatial distribution. The fusion of these highly mobile regions eventually leads to flow [10].

The different relations between strain and microscopic dynamics observed for stress and strain-controlled analogue rheological processes indicate qualitative differences that have to be explored in more detail. In this work we compare therefore the rheological response to stress- and strain-controlled shear of model colloidal glasses both with respect to the steady state and transient regimes. We use binary mixtures with large dynamical asymmetry, where different caging mechanisms are found [11–13]. We study in this way also the influence of a different glass state on the rheological response to applied strain rate or stress. Moreover, glass softening as a function of mixing ratio between small and large spheres was observed in these systems: This phenomenon gives us the possibility to systematically study how much the response in strain and stress controlled experiments differs, depending on how glassy or fluid the system is by simply changing the relative amount of the mixture components.

2 Materials and methods

Sample

Our samples are sterically stabilized polymethylmethacrylate (PMMA) particles [Antl1986]. We used PMMA spheres with different radii: $R_{L1} = 304\,\mathrm{nm}$ (polydispersity 0.10) and $R_{S1} = 63\,\mathrm{nm}$ (polydispersity 0.15) resulting in size ratio $\delta = R_{S1}/R_{L1} = 0.207$. In a second system we used $R_{L2} = 358\,\mathrm{nm}$ (polydispersity 0.14) and $R_{S2} = 137\,\mathrm{nm}$ (polydispersity 0.12) resulting in $\delta = 0.38$. The radii and polydispersities were determined by using static and dynamic light scattering with very dilute samples at $\phi < 10^{-3}$.

[a] *Condensed Matter Physics Laboratory, Heinrich-Heine University, Universitätsstraße 1, 40225 Düsseldorf, Germany. E-mail: tatjana.sentjabrskaja@hhu.de*
[b] *Department of Materials Science and Technology and IESL-FORTH, University of Crete, Hereklion, Greece.*
[c] *Soft Matter, Rheology and Technology Section, University of Leuven, Belgium.*

The particles with $\delta = 0.207$ are suspended in a cis-decalin and cycloheptyl bromide (CHB) mixture which matches the density and the refractive index of the particles. In decalin/CHB solvent colloids acquire charge which was screened by adding salt, namely 4 mM tetrabutylammonium-chloride[14]. The particles with $\delta = 0.38$ are suspended in a mixture of octadecene and bromonaphtalene to minimize the solvent evaporation. In both solvent mixtures the PMMA particles behave like hard-spheres.

The volume fraction of sediments, obtained by centrifuging dilute suspensions, were roughly estimated to be $\phi = 0.67 - 0.68$ depending on the size and corresponding polydispersity. One-component colloids stock solutions with $\phi = 0.61$ were obtained by subsequently diluting sediments until the linear viscoelastic moduli (after subtracting the trivial size dependence of the signal) match the values of a reference sample (as described in Ref. [13]). By mixing the batches of one-component samples we prepared binary mixtures with constant total volume fraction $\phi = 0.61$ and different fractions of small particles $x_s = \phi_s/\phi$ where ϕ_s the volume fraction of small component.

Rheology

SmallSet creep: AR2000ex stress-controlled rheometer from TA instruments, cone and plate geometries of diameter $D = 20$ mm, cone angle $\alpha = 2^\circ$, gap $d = 0.054$ mm and $D = 40$ mm, $\alpha = 0.3^\circ$ and $d = 0.012$ mm.

SmallSet step rate relaxations: ARES G2 strain-controlled rheometer from TA instruments, cone and plate geometries of diameter $D = 25$ mm, cone angle $\alpha = 2^\circ$, gap $d = 0.048$ mm and (a part of relaxations) $D = 50$ mm, cone angle $\alpha = 1.16^\circ$, gap $d = 0.051$ mm.

Rejuvenation procedure was performed before each measurement to reduce an influence of loading, aging and sample history effects and to ensure a reproducible initial state of the sample. For this reason, directly after loading, a Dynamical Strain Sweep was performed, i.e. an application of oscillatory shear to the sample with a frequency $\omega = 1$ rad/s and increasing strain γ from 0.01 % to 700-1000 % (depending on the sample). After that and before each measurement two Dynamical Time Sweeps (DTS) were performed: at first a DTS by a strain γ = 300 % for a waiting time of 100 s to fluidize the sample and then a DTS by very low strain 0.01-0.1 % (depending on the sample) until the elastic, G', and viscous, G'', moduli reached constant steady-state values. A solvent trap was used to minimize solvent evaporation.

3 Flow

In this chapter we are going to discuss the steady-shear flow of colloidal binary mixtures. For this we display the flow curves, where the stress response of the sample is measured as a function of the applied shear rate. The stress σ is measured in the steady-flow state under application of a constant shear rate $\dot{\gamma}$. Flow curves for increasing (continuous line) and decreasing (dashed line) shear rate are measured. In order to account for trivial effects due to the different average size of particles in the samples, the stress is expressed in units of energy density $k_BT/ < R^3 >= k_BT[1 - x_s(1 - 1/\delta^3)]/R_L^3$ and plotted against Peclet number $Pe_{\dot{\gamma}} = \dot{\gamma} < \tau^{short} >$, with $< \tau^{short} >=< \tau_0^{short} > /f$ and $< \tau_0^{short} >= 6\pi\eta < R^3 > /k_BT$ the composition-averaged short-time Brownian time in the dilute limit. The ϕ-dependent factor f is estimated to be $f \approx 1/32$ for volume fraction 0.61 (extrapolate the data in Fig.8 of reference [15]).

Figure 1 shows the flow curves measured for samples with δ=0.207, ϕ = 0.61 and different mixing ratios x_s. For all mixing ratios, $0 \leq x_s \leq 1$, shear-thinning behavior characteristic of colloidal dispersions**?** , indicated by an increase of the stress σ with increasing shear rate $\dot{\gamma}$, was found. For glassy system, in the regime $\dot{\gamma} \to 0$, the stress tends to a constant value, associated to the yield stress of the system**?** . Due to the limited accessible range of $Pe_{\dot{\gamma}}$, the existence of an yield stress at $\dot{\gamma} \to 0$ cannot be clearly determined for the measurements discussed here.

For the one-component systems, $x_s = 0$ and $x_s = 1$, comparable values of stress $\sigma\dot{\gamma}$ in units of energy density are observed. This observation indicates a similar glass state for both. Nevertheless, the flow curves differ in their slopes. For $x_s = 0$, the slope of the flow curve is approximately 1, in contrast to $\sim 0.???$ observed for $x_s = 1$, what may be attributed to a certain degree of softness of the small particles. The slope of $\sigma(Pe_{\dot{\gamma}})$ for $0 < x_s < 1$ shows a smooth transition from 1 at $x_s = 0$ to a smaller value obtained for $x_s = 1$. In previous studies of colloidal glasses [16,17] it was shown that for hard spheres at large $Pe_{\dot{\gamma}}$ the stress is linearly proportional to $\dot{\gamma}$ while for soft spheres the slope of the stress tends to 0.5, i.e $\sigma \sim \dot{\gamma}^{0.5}$, supporting the suggestion of a certain degree of softness for the small particles.

Adding small spheres to a glass of large particles, i.e. increasing x_s, leads to a rapid decrease of the stress, which reaches its minimum at $x_s = 0.3$ at any $Pe_{\dot{\gamma}}$. By further increasing x_s, for $0.3 < x_s < 1$, the stress at certain $Pe_{\dot{\gamma}}$ increases again approaching the stress value of the one-component system with $x_s = 1$. This behavior of the stress as a function of x_s at a constant $Pe_{\dot{\gamma}}$ indicates the softening and re-vitrification of the system for intermediate x_s. The presence of a minimum of σ for $x_s = 0.3$ at certain $Pe_{\dot{\gamma}}$ and the glass softening observed for intermediate x_s qualitatively agrees with previous experimental results [18], including DSS tests [13] and step-rate experiments [12], and theoretical work [19,20].

For comparison, $\sigma(\dot{\gamma})$ is also extracted from a series of step-rate experiments, where a constant shear rate is applied and the

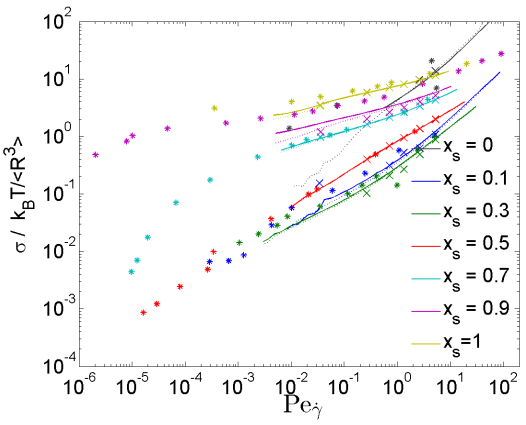

Fig. 1 Flow curves, i.e. stress σ in units of energy density as a function of Peclet number. Continuous lines: measured from small to large $\dot{\gamma}$; dashed lines: measured from large to small $\dot{\gamma}$; cross: extracted from step rates experiments; asterisk: extracted from step stress (creep) experiments.

stress σ as a function of strain γ is measured. The steady-flow state is reached at large γ, where the stress σ_{steady} is extracted. Note that in the step-rate experiment the initial state of the sample is the quiescent state obtained after rejuvenation. This is different from the measurement of the flow curve, where the initial state of the sample is the steady-flow state reached by the application of the previous $\dot{\gamma}$. However, both protocols result in comparable $\sigma(\dot{\gamma})$ as it is shown in Figure 1. The values of shear stress σ_{steady} extracted from step-rate experiments (cross) are in a good agreement with those from flow curves (line).

One other way to measure the relation $\sigma(\dot{\gamma})$ is a series of creep experiments, where a constant stress σ is applied to the sample and the shear rate $\dot{\gamma}$ (or the strain γ) is measured as a function of time t (Fig.2b). For stress above the yield stress, $\sigma > \sigma_y$, the shear rate $\dot{\gamma}$ reaches a steady value $\dot{\gamma}_{const}$ after a transient regime at intermediate times. The values $\dot{\gamma}_{const}(\sigma)$ lie typically on the flow curve or slightly above, indicating a good agreement between results obtained with different shear protocols (Fig.1). In the creep regime, $\sigma \lesssim \sigma_y$, the shear rate slowly decreases all the time and does not reach a constant value. In this regime, the steady-flow state cannot be reached. In this case, $\dot{\gamma}_{const}$ is defined as the last measured point. The points collected in this regime deviate from the expected evolution of the flow curve for $\dot{\gamma} \to 0$. The deviation becomes pronounced for the mixture with $x_s = 0.7$.

In summary, these results show that both routes followed by the system, the strain- and stress-controlled shear for $\sigma > \sigma_y$, result in a comparable steady-flow state of the system. It holds for one-component systems as well as for binary mixtures, independent on the mixing composition x_s.

4 Creep

In creep experiments a constant shear stress σ is applied to the system and the induced deformation γ or deformation rate $\dot{\gamma}$ is recorded as a function of time t. For a material characterized by a yield stress σ_y, at least two regimes can be distinguished on the basis of the applied stress: for $\sigma < \sigma_y$, the material presents a solid-like response and usually creep is observed; second, for $\sigma > \sigma_y$ a flow response is observed. For $\sigma \approx \sigma_y$ an intermediate response is found. These regimes are observed in our measurements.

Figure 2 a) shows some of the results obtained for the one-component glass of small spheres with radius R_{S1} and volume fraction $\phi \approx 0.61$. At short times, the initial super-linear increase of strain $\gamma(t)$ is followed by oscillations which are an effect of instrument inertia[21,22] and will not be discussed further. After this initial stage, for small applied stress $\sigma < \sigma_y$, a creep response is observed. This creep response is characterized by a slow, sub-linear increase of strain with time. The sub-linear increase can be separated in two additional regimes: one at intermediate times (immediately after the regime affected by instrument inertia) showing a very slow, nearly plateau-like increase of $\gamma(t)$, and one at long times, where the increase of strain becomes faster, but still remains sub-linear. Recently it was shown that these two regimes are characteristics of creep in colloidal glasses[9,21] and colloidal gels[23]. For considerably larger applied stress, $\sigma > \sigma_y$, the system flows and the linear dependence of strain on time is observed. For stress $\sigma \approx \sigma_y$, an intermediate behavior is found. The creep-like response at intermediate times is followed by a rapid, super-linear increase of $\gamma(t)$ observed over a restricted time interval, before finally the flow regime is entered. For one-component glasses it has been shown that the super-linear increase of $\gamma(t)$, like the stress overshoot observed in step-rate experiments, originates at the structural breakdown of the cage[9,10].

The strain response of mixtures at similar applied stresses σ in units of energy density $\langle R^3 \rangle / k_B T$, as is shown in Figure 3. Different scenarios depending on the mixing composition x_s are observed. One-component glasses show a creep-like response, what indicates that the selected value of the applied stress lies below the yield stress of these systems. In contrast to that, a fluid-like response was found for mixtures with intermediate x_s. An intermediate behavior, where a transition from creep to flow is observed, was found for the mixture with $x_s = 0.7$ and size ratio $\delta \approx 0.207$. Therefore, for mixtures with intermediate x_s, the applied stresses are larger (or comparable for $\delta = 0.207$ $x_s = 0.7$) to their yield stresses. The different responses observed for binary mixtures in creep measurements at similar applied stress $\sigma \langle R^3 \rangle / k_B T$, show the effect of softening induced by mixing. The result is in agreement with the previous study of binary mixtures[11,12], where it was shown

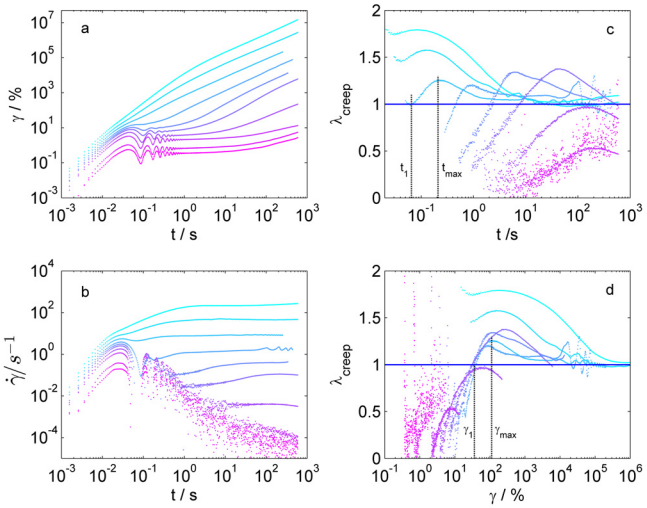

Fig. 2 (a) Strain γ and (b) shear rate $\dot{\gamma}$ as a function of time t, measured in step stress (creep) tests performed on samples with ϕ = 0.61 and radius R_{S1} (for applied stress σ = 10 Pa, 15 Pa, 35 Pa, 50 Pa, 65 Pa, 80 Pa, 100 Pa, 140 Pa, 200 Pa, 300 Pa from bottom to top). (c) Logarithmic time derivative of the strain $\lambda_{creep}(t) = d\log(\gamma)/d\log(t)$ which corresponds to the exponent of the time dependence of strain γ on time t and can be used to distinguish regimes of linear, sub and super-linear dependence. The time t_{max} is defined at the maximum of λ_{creep}. The time t_1 is the time where $\lambda_{creep} = 0$, i.e. where transition from sub- to super-linear regime happens. (d) Logarithmic time derivative of the strain λ_{creep} as a function of strain γ. γ_1 indicate the value of strain where $\lambda_{creep} = 1$ and γ_{max} is the value of strain at maximum of λ_{creep}.

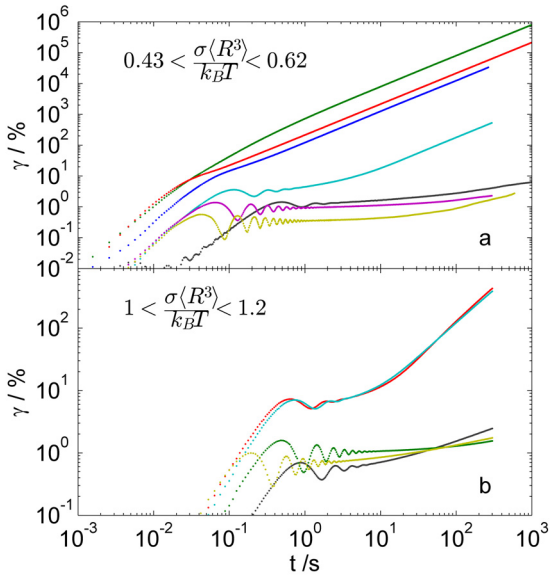

Fig. 3 Strain γ as a function of time t, measured in creep tests performed on samples with ϕ = 0.61 and a) δ = 0.207 and composition x_s = 0 (black), 0.1 (blue), 0.3 (green), 0.5 (red), 0.7 (turquoise), 0.9 (purple), 1 (yellow) and b) δ = 0.38 at x_s = 0 (black), 0.25 (green), 0.5 (red), 0.75 (turquoise), 1 (yellow) at similar applied stress $\sigma\langle R^3\rangle/k_BT$.

that the addition of a second component leads to glass softening, i.e. the reduction of the yield stress. The pronounced effect of glass softening occurs in mixtures with small size ratios $\delta \approx 0.2$, and is not symmetric with respect to the mixing composition. The strongest softening effect is observed at $x_s \approx 0.3$[11,12].

The evolution of $\gamma(t)$ measured at one constant applied stress σ may show different regimes as it was already discussed. To quantify the transition between these regimes, the logarithmic derivative λ_{creep} of strain γ with respect to time t, i.e. $\lambda_{creep}(t) = d\log(\gamma)/d\log(t)$, is calculated. Figures 2 c), d) show λ_{creep} for the one-component glass of small spheres as a function of t or γ, respectively. The initial regime due to instrument inertia is characterized by a fast decrease from an initial exponent λ_{creep} = 2 and a regime of oscillations. After that, for $\sigma \approx \sigma_y$, the value of λ_{creep} starts to increase from a value < 1 and presents a peak value larger than 1 before tending finally to this value, which characterizes flow. The deviations from this behavior are observed for $\sigma \approx \sigma_y$, where the peak value is smaller than 1, and for $\sigma \gg \sigma_y$, where no maximum is observed.

The transition between different regimes is analyzed more closely. We extract the time t_{max} at the maximum of λ_{creep} (see Figure 4 a)). This represents the time at which the deformation increases most sharply. For all studied mixtures we found a decrease of t_{max} with increasing applied stress σ. Approaching the yield stress σ_y from higher values of σ, the transition between creep and flow tends to move to increasingly longer times. This suggests the presence of a divergent timescale in the transition, where eventually the sub-linear increase will continue indefinitely. The same phenomenon has already been observed for one-component hard-sphere glasses[9] and colloidal gels[23,24].

From the logarithmic time derivative of the strain, λ_{creep}, we also extract the strain $\gamma_{max} = \dot{\gamma}t_{max}$ and the strain γ_1, where $\lambda_{creep} = 1$. The parameters, γ_{max} and γ_1, are shown in Figure 4 b) and c), respectively. The strain γ_{max} increases continuous by increasing σ. Moreover, we find a scaling $\gamma_{max} \sim \sigma^{\alpha}$, with $\alpha = 0.3$, independent of the composition x_s and size ratio δ. A similar dependence is found in the evolution of $\gamma_1(\sigma)$. The strain γ_1 indicates the transition from the creep regime (characterized by $\lambda_{creep} < 1$) to the super-linear regime (with $\lambda_{creep} > 1$). The evolutions of γ_1 and γ_{max} showing the slow increasing of shear strain with increasing stress, can be

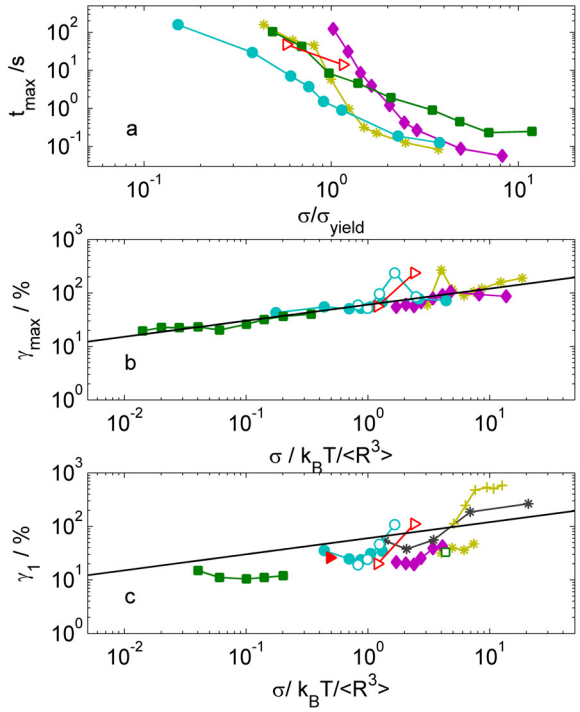

Fig. 4 a) Time t_{max} where λ_{creep} is maximal as a function of reduced stress σ/σ_{yield} for samples with $\delta = 0.207$ and composition $x_s = 0$ (∗), 0.1 (◀), 0.3 (■), 0.7 (●), 0.9 (♦), 1 (∗) and $\delta = 0.38$ at x_s = 0.5 (▷), 0.75 (○). b) Strain γ_{max} where λ_{creep} is maximal as a function of applied stress in units of energy density and fit $\gamma_{max} \sim \sigma^{\alpha}$ with $\alpha = 0.3$. c) Strain γ_1 where λ_{creep} crosses 1 by transition from creep to super-linear regime.

compared to the dependence of γ on shear rate $\dot{\gamma}$, discussed in Ref.[12]. The behavior can be understood within the cage picture: the increase of σ induces more affine displacements of particles and reduces the probability of collisions between particles associated with Brownian motion. Consequently, increasing σ the cage can be deformed more before it breaks. We suppose to see an intermediate behavior between two extremes: a regime of $\sigma \to 0$ dominated by Brownian motion and a regime of $\sigma \to \infty$, where the particle dynamics is controlled by the affine motion imposed by the shear.

5 Step-rate experiment

In a step-rate experiment the evolution of stress σ is measured as a function of strain γ (or time t) under application of shear at constant shear rate $\dot{\gamma}$. Typically, $\sigma(\gamma)$ shows an initial linear increase, followed by a maximum of the stress, i.e. a stress overshoot, and finally a regime of constant stress corresponding to the steady state flow, as it is shown in Figure

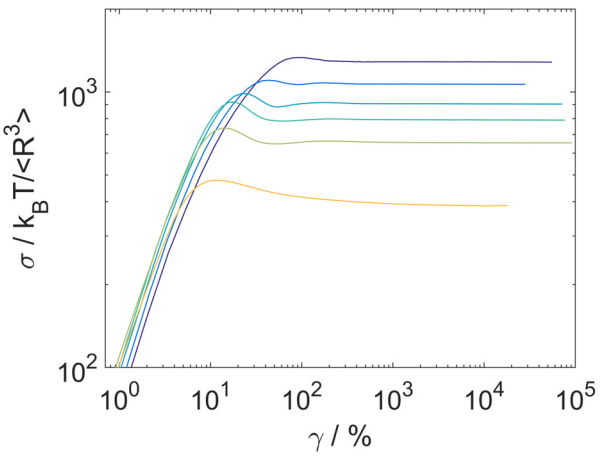

Fig. 5 a) Stress σ as a function of strain γ and b) derivative of the stress $\lambda_{StepRate} = dlog(\sigma)/dlog(\gamma)$ as a function of strain γ, measured in step rate experiment for applied shear rates which correspond to $Pe_{\dot{\gamma}}$ = 4.7, 2.4, 1.2, 0.64, 0.24 and 0.032 (from top to bottom) for composition $x_s = 1$.

5 a). For colloidal glasses the appearance of a stress overshoot was observed and studied earlier. It was found that the stress overshoot is related to the maximum cage deformation before the cage breaks[6,8]. Moreover, the singe-particle dynamics under shear reveal a transient super-diffusive regime of the particle motions at deformations which are comparable to those at which the stress overshoot is observed[5,7,8].

Introducing the small particles into the large-sphere glass leads, similar to results of other tests described before, to softening, which is more pronounced at intermediate mixing ratios and large size disparity[11,13]. Moreover, for the size ratio $\delta \approx 0.2$, two different caging mechanisms depending on the mixing composition x_s are found[12]. It was shown that for $0.5 \leq x_s < 1$ the localization of the large particles occurs due to caging by the neighboring large particles. In contrast to that, for $0.1 \lesssim x_s \leq 0.5$, large spheres are surrounded by the small ones and become localised in small-particle cages. Two different caging mechanisms result in a non-trivial dependence of the magnitude of the stress overshoot on x_s as discussed in Ref.[12]. Increasing the size ratio up to $\delta \approx 0.38$ leads to a reduction of the softening effect[?].

We study binary mixtures with size ratios $\delta \approx 0.38$ and $\delta \approx 0.207$. Figure 6 shows $\sigma(\gamma)$ measured for mixtures with different compositions, under a constant $\dot{\gamma}$, which results in the similar Peclet number for all mixtures. The stress σ is represented in units of the energy density $k_BT/\langle R^3 \rangle$. The representation highlights the similarity of the response to shear observed for one-component systems (Fig. 6 b)). For binary mixtures with $\delta \approx 0.207$, a pronounced reduction of the

steady-state stress σ_{steady} is observed at intermediate mixing ratios. For mixtures with $\delta = 0.38$ the reduction is less pronounced. The reduction of σ_{steady} follows very closely the variation of the yield stress measured by Dynamical Strain Sweep (DSS)[13] and the softening effect described before.

The strain at the overshoot, γ_{peak}, and the magnitude of the overshoot, $\sigma_{peak}/\sigma_{steady} - 1$, are extracted from the measurements and are shown in Figure 6 as functions of Peclet number $Pe_{\dot{\gamma}}$. For both δ, the strain at the overshoot γ_{peak} remains almost constant for Peclet number, $Pe_{\dot{\gamma}} < 1$, independent on the composition x_s. In this Peclet number range the influence of the affine motion is week and the shear-induced cage deformation is slow. Therefore the escape from cages in mainly due to Brownian motion. Consequently, in this regime the dependence of γ_{peak}, associated to the yield strain, shows only a weak dependence on the shear rate. For $\delta = 0.207$ we also observed that γ_{peak} remains constant for $Pe_{\dot{\gamma}} \lesssim 1$ and increases by larger $Pe_{\dot{\gamma}}$ where the particle displacements are dominated by affine motions[12]. Moreover for $\delta = 0.207$ it was found that the magnitude of the stress overshoot, associated to the stored stress, exhibits a minimum at $x_s = 0.5$ due to the transition in caging mechanism, namely caging by large or small particles. At $\delta = 0.38$, instead the magnitude of the overshoot is similar for all mixtures (Fig.6 b)) since only one caging mechanism is observed. This observation supports the idea that the stress storage occurs on the long-time structural relaxation time of the caging species and the absence of the sharp caging transition results consequently in a monotonic decrease of stored stress with x_s.

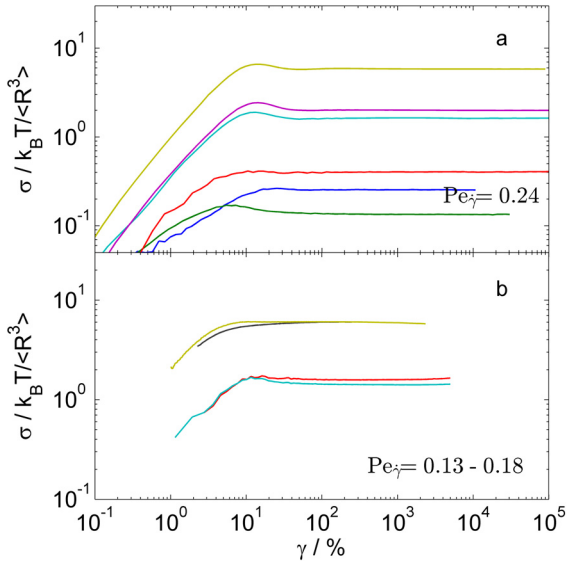

Fig. 6 Stress σ as a function of strain γ, measured in step rate experiment for applied shear rates which correspond to a) $Pe_{\dot{\gamma}} = 0.24$ for samples with $\delta = 0.207$ and composition 0.1 (blue), 0.3 (green), 0.5 (red), 0.7 (turquoise), 0.9 (purple), 1 (yellow) and b) $Pe_{\dot{\gamma}} \approx 0.25$ for samples with $\delta = 0.38$ and composition $x_s = 0$ (black), 0.5 (red), 0.75 (turquoise), 1 (yellow).

6 Comparison

In previous sections we discussed two different shear experiments: the application of constant strain or stress. It was shown that they both lead to a comparable steady-flow state, but the way to reach this state, particularly the yielding process, may be different. To investigate this transient regime, we compare the creep results to the results obtained in step-rate experiments.

Figure 8 compares two creep and two step-rate measurements for one sample. In the creep experiment, the steady flow is characterized by a linear increase of the strain with time, i.e. a regime of constant shear rate. In the step-rate experiments we selected similar applied shear rates. After the stress overshoot, the system starts to flow and the stress decays to its steady-state value. It can be seen that both shear protocols lead to the fluidization of the glass and steady flow. The results of the two tests can be directly compared by plotting the product $\sigma\dot{\gamma}$ versus time t (see Figure 8 c)). This plot evidences that the steady state of flow is the same for step rate and creep experiment.

It also reveals a second interesting point, associated to the question whether the dynamics, by which the final steady-state flow is achieved, depend on the way shear is applied. When we compare the results from strain-controlled and creep experiments it is clearly visible that steady flow is achieved earlier in time in the strain-controlled experiment. This is particularly well visible for the parameter $\sigma = 30\,\text{Pa} = ???\sigma_y$ and $\dot{\gamma} = 10.17s^{-1}$. The transient regimes prior to the onset of steady flow seems to be very different for step-rate and creep experiments in particular at large σ, $\dot{\gamma}$. The evolution of $\sigma\dot{\gamma}$ obtained from creep experiment (yellow line in Fig. 8 c)) resembles the stress overshoot measured in the step-rate experiment at $\dot{\gamma} = 2.034s^{-1}$, while it is very different for $\sigma = 30\,\text{Pa}$ and $\dot{\gamma} = 10.17s^{-1}$.

The difference between these two experiments is supported by the observation of the microscopic single-particle dynamics during the shear. In previous works[10] the dynamics of particles under strain-controlled shear was studied. For glassy systems it was shown that the transition to flow goes along with the super-diffusive dynamics of particles. The super-diffusivity was also found in the dynamics observed under an application of a constant stress[10]. For constant shear rate this also implies that the relation between MSD and γ shows a super-linear regime. On the other hand, it was found that for applied constant stress, a linear relation between MSD and γ

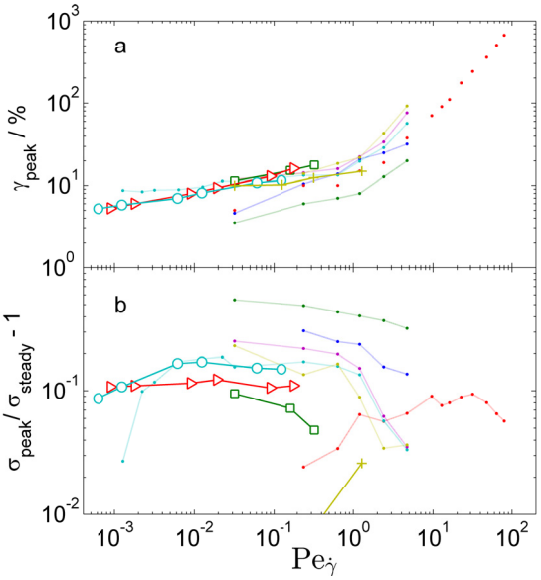

Fig. 7 a) Strain at the stress overshoot, γ_{reak}, and b) magnitude of the stress overshoot, $\sigma_{peak}/\sigma_{steady} - 1$, as a function of Peclet number for size ratio $\delta = 0.38$ and compositions $x_s = 0.25$ (□), 0.5 (▷), 0.75 (○), 1 (+) and for $\delta = 0.207$ and different x_s (points SoftMatter).

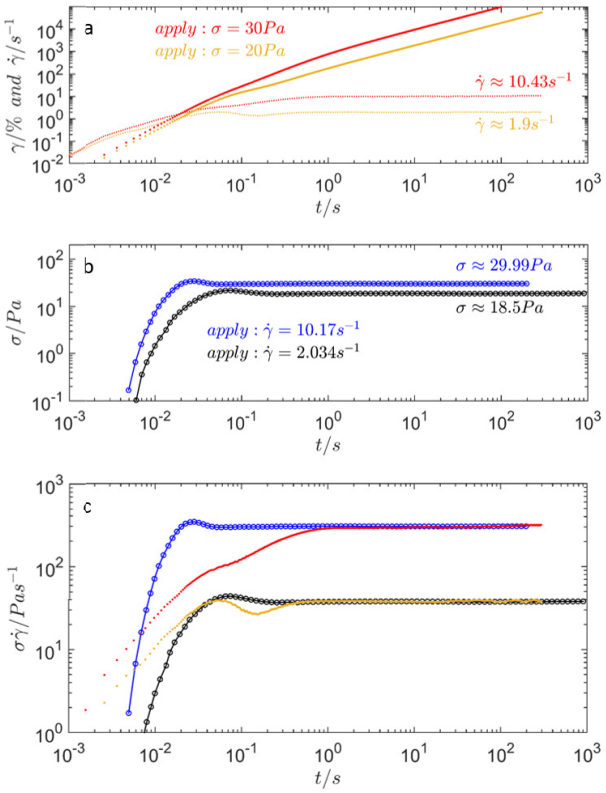

Fig. 8 a) The evolution of the strain $\gamma(t)$ (solid line) and the corresponding shear rate $\dot\gamma(t)$ (dotted line) measured in creep experiment for applied stress $\sigma = 20$ Pa and 30 Pa and b) the evolution of the stress $\sigma(t)$ obtained by applying the shear with shear rate $\dot\gamma = 2.034\,s^{-1}$ and $10.17\,s^{-1}$ on binary mixture with $\delta = 0.207$, $\phi = 0.61$ and $x_s = 0.7$. c) The curves from a) and b) plotted as $\sigma\dot\gamma(t)$.

holds also in the transient super-diffusive regime of the MSD (and even in creep regime). This could explain the faster dynamics leading to flow at constant shear rate. In addition, the presence of strong dynamical heterogeneities observed in stress-controlled experiments has no clear analogy in strain-controlled case.

7 Recovery

After stress removal in a creep experiment, the system relaxes and the recovered strain $\gamma_r = \gamma(t_0) - \gamma(t)$ is measured over time t, as it is shown in Figure 9. At small times the signal is affected by oscillations due to the instrument inertia and was excluded from the analysis []. Depending on the state of the sample at the end of the creep test priors the recovery measurement, two different scenarios of strain recovery are observed. For large stress, $\sigma > \sigma_y$, where at the end of the creep test the fluidization of the glass is observed, the initial oscillations are followed by an increase of the recovered strain γ_r which approaches a constant steady-state value γ_r^{tot} at large times. In contrast to that, for small stress, $\sigma \lesssim \sigma_y$, where the system recovers after creeping, the recovery is poor and the recovered strain increases for all times without approaching a plateau. In this regime, the shape of $\gamma_r(t)$ is concave, in contrast to the convex shape observed for large stresses.

The two regimes of strain recovery are observed in the systems of binary mixtures with different composition x_s as well (see Figure 10). As it was discussed early, the similar value of the stress $\sigma\langle R^3\rangle/k_BT$ applied on mixtures with different compositions results in flow or creep behavior, depending on the softness of the mixture, i.e. their yield stress. As expected, for soft mixtures where the shear-induced flow is observed at the end of the creep measurement, a pronounced stain recovery is found. Differently to that, creeping behavior observed for the one-component glasses and some of the mixtures (with $x_s = 0.9$ at $\delta \approx 0.207$ and $x_s = 0.25$ at $\delta \approx 0.38$), is followed by a poor strain recovery.

The results show that the state of the sample when the shear is removed determines the time-dependence and magnitude of the strain recovery. To quantify this observation we determine the total recovered strain γ_r^{tot} and its dependence on

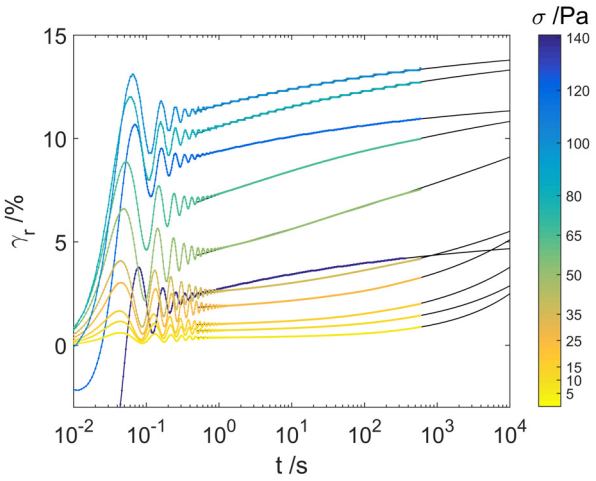

Fig. 9 Recovered strain γ_r after creep experiment at applied shear stress σ as indicated for samples with $\phi = 0.61$ and radius R_{S1}. Black lines are fits with $\gamma_r \sim t^b$.

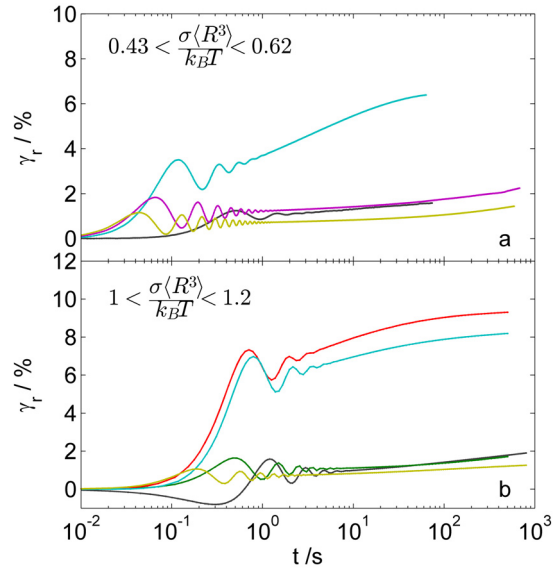

Fig. 10 Recovered strain γ_r after creep experiment for samples with a) $\delta = 0.207$ and composition $x_s = 0$ (black), 0.7 (turquoise), 0.9 (purple), 1 (yellow) and b) $\delta = 0.38$ and $x_s = 0$ (black), 0.25 (green), 0.5 (red), 0.75 (turquoise), 1 (yellow) at similar shear stresses σ in units of energy density $\langle R^3 \rangle / k_B T$ applied before in the corresponding creep text.

the stress σ. To determine γ_r^{tot}, we consider the temporal derivative $\lambda_{recov} = d\gamma_r/dt$ and determine γ_r^{tot} for low value of $\lambda_{recov} = 10^{-3}$. Figure 11 a) shows the evolution of γ_r^{tot} as a function of stress σ/σ_y, i.e. the stress σ applied in the previous creep experiment normalized by the yield stress σ_y of the respective mixture. The yield stress is determined at the cross point of the shear moduli G' and G'' measured in Dynamical Strain Sweep (DSS) experiment at angular frequency $\omega = 1$ rad/s [13]. For one-component glasses and glassy mixtures, the total recovered strain shows a strong dependence on stress. Typically γ_r^{tot} increases with increasing σ, reaches a maximum at the stress close to the yield stress to decay than to a constant value of 7-10%. For soft glasses (for example $\delta = 0.207$ and $x_s = 0.3$) γ_r^{tot} presents small values for all measured stresses and no maxima is observed.

As it was already mentioned, the shape of $\gamma_r(t)$ changes from concave, observed for recovery after creeping, to convex, if the sample flows. The transition from concave to convex is additionally studied here. For this, the recovered strain γ_r as a function of time t is characterized by a power law dependence $\gamma_r \sim t^b$, where b is a fit parameter. For $\sigma < \sigma_y$, the exponent b is typically positive and represents the concave shape (see Figure 11 b)). Increasing σ and leaving the creep regime is followed by a decrease of b to negative values, indicating the convexity of $\gamma_r(t)$. The changing from convex to concave nature of recovered strain occur at stress below the yield stress σ_y.

In a perfectly elastic solid, the elastic restoring force, i.e. $\sigma(t)$, is proportional to the deformation $\gamma(t)$ and causes a continuing acceleration. This leads to a continuing increase of the 'velocity' (recovered strain rate?) $\dot{\gamma}_r$ and an increasingly faster reduction of the deformation $\gamma(t) = \gamma(t_0) - \gamma_r(t)$ or increasingly faster increase of the recovered strain $\gamma_r(t)$. This implies a concave shape of $\gamma_r(t)$. In the ideal case, this corresponds to the motion of an extended and recoiling harmonic spring with $\gamma(t) = \gamma(t_0)\cos(\omega t)$. The concave shape remains for weak friction, although with a decreasing amplitude. However, beyond the yield stress, we do not expect an elastic restoring force and hence no proportionality between $\sigma(t)$ and $\gamma(t)$, and, in addition, we expect friction or dissipation and rearrangements to play a significant role. As a result, there is no continuing force and hence no continuing acceleration. Thus, the 'velocity' $\dot{\gamma}_r$ does not increase during recovery. This leads to the convex shape of $\gamma_r(t)$.

8 Stress relaxation

The stress relaxation is measured after cessation of shear with a constant rate $\dot{\gamma}$ starting from a well-defined steady-flow state. The relaxed stress $\sigma_{relax} = \sigma/\sigma_{plateau}$ is measured as a function of time. The stress $\sigma_{plateau}$ is the corresponding steady-state value of stress for applied rate $\dot{\gamma}$. Figure 12 shows the

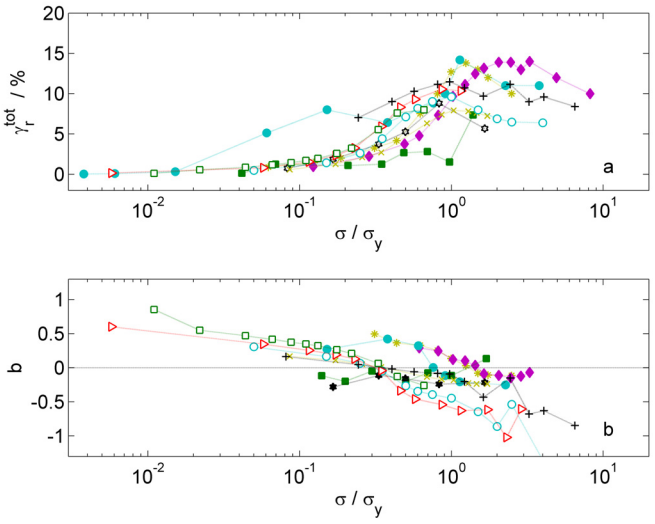

Fig. 11 a) Total recovered strain γ_r^{tot} after creep experiment created at different shear stresses σ for samples with $\delta = 0.207$ and composition $x_s = 0$ ($\star$), 0.3 ($\blacksquare$), 0.7 ($\bullet$), 0.9 ($\blacklozenge$), 1 ($*$) and $\delta = 0.38$ at $x_s = 0$ ($+$), 0.25 ($\square$), 0.5 ($\triangleright$), 0.75 ($\circ$), 1 ($\times$). b) Exponent b extracted from fits of the recovered strain vs time with $\gamma_r \sim t^b$.

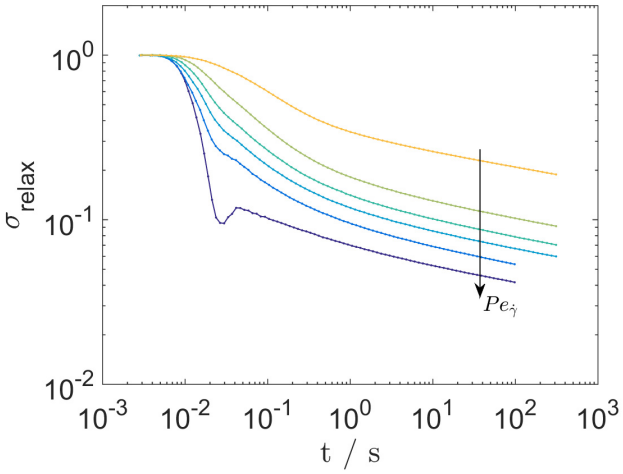

Fig. 12 Relaxed stress $\sigma_{relax} = \sigma/\sigma_{plateau}$ as a function of time t after cessation of shear with Peclet numbers $Pe_{\dot\gamma} = 0.03$, 0.24, 0.64, 1.20, 2.40 and 4.70 (from top to bottom) for one-component glass with $\phi = 0.61$ and particle radius R_{S1}.

transient decay of $\sigma_{relax}(t)$ measured after cessation of shear for various shear rates. Like recovered strain after creep experiments, the relaxed stress at short times is affected by inertia. At high Peclet number $Pe_{\dot\gamma} \sim \dot\gamma$, the oscillations due to the inertia are followed by a fast decay of the relaxed stress. In contrast to that, a slowing rate of decay is observed as $Pe_{\dot\gamma}$ decreases. This observation shows that the stress relaxation is more effective if the preshear leads to a strong fluidization. This can be understood in terms of stronger structural distortions at larger shear rates[6].

At large times, σ_{relax} approaches a constant value, i.e. a finite persistent residual stress. Decreasing the shear rate goes along with an increase of the finite persistent residual stress. The results show that a less pronounced restructuring of the sample leads to an incomplete stress relaxation and a larger residual stress. The results are consistent with previous work, where the partial stress relaxation in colloidal glasses was studied by experiments, simulations and theory[25]. Moreover, it was shown that for small shear rates, $\dot\gamma \to 0$, the finite persistent residual stress approaches the yield stress of the system.

The stress relaxation for binary mixtures with different size ratios δ and mixing compositions x_s is studied. Some of the results are shown in Figure 13. The σ_{relax} is shown as a function of $\dot\gamma$ and is measured for binary mixtures at size ratio $\delta =$ 0.207 and 0.38 at similar Peclet numbers. The glass softening, with the pronounced reduction of the yield stress for mixtures with intermediate compositions x_s and low size ratio

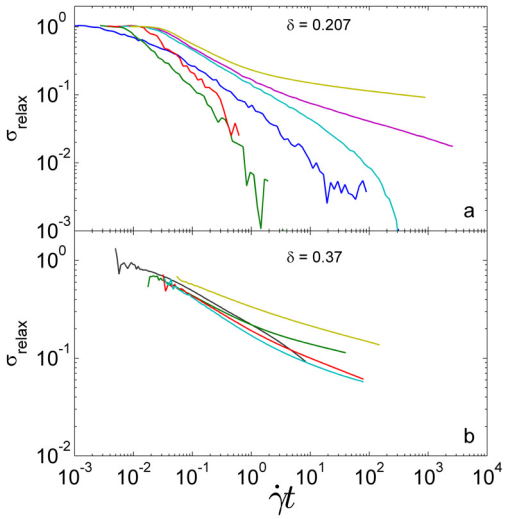

Fig. 13 Relaxed stress σ_{relax} as a function of $\dot\gamma t$ measured after cessation of shear with Peclet number a) $Pe_{\dot\gamma} = 0.24$ for samples with $\delta = 0.207$, $\phi = 0.61$ and composition $x_s = 0.1$ (blue), 0.3 (green), 0.5 (red), 0.7 (turquoise), 0.9 (purple), 1 (yellow) and b) $Pe_{\dot\gamma} \approx$ 0.13-0.18 for samples with $\delta = 0.38$, $\phi = 0.61$ and composition $x_s =$ 0 (black), 0.25 (green), 0.5 (red), 0.75 (turquoise), 1 (yellow).

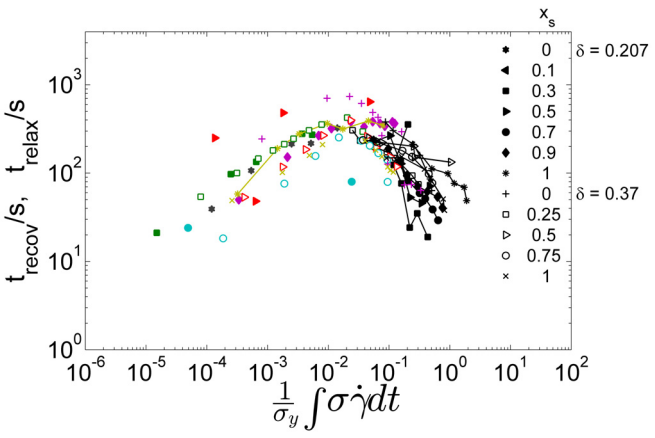

Fig. 14 Relaxation time t_{relax} (black symbols) and recovery time t_{recov} (color symbols) as a function of energy $\int \sigma\dot{\gamma}dt$ normalized by yield stress σ_y for mixtures at the volume fraction $\phi = 0.61$ and with different compositions x_s and size ratios δ as indicated.

$\delta \sim 0.2$, affects the stress relaxation. For the soft mixtures with $\delta = 0.207$ and $0.1 \lesssim x_s \lesssim 0.7$, the stress relaxes almost completely indicating small values of the yield stress. It is different for the one-component system with $x_s = 1$ and the binary mixture with $x_s = 0.9$, where σ_{relax} decays to a finite value reflecting the glass nature of the systems. Similar glass-like relaxation is observed for the mixtures with $\delta = 0.38$ for all mixing compositions $0 \leq x_s \leq 1$, in agreement with the weak softening effect observed in this case.

9 Comparison

In the first part of the paper we have shown that the strain-controlled shear as well as the stress-controlled shear (for $\sigma > \sigma_y$) result in a similar steady-flow state. An open question is, to what extent the strain recovery is similar to the stress relaxation, if both processes are started from the same steady-flow state.

To answer this question, we consider the relaxation time t_{relax}, where the temporal derivative $\lambda_{relax} = d\sigma_{relax}/dt$ reaches a low value, and the recovery time t_{recov} where the strain reaches the value γ_r^{ot}. The results are shown in Figure 14. Both times, t_{relax} and t_{recov}, are plotted as a function of energy $\int \sigma\dot{\gamma}dt$ normalized by the yield stress σ_y of the respective mixture. The black symbols correspond to the time t_{relax}, obtained in the stress relaxation experiments. It is clear, that an increase of the preshear rate leads to a faster stress relaxation, as indicated by the decreasing t_{relax} with $\dot{\gamma}$. The behavior is observed for all mixtures, independent on the size ratio or the mixing composition.

Two regimes are observed in the evolution of recovery time t_{recov} (color symbols),obtained in the strain recovery experiments. The first regime of t_{recov} is to find at large stresses, $\sigma < \sigma_y$, where t_{recov} decreases with increasing $\frac{1}{\sigma_y}\int \sigma\dot{\gamma}dt$. Moreover, for $\frac{1}{\sigma_y}\int \sigma\dot{\gamma}dt > 10^{-2}$, the overlap of the results for both times, t_{recov} and t_{relax} is observed. This reflects the similarity of the stress relaxation and the strain recovery processes. An additional regime is found for small stresses, $\sigma < \sigma_y$, where the sample recovers after creeping. This second regime is related to an increase of recovery time with increasing stress, and is not observed in the evolution of t_{relax} due to the absence of the creeping-like behavior.

The results of t_{recov} for small stresses may be compared with the relaxation time measured after cessation of shear before the steady-flow state occurs and where the structural deformations are still (partially) reversible. For this, in a future work, the preshear at constant rate should be switched off before the stress overshoot appears.

10 Conclusion

In this work we compared the rheological response of glasses characterized by different caging mechanisms to the application of stress-controlled or strain-controlled shear. We found that the transient regime previous to steady flow, particularly the yielding process, is different for the two protocols: The strain-controlled protocol is more efficient in the sense that the steady state of flow is reached more rapidly. Moreover, while the yield strain determined in strain-controlled step rate experiments is strongly dependent on the caging mechanism, and therefore the cage size, as also found in previous studies [11–13], the same quantities under stress control show no clear correlation. This might be due to the spreading of the yielding process under stress control, with a cage deformation which, possibly, is intermittent instead of continuous, as in the case of a constant strain rate. Despite the different yielding processes, both kinds of shear lead to a steady-flow state (for $\sigma > \sigma_y$ in the stress-controlled case) which is comparable for both protocols.

Given the same flowing state, the relaxation of the stress or strain from a step rate or step stress experiment is found to be comparable in the regime accessible for both cases, the one of large stresses $\sigma > \sigma_y$. This suggests that the structure of the flowing states achieved with the two protocols is comparable. Furthermore, there is no visible effect of the caging mechanism, indicating that the flowing state has lost memory of it. It is rather the particle diffusion coefficient in the quiescent state, as determined by the distance from the glass transition, which affects the dynamics of restructuring and the relaxation time. The stress-controlled measurements in addition show that re-

laxation from a non-flowing state, like that of a creeping glass, has characteristics of rather an elastic recovery, with the relaxation time increasing with the applied stress and accumulated strain.

References

1 T. G. Mason and D. A. Weitz, *Phys. Rev. Lett.*, 1995, **75**, 2770–2773.

2 K. N. Pham, G. Petekidis, D. Vlassopoulos, S. U. Egelhaaf, P. N. Pusey and W. C. K. Poon, *Europhys. Lett*, 2006, **75**, 624.

3 K. N. Pham, G. Petekidis, D. Vlassopoulos, S. U. Egelhaaf, W. C. K. Poon and P. N. Pusey, *J. Rheol.*, 2008, **52**, 649.

4 R. Besseling, E. R. Weeks, A. B. Schofield and W. C. K. Poon, *Phys. Rev. Lett.*, 2007, **99**, 028301.

5 J. Zausch, J. Horbach, M. Laurati, S. U. Egelhaaf, J. M. Brader, T. Voigtmann and M. Fuchs, *J. Phys.: Condens. Matter*, 2008, **20**, 404210.

6 N. Koumakis, M. Laurati, S. U. Egelhaaf, J. F. Brady and G. Petekidis, *Phys. Rev. Lett.*, 2012, **108**, 098303.

7 M. Laurati, K. J. Mutch, N. Koumakis, J. Zausch, C. P. Amann, A. B. Schofield, G. Petekidis, J. F. Brady, J. Horbach and M. Fuchs, *J. Phys.: Condens. Matter*, 2012, **24**, 431207.

8 K. J. Mutch, M. Laurati, C. P. Amann, M. Fuchs and S. U. Egelhaaf, *Eur.Phys.J.SpecialTopics*, 2013, **222**, 28032817.

9 M. Siebenbrger, M. Ballauff and T. Voigtmann, *Phys. Rev. Lett.*, 2012, **108**, 255701.

10 T. Sentjabrskaja, P. Chaudhuri, M. Hermes, W. C. K. Poon, J. Horbach, S. U. Egelhaaf and M. Laurati, 2015.

11 T. Sentjabrskaja, D. Guu, M. P. Lettinga, S. U. Egelhaaf and M. Laurati, *AIP Conf. Proc.*, 2013, **1518**, 206.

12 T. Sentjabrskaja, M. Hermes, W. C. K. Poon, C. D. Estrada, R. Castaneda-Priego, S. U. Egelhaaf and M. Laurati, *Soft Matter*, 2014, **10**, 6546.

13 T. Sentjabrskaja, R. Babaliari, J. Hendricks, M. Laurati, G. Petekidis and S. U. Egelhaaf, *Soft Matter*, 2013, **9(17)**, 4524 – 4533.

14 A. Yethiraj and A. van Blaaderen, *Nature*, 2003, **421**, 513–517.

15 W. van Megen, T. C. Mortensen, S. R. Williams and J. Müller, *Phys. Rev. E*, 1998, **58**, 6073–6085.

16 G. Petekidis, D. Vlassopoulos and P. N. Pusey, *J. Phys.: Condens. Matter*, 2004, **16**, S3955.

17 K. N. Nordstrom, E. Verneuil, P. E. Arratia, A. Basu, Z. Zhang, A. G. Yodh, J. P. Gollub and D. J. Durian, *Phys. Rev. Lett.*, 2010, **105**, 175701.

18 B. E. Rodriguez, E. W. Kaler and M. S. Wolfe, *Langmuir*, 1992, **8**, 23822389.

19 R. A. Lionberger, *Phys. Rev. E*, 2002, **65**, 061408.

20 R. J. Farris, *Trans. Soc. Rheol.*, 1968, **12**, 281.

21 P. Coussot, H. Tabuteau, X. Chateau, L. Tocquer and G. Ovarlez, *J. Rheol.*, 2006, **50**, 975.

22 R. H. Ewoldt and G. H. McKinley, *Rheol. Bull.*, 2007, **76**, 4.

23 M. Laurati, S. U. Egelhaaf and G. Petekidis, *J. Rheol.*, 2011, **55**, 673–706.

24 T. Divoux, C. Barentin and S. Manneville, *Soft Matter*, 2011, **7**, 8409.

25 M. Ballauff, J. M. Brader, S. U. Egelhaaf, M. Fuchs, J. Horbach, N. Koumakis, M. Krüger, M. Laurati, K. J. Mutch, G. Petekidis, M. Siebenbürger, T. Voigtmann and J. Zausch, *Phys. Rev. Lett.*, 2013, **110**, 215701.

This page has been left intentionally blank.

3.5. Publication 5: Creep and flow of glasses: strain response linked to the spatial distribution of dynamical heterogeneities

Journal: Scientific Reports
Reference: *Sci. Rep.*, 2015, **5**, 11884
Impact factor: 5.578
Authors: **T. Sentjabrskaja**, P. Chaudhuri, M. Hermes, W. C. K. Poon, J. Horbach, S. U. Egelhaaf and M. Laurati
1st author
TS prepared all materials, performed the experiments and analyzed the data. The confocal measurements under shear were performed on the setup developed by MH and WCKP. PC and JH performed the computer simulations. TS, ML, PC, JH and SUE conceived and discussed the project. ML and SUE supervised the project. All authors contributed to the writing of the manuscript.
45 % contribution of TS

This page has been left intentionally blank.

SCIENTIFIC REPORTS

OPEN

Creep and flow of glasses: strain response linked to the spatial distribution of dynamical heterogeneities

Received: 15 January 2015
Accepted: 08 June 2015
Published: 08 July 2015

T. Sentjabrskaja[1], P. Chaudhuri[2], M. Hermes[3], W. C. K. Poon[3], J. Horbach[2], S. U. Egelhaaf[1] & M. Laurati[1]

Mechanical properties are of central importance to materials sciences, in particular if they depend on external stimuli. Here we investigate the rheological response of amorphous solids, namely colloidal glasses, to external forces. Using confocal microscopy and computer simulations, we establish a quantitative link between the macroscopic creep response and the microscopic single-particle dynamics. We observe dynamical heterogeneities, namely regions of enhanced mobility, which remain localized in the creep regime, but grow for applied stresses leading to steady flow. These different behaviors are also reflected in the *average* particle dynamics, quantified by the mean squared displacement of the individual particles, and the fraction of active regions. Both microscopic quantities are found to be proportional to the macroscopic strain, despite the non-equilibrium and non-linear conditions during creep and the transient regime prior to steady flow.

The properties of materials not only depend on their chemical composition, but also on the arrangement and dynamics of their constituents. It is thus crucial to understand the link between the macroscopic behaviour and the microscopic single-particle level. The relation between an applied mechanical force and microscopic processes is understood for crystalline, i.e. ordered, materials. Crystalline solids (like metals, ceramics or minerals) irreversibly deform when subjected to a load which is small enough to avoid fracture, although this response is very slow. This kind of response is called creep and originates from the presence of defects in the otherwise ordered arrangement of atoms. The diffusion of vacancies and dislocations is responsible for the observed plastic deformation[1]. The same relation and microscopic processes cannot occur in amorphous, i.e. disordered, materials.

Nevertheless, in amorphous solid-like materials, a similar *macroscopic* creep response is observed under application of shear stresses below the yield stress σ_y , i.e. below the transition from an elastic to a plastic response. The macroscopic creep response has been intensively studied in metallic, polymeric and colloidal glasses[2–7]. Several models[8–15], successfully describe the time evolution of the strain measured during creep, namely its characteristic sub-linear time dependence. However, the relation of the creep response to the microscopic structure and dynamics has hardly been determined and is not well understood. Due to the disordered structure of amorphous solids the concept of defects is not applicable and a microscopic mechanism different from the one in crystalline solids must be responsible for creep. Thus, to make progress, microscopic observations on a single-particle level during creep tests are required.

[1]Condensed Matter Physics Laboratory, Heinrich Heine University, Universitätsstr. 1, 40225 Düsseldorf, Germany. [2]Theoretical Physics II, Heinrich Heine University, Universitätsstr. 1, 40255 Düsseldorf, Germany. [3]SUPA, School of Physics & Astronomy, The University of Edinburgh, Mayfield Road, Edinburgh EH9 3JZ, United Kingdom. Correspondence and requests for materials should be addressed to M.L. (email: marco.laurati@uni-duesseldorf.de)

Combining experiments and simulations, we investigated colloidal glasses when constant stress is suddenly applied, i.e. during creep tests . We reveal a quantitative link between the macroscopic rheological response and the microscopic dynamics. This is possible due to recent developments in simultaneously performing rheology and confocal microscopy[16,17]. During creep flow near the yielding threshold, we observe that very few particles undergo large non-affine displacements which leads to pronounced, but spatially localized, dynamical heterogeneities and sub-diffusive dynamics. In contrast, for stresses beyond the yield stress, transient super-diffusive dynamics mark the onset of steady flow. At the same time, growing domains of enhanced dynamic activity are present, with their number correlating with the macroscopic strain. This is reflected in a correlation between the macroscopic strain and the single particle displacements. In addition to the steady-state flow regime, this correlation also holds in the creep and transient states, specially for stresses near the yield stress. Hence, we can quantitatively relate the macroscopic rheological response of soft glasses to the average and heterogeneous microscopic dynamics which are spatially localized during creep but span the entire system at large stresses that lead to flow. The different microscopic behavior thus reflects the different macroscopic response during creep and flow, respectively. This extends previous observations to non-linear and non-equilibrium situations. Furthermore, as we observe the same behavior for different systems, realized in the experiments and simulations, this appears to be a general feature of glasses.

Results and Discussion

In our experiments and simulations we investigated two different model colloidal glasses. In the experiments, the glass is a binary mixture of sterically stabilised PMMA spheres with a size ratio of 5, dispersed in a density and refractive index matching solvent, with total volume fraction $\phi = 0.61$ and a relative volume fraction of small spheres $x_S = \phi_S/\phi = 0.1$. In this binary glass, the motion of the large particles is arrested via caging by neighbouring large particles[18–20]. In our molecular dynamics simulations, the glass is formed by a binary Yukawa fluid of large and small spheres with size ratio 1.2 and a relative number fraction of small spheres of 0.5, large enough to prevent crystallization. This system is quenched to $T = 0.10$, i.e well below the mode-coupling critical temperature of the system, $T_c = 0.14$. All times are normalized; in the experiments by the short-time one-dimensional Brownian diffusion time of the large spheres, $\tau_0^{exp} = 3\pi\eta d_L^3/8k_BT \approx 3.76\,s$, where d_L is the diameter of the large spheres , η is the viscosity and k_BT the thermal energy, and in the simulations by the time unit $\tau_0^{sim} = (md_S^2/\varepsilon_{SS})^{1/2}$, where m, d_S and ϵ_{SS} are units of mass, length and energy, respectively, with d_S the diameter of the small spheres and ϵ_{SS} the energy-scale corresponding to the interaction between small particles. The colloidal glasses investigated in experiments and simulations hence involve different interactions and different mixing and size ratios of their components. Using these different model systems allows us to explore the general features in the response of glasses to externally applied stresses.

Macroscopic Strain is Quantitatively Related to Single-Particle Mean Squared Displacement.

We performed a step to an applied constant stress ($\sigma = \text{const}$) on an initially quiescent glass. In the experiments, the stress was applied using a commercial stress-controlled rheometer, while in the simulations one wall was pulled by a constant force F_0. We monitored the macroscopic response via the time evolution of strain $\gamma(t)$. This situation is in contrast to the case of imposing a constant shear rate ($\dot\gamma = \text{const}$)[21–27], where the bulk stress $\sigma(t)$ is monitored. Unlike for an applied shear rate $\dot\gamma$, when constant stress σ is applied there is no timescale imposed and flow regimes below yielding can be investigated. The choice of control parameter, i.e. constant σ or constant $\dot\gamma$, hence determines the intermediate flow states via which a glass evolves from the quiescent state to steady flow[11]. In the following, we exploit these possibilities and link the increasing macroscopic strain to the evolution of local particle motions, using stress as the external variable and including stresses below the yield stress σ_y . In experiments, we estimated the yield stress of the glass, $\sigma_y \approx 0.010\,Pa$, from the stress at the crossing point of the storage and loss moduli in large amplitude oscillatory shear measurements at 1 rad/s. In simulations, at $T = 0.10$ the yield stress $\sigma_y = 0.072$ (in simulation units) was estimated by strain-rate controlled simulations[28].

If the applied stress $\sigma \approx \sigma_y$, a characteristic creep response is observed with the strain increasing sub-linearly with time within the experimental window, $\gamma \sim t^a$ with $a \approx 0.5$ (Fig. 1a, broken line). Furthermore, for $\sigma = 0.9\sigma_y$ (Fig. 1b, broken line), a smaller effective exponent is found, in agreement with previous results[6,12,28–30]. Hence, for $\sigma \lesssim \sigma_y$, the deformation occurs extremely slowly and the system is unable to reach a steady state within the observation time. This is reflected in the particle dynamics in vorticity (neutral) direction, namely the mean squared displacement (MSD) $\Delta y^2(t)$ (Fig. 1c,d, broken lines). In experiments and simulations, at short times the increase of the MSDs is limited, consistent with caging, while at longer times a sub-diffusive regime is observed; $\Delta y^2 \sim t^b$ with $b < 1$. We find $b \approx a$ within the explored time window. The MSDs show little change with the waiting times t_w after the beginning of the stress application (Fig. 1c,d, broken lines). The observed macroscopic creep response and the absence of steady-state flow is thus connected to the particles' inability to diffuse.

In contrast, if $\sigma \gg \sigma_y$, the strain response shows a rapid transition to a steady flow regime, which corresponds to $\gamma \sim t$, i.e. $\dot\gamma$ is constant (Fig. 1a,b, solid lines). The MSDs again display caging at intermediate times (Fig. 1c,d, solid line), while at long times diffusion[27,31–33]. The slightly lower MSD plateau observed in experiments is due to cage constriction[18], and is also observed in Brownian dynamics

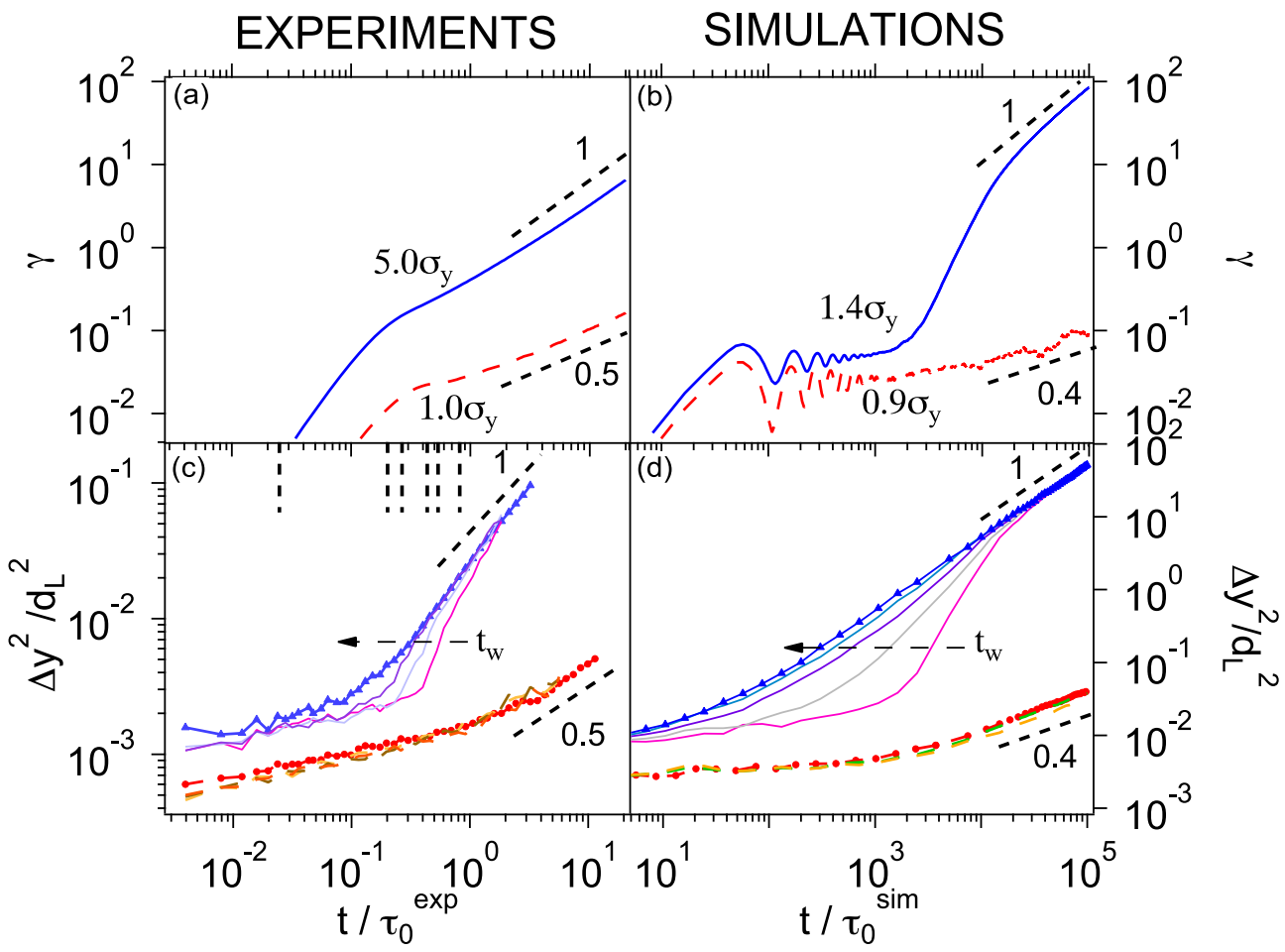

Figure 1. Comparison of (left) experimental and (right) simulation results. (top) Time-dependence of the strain $\gamma(t)$ for applied stresses σ as indicated, relative to the yield stress σ_y. (bottom) Mean squared displacement in the vorticity direction, Δy^2, (indicated by same colors and line styles), immediately after stress application, i.e. for waiting time $t_w = 0$, and larger t_w (as indicated) until the steady-state is reached, i.e. $t_w \to \infty$ (symbols). For the smaller applied stress, Δy^2 is divided by a factor 3 for clarity, both in experiments and simulations.

simulations[24,27], but not in molecular dynamics simulations where the microscopic dynamics is Newtonian. In between caging and long time diffusion, a transient super-diffusive regime is observed. This coincides with the transition of the rheological response from the initial elastic regime to the flow regime. Note that in the experiments, the initial superlinear increase in strain is a known effect of the rheometer's inertia[34]. With increasing waiting time t_w (Fig. 1c,d), super-diffusion occurs at increasingly earlier times and for increasingly shorter time intervals, until it almost disappears in the steady state. Thus, the onset of flow is characterized by transient super-diffusion and, subsequently in the steady state, by diffusion. This indicates that the different regimes in the macroscopic strain response $\gamma(t)$ are reflected in different features of the single-particle dynamics, here characterized by the MSD $\Delta y^2(t)$.

We now quantitatively investigate the relation between the macroscopic strain $\gamma(t)$ and the microscopic MSDs $\Delta y^2(t)$. In the case of steady flow $\gamma(t) = \dot{\gamma} t$ and, since then the particles diffuse, $\Delta y^2(t) \sim D(\sigma)t$, which implies that $\Delta y^2(t) \sim [D(\sigma)/\dot{\gamma}]\gamma(t) = C(\sigma)\gamma(t)$. Previous experiments and simulations under constant applied shear rate have found $D \sim \dot{\gamma}^{0.8}$ [21,22], which implies $C(\sigma) \sim \dot{\gamma}^{-0.2}$, since stress and strain control are equivalent in steady flow. In our case, in the asymptotic diffusive regime (corresponding to $\gamma \gg 10$, Fig. 1a,b) we observe an approximate linear relation $\Delta y^2(t) \sim \gamma(t)$ for a large range of σ (Fig. 2a, Sec. 1 in Supplementary Information). The slight shifts between the curves for different σ occur due to the expected behaviour of $C(\sigma)$ (Fig. 2b). If Δy^2 is rescaled by $C(\sigma)$, the data fall onto a single line of slope 1 (Fig. 2c).

Although our argument for the relation $\Delta y^2(t) \sim \gamma(t)$ is based on the assumption of steady flow, the relation surprisingly also holds in non-steady states for $\gamma \lesssim 10$, which corresponds to creep (for $\sigma \lesssim \sigma_y$) or the transient regime before steady flow (for $\sigma > \sigma_y$). In contrast, $\Delta y^2(t) \sim \gamma(t)$ does not hold for large

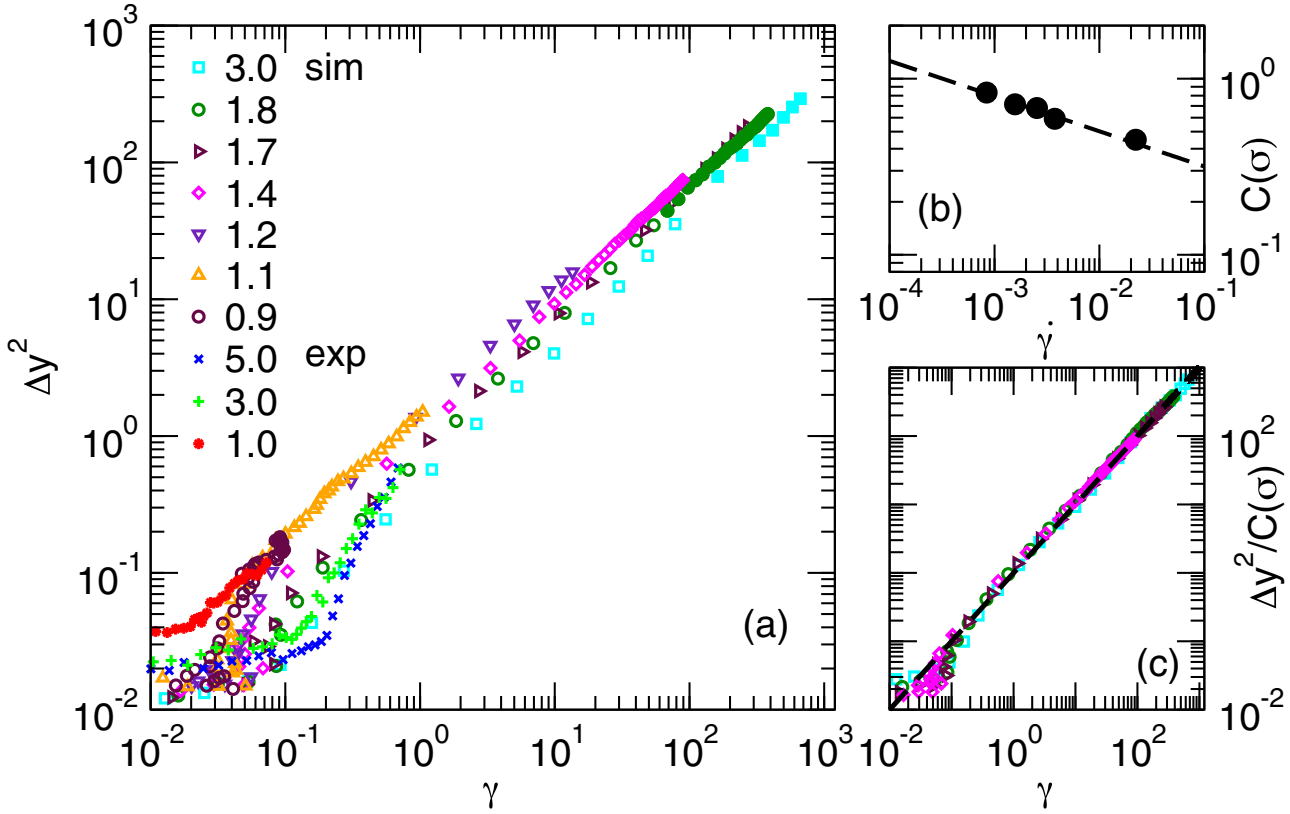

Figure 2. (**a**) Mean squared displacement in vorticity direction, Δy^2, as a function of strain γ for different values of the applied stress σ/σ_y obtained in experiments and simulations (Sec. 1 of Supplementary Information). The experimental Δy^2 values are multiplied by a constant factor in order to match the simulation data. (**b**) Ratio of diffusion coefficient to shear rate, $C(\sigma) = D(\sigma)/\dot{\gamma}$, obtained from fits (Sec. 1 of Supplementary Information), as a function of the shear rate in the steady state, $\dot{\gamma}$. The dashed line indicates a power-law $C(\sigma) \sim \dot{\gamma}^{-0.2}$. (**c**) Scaling plot of $\Delta y^2/C(\sigma)$ as a function of γ, with the dashed line indicating a slope of 1.

stresses σ and small strains γ (or short times t). In both, experiments and simulations, systematic deviations are seen to occur with increasing stress. The deviations occur due to a time lag between the particles' motion beyond their cages and the onset of macroscopic deformation (Fig. SM-1, Supplementary Information). Moreover, at very short times, i.e. in the initial elastic regime (Fig. 1), the proportionality is also not observed. This suggests that the observed correlation is a consequence of the plasticity that develops after the initial elastic regime. Our observations mark a clear difference between the yielding response under applied constant stress (investigated here) and applied constant shear rate (investigated in[24,26]). In the latter, $\Delta y^2(t) \sim \gamma(t)$ cannot hold in the transient regime, where $\Delta y^2(t)$ increases superlinearly with t while $\gamma(t)$ increases linearly. Note that this connection between nonlinear strain and the single-particle dynamics is an implicit assumption in a recent theoretical approach based on a nonlinear Langevin equation[35–37]. Our data indicates to what extent such a connection is valid.

Displacement Distributions Indicate Small Fraction of Mobile Particles. In addition to the characterisation of the particle displacements via the MSD, i.e. a mean value, we have also investigated the distribution of the displacements, namely the self part of the van Hove function $p(\Delta y)$. For $\sigma \approx \sigma_y$ (Fig. 3, left), at all times the van Hove functions exhibit a nearly Gaussian shape for small Δy, which corresponds to localised particles, and moderate exponential tails which correspond to large displacements of a small fraction of particles. The non-Gaussian tails only slightly change with increasing time. This indicates that shear-induced delocalisation is a very slow process. In particular, large displacements at the shortest time of the measurement $t_0/\tau_0^{\mathrm{exp}} = 0.0037$ hardly occur and therefore macroscopic flow is delayed.

For $\sigma > \sigma_y$ (Fig. 3, right) shear leads to a larger deviation from a Gaussian distribution with a significant number of large displacements. The deviation from Gaussian behavior was quantified by the time dependence of the integral $I_R(t)$ of the residuals of the Gaussian fits to $p(\Delta y)$, which, for each fixed time, was normalised to the integral of the distribution (Fig. 3, inset). A non monotonic trend of $I_R(t)$

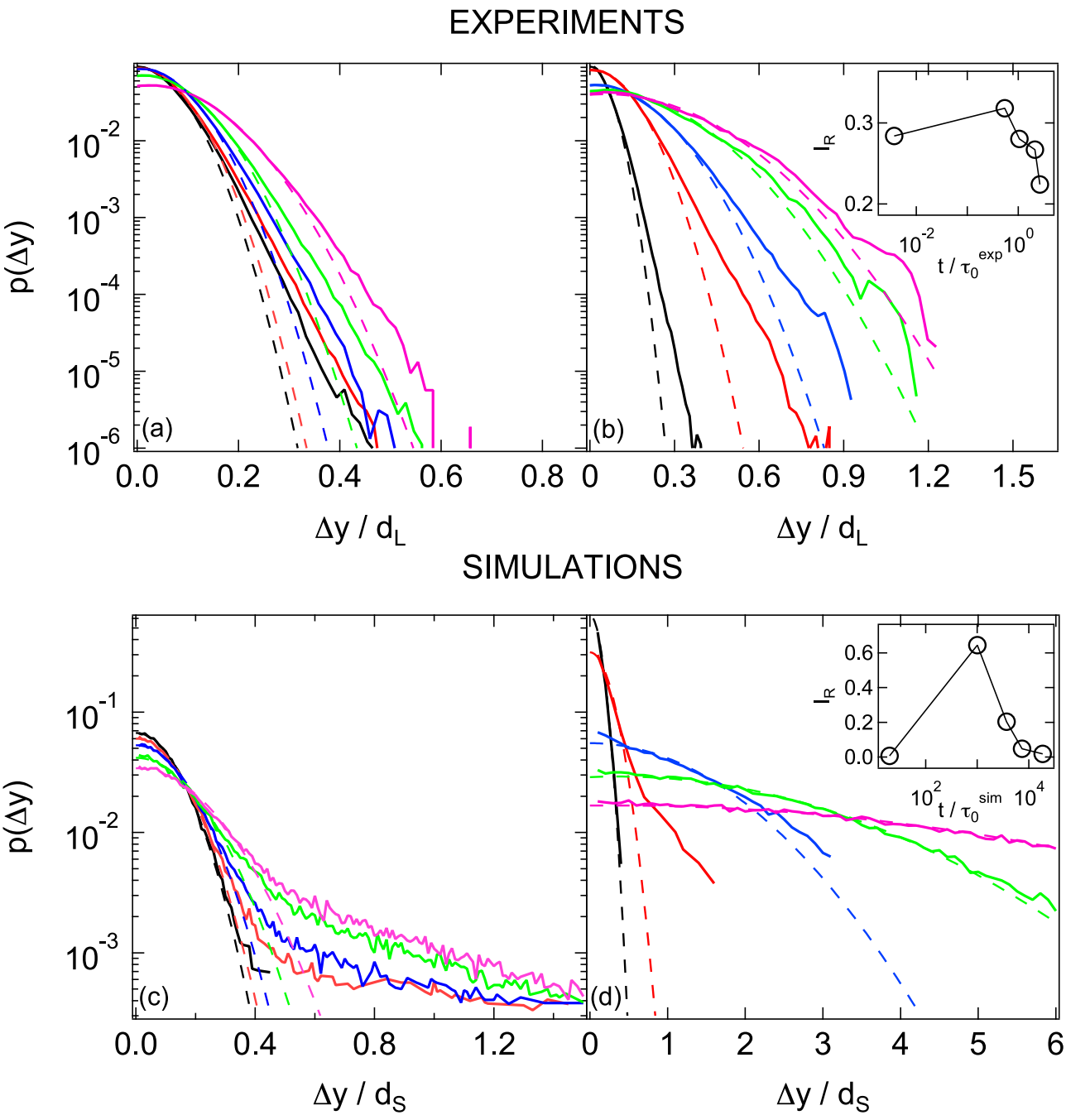

Figure 3. Van Hove self-correlation functions, i.e. distributions of displacements $p(\Delta y)$, determined (top) by experiments for (**a**) a stress $\sigma \approx \sigma_y$, a waiting time $t_w = 0$ and times $t/\tau_0^{exp} = 0.0037$, 0.54, 1.05, 2.12 and 5.31 (left to right) and (**b**) $\sigma \approx 5\sigma_y$, $t_w = 0$ and same times, except the longest time here is $t/\tau_0^{exp} = 2.65$, (bottom) by simulations for (**c**) $\sigma \approx 1.1\sigma_y$, $t_w = 0$ and $t/\tau_0^{sim} = 20$, 3.7×10^3, 11×10^3, 56×10^3 and 110×10^3 (left to right) and (**d**) $\sigma \approx 1.53\sigma_y$, $t_w = 0$ and $t/\tau_0^{sim} = 20$, 1.01×10^3, 3.7×10^3, 7.4×10^3 and 18.6×10^3 (left to right). Dashed lines represent Gaussian fits to $p(\Delta y)$ for small Δy. Insets: normalized integral I_R of the residuals of the Gaussian fits in the main plots, as a function of time t/τ_0.

is observed, with a maximum value during the intermediate super-diffusive regime. At later times $I_R(t)$ continuously decreases and eventually vanishes when diffusion sets in and a Gaussian distribution of displacements is recovered.

Evolution of Dynamical Activity Follows Macroscopic Strain. The tails in the van Hove function $p(\Delta y)$ reveal the existence of a small number of very mobile particles during the transient regime. We

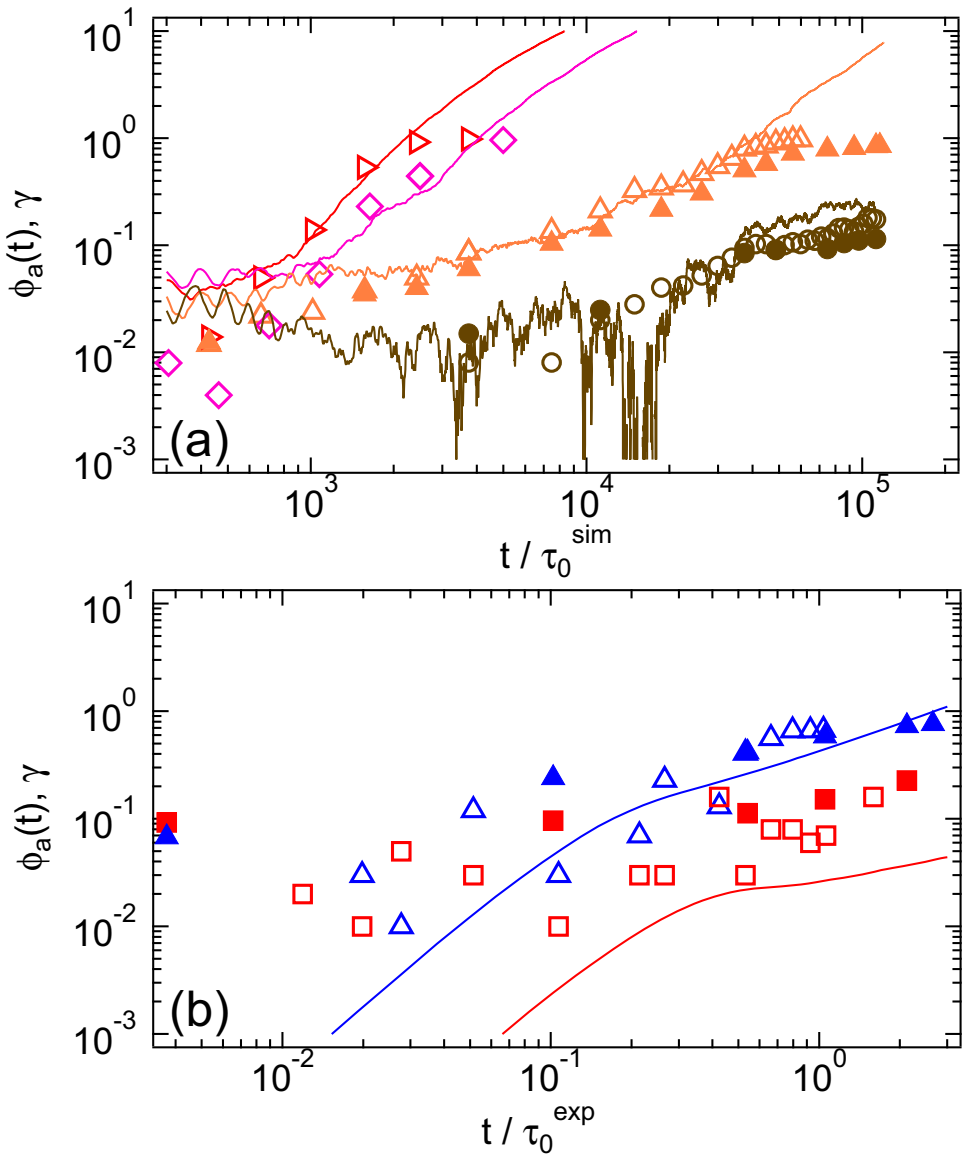

Figure 4. Fraction of active particles $\Phi_a^{vH}(t)$ (solid symbols) and active boxes $\Phi_a^{b}(t)$ (open symbols) determined (**a**) by simulations at stresses $\sigma/\sigma_y = 0.9$ (●, ○), 1.1 (▲, Δ), 1.4 (◊), 1.53 (▷) and (**b**) by experiments at $\sigma/\sigma_y \approx 1.0$ (■, □) and 5.0 (▲, Δ). Lines of the same colour represent the strain γ for the corresponding applied stresses, where the instantaneous strain is shown in the case of the simulations.

quantify the time evolution of the fraction of these mobile particles by the ratio $\Phi_a^{vH}(t) = I_a(t)$ with I_a the integral of $p(\Delta y)$ for displacements $\Delta y/d > 5\Delta y_{min}$, with $d = d_S$ and d_L in simulations and experiments, respectively (Fig. 4, solid symbols). The value $\Delta y_{min} = \sqrt{\Delta y^2(t_0)/d^2}$ is the localization length estimated from the MSDs at the shortest time t_0 (Fig. 1c,d). In simulations the time-dependence of $\Phi_a^{vH}(t)$ closely follows that of the instantaneous strain $\gamma(t)$, up to $\Phi_a^{vH}(t) = 1$ (Fig. 4a, lines). In the experiments, similar results for $\Phi_a^{vH}(t)$ are observed (Fig. 4b) except that, in contrast to the simulations, $\gamma(t)$ is not the instantaneous strain but a time average, leading to a small deviation between $\Phi_a^{vH}(t)$ and $\gamma(t)$. The macroscopic strain is therefore not only proportional to the average mean squared displacement (Fig. 2) but also the fraction of mobile particles: this indicates that the mobile, dynamically active particles contribute most significantly to the mean squared displacement. This is true both below and above the yield stress.

Spatial Distribution of Dynamical Activity is Heterogeneous. We introduce spatial coarse-graining in order to reduce noise. We divide the field of view into 10×10 square boxes, each with size $(2.8\ d_L)^2$. For

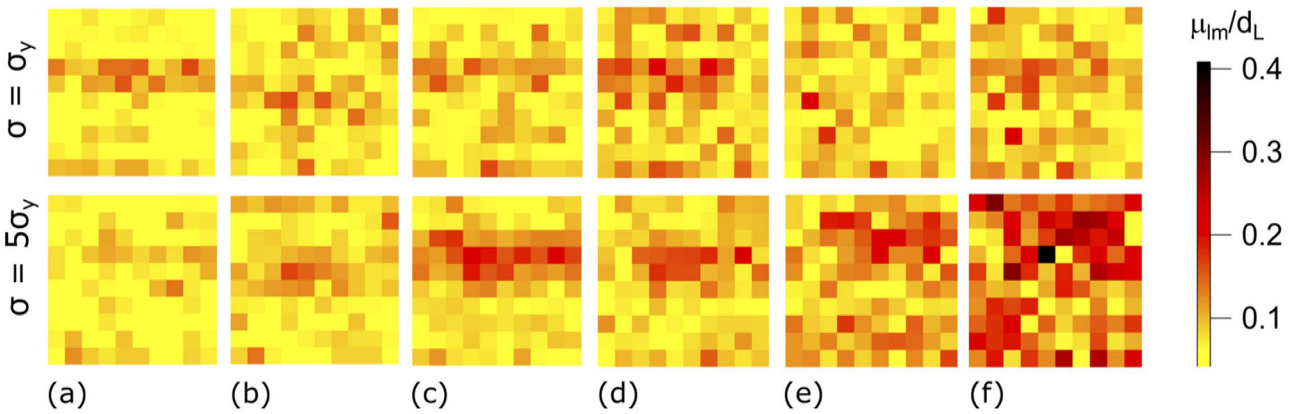

Figure 5. Maps of average particle mobilities $\mu_{lm}(t)$ within boxes *lm* (Eq. (1)) for (top) stress $\sigma \approx \sigma_y$ and (bottom) $\sigma \approx 5\sigma_y$ and times $t/\tau_0^{exp} = 0.025, 0.20, 0.27, 0.43, 0.53, 0.80$ (**a**–**f**, indicated in Fig. 1c by dashed lines) as observed in experiments. The box size is $(2.8\ d_L)^2$.

each particle *i*, the displacement in the vorticity direction, $\Delta y_i(t) = y_i(t) - y_i(t_0)$, was determined. The average particle mobility in box *lm*, with $l, m = 1 \ldots 10$, was calculated according to

$$\mu_{lm}(t) = \left\langle \Delta y_i(t) \right\rangle_{lm} \quad (1)$$

where $\langle \ldots \rangle_{lm}$ denotes an average over all the particles which were in the box *lm* at $t = t_0$. A box *lm* is defined active at time *t* if $\mu_{lm} > 5\Delta y_{min}$, following the same criterion used to distinguish largest displacements of single particles in the van Hove functions (Fig. 1c,d). The fraction of active boxes, $\Phi_a^b(t) = N_a(t)/N_{tot}$, with N_a the number of active boxes and N_{tot} the total number of boxes. With time $\Phi_a^b(t)$ grows as the fraction of the single mobile particles $\Phi_a^{vH}(t)$ (Fig. 4, symbols). Thus, the time-dependence of $\Phi_a^b(t)$ is also proportional to $\gamma(t)$. A similar connection between the number of active regions and strain growth was experimentally observed in the creep flow of frictional granular particles[38].

To investigate the existence of heterogeneity in the dynamical activity, we consider the spatial distribution of active boxes. For $\sigma \approx \sigma_y$, the distribution of local mobilities within the velocity-vorticity plane does not indicate any prominent features (Fig. 5, top). At any specific time, there are some active boxes with larger mobilities, but the locations of the boxes with the largest mobilities vary randomly with time. For $\sigma \approx 5\sigma_y$, similar mobilities occur at short times, when the localisation plateau in the MSD is observed (Fig. 5a,b, bottom). In contrast, at $t \gtrsim 0.3\tau_0^{exp}$, roughly coincident with the onset of super-diffusion in the MSDs determined for $t_w = 0$ (Fig. 1c), a region with enhanced mobilities emerges (Fig. 5c,d, bottom), expands with time (Fig. 5e, bottom) and spans almost the whole field of view once the system flows (Fig. 5f, bottom). Hence, the onset of flow (Fig. 1a,b) coincides with the appearance of a region of higher local mobility (Fig. 5) and super-diffusive dynamics (Fig. 1c,d). Furthermore, it leads to the pronounced non-Gaussian tails in the van Hove correlation function at intermediate times (Fig. 3), which disappear once steady flow has developed and the dynamics again becomes more homogeneous (Fig. 3, inset).

The enhanced local mobilities do not result from sudden large displacements, but occur through the accumulation of only slightly above-average local, non-affine particle displacements. This has been confirmed by calculating the instantaneous mobilities from $0.18\tau_0^{exp}$ to $0.46\tau_0^{exp}$ and $0.28\tau_0^{exp}$ to $0.56\tau_0^{exp}$, i.e. for 10 sampling times, instead of starting from the shortest measurement time (as in Fig. 5). No large instantaneous mobilities and no significant difference to $\sigma \approx \sigma_y$ are observed (Sec. 2 in Supplementary Information). Similar results are obtained in our simulations. The occurrence of correlated plastic events[39,40] and avalanche-like behavior[41,42] have been proposed as mechanisms driving the onset of flow. Such cooperative events might be connected to the correlated local mobilities and their spreading observed in our study. The observed intermittency in the displacements might also be related to stick-slip motion[43].

The larger area in the velocity-vorticity plane monitored in the experiments allows us to quantitatively investigate the spatial growth of active regions. If the box *lm* is active or inactive, n_{lm} is defined as 1 or 0, respectively. Based on this definition, we calculate the spatial correlation of active boxes, that is the box-box correlation function, $G(r) = \langle n_{lm} n_{l'm'} \rangle$ with $r^2 = (l-l')^2 + (m-m')^2$ (Fig. 6a). The brackets $\langle \ldots \rangle$ indicate an average over the individual boxes. The characteristic length ξ of the spatial correlation $G(r)$ was determined by fitting a stretched exponential function $f(r) = A \exp[-(r/\xi)^\beta]$ to $G(r)$. The correlation length $\xi(t)$ increases from an initial value $\xi \approx 5d_L$ at $t = 0.10\tau_0^{exp}$ to $\xi \approx 30d_L$ at $t = 0.92\tau_0^{exp}$, with

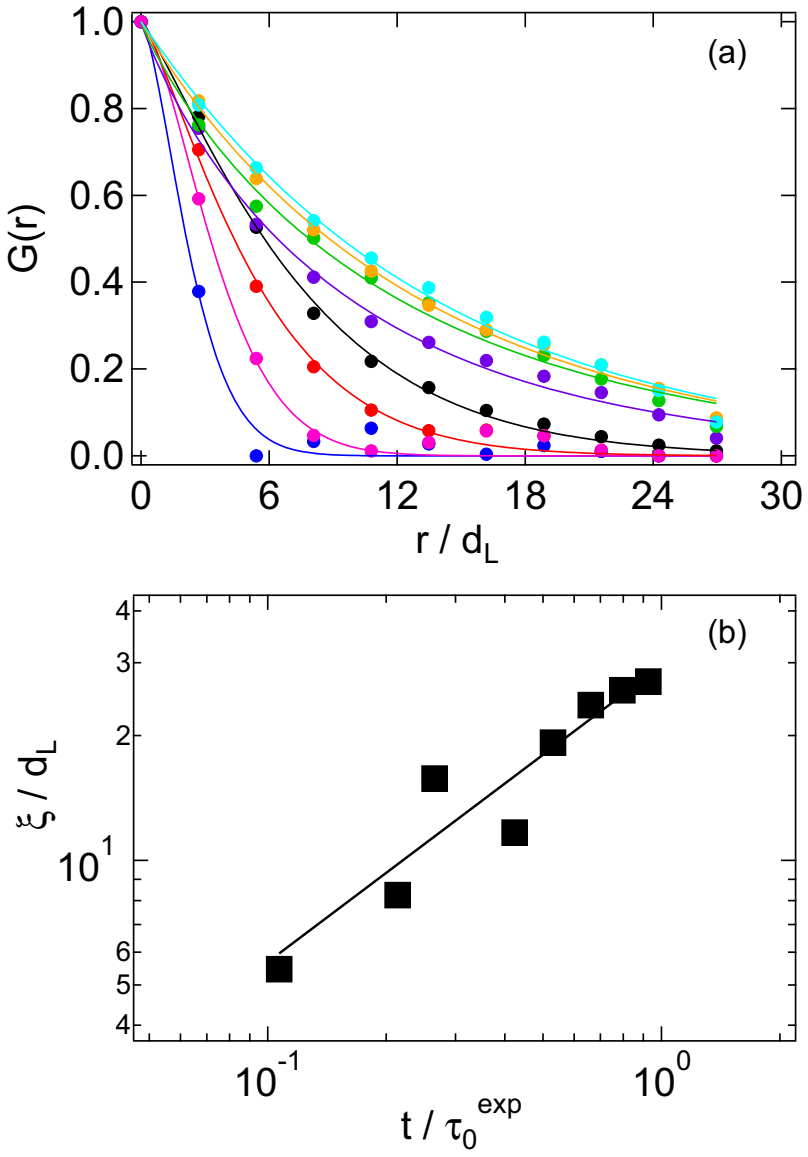

Figure 6. (**a**) Box-box correlation functions $G(r)$ for stress $\sigma/\sigma_y \approx 5$ and time $t/\tau_0^{exp} = 0.1$, 0.20, 0.27, 0.43, 0.53, 0.66, 0.80 and 0.93 (left to right) as observed in experiments. Lines represent stretched exponential fits. (**b**) Correlation length of active boxes, ξ, as a function of time for $\sigma/\sigma_y \approx 5.0$; the line indicates $\xi/d_L \sim t^{2/3}$.

$\xi(t) \sim t^{2/3}$ (Fig. 6b). For $\sigma \approx \sigma_y$ the correlation length $\xi(t)$ instead does not grow and stays approximately constant for all times t (data not shown).

Conclusions

Using experiments and simulations, we demonstrated that under applied stress, the macroscopic deformation of glasses can be linked in a consistent way to the single particle displacements. In particular, the strain is approximately linearly related to the single-particle MSD even in the time-dependent non-linear response regime, including the creep and the transient regime preceding steady flow. Furthermore, the fraction of active particles in the van Hove function as well as the fraction of active regions, i.e. of groups of particles, is also proportional to the macroscopic strain. Heterogeneities in the location of these active particles are present both for applied stresses smaller and larger than the yield stress. The spatial distribution of regions with larger displacements determines the onset of flow. For applied stresses around the yield stress, i.e. during creep, localised regions of enhanced dynamical activity allow only for sub-diffusive dynamics. Increasing the stress beyond the yield stress, the active regions grow heterogeneously and super-diffusive transients emerge leading to particle diffusion with steady flow setting in. We observe qualitatively the same behavior for the different models studied in our experiments and simulations and thus expect that our observations represent generic features of glasses.

Future work should focus on understanding how the external stress leads to the occurrence of locally enhanced mobilities, e.g. whether these are related to thermally activated local structural changes. Furthermore, the mechanisms that drive the spreading of the active regions within the plane as well as in the transverse direction need to be identified, thereby providing possible links to transient shear banding in the velocity-gradient plane[28,44]. All these would help to develop a more complete scenario for the fluidisation of glassy systems under applied stress. Furthermore, it can open the route to the rational design of materials with desired response to applied stresses.

Methods

Experiments. We investigated a mixture of sterically stabilized PMMA spheres of diameters $d_L = 1.76\,\mu$m (fluorescently labeled) and $d_S = 0.36\,\mu$m, dispersed in a cis-decalin/cycloheptyl-bromide mixture which closely matches their density and refractive index. After addition of salt (tetrabutylammoniumchloride), this system presents hard-sphere like interactions[45,46]. The total volume fraction is $\phi = 0.61$ and the relative fraction of small spheres $x_S = \phi_S/\phi = 0.1$. The formation of a glassy state in this mixture was demonstrated by using rheology and confocal microscopy measurements of the dynamics of large particles[18–20]. The presence of small spheres, with their larger energy density, increases the yield stress of the system, thereby improving the quality of the rheological data while still allowing for the simultaneous observation of the large spheres with confocal microscopy[16,17]. The rheological and confocal microscopy measurements reported in the manuscript were obtained using a combination of a commercial MCR-301 WSP stress-controlled rheometer (Anton-Paar) and a VT-Eye confocal unit (Visitech) mounted on a Nikon Ti-U inverted microscope, with a Nikon Plan Apo 60x oil immersion objective (NA = 1.40). We used a cone-plate geometry of diameter 50 mm, cone angle 1° and truncation gap 100 μm. The bottom plate consists of a microscope coverslip which was coated with a mixture of PMMA particles of radius 0.885 μm and 0.174 μm. The surface of the cone is sandblasted. The roughness of the geometries prevents wall-slip, as verified by imaging. A solvent trap was used to reduce solvent evaporation. Due to the fact that rheological measurements on colloidal glasses are affected by loading effects, shear history and aging, before each test a renjuvenation procedure was performed in order to obtain a reproducible initial state of the system. After loading, we performed a dynamic strain sweep to estimate the yield strain γ_y of the system from the crossing point of the strain-dependent storage, G′, and loss, G″, moduli. Oscillatory shear at $\gamma = 3 \gg \gamma_y$ was applied to induce flow and maintained until the time-dependent G′ and G″ reached a stationary state, typically after 200 s. Afterwards, oscillatory shear in the linear viscoelastic regime, $\gamma = 0.001$, was applied until G′ and G″ became stationary, typically for $t > 300\,s$. The state characterised by the stationary values of G′ and G″ was the initial state, prepared before each creep measurement. The relative error on the strain determination during creep measurements is smaller than 1%.

Confocal microscopy images were acquired in a velocity-vorticity plane about 6 mm from the center of the geometries and 30 μm from the bottom plate. Images with 512×512 pixels, corresponding to 51 μm $\times$ 51 μm, were acquired at a rate of 67 frames per second, which ensured accurate particle tracking even at the highest applied stresses (typical movies in Supplementary Information). By imaging the truncation gap of the cone, we verified that bending of the coverslip is negligible[16]. This is also indicated by the fact that, despite the applied stress, the particles in the imaging plane remain perfectly in focus (movies in Supplementary Information). The fact that we can image the truncation gap of the cone is also used to check that the bottom plate is perpendicular to the rotation axis of the cone. Particle coordinates and trajectories were extracted from the images using standard routines[47]. Mean squared displacements from four independent measurements were averaged. The noise contribution to our MSD data was estimated from the MSD of an immobile sample, resulting in $\Delta y^2/d_L^2 \approx 4 \times 10^{-4}$, i.e. a factor of about 2.5 times smaller than the $\Delta y^2(t)$ values measured at short times.

Simulations. In our molecular dynamics simulations, a 50:50 binary Yukawa fluid of large and small spheres with size ratio 1.2 is investigated. The model parameters have been reported earlier[26,28,48]. Our simulations have been performed for samples consisting of $N = 12800$ particles and having dimensions $L_x = 26.66 d_S$, $L_y = 13.33 d_S$, $L_z = 53.31 d_S$. We work in the NVT ensemble using periodic boundary conditions, the temperature being controlled by a Lowe thermostat[49]. The mode-coupling critical temperature of the system is $T_c = 0.14$. The system is equilibrated at $T = 0.15$ and then instantaneously quenched to $T = 0.10$, where it is aged for $10^4\ \tau_0^{sim}$. At this time, the walls are generated by freezing particles at $0 < z < 2d_S$ and $L_z - 2d_S < z < L_z$ [28]. Stress is applied by pulling one wall at a constant force F_0 in the x direction. For each applied stress, runs over 24 independent replicas of the system were averaged. Similar to the experiments, the dynamics were measured in a slice at the centre of the volume having thickness $13.3 d_S$ and distance about $18 d_S$ to the walls on each side.

References

1. Poirier, J. P. Creep of Crystals (Cambridge University Press, 1985).
2. Suryanarayana, C. & Inoue, A. Bulk Metallic Glasses (CRC Press, Taylor and Francis Group, 2011).
3. Oswald, P. Rheophysics (Cambridge University Press, 2009).
4. Larson, R. G. The Structure and Rheology of Complex Fluids (Oxford University Press, 1999).

5. Laurati, M., Egelhaaf, S. U. & Petekidis, G. Nonlinear rheology of colloidal gels with intermediate volume fraction. *J. Rheol.* **55,** 673 (2011).
6. Divoux, T., Barentin, C. & Manneville, S. From stress-induced fluidization processes to Herschel-Bulkley behaviour in simple yield stress fluids. *Soft Matter* **7,** 8409 (2011).
7. Pham, K. N. *et al.* Yielding behavior of repulsion- and attraction-dominated colloidal glasses. *J. Rheol.* **52,** 649 (2008).
8. McKenna, G. B. On the Physics Required for Prediction of Long Term Performance of Polymers and Their Composites. *J. Res. Natl. Inst. Stand. Technol.* **99,** 169 (1994).
9. Fielding, S. M., Sollich, P. & Cates, M. E. Aging and rheology in soft materials. *J. Rheol.* **44,** 323 (2000).
10. Falk, M. L. & Langer, J. S. Dynamics of viscoplastic deformation in amorphous solids. *Phys. Rev. E* **57,** 7192 (1998).
11. Derec, C., Ajdari, A. & Lequeux, F. Rheology and aging: A simple approach. *Eur. Phys. J. E* **4,** 355 (2001).
12. Siebenbürger, M., Ballauff, M. & Voigtmann, Th. Creep in Colloidal Glasses. *Phys. Rev. Lett.* **108,** 255701 (2012).
13. Spaepen, F. A microscopic mechanism for steady state inhomogeneous flow in metallic glasses. *Acta Metall.* **25,** 407 (1977).
14. Argon, A. S. Plastic deformation in metallic glasses. *Acta Metall.* **27,** 47 (1979).
15. Johnson, W. L., Demetriou, M. D., Harmon, J. S., Lind, M. L. & Samwer, K. Rheology and Ultrasonic Properties of Metallic Glass-Forming Liquids: A Potential Energy Landscape Perspective. *MRS Bull.* **32,** 644 (2007).
16. Besseling, R., Isa, L., Weeks, E. R. & Poon, W. C. K. Quantitative imaging of colloidal flows. *Adv. Coll. Int. Sci.* **146,** 1 (2009).
17. Dutta, S. K., Mbi, A., Arevalo, R. C. & Blair, D. L. Development of a confocal rheometer for soft and biological materials. *Rev. Sci. Instrum.* **84,** 063702 (2013).
18. Sentjabrskaja, T., Guu, D., Lettinga, M. P., Egelhaaf, S. U. & Laurati, M. Glasses of dynamically asymmetric binary colloidal mixtures: Quiescent properties and dynamics under shear. *AIP Conf. Proc.* **1518,** 206 (2013).
19. Sentjabrskaja, T. *et al.* Yielding of binary colloidal glasses. *Soft Matter* **9,** 4524 (2013).
20. Sentjabrskaja, T. *et al.* Transient dynamics during stress overshoots in binary colloidal glasses. *Soft Matter* **10,** 6546 (2014).
21. Varnik, F. Structural relaxation and rheological response of a driven amorphous system. *J. Chem. Phys.* **125,** 164514 (2006).
22. Besseling, R., Weeks, E. R., Schofield, A. B. & Poon, W. C. K. Three-dimensional imaging of colloidal glasses under steady shear. *Phys. Rev. Lett.* **99,** 028301 (2007).
23. Schall, P., Weitz, D. A. & Spaepen, F. Structural rearrangements that govern flow in colloidal glasses. *Science* **318,** 1895 (2007).
24. Laurati, M. *et al.* Transient dynamics in dense colloidal suspensions under shear: Shear rate dependence. *J. Phys.: Condens. Matt.* **24,** 464104 (2012).
25. Brader, J. M., Voigtmann, T., Fuchs, M., Larson, R. G. & Cates, M. E. Glass rheology: From mode-coupling theory to a dynamical yield criterion. *Proc. Natl. Acad. Sci.* **106,** 15186 (2009).
26. Zausch, J. *et al.* From equilibrium to steady state: the transient dynamics of colloidal liquids under shear. *J. Phys.: Condens. Matter* **20,** 404210 (2008).
27. Koumakis, N., Laurati, M., Egelhaaf, S. U., Brady, J. F. & Petekidis, G. Yielding of Hard-Sphere Glasses during Start-Up Shear. *Phys. Rev. Lett.* **108,** 098303 (2012).
28. Chaudhuri, P. & Horbach, J. Onset of flow in a confined colloidal glass under an imposed shear stress. *Phys. Rev. E* **88,** 040301(R) (2013).
29. Andrade, E. N. On the Viscous Flow in Metals, and Allied Phenomena. *Proc. R. Soc. Lond. A* **84,** 1 (1910).
30. Rosti, J., Koivisto, J., Laurson, L. & Alava, M. Fluctuations and Scaling in Creep Deformation. *Phys. Rev. Lett.* **105,** 100601 (2010).
31. Koumakis, N., Brady, J. F. & Petekidis, G. Complex oscillatory yielding of model hard-sphere glasses. *Phys. Rev. Lett.* **110,** 178301 (2013).
32. Mohan, L., Pellet, C., Cloitre, M. & Bonnecaze, R. Local mobility and microstructure in periodically sheared soft particle glasses and their connection to macroscopic rheology. *J. Rheol.* **57,** 1023 (2013).
33. Lin, N. Y. C. *et al.* Far-from-equilibrium sheared colloidal liquids: Disentangling relaxation, advection, and shear-induced diffusion. *Phys. Rev. E* **88,** 062309 (2013).
34. Yao, N., Larsen, R. J. & Weitz, A. D. Probing nonlinear rheology with inertio-elastic oscillations. *J. Rheol.* **52,** 1013 (2008).
35. Chen, K., Schweizer, K. S., Stamm, R., Lee, E. & Caruthers, J. M. Theory of Nonlinear Creep in Polymer Glasses. *J. Chem. Phys.* **129,** 184094 (2008).
36. Chen, K. & Schweizer, K. S. Theory of aging, rejuvenation, and the nonequilibrium steady state in deformed polymer glasses. *Phys. Rev. E.* **82,** 041804 (2010).
37. Chen, K., Saltzman, E. J. & Schweizer, K. S. Molecular Theories of Segmental Dynamics and Mechanical Response in Deeply Supercooled Polymer Melts and Glasses. *Annu. Rev. Condens. Matter Phys.* **1,** 277 (2010).
38. Amon, A., Nguyen, V. B., Bruand, A., Crassous, J. & Clement, E. Hot Spots in an Athermal System. *Phys. Rev. Lett.* **108,** 135502 (2012).
39. Bocquet, L., Colin, A. & Ajdari, A. Kinetic Theory of Plastic Flow in Soft Glassy Materials. *Phys. Rev. Lett.* **103,** 036001 (2009).
40. Chikkadi, V., Wegdam, G., Bonn, D., Nienhuis, B. & Schall, P. Long-Range Strain Correlations in Sheared Colloidal Glasses. *Phys. Rev. Lett.* **107,** 198303 (2011).
41. Lemaitre, A. & Caroli, C. Rate-Dependent Avalanche Size in Athermally Sheared Amorphous Solids. *Phys. Rev. Lett.* **103,** 065501 (2009).
42. Karmakar, S., Lerner, E. & Procaccia, I. Athermal nonlinear elastic constants of amorphous solids. *Phys. Rev. E.* **82,** 055103 (2010).
43. Gee, M. L., McGuiggan, P. M., Israelachvili, J. N. & Homola, A. M. Liquid to solid like transitions of molecularly thin films under shear. *J. Chem. Phys.* **93,** 1895 (1990).
44. Moorcroft, R. L. & Fielding, S. M. Criteria for Shear Banding in Time-Dependent Flows of Complex Fluids. *Phys. Rev. Lett.* **110,** 086001 (2013).
45. Yethiraj, A. & van Blaaderen, A. A colloidal model system with an interaction tunable from hard sphere to soft and dipolar. *Nature* **421,** 513 (2003).
46. Poon, W. C. K., Weeks, E. R. & Royall, C. P. On measuring colloidal volume fractions. *Soft Matter* **8,** 21 (2012).
47. Crocker, J. C. & Grier, D. G. Methods of Digital Video Microscopy for Colloidal Studies. *J. Colloid Interface Sci.* **179,** 298–310 (1996).
48. Zausch, J. & Horbach, J. The build-up and relaxation of stresses in a glass-forming soft-sphere mixture under shear: A computer simulation study. *Europhys. Lett.* **88,** 60001 (2009).
49. Koopman, E. A. & Lowe, C. P. Advantages of a Lowe-Andersen thermostat in molecular dynamics simulations. *J. Chem. Phys.* **124,** 204103 (2006).

Acknowledgements

We thank A.B. Schofield for the colloidal particles and K.J. Mutch for help with the analysis of the experimental data. We acknowledge support from the Deutsche Forschungsgemeinschaft through the Research unit FOR1394 (Projects P2 and P8) and EU funding through the FP7-Infrastructures "ESMI"

(CP&CSA-2010-262348). Further, NIC Jülich is thanked for providing computing time. The Edinburgh work was funded by EPSRC grant EP/J007404/1.

Author Contributions

T.S., M.H., W.C.K.P., S.U.E and M.L. performed, analysed or interpreted the experiments which are based on equipment in the lab of M.H. and W.C.K.P., P.C. and J.H. performed, analysed or interpreted the simulation. All authors contributed to the interpretation and comparison of the data as well as the writing of the manuscript.

Additional Information

Supplementary information accompanies this paper at http://www.nature.com/srep

Competing financial interests: The authors declare no competing financial interests.

How to cite this article: Sentjabrskaja, T. *et al.* Creep and flow of glasses: strain response linked to the spatial distribution of dynamical heterogeneities. *Sci. Rep.* **5**, 11884; doi: 10.1038/srep11884 (2015).

Supplemental Material for 'Creep and flow of glasses: strain response linked to the spatial distribution of dynamical heterogeneities'

T. Sentjabrskaja[1], P. Chaudhuri[2], M. Hermes[3], W. C. K. Poon[3], J. Horbach[2], S. U. Egelhaaf[1], and M. Laurati[1]
[1] *Condensed Matter Physics Laboratory, Heinrich-Heine University, Universitätsstr. 1, 40225 Düsseldorf, Germany.*
[2] *Theoretical Physics II, Heinrich-Heine University, Universitätsstr. 1, 40255 Düsseldorf, Germany.*
[3] *SUPA, School of Physics & Astronomy, The University of Edinburgh, Mayfield Road, Edinburgh EH9 3JZ, United Kingdom.*

In the first section we report the time evolution of the strain $\gamma(t)$ for further values of the applied stress σ, and the corresponding transient mean squared displacements for waiting time $t_w = 0$, complementing the data of Fig. 1 in the main manuscript. In the second section, maps of instantaneous experimental particle mobilities are shown for comparison with the average mobilities.

I. STRAIN EVOLUTION AND TRANSIENT MEAN SQUARED DISPLACEMENTS FOR ADDITIONAL APPLIED STRESSES

The time evolution of the strain $\gamma(t)$ is shown for additional values of the applied stress σ (Fig. SM-1), complementing the data presented in Fig. 1a,b of the manuscript. The corresponding mean squared displacements $\Delta y^2(t)$, determined immediately after application of stress, i.e. with waiting time $t_w = 0$, are also shown (lower panels). The data of Fig. 1 are also reported for comparison. The transition from a creep to a flow response occurs with increasing σ and is found to be gradual. The simulations show that the super-linear regime of the stress and the super-diffusion, both observed for $\sigma \gtrsim \sigma_y$, are especially pronounced for $\sigma \approx \sigma_y$, while they become less pronounced for larger stresses.

For the imposed stresses, when diffusion is observed at long times, we can determine the corresponding diffusion constants $D(\sigma)$ from the mean squared displacement $\Delta y^2(t)$. Similarly, the steady state strain rate $\dot\gamma$ can be obtained from the corresponding long-time data for strain $\gamma(t)$. Thus, $C(\sigma) = D(\sigma)/\dot\gamma$, defined in the main text, can be calculated and yields $C(\sigma) \sim \dot\gamma^{-0.2}$ (Fig. 2b). Taking this into account, i.e. by plotting $\Delta y^2/C(\sigma)$ as a function of strain γ, we obtain a collapse of the data, as shown in Fig. 2c.

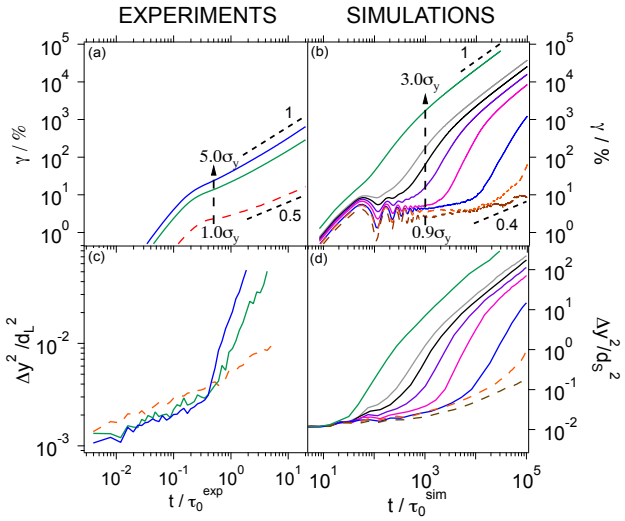

Fig-SM. 1. Comparison of (left) experimental and (right) simulation results. (top) Time-dependence of the strain $\gamma(t)$ for applied stresses (a) $\sigma/\sigma_y \approx 1.0$, 3.0 and 5.0, and (b) $\sigma/\sigma_y = 0.90, 1.10, 1.18, 1.39, 1.53, 1.67$, 1.80 and 3.0 (bottom to top). (bottom) Mean squared displacement in the vorticity direction, $\Delta y^2(t)$, for the same applied stresses (indicated by the same colors and line styles) immediately after stress application, i.e. for waiting time $t_w = 0$.

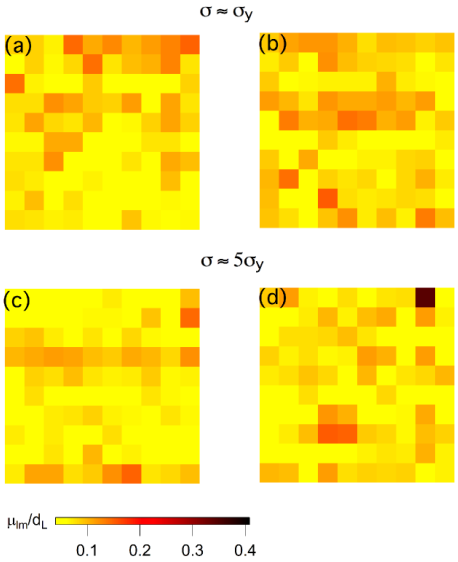

Fig-SM. 2. Maps of instantaneous experimental particle mobilities $\mu_{lm}(t)$ for $\sigma/\sigma_y \approx 1$ (top) and $\sigma/\sigma_y \approx 5$ (bottom), from (a,c) $0.18\tau_0^{\rm exp}$ to $0.46\tau_0^{\rm exp}$ and (b,d) $0.28\tau_0^{\rm exp}$ to $0.56\tau_0^{\rm exp}$. Each box has size $(2.8d_L)^2$.

II. MAPS OF INSTANTANEOUS DISPLACEMENTS

Instantaneous mobilities were calculated from $0.18\tau_0^{\rm exp}$ to $0.46\tau_0^{\rm exp}$ and $0.28\tau_0^{\rm exp}$ to $0.56\tau_0^{\rm exp}$, for $\sigma/\sigma_{\rm y} = 1.0$ (Fig. SM-2a,b) and $\sigma/\sigma_{\rm y} = 5.0$ (Fig. SM-2c,d). No regions of large instantaneous and correlated mobilities are observed. Moreover, the maps for $\sigma/\sigma_{\rm y} \approx 1$ and $\sigma/\sigma_{\rm y} \approx 5$ are comparable, contrary to what was observed in the average mobility maps (Fig. 4). This indicates that the enhanced average mobilities observed in Fig. 4 are not the result of sudden large displacements but rather occur through the accumulation of slightly above-average displacements of particles in a specific region which seem to occur with a slightly larger probability in the beginning (compare Fig. SM-2c,d to Fig. 4c).

III. MOVIES OF SHEARED SUSPENSIONS

Typical movies corresponding to series of confocal microscopy images of the sheared glass, for $\sigma \approx \sigma_{\rm y}$ and $\sigma \approx 5\sigma_{\rm y}$, acquired in a velocity-vorticity plane about 6 mm from the center of the geometries and 30 μm from the bottom plate. Images with 512×512 pixels, corresponding to 51 μm × 51 μm, were acquired at a rate of 67 frames per second.

This page has been left intentionally blank.

3.6. Publication 6: Moving in a mobile crowded environment: anomalous dynamics beyond the Lorentz gas model

submitted to Nature Communications

Authors: **T. Sentjabrskaja**, E. Zaccarelli, C. De Michele, F. Sciortino, P. Tartaglia, Th. Viogtmann, S. U. Egelhaaf and M. Laurati

1st author

TS prepared all materials, performed the experiments and analyzed the data. EZ, CDM, FS, PT run the computer simulations. TV obtained MCT predictions. TS, ML, EZ and SUE conceived and discussed the project and ML and SUE supervised the project. All authors contributed to the writing of the manuscript.

55 % contribution of TS

This page has been left intentionally blank.

Moving in a mobile crowded environment: anomalous dynamics beyond the Lorentz gas model

Tatjana Sentjabrskaja[1,§], Emanuela Zaccarelli[2,3,§,*] Cristiano De Michele[3], Francesco Sciortino[2,3], Piero Tartaglia[3], Thomas Voigtmann[4,5], Stefan U. Egelhaaf[1], and Marco Laurati[1,6†]

[1] *Condensed Matter Physics Laboratory, Heinrich Heine University, 40225 Düsseldorf, Germany*

[2] *CNR-ISC, Università di Roma "La Sapienza", Piazzale A. Moro* 2, 00185 *Roma, Italy*

[3] *Dipartimento di Fisica, Università di Roma "La Sapienza", Piazzale A. Moro* 2, 00185 *Roma, Italy*

[4] *Institut für Materialphysik im Weltraum, Deutsches Zentrum für Luft- und Raumfahrt (DLR), 51170 Köln, Germany*

[5] *Heinrich Heine University, Universitätsstraße 1, 40225 Düsseldorf, Germany and*

[6] *División de Ciencias e Ingeniería, Universidad de Guanajuato, Loma del Bosque 103, 37150 León, Mexico*

Many natural and industrial processes rely on constrained transport, such as proteins moving through cells [1–3], cell migration [4], particles confined in nanocomposite materials and gels [5–10], and individuals in highly dense groups of humans and animals or vehicular traffic conditions [11, 12]. These are examples of motion through crowded environments, in which the host matrix may retain some slow, glass-like dynamics. Here we investigate constrained transport in a slowly rearranging environment using binary colloids as model system, in which the dilute small spheres act as intruders and the large spheres form the mobile matrix, generalizing the work of Lorentz [13]. Using confocal differential dynamic microscopy to resolve the small particles dynamics, we discover a critical size asymmetry at which anomalous collective transport appears, manifested as a logarithmic decay of the density autocorrelation functions. Numerical simulations elucidate the crucial role played by the host mobility, an aspect which has not been previously considered [13–16]. We demonstrate that the continuous creation and disruption of channels within the matrix is central for the observed anomalous behaviour. These results, crucially depending on the presence of size-induced dynamic asymmetry, are of relevance for a wide range of phenomena ranging from glassy systems to cell biology.

In the presence of a confining medium, the transport of objects deviates from normal diffusion. Anomalous behaviour, usually manifested by the presence of sub-diffusivity [17, 18], emerges as a common feature of the dynamics. In the Lorentz gas [13, 15], the prototype model for anomalous transport, point-like intruders move in voids between immobile, randomly-distributed particles. Their motion becomes sub-diffusive once the voids are barely interconnected. When a critical density of immobile particles is reached, they percolate and the intruder becomes localized [13]. Softness of the immobile particles or interactions among the intruders are known to modify this picture [16, 19–22].

So far the slow movement of the host matrix has been largely ignored, despite representing realistic situations of biological [1–4, 12, 23] and industrial interest [5–11]. To address confined transport in slowly moving matrices, here we investigate a binary colloidal mixture of small and large hard spheres, of diameters σ_s and σ_l, which represent intruders and host matrix, respectively. Changing the size ratio $\delta = \sigma_\mathrm{s}/\sigma_\mathrm{l}$ we also modify the dynamic asymmetry of the system. We focus on volume fractions of large particles $\phi_l > 0.5$ approaching the glass transition, occurring at $\phi_l^g \approx 0.58$. In contrast the volume fraction of the intruders ϕ_s is very small with $x_\mathrm{s} \equiv \phi_\mathrm{s}/\phi = 0.01$. Such a system combines the confinement of a dilute fluid of mobile intruders with the slow dynamics of the matrix (Fig. 1a). It thus provides the simplest minimal model for the investigation of motion in crowded soft and biological matter.

Despite its conceptual simplicity, experimental investigations of the dynamics of small intruders in mixtures of Brownian particles with large size-asymmetry are scarce. This might be due to limitations in the spatial and temporal resolution of confocal microscopy which make it difficult to track particles that are significantly smaller than another species of Brownian, i.e. at most micron-sized, particles. To overcome these limitations, we keep the selectivity of fluorescent labelling (Fig.1b), which allows us to separately determine the small and large particles. However, instead of tracking we employ the recent Differential Dynamic Microscopy (DDM) technique [24–26]. This is based on the time correlation in Fourier space of the difference between images separated by a time delay Δt (Fig.1c) and provides a measure of the (isotropic) collective intermediate scattering function or density autocorrelation function $f(q, \Delta t)$, where q is the modulus of the wavevector $\mathbf{q}$ (Fig.1d). The decay of $f(q, \Delta t)$ as a function of time delay Δt corresponds to the loss of correlation of the particle density on a length scale determined by q^{-1} within the time delay

*emanuela.zaccarelli@cnr.it

†marco.laurati@uni-duesseldorf.de

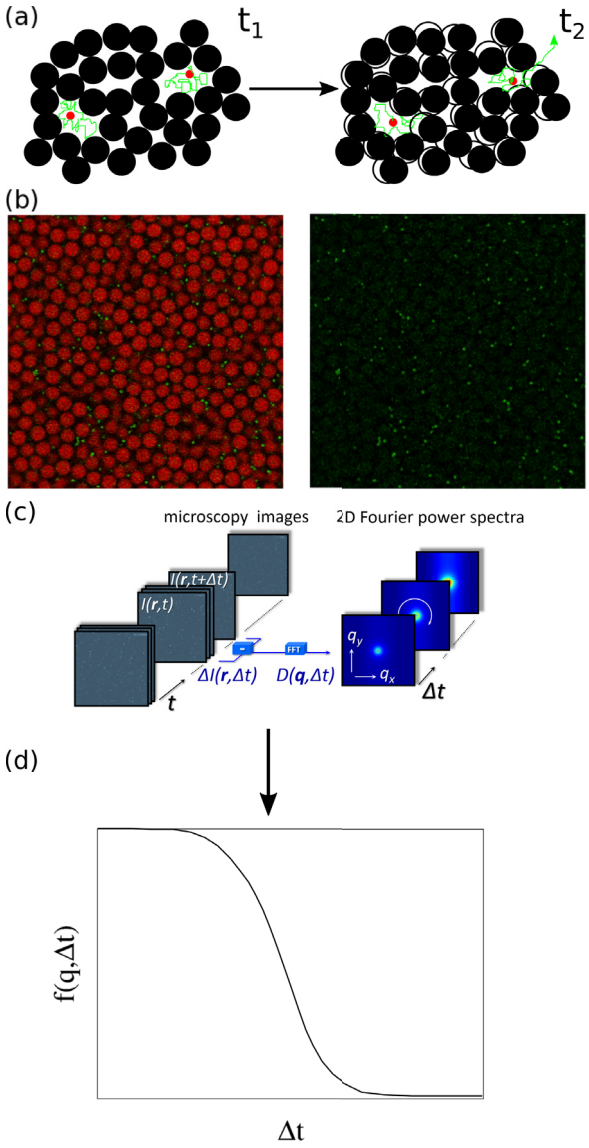

FIG. 1: **Illustration of the system and measurement method:** (a) Schematic illustration of our system at two times t_1 and $t_2 > t_1$ highlighting the trajectories (green lines) of the intruders (red beads) in voids and between voids made possible due to the mobility of the matrix particles. (b) An exemplary confocal microscopy image of a mixture with $\delta = 0.18$ and $\phi = 0.58$ in which (left) both particles and (right) only the small particles are shown. (c) Image differences at different delay times Δt are Fourier transformed to give 2D Fourier power spectra for different Δt. (d) After azimuthal averaging and additional treatment the intermediate scattering function $f(q, \Delta t)$ is obtained.

Δt. The decay time is therefore related to the characteristic time of the particle motions on the length scale q^{-1}. Approaches similar to DDM, like fluorescence correlation spectroscopy, do not provide information on the probed length scale. This information is crucial to investigate the effect on the dynamics of the size of the voids in which the small particles move. The function $f(q, \Delta t)$ can also be obtained by dynamic light scattering, which, however, does not allow us to distinguish the two species by fluorescent labeling. We also study the same system by mode coupling theory of the glass transition (MCT) and, both in the case of mobile and immobile matrix particles, by numerical simulations, complementing the experimental results and providing insights on the underlying microscopic mechanisms.

Fig. 2a-d shows the measured collective intermediate scattering functions $f(q, \Delta t)$ of the small particles for size ratios $\delta = 0.18$ (Fig.2a,c) and $\delta = 0.28$ (Fig.2 b,d) for different ϕ and q. For $\delta = 0.18$ and all ϕ and q, $f(q, \Delta t)$ vs.

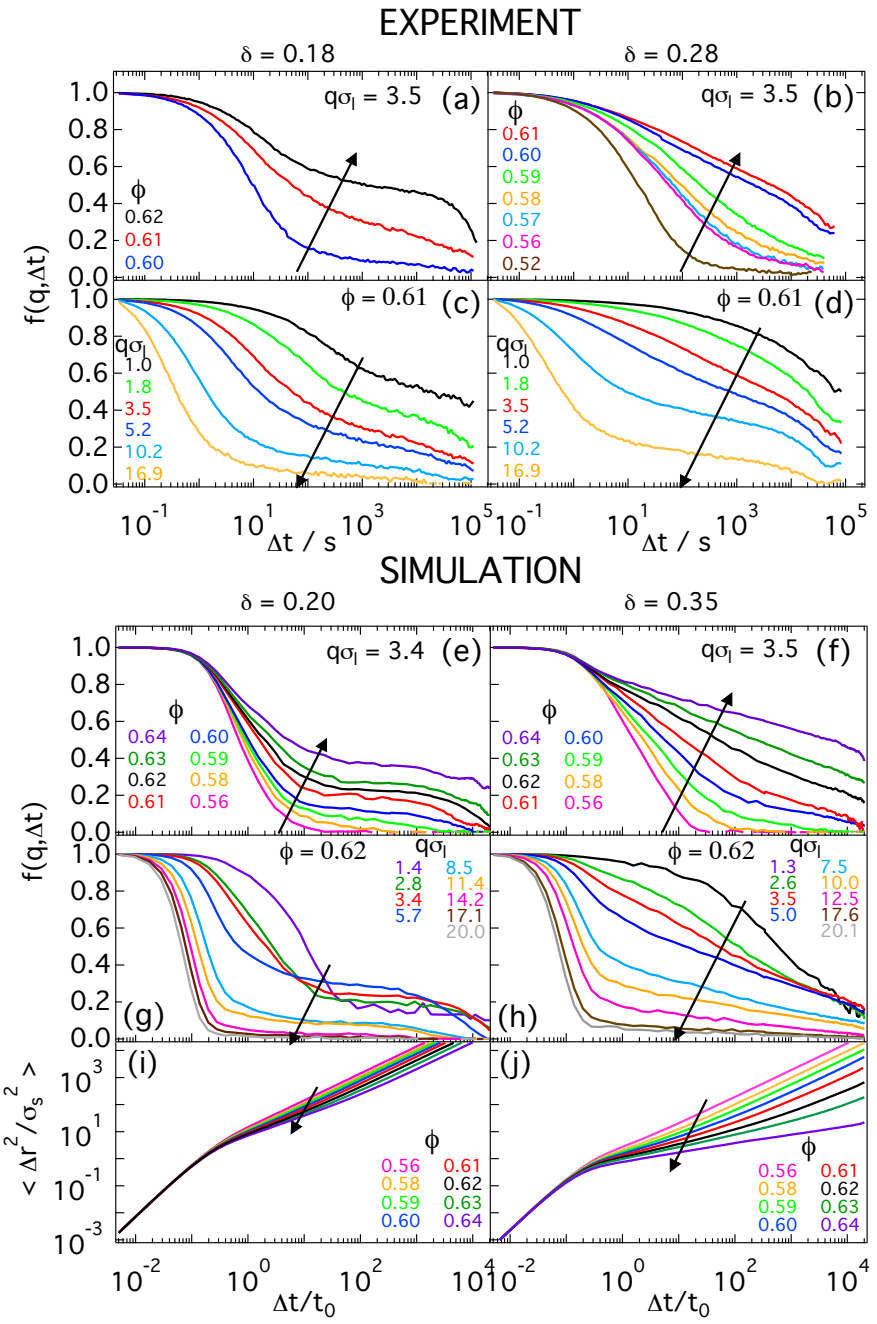

FIG. 2: **Dynamics of the intruders as observed in experiments and simulations:** Intermediate scattering functions $f(q, \Delta t)$ (a–h) and mean-squared displacements $\langle \Delta r^2/\sigma_s^2 \rangle$ (i–j) as a function of delay time Δt, describing the dynamics of small spheres in binary mixtures with size ratios δ below (left) and around (right) the onset of anomalous dynamics, for different magnitudes of the scattering vector q and total volume fraction ϕ (as indicated).

Δt shows an initial decay, followed by a ϕ-dependent intermediate plateau, and eventually a decay to zero at longer times (Fig.2a). The initial decay can be associated with the Brownian motion of small particles within the voids of the large particles matrix. It becomes increasingly slower for increasing ϕ (Fig.2a) and decreasing q, which means increasing length scale (Fig.2c). The intermediate plateau indicates the dynamical arrest of the collective dynamics, i.e. of density fluctuations, and hence the absence of diffusion on the length scale determined by q^{-1}. The height of the plateau increases progressively with increasing ϕ, similarly to the scenario in which a percolation-type transition

is approached [19, 27], and indicates that voids become smaller and particles are increasingly localised [28]. The final decay to zero of $f(q, \Delta t)$ shows that particles are still able to diffuse at long times. For a larger size ratio, $\delta = 0.28$, and comparable ϕ values, a completely different scenario appears. Beyond $\phi \approx 0.60$, $f(q, \Delta t)$ shows remarkable anomalous dynamics, manifested in an extended logarithmic decay over three decades in time. This intriguing behavior is mostly visible at $\phi \gtrsim 0.60$ and $q\sigma_{\rm l} \approx 3.5$, i.e. when probing a length scale of about $2\sigma_{\rm l}$ (Fig.2b), which is comparable to the size of the matrix particles.

The experimental findings are confirmed by simulations. For $\delta = 0.20$ no anomalous behavior of the small particles is detected in the collective $f(q, \Delta t)$ (Fig.2e,g) and in the self $f^{self}(q, \Delta t)$ correlation functions (Supplementary, Fig. S1). Note that for $\delta = 0.20$, $f(q, \Delta t)$ displays a two step-relaxation and the presence of localisation (Fig.2e,g), which is absent in $f^{self}(q, \Delta t)$. Also the mean squared displacements (MSD) $\langle \Delta r^2 \rangle \equiv \langle |\vec{r}(t) - \vec{r}(0)|^2 \rangle$, with $\vec{r}(t)$ the position of a particle at time t, show almost no localisation at all ϕ (Fig.2i). This decoupling between collective ($f(q, \Delta t)$) and self dynamics ($f^{self}(q, \Delta t)$, MSD) originates from the glassy environment in which the intruders move. Correlated motions of a group of intruders distributed within the matrix are more influenced by the slow dynamics of the matrix particles than uncorrelated single particle motions, which are mostly sensitive to the local structure of the voids [19, 29]. For $\delta = 0.35$ we find the emergence of logarithmic anomalous relaxations of $f(q, \Delta t)$ (Fig. 2f,h) and $f^{self}(q, \Delta t)$ (Supplementary, Fig.S1), for comparable q as in the experiments. Additional simulations for $\delta = 0.30$ and $\delta = 0.40$ also show a logarithmic decay over a smaller time window (Supplementary, Figs. S1,S2). Furthermore, for $\delta = 0.35$ and $\phi \gtrsim 0.60$ the MSD displays a clear sub-diffusive behavior, i.e. $\langle \Delta r^2 \rangle \sim t^{\alpha}$ with $\alpha < 1$ (Fig. 2j). Finally, for $\delta = 0.5$, $f(q, \Delta t)$ and $f^{self}(q, \Delta t)$ show a two-step decay and the MSD a localisation plateau at large ϕ (Supplementary, Fig. S2), consistent with a standard glass transition of the small particles. At all investigated δ and for $\phi_l > 0.55$, the dynamics of the large particles are typical of glassy states and within the investigated time window are indicating localisation and motion within nearest neighbour cages of approximate size $0.1\sigma_{\rm l}$ (Supplementary, Fig. S3).

These results suggest the existence of a critical size ratio $\delta_c \simeq 0.35$ at which pronounced anomalous dynamics mark the transition from a diffusive to a glassy regime of the small particles moving in the large particles matrix. The δ_c and ϕ values where this transition is observed are slightly smaller in the experiments than in the simulations. This is attributed to the fact that in the experiments small particles are polydisperse, while in the simulations they are monodisperse. Polydispersity is expected to affect the transition since the average size particles might still be able to diffuse through the void spaces in the matrix, whereas the largest particles of the size distribution might no longer be able to diffuse through them. The crossover observed at δ_c is analogous to the transition from a diffusive to a localized state in the Lorentz gas. However, the excluded volume of the intruder generates a coupling with the host matrix and, due to the mobility of the matrix, also between intruders in different voids, mutating localization into a glass transition due to the (slow) mobility of the matrix particles. Although this is apparently similar to intruders in a fixed matrix [16, 19, 20], the logarithmic decay of $f(q, \Delta t)$ stands out as a novel feature.

On the basis of mode coupling theory (MCT), the appearance of logarithmic decays in $f(q, \Delta t)$ [30–32] is usually attributed to competing collective arrest mechanisms, like caging and bonding, and to higher-order glass transition singularities [29, 33–35]. We solved MCT equations for a binary mixture of hard spheres and $x_{\rm s} = 0.01$. The resulting correlators $f(q, \Delta t)$ for a range of packing fractions around the MCT glass transition, $\phi_c \approx 0.516$ and $\delta = 0.20$ and 0.35, are shown in Fig. 3. No clear sign of logarithmic decay of $f(q, \Delta t)$ is found for these states in MCT: while an approximate logarithmic dependence of the decay is observed at $\delta = 0.35$, $\phi = 0.51$ and $q\sigma_l = 3.4$, this extends over an interval of times much shorter than in experiments and simulations. In addition, upon further increasing ϕ the logarithmic dependence does not take over, but instead a two-step decay is found, followed by the arrest of the dynamics (Supplementary, Fig. S6). Indeed higher-order singularities are not present in this region of ϕ and $x_{\rm s}$ values [29]. On the other hand, the MSD obtained from MCT shows the qualitative signatures found in simulations: for $\delta = 0.20 < \delta_c$, the long-time diffusion barely slows down with increasing ϕ, indicating a partially frozen glass in which the small particles are mobile. For $\delta = 0.35 \approx \delta_c$, anomalous sub-diffusion is observed, indicating that the glass-transition of the large particles and the localization transition of the small particles are close to each other. Thus, the appearance of approximately logarithmic decay in Fig. 3 could be a signal of the transition from coupled dynamics of the two species at large δ to decoupled dynamics at small δ.

A direct visualisation of small particle locations shows that the transition from diffusive dynamics at small δ to localised dynamics at large δ observed in experiments, simulations and theory is associated, similarly to the Lorentz gas, with the transition from percolating to non-percolating voids within the matrix. However, a static picture of the void geometry cannot describe this transition, because the evolution of the void space involves a second timescale t_2 (Fig. 1a, right) associated with the mobility of the matrix. To analyse the dynamic rearrangements of the void structure, we monitor the evolution of the position of the small particles which explore this evolving structure. Accordingly, in Fig. 4a,b we show superpositions of small particle locations in 2D time series of confocal images over a long total observation time $t_f^{\rm exp} = 297$ s, at which $f(q, \Delta t)$ for $\delta = 0.18$ shows a decay of correlations, while $f(q, \Delta t)$ for $\delta = 0.28$ is in the logarithmic regime. For $\delta = 0.18$ we find that, within the observation time, small particles

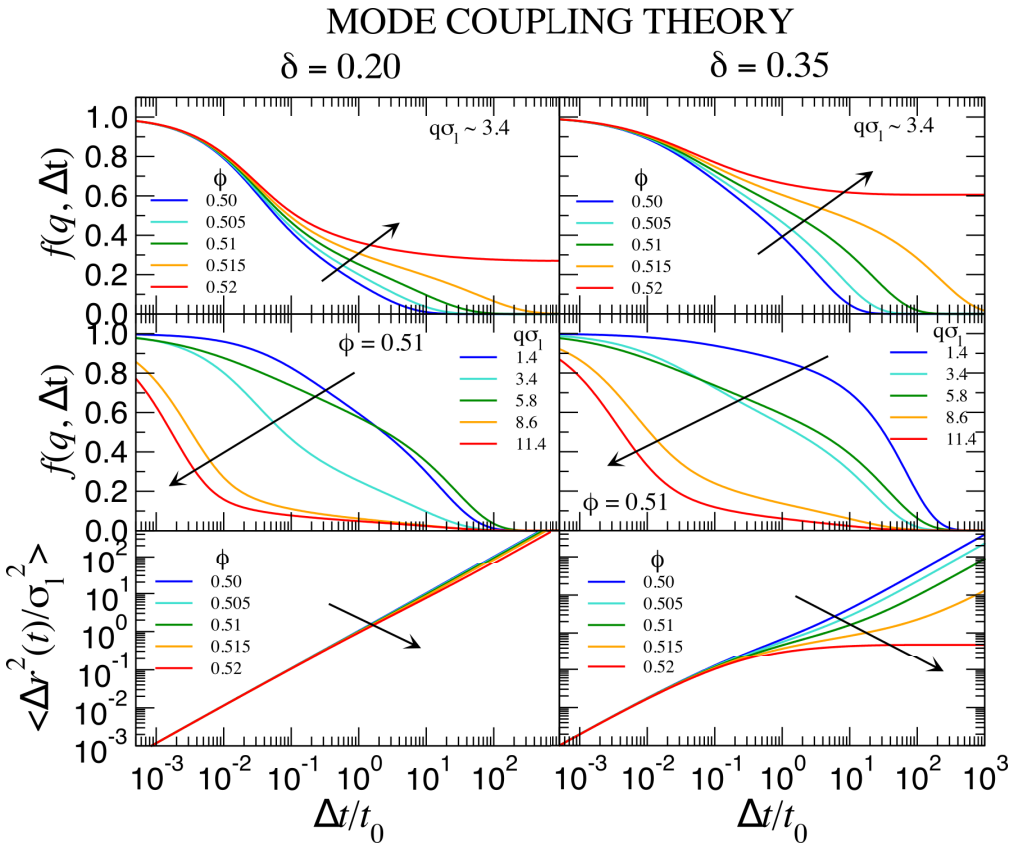

FIG. 3: **Dynamics of the intruders as predicted by MCT:** Intermediate scattering functions $f(q, \Delta t)$ (top, middle) and mean-squared displacements $\langle \Delta r^2/\sigma_1^2 \rangle$ (bottom) describing the dynamics of small spheres in binary mixtures with size ratios delta below (left) and around (right) the onset of anomalous dynamics, for different magnitudes of the scattering vector q and total volume fraction ϕ (as indicated).

easily explore the whole space of the accessible voids which form a percolating network. In contrast, for $\delta = 0.28$ particles mostly explore their local environment, since voids only barely connect even at long times, allowing only a slow, partial exploration of the available void space. Simulations provide not only particle locations but also single-particle trajectories in three dimensions allowing a more quantitative determination of the percolation of the explored space. Visualisations of typical small particle trajectories for a fixed observation time $t_f^{\rm sim} = 100 t_0$ (comparable to the experiments) and three different values of δ confirm the experimental features (Fig.4c): within the observation time small particles explore a percolated space for small δ, while for the critical size ratio the space is barely connected, indicating that particles can rarely escape the local environment which is only possible due to the stochastic opening and closing of channels between neighbouring void spaces, associated with the matrix motion on the long time scale t2. In addition the simulations show that for even larger δ the explored space is disconnected. To quantify these observations we calculate the size distribution $n(s)$ of the space s explored by small particles within a certain time interval, as explained in Methods. The results are shown in Fig.4d for different δ values for an observation time equal to $t_f^{\rm sim}$. This time corresponds to the interval over which the cluster size distribution of the explored space for δ_c is close to percolation, as indicated by the power-law dependence $n(s) \sim s^{-2.19}$, consistent with random percolation predictions [36]. Percolation at $t_f^{\rm sim}$ for δ_c is also indicated, in a finite-size system, by the maximum of the average size of finite-size clusters (excluding percolating clusters, calculated as explained in Methods) $L_{\rm c}$ as a function of time (Fig.4e). For the other size ratios instead $L_{\rm c}$ is very small at $t_f^{\rm sim}$. At small δ this is due to the fact that particles can easily move through channels connecting voids, and thus the explored space quickly associates into a percolating cluster. On the other hand, for large δ the creation of channels that allow the small particles to move between neighbouring void spaces is rare, and thus percolation of the explored space does not occur at $t_f^{\rm sim}$ and only voids corresponding to the size of monomers, dimers and few-mers are observed. This analysis reveals very different timescales at which the explored space percolates at different δ. These timescales depend, besides δ, on the timescale t_2 of the evolution of the void space, associated with the thermal motion of the matrix particles: yet this analysis is

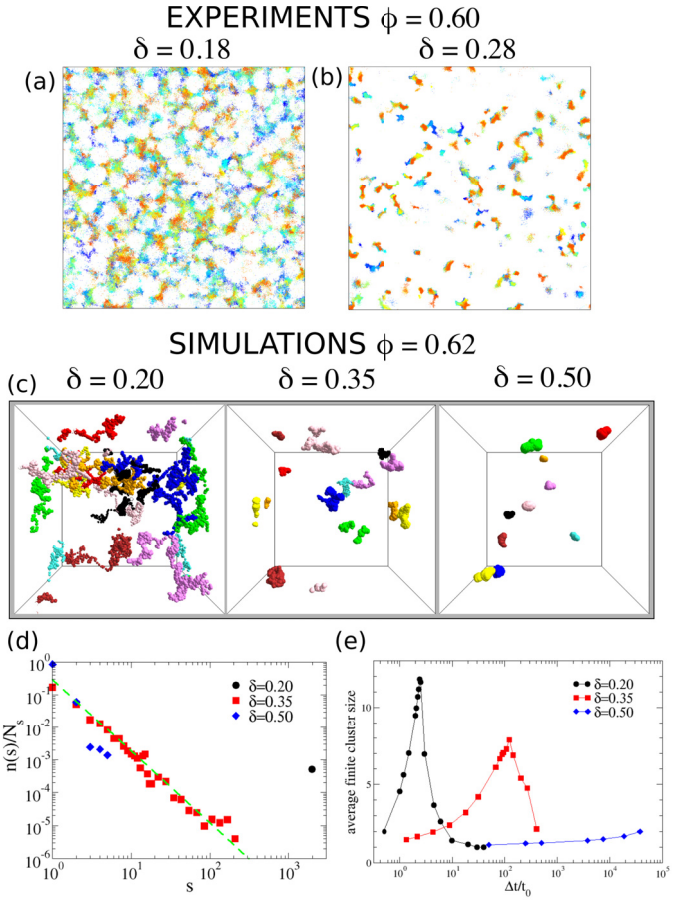

FIG. 4: **Illustration of the space explored by small particles during their motions:** (a-b) Overlay of small particle positions at different times (colour coded from blue, corresponding to $t_i^{\rm exp} = 0$ s to red, corresponding to $t_f^{\rm exp} = 297$ s with time steps of 33 s), obtained by particle tracking applied to 2D confocal microscopy images, for $\phi = 0.60$ and (a) $\delta = 0.18$, (b) $\delta = 0.28$. (c) Positions of ten small particles (distinguished by different colours) for (left) $\delta = 0.2$, (middle) $\delta = 0.35$, and (right) $\delta = 0.5$, for a fixed total time of the trajectories $t_f^{\rm sim} = 100t_0$, comparable to the experiments r(d) Distribution $n(s)$ (normalized by the number of small particles N_s) of the size s of the space explored by small particles, evaluated within a fixed time interval $t_f^{\rm sim} = 100t_0$. For $\delta = 0.35$ data are consistent with a power-law dependence $n(s) \sim s^{-2.19}$, consistent with random percolation (dashed line), while for $\delta = 0.20$ all particles belong to the same cluster. (e) Average size $L_{\rm c}$ of finite clusters as a function of time, for different δ, as indicated. The maximum in each curve signals the onset of percolation.

not offering substantial evidence that this mobility of the matrix is causing the logarithmic decays of the correlators observed at δ_c.

To go one step further and link the residual mobility of the matrix particles with the anomalous logarithmic decays, we perform additional simulations (for $\phi = 0.62$) for immobile matrix particles and compare the dynamics of the intruders with the case of a mobile matrix. When the large particles are immobile (Fig. 5a), the MSD shows a sub-diffusive regime (MSD$\sim t^{\alpha}$) followed by diffusion at long times (upward curvature) or localization (downward curvature), depending on δ. The crossover between these two long time behaviors takes place at a critical size ratio $\delta_c^{\rm imm} \sim 0.275$ where the MSD remains subdiffusive also at long times [18]. The value of δ_c is smaller for the simulation with immobile large particles. This finding is consistent with the opening of channels as a consequence of the thermal motion of the matrix particles. In the case of mobile matrix particles localisation is *never* observed (Fig. 5b): even for large δ, the residual motion of the matrix allows the small particles to move and hence their MSD increases at long times. Furthermore, the subdiffusive regime is only observed for $\delta < \delta_c^{\rm imm}$ and thus in a smaller range than for mobile particles. This is consistent with the opening of channels as a consequence of the thermal motion of the matrix particles, which allows larger particles to move between voids. We also find that $f^{self}(q, \Delta t)$ calculated for the case of an immobile matrix displays a power-law dependence on time extending for several decades (Fig. 5c), in agreement with the Lorentz gas model [37], while the collective $f(q, \Delta t)$ displays neither a power-law nor a logarithmic dependence (Supplementary, Fig. S4). In the case of a mobile matrix, however, power law behaviour is not observed

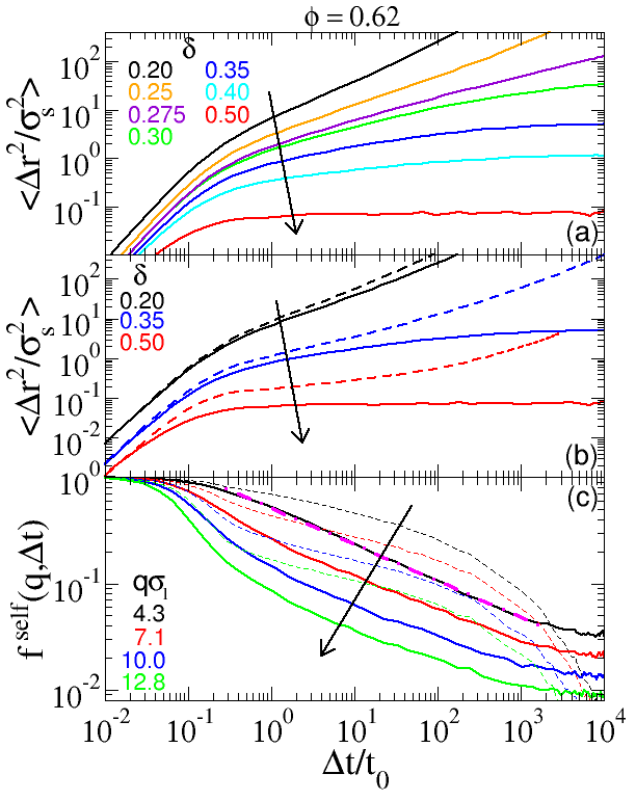

FIG. 5: **Comparison of the dynamics of small particles in a mobile or immobile large particles matrix:** (a) MSDs of the small particles for immobile large particles at $\phi = 0.62$ and various values of δ, as indicated. For $\delta_c^{\rm imm} \sim 0.275$ a clear subdiffusive behavior is observed at all times. (b) Comparison of the MSDs of the small particles at $\phi = 0.62$ for mobile (dashed lines) and immobile (full lines) large particles, for increasing δ, as indicated. (c) Self intermediate scattering functions $f^{\rm self}(q, \Delta t)$ at $\phi = 0.62$ and different wavevectors $q\sigma_1$, as indicated, for $\delta = 0.25$ (immobile, full lines) and $\delta = 0.35$ (mobile, dashed lines) highlighting the power-law dependence (dot-dashed line) in the immobile case.

but, close to δ_c, a logarithmic dependence is found. Thus, thermal motion of the matrix particles gives rise to the logarithmic decay, a novel type of dynamics which does not occur in the Lorentz model.

Our combined experimental, simulation and theoretical study shows that dynamics of intruders in a mobile crowded environment requires a description beyond the classical Lorentz gas model. The novel application of the confocal DDM technique to concentrated binary colloidal mixtures allows us to investigate the collective dynamics of intruders in a mobile matrix, revealing extended anomalous dynamics for specific values of the size asymmetry and of the probed length scale. While the Lorentz model predicts a power-law behavior, which is typical for systems close to a percolation transition, in the case of a mobile matrix we observe a logarithmic decay of the collective and self density fluctuations over at least three decades in time, at length scales comparable to the size of the matrix particles. This logarithmic decay marks the transition between a diffusive behaviour of intruders in a glassy medium for small size ratios $\delta < \delta_c$, where transient localization is due to the excluded volume of the mobile matrix, and glassy dynamics of the intruders at large size ratios $\delta > \delta_c$, due to crowding. Our results thus show that both percolation and glassy dynamics have to be considered. By comparing mobile and immobile matrix environments, we demonstrate that the dynamics of the small particles is profoundly altered, in a qualitative way, by the continuous evolution of channels in the mobile matrix, due to the thermal motion of large particles. A mobile matrix corresponds to an environment in which small intruders move in many real systems and applications, like in glasses, nanocomposite materials, chromatography, catalysis, oil recovery, drug delivery or cell signaling, cell interiors, human and animal crowds and vehicular traffic. We thus expect that our findings will inspire the development of a more realistic description of these situations.

Methods

Materials We investigated dispersions of sterically stabilized PMMA spheres of diameters $\sigma_{l(1)} = 3.10$ μm (polydispersity 0.07) or $\sigma_{l(2)} = 1.98$ μm (polydispersity 0.07) mixed with spheres of diameter $\sigma_s = 0.56$ μm (polydispersity 0.13) (fluorescently labeled with nitrobenzoxadiazole (NBD)), in a cis-decalin/cycloheptyl-bromide mixture which closely matches their density and refractive index. The size ratio of the mixtures is $\delta = 0.18$ ($\sigma_{l(1)}$) and $\delta = 0.28$ ($\sigma_{l(2)}$), respectively. After adding salt (tetrabutylammoniumchloride), this system presents hard-sphere like interactions [38, 39]. A sediment of the large spheres with $\phi = 0.65$ or of the small spheres with $\phi = 0.67$, as estimated from comparison with numerical simulations and experiments [40, 41], is diluted to obtain one-component dispersions with desired volume fraction ϕ. Following a recent study [42], the uncertainty $\Delta\phi$ can be as large or above 3 %. Using the nominal volume fraction ϕ of the large spheres as a reference, the volume fraction of the samples containing the small particles are adjusted in order to obtain comparable linear viscoelastic moduli in units of the energy density $3k_BT/4\pi R^3$, where k_B is the Boltzmann constant, T the temperature and R the particles' radius, while multiplying the frequency by the free-diffusion Brownian time $\tau_0 = 6\pi\eta R^3/k_BT$, where $\eta = 2.2$ mPa s is the solvent viscosity. In this way we obtain samples with comparable rheological properties and, according to the generalised Stokes-Einstein relation [43], also dynamics and hence a similar location with respect to the glass transition. The comparable dynamics but different polydispersities of the one-component samples imply slightly different ϕ. Samples with different total volume fractions and a fixed composition, namely a fraction of small particles $x_s = \phi_s/\phi = 0.01$, where ϕ_s is the volume fraction of small particles, are prepared by mixing the one-component samples.

DDM measurements Confocal microscopy images were acquired in a plane at a depth of approximately 30 μm from the coverslip. Images with 512×512 pixels, corresponding to 107 μm × 107 μm, were acquired at a fast rate of 30 frames per second to follow the short-time dynamics and at a slow rate, between 0.07 and 0.33 frames per second, depending on sample, to follow the long-time dynamics. Image series were acquired using a Nikon A1R-MP confocal scanning unit mounted on a Nikon Ti-U inverted microscope, with a 60x Nikon Plan Apo oil immersion objective (NA = 1.40). The pixel size at this magnification is 0.21 μm × 0.21 μm. The confocal images were acquired with the maximum pinhole size allowed by the microscope, corresponding to a pinhole diameter of 255 μm. Time series of 10^4 images were acquired for 2 to 5 different volumes, depending on sample.

DDM analysis Particle movements induce fluctuations of the fluorescence intensity in the images, $i(x, y, t)$, with x, y the coordinates of a pixel in the image and t the time at which the image was recorded. To obtain additional information on the characteristic length scales of particle motions, $i(x, y, t)$ can be Fourier transformed, yielding $\hat{i}(\mathbf{q}, t)$, with $\mathbf{q}$ the wave vector in Fourier space, and then differences of the Fourier transformed image intensities can be correlated (Fig. 1c) to obtain the image structure function $D(\mathbf{q}, \Delta t)$:

$$D(\mathbf{q}, \Delta t) = \langle |\hat{i}(\mathbf{q}, t + \Delta t) - \hat{i}(\mathbf{q}, t)|^2 \rangle \quad (1)$$

where $\langle\rangle$ represents an ensemble average. This analysis technique is named Differential Dynamic Microscopy (DDM) [24]. The intermediate scattering function $f(\mathbf{q}, \Delta t)$ (Fig. 1d) can be extracted from the image structure function:

$$D(\mathbf{q}, \Delta t) = A(\mathbf{q})[1 - f(\mathbf{q}, \Delta t)] + B(\mathbf{q}) \quad (2)$$

with $A(q) = N|\hat{K}(q)|^2 S(q)$, where N is the number of particles in the observed volume, $\hat{K}(q)$ is the Fourier transform of the Point-Spread Function of the microscope, $S(q)$ is the static structure factor of the system, and $B(q)$ accounts for the camera noise. The inverse of the wave vector q determines the length scale over which the particle dynamics are probed. Thus $f(\mathbf{q}, \Delta t)$ is obtained, similarly to dynamic light scattering (DLS)[44], but for the present system the advantage of DDM over DLS is that fluctuations of the incoherent fluorescence signal can be correlated, a possibility which is excluded by the requirement of coherence of light in DLS. Furthermore, use of a confocal microscope drastically reduces the amount of background fluorescence of the measurements, significantly improving the determination of $f(\mathbf{q}, \Delta t)$. The effect of particles moving in and out of the observation plane on $f(\mathbf{q}, \Delta t)$ was found to be negligible for all samples, as determined by the q-dependence of the relaxation times of the initial decay of $f(\mathbf{q}, \Delta t)$, where no plateau at small q values was observed [25, 45].

Particle Localization Coordinates of the small particles were extracted from time series of 2-dimensional images using standard particle localization routines based on the centroiding technique [46]. Only the particle positions at each time could be determined, not the full trajectories. Indeed the displacement of small particles during the time delay Δt between two successive frames is comparable or larger than their diameter, which implies that identifying particles after a Δt becomes too uncertain.

Simulations We perform event-driven Molecular Dynamics simulations[47] in the NVT ensemble in a cubic box with periodic boundary conditions for binary mixtures of hard spheres, of which the large components are 7% polydisperse by a discrete Gaussian distribution[48] and the small ones are monodisperse. For each studied δ we vary the total number of particles in the range of a few thousands. The number of small particles thus varies from 1980 for $\delta = 0.2$ to 292 for $\delta = 0.5$. Mass and length are measured in units of particle mass m, average large particle diameter σ_l, whereas time is in units of $t_0 = \sqrt{m\sigma_l^2/\kappa_B T}$, where k_B is the Boltzmann constant and T the temperature. For the simulations with immobile hard spheres, after equilibration of the mixture, we freeze the large particles only. To roughly estimate the critical size ratio which demarcates the transition between diffusive and localized states, we averaged results over ten different matrix realizations.

Mode Coupling Theory The equations determining $f(q,t)$ and $\langle \Delta r^2(t) \rangle$ within MCT were solved for a binary mixture of hard spheres within the Percus-Yevick approximation for the static structure; for details on the theory and the numerical procedure, see Ref. [29]. The $f(q,\Delta t)$ were obtained using a wave-number grid of equidistant steps $\Delta q = 0.4/\sigma_{\rm l}$, with large-$q$ cutoff $q\sigma_{\rm l} = 400$. Brownian dynamics is assumed with the short-time diffusion coefficients following the Stokes-Einstein relation; the diffusion coefficient of the large particles sets the unit of time τ_0. In the calculations, the total packing fraction ϕ is varied, keeping $x_{\rm s} = \phi_s/\phi = 0.01$ fixed.

Calculation of the size distribution of the explored space To evaluate the distribution of space sampled by the small particles during time we employ the following procedure.

1. We generate a sequence of N_c configurations saved at equally spaced times t_i (with $i = 1 \dots N_c$) within a given time window t_{N_c}. The time interval Δt_c between two successive configurations, i.e. $\Delta t_c = t_{i+1} - t_i$ is chosen in such a way that $\langle \Delta r^2(\Delta t_c) \rangle / \sigma_{\rm s}^2 = 0.5$.

2. We overlap all N_c configurations and perform a cluster size analysis according to the following criteria: (i) the same particle at different times t_i belong to the same cluster; (ii) if two particles overlap, they belong to the same cluster; (iii) the size s of a cluster is defined as the number of distinct particles belonging to the same cluster (running from one to the total number of small particles)

To improve statistics we average the cluster size distribution $n(s)$ over a set of at least 10 independent groups of N_c configurations. The average size of finite clusters is calculated as $L_{\rm c} = \sum s^2 n(s) / \sum s n(s)$, excluding percolating clusters.

Acknowledgments

We thank Andrew Schofield (University of Edinburgh) for providing the PMMA particles and Manuel A. Escobedo-Sánchez for discussions. TS, SUE and ML acknowledge funding by the Deutsche Forschungsgemeinschaft (DFG) through the research unit FOR1394, project P2, and funding of the confocal microscope through grant INST 208/617-1 FUGG. EZ and CDM acknowledge support from MIUR through a Futuro in Ricerca grant FIRB ANISOFT (RBFR125H0M). EZ, CDM and FS acknowledge support from ERC-226207-PATCHYCOLLOIDS and ETN-COLLDENSE (H2020-MCSA-ITN-2014, Grant No. 642774).

Author contributions

§ These authors contributed equally to this work. TS, SUE and ML planned, performed, analysed and interpreted the experiments, EZ, PT, CDM and FS planned, ran and interpreted the simulations, TV obtained MCT predictions. All authors contributed to the interpretation and comparison of the data as well as the writing of the manuscript.

Additional Information

Competing financial interests: The authors declare no competing financial interests.

[1] Ellis, R. J. & Minton, A. P. Cell biology: Join the crowd. *Nature* **425**, 27–28 (2003).

[2] Di Rienzo, C., Piazza, V., Gratton, E., Beltram, F. & Cardarelli, F. Probing short-range protein brownian motion in the cytoplasm of living cells. *Nat. Commun.* **5**, 5891 (2014).

[3] Sadati, M., Nourhani, A., Fredberg, J. J. & Taheri Qazvini, N. Glass-like dynamics in the cell and in cellular collectives. *WIREs Syst Biol Med* **6**, 137–149 (2014).

[4] Angelini, T. E. *et al.* Glass-like dynamics of collective cell migration. *Proc. Natl. Acad. Sci.* **108**, 4714–4719 (2011).

[5] Cherdhirankorn, T. *et al.* Fluorescence correlation spectroscopy study of molecular probe diffusion in polymer melts. *Macromolecules* **42**, 4858–4866 (2009).

[6] Kalathi, J. T., Yamamoto, U., Schweizer, K. S., Grest, G. S. & Kumar, S. K. Nanoparticle diffusion in polymer nanocomposites. *Phys. Rev. Lett.* **112**, 108301 (2014).

[7] Salami, S., Rondeau-Mouro, C., van Duynhoven, J. & Mariette, F. Probe mobility in native phosphocaseinate suspensions and in a concentrated rennet gel: Effects of probe flexibility and size. *J. Agric. Food Chem.* **61**, 5870–5879 (2013).

[8] Grabowski, C. A. & Mukhopadhyay, A. Size effect of nanoparticle diffusion in a polymer melt. *Macromolecules* **47**, 7238–7242 (2014).

[9] Narayanan, S., Lee, D. R., Hagman, A., Li, X. & Wang, J. Particle dynamics in polymer-metal nanocomposite thin films on nanometer-length scales. *Phys. Rev. Lett.* **98**, 185506 (2007).

[10] Babu, S., Gimel, J. C. & Nicolai, T. Tracer diffusion in colloidal gels. *J. Phys. Chem. B* **112**, 743–748 (2008).

[11] Helbing, D. Traffic and related self-driven many-particle systems. *Rev. Mod. Phys.* **73**, 1067–1141 (2001).

[12] Gravish, N., Gold, G., Zangwill, A., Goodisman, M. A. D. & Goldman, D. I. Glass-like dynamics in confined and congested ant traffic. *Soft Matter* **11**, 6552–6561 (2015).

[13] Lorentz, H. A. Le mouvement des électrons dans les métaux. *Arch. Neerl. Sci. Exact Natur.* **10**, 336 (1905).

[14] Skinner, T. O. E., Schnyder, S. K., Aarts, D. G. A. L., Horbach, J. & Dullens, R. P. A. Localization dynamics of fluids in random confinement. *Phys. Rev. Lett.* **111**, 128301 (2013).

[15] Höfling, F., Franosch, T. & Frey, E. Localization transition of the three-dimensional lorentz model and continuum percolation. *Phys. Rev. Lett.* **96**, 165901 (2006).

[16] Kurzidim, J., Coslovich, D. & Kahl, G. Single-particle and collective slow dynamics of colloids in porous confinement. *Phys. Rev. Lett.* **103**, 138303 (2009).

[17] Klafter, J. & Sokolov, I. M. Anomalous diffusion spreads its wings. *Physics World* **18**, 29–32 (2005).

[18] Höfling, F. & Franosch, T. Anomalous transport in the crowded world of biological cells. *Rep. Prog. Phys.* **76**, 046602 (2013).

[19] Krakoviack, V. Liquid-glass transition of a fluid confined in a disordered porous matrix: A mode-coupling theory. *Phys. Rev. Lett.* **94**, 065703 (2005).

[20] Kim, K., Miyazaki, K. & Saito, S. Slow dynamics in random media: Crossover from glass to localization transition. *Europhys. Lett.* **88**, 36002 (2009).

[21] Voigtmann, Th. & Horbach, J. Double transition scenario for anomalous diffusion in glass-forming mixtures. *Phys. Rev. Lett.* **103**, 205901 (2009).

[22] Schnyder, S. K., Spanner, M., Höfling, F., Franosch, T. & Horbach, J. Rounding of the localization transition in model porous media. *Soft Matter* **11**, 701–711 (2015).

[23] Trimble, W. S. & Grinstein, S. Barriers to the free diffusion of proteins and lipids in the plasma membrane. *J. Cell Biol.* **208**, 259–271 (2015).

[24] Cerbino, R. & Trappe, V. Differential dynamic microscopy: Probing wave vector dependent dynamics with a microscope. *Phys. Rev. Lett.* **100**, 188102 (2008).

[25] Lu, P. J. *et al.* Characterizing concentrated, multiply scattering, and actively driven fluorescent systems with confocal differential dynamic microscopy. *Phys. Rev. Lett.* **108**, 218103 (2012).

[26] Wilson, L. G. *et al.* Differential dynamic microscopy of bacterial motility. *Phys. Rev. Lett.* **106**, 018101 (2011).

[27] Götze, W. & Hausmann, R. Further phase transition scenarios described by the self consistent current relaxation theory. *Z. Phys. B: Condens. Matter* **72**, 403–412 (1988).

[28] Bosse, J. & Kaneko, Y. Self-diffusion in supercooled binary liquids. *Phys. Rev. Lett.* **74**, 4023–4026 (1995).

[29] Voigtmann, T. Multiple glasses in asymmetric binary hard spheres. *Europhys. Lett.* **96**, 36006 (2011).

[30] Moreno, A. J. & Colmenero, J. Logarithmic relaxation in a kinetically constrained model. *J. Chem. Phys.* **125**, 016101 (2006).

[31] Moreno, A. J. & Colmenero, J. Relaxation scenarios in a mixture of large and small spheres: Dependence on the size disparity. *J. Chem. Phys.* **125**, 164507 (2006).

[32] Mayer, C. *et al.* Multiple glass transitions in star polymer mixtures: Insights from theory and simulations. *Macromolecules* **42**, 423–434 (2009).

[33] Dawson, K. *et al.* Higher-order glass-transition singularities in colloidal systems with attractive interactions. *Phys. Rev. E* **63**, 011401 (2000).

[34] Sciortino, F., Tartaglia, P. & Zaccarelli, E. Evidence of a higher-order singularity in dense short-ranged attractive colloids. *Phys. Rev. Lett.* **91**, 268301 (2003).

[35] Gnan, N., Das, G., Sperl, M., Sciortino, F. & Zaccarelli, E. Multiple glass singularities and isodynamics in a core-softened model for glass-forming systems. *Phys. Rev. Lett.* **113**, 258302 (2014).

[36] Stauffer, D. & Aharony, A. *Introduction to Percolation Theory (2nd ed.)* (CRC Press, 1994).

[37] Spanner, M., Schnyder, S. K., Hofling, F., Voigtmann, T. & Franosch, T. Dynamic arrest in model porous media-intermediate scattering functions. *Soft Matter* **9**, 1604–1611 (2013).

[38] Yethiraj, A. & van Blaaderen, A. A colloidal model system with an interaction tunable from hard sphere to soft and

dipolar. *Nature* **421**, 513–517 (2003).
[39] Royall, C. P., Poon, W. C. K. & Weeks, E. R. In search of colloidal hard spheres. *Soft Matter* **9**, 17–27 (2013).
[40] Schaertl, W. & Sillescu, H. Brownian dynamics of polydisperse colloidal hard spheres: Equilibrium structures and random close packings. *J. Stat. Phys.* **77**, 1007–1025 (1994).
[41] Desmond, K. W. & Weeks, E. R. Influence of particle size distribution on random close packing of spheres. *Phys. Rev. E* **90**, 022204 (2014).
[42] Poon, W. C. K., Weeks, E. R. & Royall, C. P. On measuring colloidal volume fractions. *Soft Matter* **8**, 21–30 (2012).
[43] Mason, T. G. Estimating the viscoelastic moduli of complex fluids using the generalized stokes-einstein equation. *Rheol. Acta* **39**, 371–378 (2000).
[44] Berne, B. J. & Pecora, R. *Dynamic Light Scattering: With Applications to Chemistry, Biology, and Physics (Dover Books on Physics)* (Dover Publications, 2000).
[45] Giavazzi, F. & Cerbino, R. Digital fourier microscopy for soft matter dynamics. *J. Opt.* **16**, 083001 (2014).
[46] Crocker, J. C. & Grier, D. G. Methods of digital video microscopy for colloidal studies. *J. Coll. Interf. Sci.* **179**, 298 – 310 (1996).
[47] De Michele, C. Simulating hard rigid bodies. *J. Comput. Phys.* **229**, 3276 – 3294 (2010).
[48] Zaccarelli, E. *et al.* Crystallization of hard-sphere glasses. *Phys. Rev. Lett.* **103**, 135704 (2009).

Supplementary Online Material

Tatjana Sentjabrskaja[1], Emanuela Zaccarelli[2,3], Cristiano De Michele[3], Francesco Sciortino[2,3], Piero Tartaglia[3], Thomas Voigtmann[4,5], Stefan U. Egelhaaf[1], and Marco Laurati[1,6]

[1] *Condensed Matter Physics Laboratory, Heinrich Heine University, 40225 Düsseldorf, Germany*

[2] *CNR-ISC, Università di Roma "La Sapienza", Piazzale A. Moro* 2, 00185 *Roma, Italy*

[3] *Dipartimento di Fisica, Università di Roma "La Sapienza", Piazzale A. Moro* 2, 00185 *Roma, Italy*

[4] *Institut für Materialphysik im Weltraum, Deutsches Zentrum für Luft- und Raumfahrt (DLR), 51170 Köln, Germany*

[5] *Heinrich Heine University, Universitätsstraße 1, 40225 Düsseldorf, Germany and*

[6] *División de Ciencias e Ingeniería, Universidad de Guanajuato, Loma del Bosque 103, 37150 León, Mexico*

Additional Simulation data

Self correlators

The self intermediate scattering functions $f^{self}(q,\Delta t)$ are reported in Fig.S1 to complement the data of the collective intermediate scattering function in the manuscript. It is evident that for $\delta = 0.20$ (Fig.S1(a)) the self dynamics of large and small particles are completely decoupled; $f^{self}(q,\Delta t)$ for the small particles fully decay to zero on a much shorter timescale than those for larger particles. In addition, the self dynamics is also decoupled from the collective dynamics for small particles, similarly to early predictions by Bosse and Kaneko[1]. This confirms the scenario that small particles are fully diffusive within the voids of the large particles at all explored ϕ (up to $\phi = 0.67$, not shown). For $\delta = 0.35$ (Fig.S1(b)), $f^{self}(q,\Delta t)$ for small particles show a logarithmic decay similarly to the collective ones. Moreover, the self dynamics of the small and large particles starts to couple, as the logarithmic decay extends over timescales comparable to the large particle relaxation time. Finally, for $\delta = 0.50$ (Fig.S1(c)), small and large particles are fully coupled, both exhibiting a standard (and almost simultaneous) glass transition, with no sign of logarithmic dynamics.

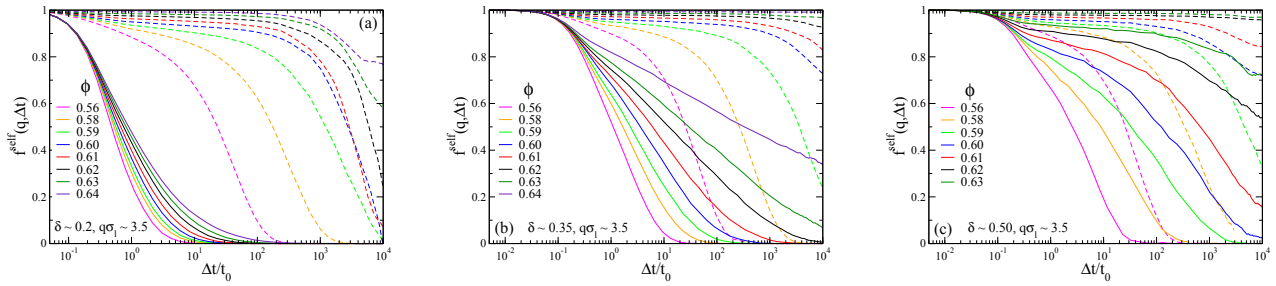

FIG. S1: Self intermediate scattering functions $f^{self}(q,\Delta t)$ for large (dashed lines) and small (full lines) particles calculated in simulations for $q\sigma_l = 3.5$ and different ϕ (as indicated) at $\delta = 0.20$ (a), $\delta = 0.35$ (b) and $\delta = 0.50$ (c).

Dependence on δ

In the manuscript we have shown that there exists a critical size ratio $\delta_c = 0.35$ above which, for $\phi \gtrsim 0.60$, an enhanced logarithmic decay of the correlators is observed, which extends over 3 decades. Here we complement these results by reporting the collective density auto-correlation functions for other values of δ. In particular, for $\delta = 0.30$ (Fig. S2(a)) we find that the correlation function starts to develop an incipient logarithmic behavior for a limited time window at the highest studied ϕ; for $\delta = 0.40$ (Fig. S2(b)) we see quite clearly an intermediate time regime of logarithmic decay for about two decades, which is followed at long times by a standard (stretched exponential) final decay. Finally for $\delta = 0.50$ (Fig. S2(c)) there is no evidence of any logarithmic decay and a standard two-step behavior characteristic for concentrated suspensions is recovered, as also seen in the MSD (Fig. S2(d)).

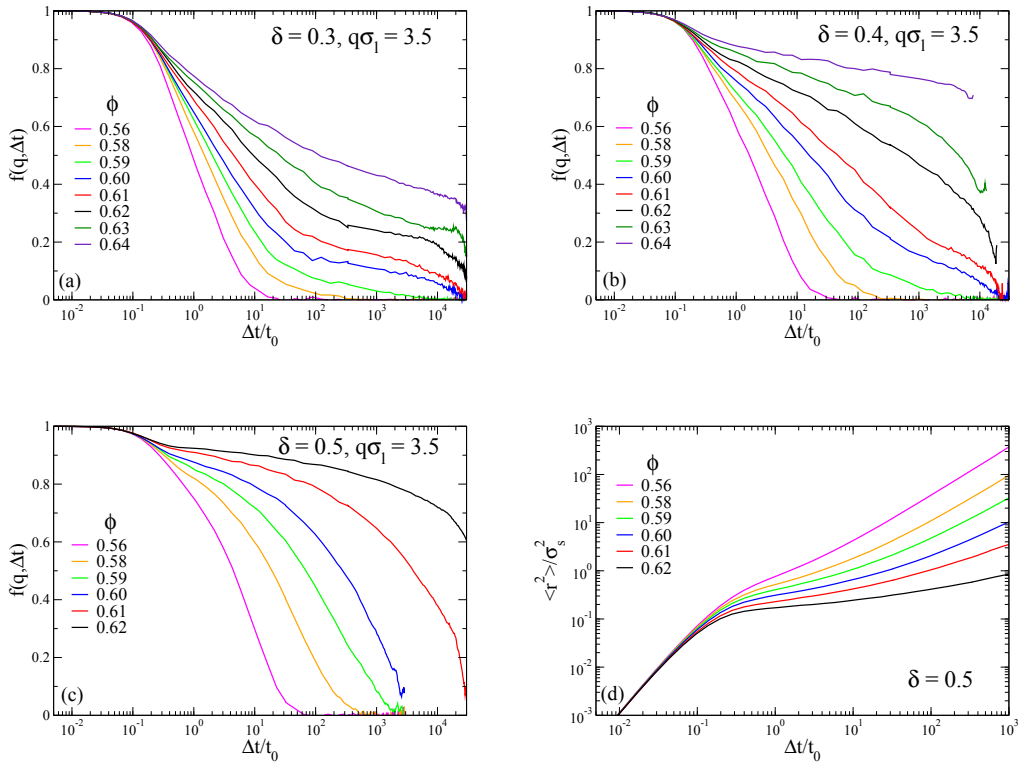

FIG. S2: Collective intermediate scattering functions $f(q, \Delta t)$ for the small particles calculated for fixed $q\sigma_1 \sim 3.5$ and different ϕ (as indicated) for $\delta = 0.30$ (a), $\delta = 0.40$ (b) and $\delta = 0.50$ (c); MSD for the small particles for $\delta = 0.50$, and different ϕ (as indicated) (d).

Large particle dynamics

The small particle dynamics display a dramatic change of behaviour at the critical size ratio, which can be associated with changes in the mechanism of arrest and the transition from caging at large δ to localisation at small δ, related to the decoupling of the dynamics of the two species. On the other hand the arrest mechanism of the large particles, caging by other large particles, is not significantly affected by the presence of the small fraction, $x_s = 0.01$, of small particles, irrespective of size ratio. As an example, Fig.S3(a) shows that large particles at $\delta_c = 0.35$, where the small particles show anomalous dynamics, approach a standard glass transition upon increasing ϕ, characterised by a typical two-step decay. Furthermore, Fig.S3(b) and (c) show that, upon changing δ, the localisation length, i.e. the cage size, does not change significantly, as evident from the plateau height of both the MSDs ($\sim 0.1\sigma_l^2$) and the density correlators. The cage though becomes more mobile with decreasing δ, as shown by the faster dynamics at long times, possibly as a consequence of the fact that at small δ the small particles do not hinder the large particle movements due to their small size and large mobility.

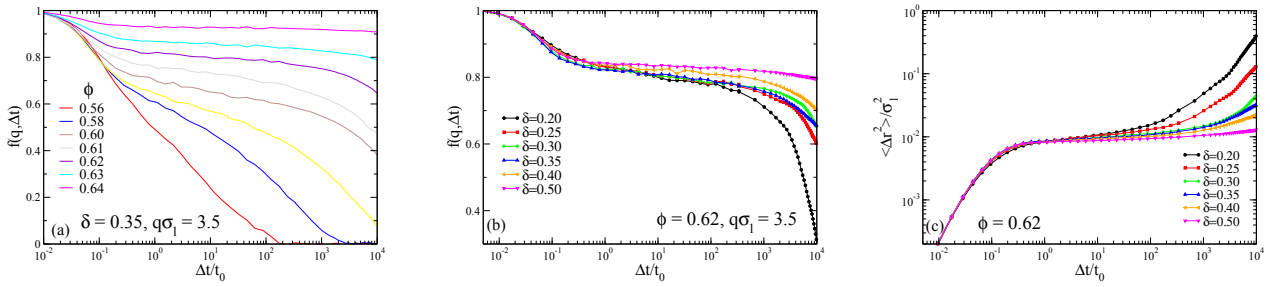

FIG. S3: (a) Collective intermediate scattering functions $f(q, \Delta t)$ for the large particles calculated in the simulations for $\delta = 0.35$, $q\sigma_1 \sim 3.5$ and different ϕ (as indicated); $f(q, \Delta t)$ for $q\sigma_1 \sim 3.5$ (b) and large particles MSD (c), calculated for $\phi = 0.62$ and different values of δ (as indicated).

Frozen vs. mobile matrix of large particles

Here we want to compare simulations of a fully mobile binary mixture of hard spheres and one where the large particles are immobile. For the latter situation, *quantitatively* accurate results can only be obtained when one considers a large system size and also performs an average over several matrix realizations, as done in previous works [2–4]. However, our aim is only to provide a *qualitative* comparison with the mobile case, for which our approach, based on a single realization for a system size of $O(10^3)$ particles, is sufficient, as indicated by the fact that the MSD for the immobile matrix case reported in Fig.4(a) displays the correct behaviour with a critical exponent compatible with the analytical predictions[4].

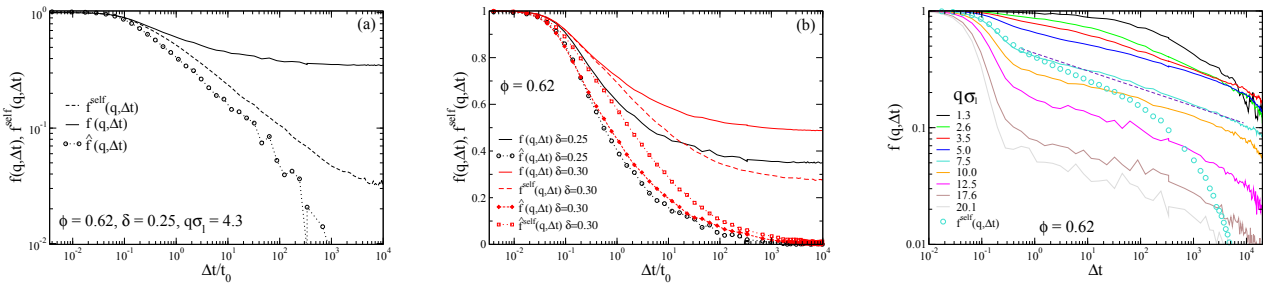

FIG. S4: (a) Collective (full curve), self (dashed curve) and scaled $\hat{f}(q,\Delta t)$ (see text, circles) intermediate scattering functions for $\phi = 0.62$, $\delta = 0.25$ and $q\sigma_1 \simeq 4.3$ in log-log plot; (b) collective (full curve), self (dashed curve) and scaled $\hat{f}(q,\Delta t)$ (symbols) for $\phi = 0.62$ and $\delta = 0.25, q\sigma_1 \simeq 4.3$ (black), $\delta = 0.30, q\sigma_1 \simeq 3.7$ (red) in semi-log plot; (c) Same data as in Fig.2h of the manuscript, but in log-log scale instead of semi-log scale: collective correlators for $\phi = 0.62$ for various wavevectors.

Fig. 5(c) shows that the small particle self correlators for the immobile matrix case display (at intermediate time) a power-law behavior. It is to be noted that these correlators, even below the critical size ratio ~ 0.3, display a long-time finite value, i.e. a residual non-ergodicity. Indeed, different from studies on the Lorentz gas [5], we include among the intruders small particles trapped in finite size voids, i.e. not pertaining to the percolating cluster of voids, to make the analogy with the fully mobile case. The collective correlators, for the situation where the self ones show a power-law dependence on time, do not present the same behavior (Fig.S4(a)). Nevertheless, defining a scaled correlator $\hat{f}(q,\Delta t) = (f(q,\Delta t) - f(q,\infty))/(1 - f(q,\infty))$, which allows us to remove the contribution of the frozen-in component to the correlation function [6], we see that a power-law behavior seems to emerge also for the collective correlators, even though our current numerical resolution is not good enough to determine this clearly. However, the important point is that in semi-log plot (Fig.S4(b)) all correlators (self, collective and scaled) for frozen matrix conditions do not show a logarithmic decay in any time window or wavevector. Finally, in Fig.S4(c) the correlators for the mobile matrix at the critical size ratio are reported in log-log plot showing that at $q\sigma_1 = 3.5$, where the anomalous logarithmic behavior is observed, a power-law decay cannot describe the data. It is interesting to note that at a larger value of $q\sigma_1 = 7.5$ the data might approach this behavior at long times, even though within a two-step decay. The power-law exponent of about 0.5 is also close to the Lorentz gas (0.527) and to MCT predictions. This suggests that at the smaller length scales probed at larger q values, the particles mainly see the local environment and localisation, while only at smaller q values the network structure of voids is explored and leads to anomalous behavior. Note though that the self correlators significantly deviate from power-law behavior. In summary, these results complement those provided in the manuscript and show that small particles moving in a frozen matrix behave very differently from those moving in a glassy but mobile matrix of large particles.

Additional MCT data

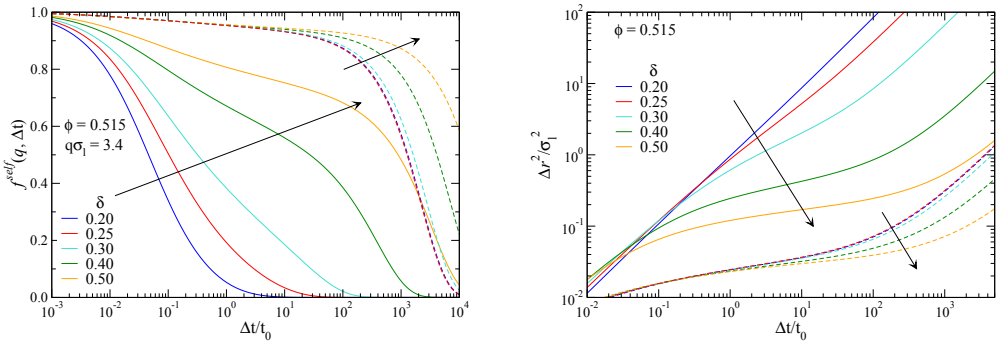

FIG. S5: Left: self-intermediate scattering functions $f^{self}(q, \Delta t)$ for the small particles (solid lines) and the large particles (dashed lines), for $\phi = 0.515$, $q\sigma_1 = 3.4$ and various size ratios δ, as indicated (increasing in the direction of the arrows). Right: corresponding mean-squared displacements (MSD).

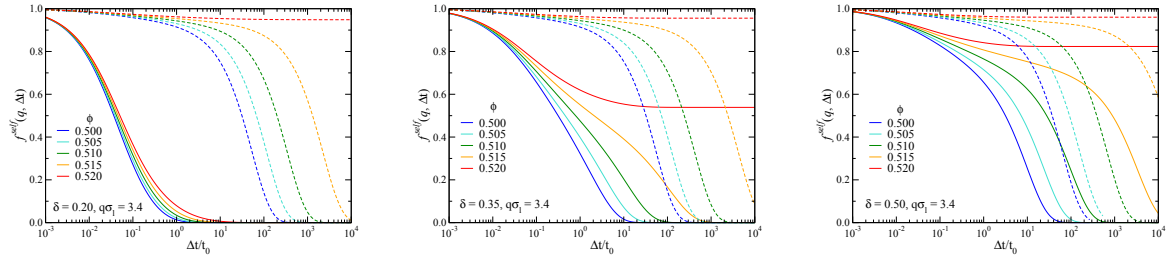

FIG. S6: Self-intermediate scattering functions $f^{self}(q, \Delta t)$ of the small (solid lines) and the large particles (dashed lines), for $q\sigma_1 = 3.4$ and various packing fractions ϕ, as indicated. Left: size ratio $\delta = 0.2$; middle: $\delta = 0.35$; right: $\delta = 0.5$.

Since the relative volume fraction of small particles is small, the main dynamical arrest mechanism for the large particles (caging) is not qualitatively affected by changing the size ratio δ. This is captured by MCT, see Fig. S5, where the self-intermediate scattering functions are shown for various δ at fixed packing fraction, for both the large and the small particles, together with the corresponding mean-squared displacements. At all size ratios, the large particles indicate caging on the same length scale, indicated by the plateau of the MSD corresponing to a localization length of about 10% of σ_1 (Lindemann criterion). At the same time, the dynamics of the small particles changes qualitatively, from caged at large δ, to diffusive at $\delta = 0.2$, with a localization length that grows continuously as δ is decreased.

The difference in dynamical behavior of the small particles at the glass transition, depending on δ, is elucidated by Fig. S6, where MCT predictions corresponding to the simulation data shown in Fig. S2 are shown. The theory qualitatively captures the change from localization-type behavior and a partially frozen glass at $\delta = 0.2$, to an ordinary glass transition showing caging for both species at $\delta = 0.5$.

[1] Bosse, J. & Kaneko, Y. Self-diffusion in supercooled binary liquids. *Phys. Rev. Lett.* **74**, 4023–4026 (1995).

[2] Kurzidim, J., Coslovich, D. & Kahl, G. Single-particle and collective slow dynamics of colloids in porous confinement. *Phys. Rev. Lett.* **103**, 138303 (2009).

[3] Kim, K., Miyazaki, K. & Saito, S. Slow dynamics in random media: Crossover from glass to localization transition. *Europhys. Lett.* **88**, 36002 (2009).

[4] Höfling, F., Franosch, T. & Frey, E. Localization transition of the three-dimensional lorentz model and continuum percolation. *Phys. Rev. Lett.* **96**, 165901 (2006).

[5] Spanner, M., Schnyder, S. K., Hofling, F., Voigtmann, T. & Franosch, T. Dynamic arrest in model porous media-intermediate scattering functions. *Soft Matter* **9**, 1604–1611 (2013).

[6] Kertesz, J. & Metzger, J. Properties of the density relaxation function in classical diffusion models with percolation transition. *J. Phys. A: Math. Gen.* **16**, L735 (1983).

A. Appendix: Experimental methods

A.1. Rheology

The study of the flow behaviour of materials, including complex fluids, is a broad research field summarized as rheology. Classically, materials are classified as elastic solids and viscous fluids. For viscous liquids the stokes relation,

$$\sigma = \eta\dot{\gamma} \tag{A.1}$$

describes the the proportionality of stress σ, or force per area, and shear rate $\dot{\gamma}$ via the proportionality factor η, the viscosity. Similarly, for elastic solids Hookes' law states

$$\sigma = G\gamma, \tag{A.2}$$

where the constant G is called shear modulus and γ is the strain or deformation. Ideally elastic solids return to their initial shape after removing the force causing the deformation. In contrast to that, an ideal viscous liquid keeps the new form after removing the force. The ideal cases of a solid and a liquid may be modeled by mechanical systems. The ideal solid can be represented as a completely elastic spring, whereas the ideal liquid corresponds to a purely viscous damper. The visco-elastic behavior of complex fluids may be represented by a combination of these two mechanical systems. Spring and damper may be connected sequentially (Maxwell model) or in parallel (Kelvin model) to give a qualitative description of viscoelasticity. Obviously these simplified mechanical toy models are not capable of reflecting any quantitative behavior of real complex fluids.

The resistance to shear, or viscosity, is one of the properties characterizing a fluid. Different kinds of instruments for viscosity measurements have been developed over the centuries, e.g. falling ball, U-tube, or the oscillating piston viscometer. The common feature of all these instruments is that the measurement of viscosity occurs under only one flow condition. Nevertheless, the viscosity of Newtonian fluids, like water and thin

motor oil, can be measured correctly. Newtonian fluids are characterized by a constant viscosity, i.e. by a direct proportionality between shear stress and shear rate.

Complex fluids, including biological fluids like blood and many materials used in applications, show a non-Newtonian behavior. The viscosity is no longer a constant value, but depends on the shear conditions, in particular the shear rate. This introduces a non-linearity into the system response. Most polymer solutions and colloidal dispersions are shear thinning, i.e. a decrease of viscosity for increasing shear rate. The liquification of material is due to the breaking of internal structures, like stretching and disentanglement of polymers in the solution. The opposite behavior is shear thickening, where the viscosity increases with increasing shear rate. A famous example for such materials is corn starch dissolved in water. The study of non-linear phenomena requires a number of parameters to be controlled, set and measured. That led to the development of such instrument as rheometers.

An additional point in the study of non-linear phenomena is the flow field. Complex flow fields result in complex fluid mechanics. The interaction between the flow field and non-linear fluid becomes sophisticated and strongly nonlinear. In order to decouple material properties and fluid mechanics, rheological measurements are typically performed using simple, well defined flow fields. One of the most simple geometries used in rheology is a combination of two parallel plates, where one plate is moved with velocity v by applying a force F. In the gap of width h between fixed and moving plate, a constant shear profile is generated. The resulting shear rate $\dot{\gamma}$ is

$$\dot{\gamma} = v/h\,. \tag{A.3}$$

The ratio between required force and surface area A of the plate is the stress σ,

$$\sigma = F/A. \tag{A.4}$$

In the plate-plate geometry one plate rotates above the second, fixed, plate. The velocity, and consequently the shear rate, increases from zero in in the center to maximum value on the rim. To avoid this, a cone-plate geometry is used, the gap width h increases with distance from the center. If properly adjusted, the ratio v/h becomes constant. The shear flow created in cone-plate geometry is homogenous and for a small cone angle $\alpha < 4°$ the shear rate is given by

$$\dot{\gamma} = \Omega/\alpha, \tag{A.5}$$

where Ω is the angular velocity of the cone.

Oscillatory shear can be easily achieved by applying a sinusoidal angular velocity

$\Omega(t) = \Omega_0 \sin(\omega t)$, with frequency ω. The strain amplitude γ_0 imposed on the sample is given by

$$\gamma_0 = \frac{\Omega_0/\omega}{\tan \alpha}. \tag{A.6}$$

For small strain amplitudes $\gamma_0 \ll 1$ the linear viscoelastic regime is observed. In this regime the deformations are so small that the structure distortions caused by shear are reversible. The shear stress $\sigma(t)$ and the strain $\gamma(t)$ are sinusoidal and proportional to each other, but not necessarily in phase. The shear stress is given by

$$\sigma(t) = \gamma_0\{G'(\omega)\sin(\omega t) + G''(\omega)\cos(\omega t)\}, \tag{A.7}$$

where the term containing G' is in phase with the strain and the term with G'' is in phase with the shear rate. G' represents the storage of energy, a typical feature of a solid, and is called storage modulus. The loss modulus G'' describes the dissipation of the energy, typical for liquids. The structures at small and large scales can be probed by application of high and low frequencies, respectively.

For large oscillation amplitudes the response becomes nonlinear and the stress contains contributions of higher harmonics of ω,

$$\sigma(t) = \gamma_0 \sum_n \{G'_n(\omega)\sin(n\omega t) + G''_n(\omega)\cos(n\omega t)\}. \tag{A.8}$$

In Fourier-Transform rheology the spectra of $\sigma(t)$ are analyzed for signals at higher harmonics of ω. Usually, the contributions of additional Harmonics ($n > 1$) is neglected.

The non-linear regime can be studied in rotational measurements, where a constant stress (creep test) or a constant shear rate (step rate test) is applied. By applying a constant shear rate in a step rate experiment, the evolution of stress as a function of time or strain is measured. Compared to this, a creep experiment is performed at a constant shear stress and the deformation as a function of time is measured. For these kinds of experiments it is important to use suitable rheometers. A distinction is made between stress- and strain-controlled rheometres. In principle, both experiments can be performed on the same rheometer. But in this case it should be taken into account that the use of an alternative measuring mode (for example application of constant shear stress in a strain-controlled rheometer) leads to a long regulation time until the target value of stress or strain is achieved.

A.2. Confocal Microscopy

Microscopic structure and local dynamics can be studied by using microscopy. The use of confocal microscopy [1,2] reduces a number of problems caused by multiple scattering in classical microscopy, like the resolution in z-direction. Confocal microscopy is based on two ideas. First, only a small volume of the sample is illuminated. Secondly, out-of-focus light is rejected by placing a pinhole in the conjugate focal plane. Intense illumination of only a small volume is achieved via laser light which is guided to the observation volume by a pair of mirrors. Through the movement of these mirrors, the x-y-position of the illuminated volume can be changed and the sample scanned point by point. The light coming from only a thin sample layer is collected, which increases the resolution in the x-y-plane as well as in z-direction. The illumination of a fluorescent sample leads to emission of light by fluorescent substances, which have previously been attached to the particle [3,4]. Of course, the laser light has to match the absorption spectrum of the fluorophores. The wavelength of the emitted light is longer than the laser wavelength [5]. A part of the emitted light passes through the objective, is redirected by mirrors and finally passes through a dichroic mirror and the pinhole to be collected by the detector, a photomultiplier tube. A 2D image acquired by scanning is reconstructed by the computer. A number of 2D images, collected at different focal depths, constitude a 3D stack. The resolution of a confocal microscope is limited by diffraction. The limit of resolution amounts to around 200 nm and slightly depends on the wavelength of the laser source and the numerical aperture of the objective. Direct imaging of colloids is possible in the upper range of colloidal length.

One of the main advantages of confocal microscopy is the 3D resolution of single particles even at high concentration and in the bulk, if the refractive index is matched. On the other hand, the aquisition of images by scanning through the volume limits the acquisition speed.

From confocal microscopy images the particle positions and trajectories can be extracted using particle tracking algorithms [6]. To characterize the local microstructure of the system we calculate the radial distribution function $g(r)$ (or pair correlation function) from the obtained data. The function gives the conditional probability of finding a center of a particle at a distance r from a given particle center, relative to the probability in an ideal gas. Determining trajectories of particles, i.e. measuring the position of particle at different times, allows us to calculate the squared displacement averaged over all particles $\delta r(t)^2$.

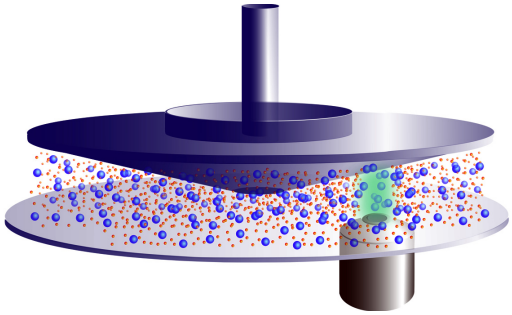

Figure A.1.: Schematic representation of the central part of a confocal rheoscope. The cone geometry is connected to the rheometer and can be rotated. The bottom part of the geometry is a thin cover slip. Note that the cover slip is placed on the top of a metal plate with an imaging slit (not shown in the Figure). The objective is the top part of the imaging system contained in the confocal scanner. The sample is placed in-between cone and plate geometries.

A.3. Rheoscopy

The mapping of structure and local dynamics of complex fluids to their flow properties is one of the interesting points which brings rheology and microscopy together [7]. The microscopy of sheared colloidal systems can be studied in flow cells. In a flow cell the complex fluid is placed between two parallel plates with a gap h much smaller that the size of the plates. Once the two plates move relative to each other with velocity v a linear shear profile with shear rate $\dot{\gamma} = v/h$ is established[8–10]. Such a flow cell is then combined with a microscope or a light scattering setup.

Also rotational shear cell combined with confocal microscopes have been developed [11,12]. The bottom is still a plate, e.g. a thin glass cover slip, but the top geometry is now a cone. Both, cone and plate, can be rotated independently from each other in opposite directions. In between, at a certain height z above the bottom plane a zero velocity plane is established. The z position of the zero velocity plane can be adjusted by changing the ratio of cone and plate rotational velocities. The advantage of imaging particles in the zero velocity plane is that the particles stay in the field of view. On the other hand, all types of shear cells have a common disadvantage, namely they do not measure (at least directly) the resulting shear stress, i.e. the response of the material to the application of the constant shear rate.

This is different for the combination of a confocal microscope and a rheometer, which is a so called rheoscope. The setup permits simultaneous measurement of shear stress (or other rheological quantities) during the imaging process. The most popular geometries used for colloidal suspensions are plate-plate and cone-plate geometries. For the

measurements presented in the thesis, the rheometer of the Edinburgh group with cone-plate geometry was used. The setup is described in detail by R. Besseling et al. [13]. For the setup a stress controlled rheometer (AR200, TA instruments) is used. The space for the imaging optics is secured by an open base construction of the rheometer. A plate with an imaging slit is mounted on the rheometer. The top of the plate is covered with a large circular cover slide, which builds the bottom part of the shear geometry. The imaging is possible at different distances from the geometry center. Below the plate, an inverted microscope is placed. The microscope is connected to the confocal scanner (VTEye, Visitech), which allows 2D and 3D imaging of single particles during shear.

A.4. Differential Dynamic Microscopy

A.4.1. Main idea

The main idea of Differential Dynamic Microscopy (DDM) is to characterize the motion of mesoscopic particles, such as macromolecules, colloids or bacteria due to the fluctuations in the fluorescence intensity in the images caused by the variations in the particle number density. From the time correlation of the fluorescence intensity the intermediate scattering function (ISF), which usually acquired in light scattering, can be determined. A detailed description and the theoretical background of this technique was described by R. Cerbino et al. [14] and others [15,16]. A schematic summary of the procedure is shown in Figure A.2. The raw data are microscope images recorded in a time loop. The images contain the intensity distribution in the image plane $I(\vec{r},t)$, at pixel position $\vec{r}$ and time t. From these data the differential intensity correlation function (DICF)

$$D(\vec{q},\delta t) = \langle |I(\vec{q},t+\delta t) - I(\vec{q},t)|^2 \rangle, \tag{A.9}$$

can be calculated. Here δt is a fixed time-span and $\langle ... \rangle$ represents the time-average starting at time t. $I(\vec{q},t)$ is the Fourier-transform of $I(\vec{r},t)$, i.e. $D(\vec{q},t)$ can be interpreted as a time averaged Fourier power-spectrum [14].

For isotropic systems, where the motion of the particles is direction independent, an azimuthal averaging of $D(\vec{q},\delta t)$ is useful. This leads a one-dimensional Fourier power-spectrum $D(q,\delta t)$, which may be written as

$$D(q,\delta t) = A(q)(1 - f(q,\delta t)) + B(q), \tag{A.10}$$

where $f(q,\delta t)$ is the intermediate scattering function. The amplitude $A(q)$ depends on

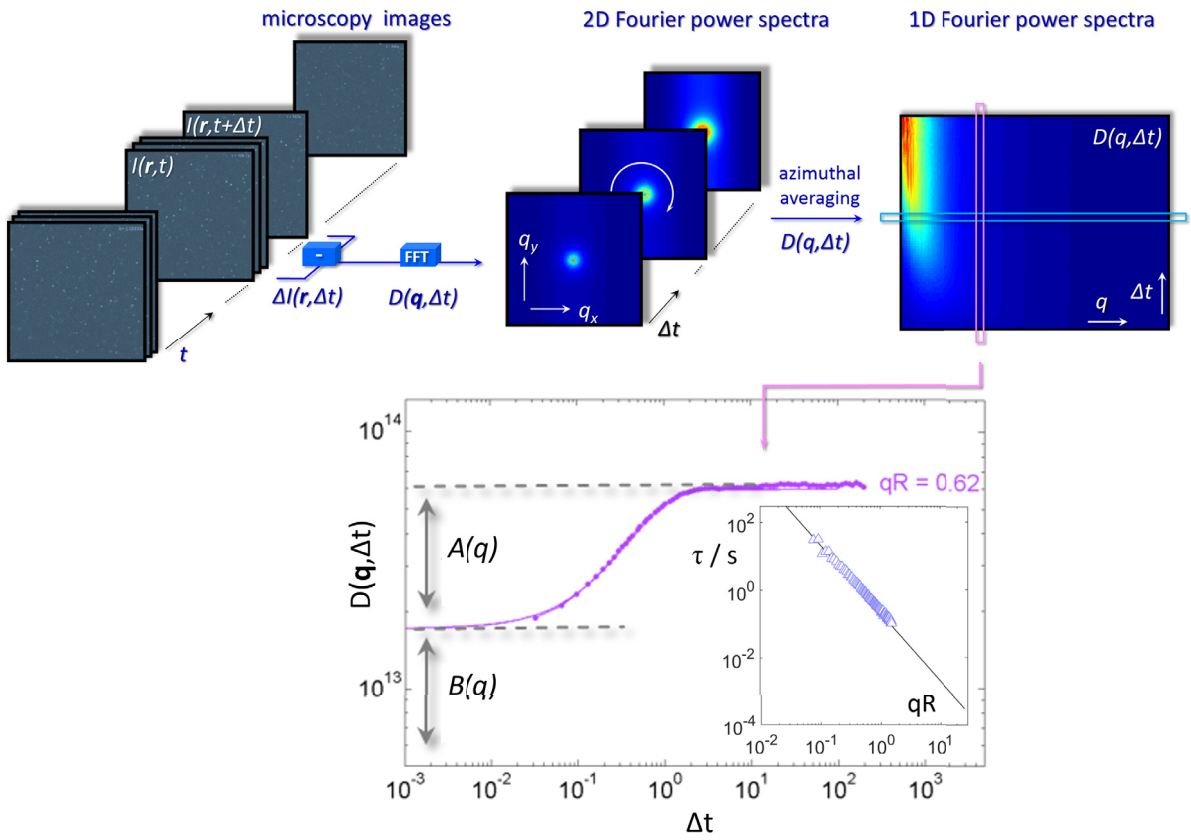

Figure A.2.: Schematic representation of the DDM method. From microscopy images a 2D Fourier power spectrum is calculated. Azimuthal averaging results in the 1D Fourier power-spectrum $D(q, \delta t)$, if the system is isotropic. In the bottom plot, $D(q, \delta t)$ is shown as a function of the time delay δt for one selected q. The line is fitted with an exponential function, see equations (A.10) and (A.11). The parameter $A(q)$ and $B(q)$ are indicated. Inset: the fit parameter τ as a function of qR(R is the particle radius), in comparison to the theoretical prediction given by $\tau(q) = \dfrac{1}{D_0 q^2}$ (black line).

the imaging system and sample structure, the offset $B(q)$ contains information on the camera noise[15,17]. In case of Brownian motion, in very dilute solutions of colloids with volume fraction 10^{-4}, each Fourier mode decays exponentially with time. Thus, the ISF is given by

$$f(q, \delta t) = e^{-\delta t/\tau(q)}, \tag{A.11}$$

with characteristic time $\tau(q)$.

For the example in Figure A.2, we used a very dilute dispersion of colloidal hard spheres with radius $R = 0.266\,\mathrm{nm}$ dispersed in decalin/CHB solution. The Stokes-

Einstein relation $D_0 = \frac{k_B T}{6\pi\eta r}$ gives a diffusion coefficient $D_0 = 0.33\mu m^2/s$. By using confocal microscopy 10^4 images with a size 512×512 were taken at 30 frames per second, resulting in a total recording time of $\sim$ 5.5 minutes. After the procedure described above, the DICF is determined and fitted to the function (A.10) with $f(q)$ from Eq. (A.11). The fit parameter $\tau(q)$ is consistent with the theoretical prediction given by $\tau(q) = \frac{1}{D_0 q^2}$ [14,18], as shown in Figure A.2 inset.

Dynamics of particles in dilute systems can be studied by DDM. Examples of such systems are found in biology, e.g. solutions of bacteria or algae. From the ISF, different quantities to characterize the dynamics of cells can be determined, e.g. distribution of swimming speeds, amount of mobile cells or the diffusion coefficient [16,19].

A.4.2. From DICF to ISF

Complex systems can consist of particles with different size, shape or composition, where each component behaves differently which can lead to complicated correlation functions. The relaxation times for example may be longer than experimentally measurable and therefore only a part of the DICF function can be obtained. According to equation (A.10) the DICF can be converted to the ISF under the assumption that $A(q)$ and $B(q)$ are known. For dilute solutions $A(q)$ and $B(q)$ are determined by fitting. For concentrated and complex systems, the determination of the parameters by fitting is impossible if only a part of the DICF function is measured (due to long, or infinitely long relaxation time) and the fit function $f(q, \delta t)$ is unknown.

To use DDM for an experimental determination of the intermediate scattering function in the case of concentrated complex systems, the parameters $A(q)$ and $B(q)$ are approximated via image correlation. Figure A.3 visualizes a schematical comparison between the DDM and the image correlation method. The temporal image correlation results in the image correlation function, given by

$$IC(q, \delta t) = \langle I(q, t) I^*(q, t + \delta t) \rangle, \tag{A.12}$$

where $\langle ... \rangle$ corresponds to averaging over different starting times t. For constant q the function $IC(q, \delta t)$ is described as

$$IC(q, \delta t) = 0.5 A(q) f(q, \delta t) + 0.5 B(q) \delta_{\delta t, 0} + C(q), \tag{A.13}$$

where $C(q)$ is the background contribution [17]. For confocal microscope measurements we was found that the background contribution is negligible (not shown here). This

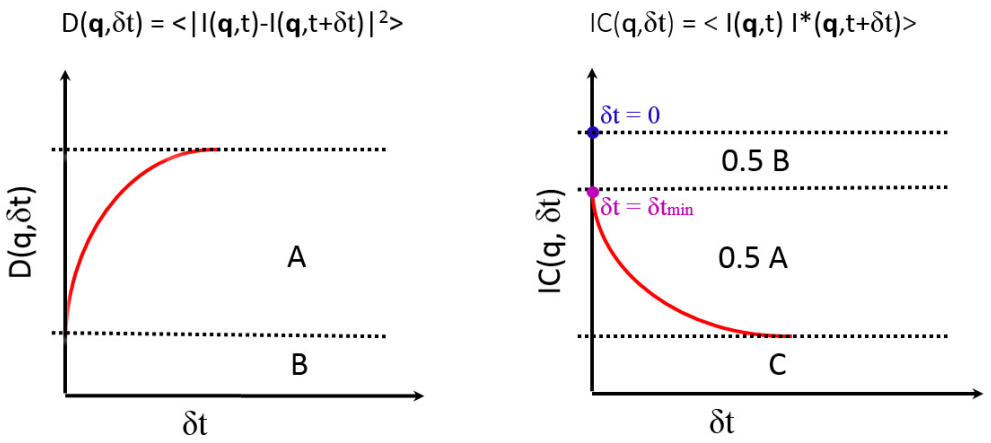

Figure A.3.: Schematical representation of the functions obtained from Differential Dynamic Microscopy (left) and the q-dependent image correlation (right)[17]. The differential intensity correlation function $D(q, \delta t)$ given by equation (A.9) for a fixed q is an increasing function of δt with amplitude A and offset B (s. Eq. (A.10)). Image correlation results in a decreasing function of δt (s. Eq. (A.12) and (A.13)) where additionally the contribution of the background C is present.

simplifies the relations for the determination of $A(q)$ and $B(q)$, resulting in

$$A(q) = 2IC(q, \delta t_{min}) \tag{A.14}$$

and

$$B(q) = 2IC(q, 0) - 2IC(q, \delta t_{min}), \tag{A.15}$$

where δt_{min} is the shortest time delay obtained in the measurements (here $1/30\,\mathrm{s}$).

Now, for the case of a diluted suspension, the determination of these parameters can be done in two ways, either fitting or approximation by image correlation according to Eq. (A.14), (A.15). The obtained results are shown in Figure A.4, demonstrating and excellent agreement between the data obtained in these different ways.

The relation between DDM and image correlation, namely $D(q, \delta t) = 2[IC(q, 0) - IC(q, \delta t)]$, has already been mentioned earlier[15]. This relation holds under the assumption that $IC(q, \delta t)$ decreases from $IC(q, 0)$ to 0 for $\delta t \to \infty$, which implies $B(q) = 0$ and $C(q) = 0$. Under this assumption it was shown that the amplitude is given by $A(q) = 2IC(q, 0)$.

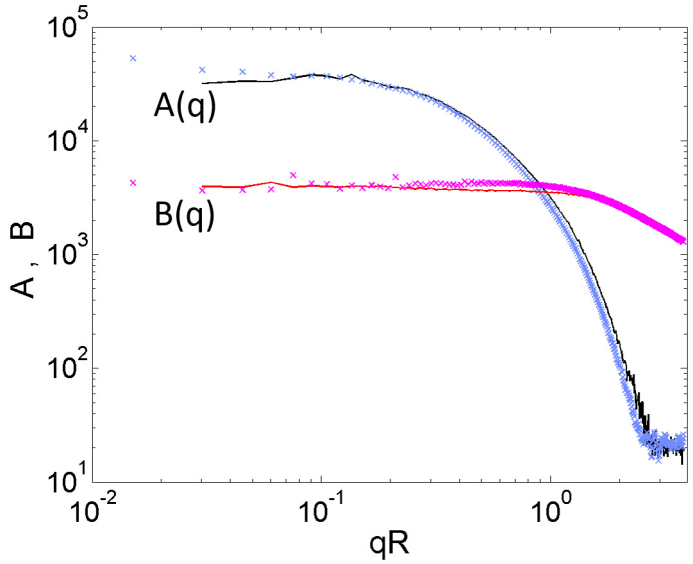

Figure A.4.: The parameters $A(q)$ and $B(q)$ extracted from the fit (solid lines) and approximated using image correlation method via Eq.(A.14) and Eq.(A.15) (crosses).

A.4.3. Applying DDM for high concentrations

To see how DDM can be used for suspensions with high concentration, we increased the concentration from an initially diluted dispersion of colloidal particles step by step. The particles used for these experiments are PMMA spheres of radius is $R = 0.838\,\mu\text{m}$ diluted in the CHB/cis-decalin/salt mixture. From light scattering experiments we estimate a polydispersity of about 6%. The dispersed particles behave like hard spheres and are fluorescently marked with Nile red. For the DDM measurements the confocal microscope Nikon AR-I-MP with a 60 × objective and numerical aperture 1.4 is used. A series of 10^4 images, each with size 512×512 pixel, is collected. The wave-numbers q_i which can be uniquely resolved on an image of size $N \times N$ are

$$q_i = \frac{2\pi}{N d_{pix}} i\,, \quad i = 1, \ldots, N/2. \tag{A.16}$$

The pixel pitch $d_{pix} = 0.42\,\mu\text{m}$ results in a q-range from $0.029\,\mu\text{m}^{-1}$ up to $7.48\,\mu\text{m}^{-1}$. The recording speed is 30 fps (frames per second). The series of images are analyzed using the DDM method.

The resulting intermediate correlation functions for different q-values are shown in Figure A.5 (b-d). Increasing the volume fraction of the particles results in the slowing of the decay of $f(q, \delta t)$. The exponential decay, found for diluted dispersion, becomes a

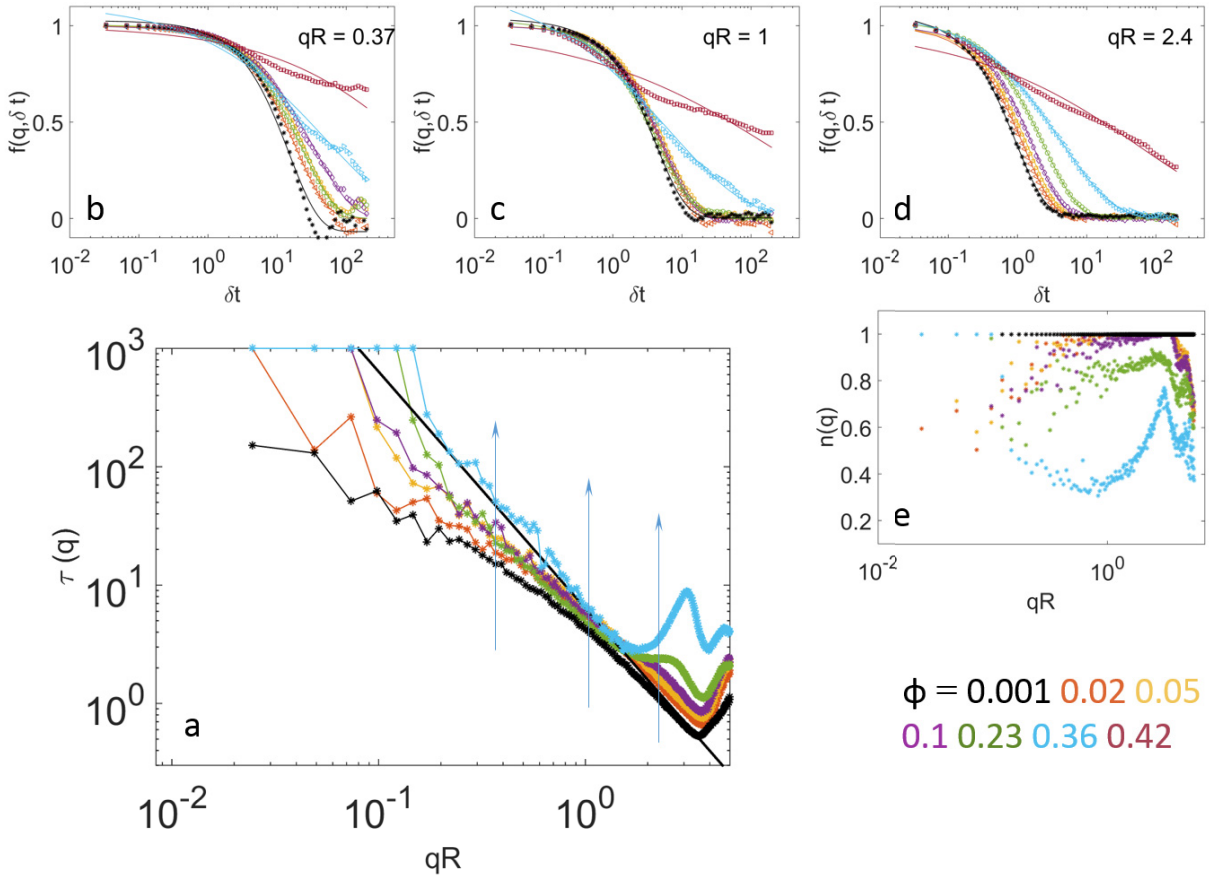

Figure A.5.: a) Characteristic time τ for different volume fractions ϕ as function of qR, where R is the particle radius. The black line corresponds to the Stokes-Einstein prediction. b)-d) Intermediate scattering functions $f(q, \delta t)$ (symbols) and fit with stretched exponential function (lines) for different volume fractions ϕ and at different q, which are marked in a) by arrows. e) The exponent n for different ϕ as function of qR.

stretched exponential given by

$$f(q, \delta t) = e^{-(\delta t/\tau(q))^n}, \quad n \leq 1\,. \tag{A.17}$$

The regime where a stretched exponential decay is found covers a broad range of volume fractions $0.02 \leq \phi \leq 0.36$. Further increase of the concentration leads to the formation of a localization plateau. The formation of the plateau is observed for $\phi = 0.42$, where the disparity between stretched exponential fit and $f(q, \delta t)$ becomes apparent.

The dependence of the exponent n on the volume fraction is shown in Figure A.5 e). The decrease of n with increasing volume fraction indicates, as expected, the broadening of the relaxation-time distribution. Moreover, the increase of concentration leads to the formation of peaks in the curve $n(qR)$. This illustrate the influence of the structure factor.

The characteristic times τ obtained by fitting are shown in Figure A.5 a). As expected, for dilute dispersions the proportionality $\tau \sim 1/D_0 q^2$ with $D_0 = 0.1042\,\mu\mathrm{m}^2/\mathrm{s}$ is found for intermediate q. A deviation from this behavior observed for small q is due to the limited confocal slice thickness δz[15,20]. The value of the characteristic time for $q \to 0$ is estimated to be $\tau_{plateau} = 60\ pm10\,\mathrm{s}$ and is related to the time that the particles need to diffuse out of the layer. Consequently, the thickness of the layer can be estimated as $\delta z = \sqrt{\tau_{plateau} D_0} = 2.5 \pm 0.2\,\mu\mathrm{m}$. This result is very close to the optical-thickness value $2.32\,\mu\mathrm{m}$, which is provided by the software of the mocroscope. Note that the optical thickness can be set by the size of the pinhole. To reduce the influence of the limited δz a fully opened pinhole is beneficial. At large q-values the evolution of $\tau(q)$ becomes affected by the structure factor. This influence is pronounced at high concentrations, which is indicated by formation of peaks in $\tau(q)$.

The structure factor $S(q)$ is reflected in the amplitude $A(q)$ which is given by

$$A(q) = \phi P(q) S(q) T(q), \tag{A.18}$$

with form factor $P(q)$, structure factor $S(q)$ and optical transfer function $T(q)$[15,20]. According to Ref.[15] the function $T(q)$ considers coherence of the light source, properties of the lens and the 3D nature of the object.

In the case of a dilute solution the structure factor is equal to 1, i.e. $S_0(q) = 1$, which results in $A(q) = \phi P(q) T(q)$. The form factor $P(q)$ of a dilute solution can be measured in light scattering experiments, complementing the DDM measurements. For this, the intensity I of the scattered light as a function of angle, or wave-vector q, is measured. The resulting $I(q) \sim P(q)$ continues the progression of $A(q)$, as it is shown in

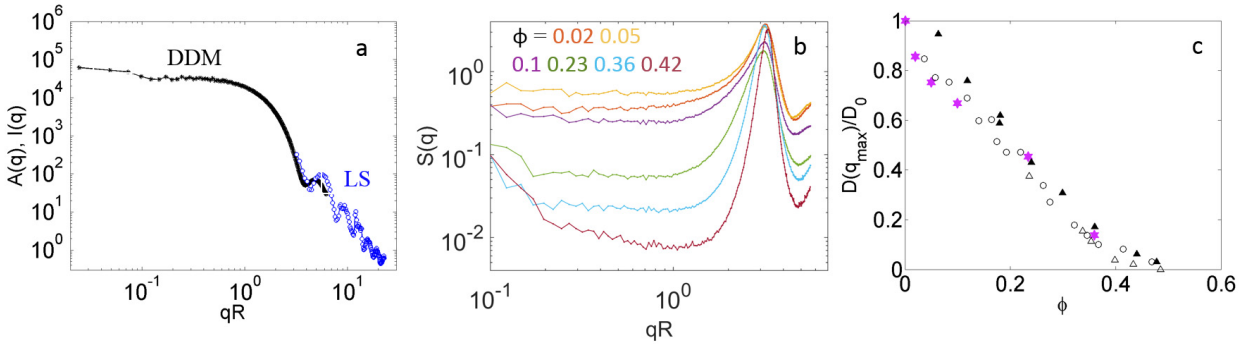

Figure A.6.: a) Amplitude $A(q)$ (Eq.(A.14)) for a dilute solution (black) and intensity $I(q)$ measured in a light scattering experiment (blue) as a function of q. Note that $I(q)$ was multiplited by a constant to allow for the comparison of the data. b) Structure factor $S(q)$ as a function of qR for different particle concentrations. c) The normalized diffusion coefficient $D(q_{max})/D_0$, where D_0 is the diffusion coefficient for the dilute solution, for different particle concentrations ($*$) obtained by DDM. (▲) Long-time diffusion coefficient of Ref.[21], (○) Ref.[22], (△) Ref.[23].

the Figure A.6 a). However, a slight shift to smaller q-values of $A(q)$ relative to $I(q)$ can be observed. This shift can be associated with the contribution of the transfer function $T(q)$ to the amplitude $A(q)$.

With increasing concentration, the functions $P(q)$ and $T(q)$ remain unchanged, since the particles and optical settings do not change. The structure factor on the other hand deviates more and more from 1 with increasing ϕ, see Figure A.6 b). The structure factor $S(q)$ is given by $S(q) = \phi_0 A(q)/\phi A_0(q)$, where ϕ_0 is the volume fraction and $A_0(q)$ the amplitude of the dilute solution, respectively[20]. It should be noted that the pinhole set for $\phi = 0.02, 0.05$ are smaller as for all other measurements (7.2 a.u. for $\phi = 0.02, 0.05$ and 7.8 a.u. otherwise). This difference in the size of the pinhole results in a deviation in the transfer function and as a consequence also in the corresponding $S(q)$[15,20] .

From the DDM measurements the diffusion coefficient can be determined according to $D(q_{max}) = 1/q_{max}^2 \tau^n$, with q_{max} the q-value at the maximum of $S(q)$. Figure A.6 c) shows the normalized diffusion coefficient $D(q_{max})/D_0$ for different particle concentrations, with D_0 the diffusion coefficient for the diluted solution. The dependence of $D(q_{max})/D_0$ on ϕ indicates a rapid decay with increasing concentration, as expected for a long-time diffusion coefficient. The results are in good agreement with previous light scattering measurements yielding the long-time diffusion coefficient $D(\phi)$ of hard spheres[21–23].

A.4.4. Limitations

This section brings into focus the limitations regarding the use of the DDM technique for the study of multi-component and highly-concentrated systems. Usually if we deal with multi-component systems we are interested in the dynamical properties of each component in the presence of the other species. Therefore, each population of particles should be distinguishable from the others.

One of the methods to determine the dynamical properties of dispersed particles is light scattering. This method is based on the analysis of light which is scattered off particle due to differences in the refractive indices of the particles and the liquid in which they are dispersed. Consequently, to measure dynamics of only one population of particles a variation of the refractive index is unavoidable. On the other hand, the variation of the refractive index, i.e. changing of the dielectric constant, implies some chemical modification and therefor also a modification of the interactions between the particles. To avoid this, the use of fluorescence microscopy is favorable. One species of the chemically identical particles is marked with a fluorescent marker. Moreover, the use of different markers allows to image each particle population separately. The illumination with light of a suitable wavelength excites the fluorescence. In this work different setups were tested.

The epi-fluorescence setup is composed of a LED fluorescence lamp used for illumination and an Andor Neo camera for image acquisition. Dispersions of fluorescently-labeled particles with different concentrations were studied. The increase of the particle concentration leads a reduction of the space in-between the spheres. Therefore more and more spheres are in the field of view and, consequently, the amount of the emitted light becomes larger as well. Additionally, the out-of-focus signal and the noise contribution becomes larger. At some critical concentration the intensity fluctuations due to the changes in the local density are not distinguishable from the noise anymore. The critical volume fraction depends on the resolution, i.e. the number of pixels per particle. Let us discuss two examples. If we take the images at high resolution with around $\frac{d}{d_{pix}} \approx 7.7$ pixels per particle diameter d, the resolution allows to detect small intensity fluctuations even at a concentration of $\phi \approx 0.4$. At the same time however the accessible q-range contains large values, which may be out of the range of interest (which is typically at small q-values). When we study particles with a small diameter resulting in $\frac{d}{d_{pix}} \approx 2.3$, the critical volume is reached already at $\phi \approx 0.2$. Note, that the same effect can be achieved by an increase of d_{pix}. Having taken this into account, it will not be surprising, that only very dilute suspension can be studied in the regime with $\frac{d}{d_{pix}} \lesssim 1$. In summary, the choice of the resolution has to be done with respect to the volume fraction of the

dispersed particles and the q-range of interest.

The second setup is a confocal microscope Nikon AR-I-MP. The illumination source used here is a laser. One of the main advantages of this kind of microscope is the reduction of the out-of-focus light, due to the integrated pinhole in the conjugate focal plane. Additionally, only a very small volume (a point) is illuminated. The full image is now acquired trough point-by-point scanning. Such a scanning method implies several limitations. If the particle is so fast that it moves significantly during the scan, not the particle itself but its track is imaged. In this case, instead of speckles, bright lines appear in the image. Also the imaging of half or part of a particle may appear, if the particle is initially in the focus and then moves out of focus before scanning the next line. In other words, the image obtained by scanning is not a snapshot at some time t, but it contains already the information of the short-time dynamics. Therefore, the choice of the particle size is limited not only by the resolution due to light diffraction, but rather by the scanning and recording speed of the microscope.

Another factor to be taken into account is the size of the pinhole. Advantageous for DDM is the imaging at fully opened pinholes. As discussed earlier, the size of the pinhole determines the optical thickness, i.e. the thickness of the layer from which light is collected. Reducing the size of the pinhole means that light from only a thin, nearly 2D sheet of the sample will be collected, resulting in a sharp image. The sharpness of the image may be important for particle tracking, but not for DDM. Much more important than the sharpness is the information about the density fluctuations in all three directions.

Bibliography

[1] T. Wilson, *Confocal Microscopy*, Academic Press, London, 1990.

[2] M. Minsky, *Scanning*, 1988, **10**, 128–138.

[3] R. S. Jardine and P. Bartlett, *Colloids Surf.*, 2002, **211**, 127 – 132.

[4] G. Bosma, C. Pathmamanoharan, E. H. de Hoog, W. K. Kegel, A. van Blaaderen and H. N. Lekkerkerker, *J. Colloid and Interf. Sci.*, 2002, **245**, 292 – 300.

[5] D. Woehrle, M. W. Tausch and W.-D. Stohrer, *Die konzeptionellen und theoretischen Grundlagen der Photochemie, in Photochemie: Konzepte, Methoden, Experimente*, Wiley-VCH Verlag GmbH and Co. KGaA, Weinheim, 1998.

[6] J. C. Crocker and D. G. Grier, *Journal of Colloid and Interface Science*, 1996, **179**, 298 – 310.

[7] R. G. Larson, *The Structure and Rheology of Complex Fluids*, Oxford University Press, Oxford, England, 1998.

[8] M. D. Haw, W. C. K. Poon, P. N. Pusey, P. Hebraud and F. Lequeux, *Phys. Rev. E*, 1998, **58**, 4673.

[9] P. Hébraud, F. Lequeux, J. P. Munch and D. J. Pine, *Phys. Rev. Lett.*, 1997, **78**, 4657.

[10] G. Petekidis, A. Moussaid and P. N. Pusey, *Phys. Rev. E*, 2002, **66**, 51402.

[11] D. Derks, H. Wisman, A. van Blaaderen and A. Imhof, *J. Phys.: Condens. Matter*, 2004, **16**, S3917.

[12] Y. Nicolas, M. Paques, D. van den Ende, J. K. Dhont, R. C. van Polanen, A. Knaebel, A. Steyer, J.-P. Munch, T. B. Blijdenstein and G. A. van Aken, *Food Hydrocolloids*, 2003, **17**, 907 – 913.

[13] R. Besseling, L. Isa, E. R. Weeks and W. C. Poon, *Adv. Colloid and Interf. Sci.*, 2009, **146**, 1 – 17.

[14] R. Cerbino and V. Trappe, *Phys. Rev. Lett.*, 2008, **100**, 188102.

[15] F. Giavazzi, D. Brogioli, V. Trappe, T. Bellini and R. Cerbino, *Phys. Rev. E*, 2009, **80**, 031403.

[16] V. A. Martinez, R. Besseling, O. A. Croze, J. Tailleur, M. Reufer, J. Schwarz-Linek, L. G. Wilson, M. A. Bees and W. C. Poon, *Biophys. J.*, 2012, **103**, 1637–1647.

[17] F. Giavazzi and R. Cerbino, *J. Opt.*, 2014, **16**, 083001.

[18] B. J. Berne and R. Pecora, *Dynamic Light Scattering: With Applications to Chemistry, Biology, and Physics*, Dover, New York, 2000.

[19] L. G. Wilson, V. A. Martinez, J. Schwarz-Linek, J. Tailleur, P. N. Pusey, G. Bryant and W. C. K. Poon, *Phys. Rev. Lett.*, 2011, **106**, 018101.

[20] P. J. Lu, F. Giavazzi, T. E. Angelini, E. Zaccarelli, F. Jargstorff, A. B. Schofield, J. N. Wilking, M. B. Romanowsky, D. A. Weitz and R. Cerbino, *Phys. Rev. Lett.*, 2012, **108**, 218103.

[21] A. van Blaaderen, J. Peetermans, G. Maret and J. K. G. Dhont, *J. Chem. Phys.*, 1992, **96**, 4591.

[22] W. van Megen and S. M. Underwood, *J.Chem.Phys.*, 1989, **91**, 552.

[23] W. van Megen and S. M. Underwood, *Langmuir*, 1990, **6(1)**, 35–42.

Eidesstattliche Versicherung

Ich versichere an Eides Statt, dass die Dissertation von mir selbstständig und ohne unzulässige fremde Hilfe unter Beachtung der Grundsätze zur Sicherung guter wissenschaftlicher Praxis an der Heinrich-Heine-Universität Düsseldorf erstellt worden ist.